DIRECT STRENGTH METHOD FOR THE DESIGN OF COLD-FORMED STEEL HAT SECTIONS UNDER LOCALISED LOADING

Zhehang Chen

Supervisors:

A. Prof. Cao Hung Pham

Prof. Gregory J. Hancock

A thesis submitted in fulfilment of the requirements for the degree of
Doctor of Philosophy

School of Civil Engineering
Faculty of Engineering
The University of Sydney
2025

Keywords

Direct Strength Method, cold-formed steel, hat sections, localised loading, Finite Element Method, Finite Strip Method, buckling load, yield/plastic mechanism model.

Abstract

This thesis investigates the application of the Direct Strength Method (DSM) in predicting the localised loading capacity of cold-formed steel hat sections. Four loading cases with various fastening conditions are studied. Experimental data from this study and previous research are utilised to develop a yield/plastic mechanism model for use in DSM, and to propose simplified and consistent DSM design equations for practical applications. The potential of utilising the DSM design equations for localise loading design is established through numerical, experimental and analytical investigations. Methods for calculating two significant inputs for DSM design equations, buckling load (P_{cr}) and yield load (P_y), have been investigated.

Finite Element Method (FEM) and Finite Strip Method (FSM) are widely accepted for calculating the buckling load of channel sections. A software program named THIN-WALL-PYTHON is developed and optimised for hat sections, employing FSM to calculate the buckling load. The buckling load results calculated by FSM are benchmarked with the result obtained using FEM software (ABAQUS).

Simplified yield/plastic mechanism models are developed for use in the hat sections under localised loading in various cases to calculate the yield load for DSM design equations. Extra considerations are included for accounting for the influence of web slope angle and the reduction of plastic moment capacity subject to axial compression, expanding the applicable range to sloped web sections. A complex but effective quadratic equation is derived to calculate the yield load and is validated using an iterative method. Experiments on hat sections with varying dimensions, particularly in the stocky range, are conducted to verify the analytical theory and numerical models. Two sets of numerical models featuring solid and shell elements are developed for parametric studies to provide better simulation results across different thicknesses. Factors influencing the localised loading capacity are investigated, identifying the e/t (eccentricity-to-thickness) value as a key determinant governing the shape of the DSM design curves.

Two sets of DSM design equations for hat sections under localised loading are developed based on experimental and numerical datasets. The Minimum Design Method (MDM) provides a conservative design by selecting preset curves based on

e/t values, while the Smooth Transition Method (STM) offers a convenient design approach by shifting curves based on the e/t value. Deviation and reliability analyses are conducted using the experimental data, and design capacity factors for both methods are proposed for all the investigated loading cases. The prediction results are compared with current standards and specifications (AS4600:2018 and AISI S100-16), demonstrating significant advancements in accuracy and applicability.

Statement of Original Authorship

This is to certify that to the best of my knowledge, the content of this thesis is my own work. This thesis has not been submitted for any degree or other purposes.

I certify that the intellectual content of this thesis is the product of my own work and that all the assistance received in preparing this thesis and sources has been acknowledged.

Zhehang Chen

26 June 2024

Acknowledgements

I would like to express my profound gratitude to my supervisors, Associate Professor Cao Hung Pham and Emeritus Professor Gregory J. Hancock, for their steadfast support and invaluable guidance throughout my research journey. Their deep expertise and unwavering commitment have been pivotal in the completion of this thesis. Without their continuous encouragement, achieving this milestone would not have been possible.

My heartfelt thanks also extend to the team at the JWR Laboratory. I am particularly grateful to Mr. Garry Towell, Mr. Paul Bustra, Mr. Alexandria Moore, Mr. James Ryder, and Mr. Paul Burrell for their assistance in the planning, preparation, and execution of my experiments.

I owe a special debt of gratitude to my parents, whose unending encouragement and financial backing have been crucial to my academic pursuits. As professionals in their respective fields, my mother, an English teacher, and my father, a civil engineer, have inspired me profoundly. I am equally thankful to my partner, whose enduring support and patience have been a great comfort to me throughout my PhD studies.

I am appreciative of Associate Professor Hao Zhang and Dr. Mike Bambach, who, as members of my annual progress review panel, provided insightful comments and recommendations that greatly enhanced my research. Additional thanks go to my classmates and colleagues, particularly Dr. Gen Li and Dr. Yang Hu from the University of Sydney, for their support during my PhD journey. A special mention goes to Germaine June Kennedy from Bundaberg, QLD, who first met my mother in China during the 1990s while my mother was working as her interpreter. Germaine's early support in my English study laid the foundation for my educational endeavours in Australia.

I would like to acknowledge the assistance provided by ChatGPT and Claude, which offered editorial suggestions that improve the readability of my content while preserving my original ideas.

This research is supported by an Australian Government Research Training Program (RTP) Fees Offset Scholarship.

Co-Author Signatures for Publications

The co-authors listed below certify that they have contributed to publications and/or manuscripts in this thesis and that they agree to the use of those publications and/or manuscripts in this thesis.

Cao Hung Pham

School of Civil Engineering, The University of Sydney, NSW 2006, Australia

Gregory J. Hancock

School of Civil Engineering, The University of Sydney, NSW 2006, Australia

Authorship attribution statement

This thesis contains material published in following two conferences:

Chen, Z., Pham, C.H., and Hancock, G.J., 2022. Yield Models for use in DSM Localised Loading Design of Hat Sections. *Cold-Formed Steel Research Consortium Colloquium 2022*.

Chen, Z., Pham, C.H., and Hancock, G.J., 2023. Plastic mechanism models for use in DSM localised loading design of hat sections under one-flange-loading. *Ninth International Conference on Thin-Walled Structures.*

Chen, Z., Pham, C.H., and Hancock, G.J., 2025. Plastic mechanism models for use in DSM localised loading design of hat sections. *Thin-Walled Structures Volume 206, Part B, January 2025, 112683.*

Contribution: Methodology, Software, Numerical and Experimental Study, Analysis, Data Curation and Writing – Original Draft.

Zhehang Chen

26 June 2024

Table of Contents

Keywords i

Abstract ii

Statement of Original Authorship iv

Acknowledgements v

Co-Author Signatures for Publications vi

Authorship attribution statement vii

Table of Contents viii

List of Figures xi

List of Tables xvii

Chapter 1 Introduction 1

1.1 Background 1

1.2 Significance of study 2

1.3 Objective of study 3

1.4 Research methodology 3

1.5 Thesis Outline 5

Chapter 2 Literature Review 7

2.1 Introduction 7

2.2 Current design standard and specifications 7

2.3 Crushing behaviour of hat sections subject to localised loading 10

2.4 Experimental study of hat sections subject to localised loading 14

2.5 Numerical study 18

2.6 The determination of Py – Plastic mechanism model 20

2.7 Direct Strength Method 23

2.8 A unified form of DSM design equations across different types of loadings 25

2.9 Summary of literature review 26

Chapter 3 Numerical study – buckling 27

3.1 Introduction 27

3.2 Buckling analysis using THIN-WALL-PYTHON 28

3.3 Buckling analysis using ABAQUS 40

3.4 Conclusion 51

Chapter 4 Experimental study on failure modes of cold formed steel sections 53

4.1 Introduction 53

4.2 Experimental program 54

4.3 Test result and discussion 71
4.4 Summary 86
Chapter 5 Numerical study – nonlinearities 89
5.1 Introduction 89
5.2 FEM modelling of hat sections 90
5.3 Parametric study: effect of section parameters 119
5.4 Conclusion 135
Chapter 6 Plastic mechanism models and preliminary DSM design 137
6.1 Introduction 137
6.2 The development of Plastic mechanism model 137
6.3 the preliminary proposal of DSM design equations 151
6.4 Initial findings from the preliminary DSM design equations 152
6.5 Conclusion 157
Chapter 7 Advanced DSM design equations for hat sections under localised loading 161
7.1 Introduction 161
7.2 Exploration of the DSM design equation options 162
7.3 Selection of DSM design curves 176
7.4 Comparison Between the prediction results and AS4600 191
7.5 Reliability analysis 194
7.6 Calculation example 197
7.7 Comaprsion between current design standard and DSM design equations 202
7.8 Conclusion 203
Chapter 8 Conclusions and future study 205
8.1 Introduction 205
8.2 Conclusion of the thesis 205
8.3 Limitations and suggestions for future research 207
Bibliography 211
Appendices 217
Appendix A Coupon test data (stress – strain curve) 217
Appendix B Measured dimensions of hat sections 220
Appendix C List of all valid experimental results by Chen (Load – Displacement curve) ..222
Appendix D e/t data in Figure 132 229
Appendix E Experimental data for use in calibration of DSM design equations 230
Appendix F DSM design equations calculation data 245
Appendix G Numerical study data set used in Chapter 7 252
Appendix H Alternative method for the calculation of reduced plastic moment capacity ...266

Appendix I Comparison between AS4600 and DSM design equations (MDM) 276
Appendix J Miscellaneous 280

List of Figures

Figure 1 Research methodology ... 4

Figure 2 Rolling mechanism modelled with the moving yield lines presented in [4] ... 10

Figure 3 Web deformation in the yield arc mechanism ... 11

Figure 4 Determination of the experimental mechanism initiation load in members failing by the rolling mechanism presented in [4] ... 12

Figure 5 Idealised yield line pattern in a member failed by the rolling mechanism presented in [4] ... 13

Figure 6 Testing arrangements reported in Santaputra and Yu [15] ... 16

Figure 7 Plastic mechanism models for different loading cases and sections developed by Nguyen [23] ... 21

Figure 8 Main window of the THIN-WALL-PYTHON ... 29

Figure 9 Hat sections with return lips (L) and without return lips (R) ... 30

Figure 10 Node allocation of typical hat sections with lips ... 31

Figure 11 Node allocation of typical hat sections without lips ... 32

Figure 12 Boundary condition demonstration for a typical hat section with fastened condition ... 33

Figure 13 Input length for ITF and ETF loading cases ... 35

Figure 14 Input length for IOF loading case ... 35

Figure 15 Input length for EOF loading case ... 36

Figure 16 Typical setup of THIN-WALL-PYTHON for ITF-F loading case ... 36

Figure 17 Typical setup of THIN-WALL-PYTHON for ETF-F loading case ... 37

Figure 18 Typical setup of THIN-WALL-PYTHON for IOF-F loading case ... 37

Figure 19 Typical setup of THIN-WALL-PYTHON for EOF-F loading case ... 37

Figure 20 Typical setup of THIN-WALL-PYTHON for EOF-UF loading case ... 38

Figure 21 Hat section cross section dimension, H120-RIN3-DEG0 ... 38

Figure 22 Typical result page from THIN-WALL-PYTHON ... 38

Figure 23 Buckling shape for ITF-F-H120-RIN3-DEG0-N50 at Section No. 10 ... 39

Figure 24 Typical 3D Wireframe Plot in ITF-F loading condition (3D buckling mode) ... 40

Figure 25 Typical 3D Surface Filled with Colour Contour in ITF-F loading condition (3D buckling mode) ... 40

Figure 26 Distribution of datum plates and application of point loads ... 43

Figure 27 Global seeds setting in buckling analysis ... 45

Figure 28 Buckling analysis result from ABAQUS for specimen ITF-F-H120-RIN3-DEG0-N50 (first buckling mode) 45

Figure 29 Comparison of buckling load between ABAQUS (FEM) and THIN-WALL-PYTHON (FSM) 46

Figure 30 Typical BC setup in ABAQUS using PRM (restraint only apply within bearing length) 47

Figure 31 Comparison of buckling load between THIN-WALL-PYTHON and ABAQUS with different methods 48

Figure 32 single and double ribs hat sections tested by Wu et al. [16] 53

Figure 33 Detail of dimension 55

Figure 34 Typical coupon test setup 57

Figure 35 Typical stress – strain curve for HA250, 3 mm, strain = 0 - 0.1 (L) and 0 - 0.5 (R) 57

Figure 36 Correlation between specimen direction and material direction 59

Figure 37 End view of two flange loading test setup in MTS Machine 64

Figure 38 Interior Two-Flange Loading (ITF) in AISI S909-17 65

Figure 39 End Two-Flange Loading (ETF) in AISI S909-17 65

Figure 40 ITF loading case setup 66

Figure 41 ETF loading case setup (view from the unsupported end) 66

Figure 42 Test rig for OF loading cases 69

Figure 43 Assembly with bearing plates (IOF loading case) including half rounds and specimen 69

Figure 44 Stiffening plate for EOF loading cases (painted orange) bolted to the side of the web 69

Figure 45 Interior One-Flange Loading (IOF) in AISI S909-17 70

Figure 46 End One-Flange Loading (EOF) in AISI S909-17 70

Figure 47 Out-of-plane bending for ITF loading case, 3mm radius section 74

Figure 48 Out-of-plane bending for ITF loading case, 8 mm radius section 74

Figure 49 Typical L-D curve for small-radius and large-radius sections in ITF load case 74

Figure 50 L - D curve, ITF-F-H120-DEG30-N50 76

Figure 51 Bearing plate rotation for ETF-F 77

Figure 52 ETF-F plastic hinge for small (L) and large (R) corner radii 77

Figure 53 L - D curve comparison between vertical web and sloped web sections, ETF-F 78

Figure 54 Figure of IOF-F-H120-RIN3-DEG0-N50 79

Figure 55 IOF-F loading case typical initial rolling mechanism at lower deformation 80

Figure 56 Hinge formation (indicated by yellow arrow) on the web for large corner radius section under IOF-F loading case 80

Figure 57 Comparison of L - D curves between vertical web sections and sloped web sections, IOF-F for small and large corner radii 81

Figure 58 Typical failure mode of vertical web sections with small RIN for EOF-F loading case... 82

Figure 59 Typical failure mode of vertical web sections with large RIN for EOF-F loading case... 83

Figure 60 Typical asymmetric deformation for EOF-F loading case 83

Figure 61 flexural failure followed by web crippling 84

Figure 62 EOF-F-H120-RIN8-DEG30-N50, with 50 mm middle bearing plate....... 85

Figure 63 comparison of L-D curves between 50 mm mid bearing plate (MB50, dash line) and 100 mm mid bearing plate (MB100, solid/dotted line) 85

Figure 64 Typical photo of curling of bottom flange.. 86

Figure 65 Comparison of the L-D curves regard EOF-F and EOF-UF 86

Figure 66 Typical experimental setup for ITF loading case 94

Figure 67 Typical experimental setup for ETF loading case 94

Figure 68 L - D curve comparison between “hard” contact and “linear” contact with k = 5000 96

Figure 69 Typical master and slave surface in contact setting.................................. 97

Figure 70 Typical example of reference point location referencing to the bearing plate 97

Figure 71 Typical mesh size setup for the specimen 100

Figure 72 L - D curves with imperfections (L: RIN = 3 mm, R: RIN = 8 mm) 103

Figure 73 Typical experimental setup for IOF loading case................................... 105

Figure 74 Typical experimental setup for IOF loading case................................... 105

Figure 75 IOF & EOF “rigid body” setup locations 105

Figure 76 ITF-F-RIN3 107

Figure 77 ITF-F-RIN8 107

Figure 78 ETF-F-RIN3 107

Figure 79 ETF-F-RIN8 107

Figure 80 IOF-F-RIN3 108

Figure 81 IOF-F-RIN8 108

Figure 82 EOF-F-RIN3 108

Figure 83 EOF-F-RIN8 108

Figure 84 EOF-UF-RIN3 109

Figure 85 EOF-UF-RIN8 109

Figure 86 ITF-F-H120-DEG0-N50 (L: RIN=3, R: RIN=8) 110
Figure 87 ITF-F-H120-DEG15-N50 (L: RIN=3, R: RIN=8) 110
Figure 88 ETF-F-H120-DEG0-N50 (L: RIN=3, R: RIN=8) 110
Figure 89 ETF-F-H120-DEG15-N50 (L: RIN=3, R: RIN=8) 111
Figure 90 IOF-F-H120-DEG0-N50-L600 (L: RIN=3, R: RIN=8) 111
Figure 91 IOF-F-H120-DEG15-N50-L600 (L: RIN=3, R: RIN=8) 111
Figure 92 EOF-F-H120-DEG0-N50-600 (L: RIN=3, R: RIN=8)........................... 112
Figure 93 EOF-F-H120-DEG15-N50-L600 (L: RIN=3, R: RIN=8) 112
Figure 94 EOF-UF-H120-DEG0-N50-L600 (L: RIN=3, R: RIN=8) 112
Figure 95 Symmetric failure at two ends for EOF loading case, experimental study photo 113
Figure 96 ABAQUS simulation – symmetric failure... 114
Figure 97 Asymmetric failure at two ends for EOF loading case, experimental study photo 114
Figure 98 ABAQUS simulation – asymmetric failure 114
Figure 99 Comparison of experimental results and numerical results using solid and shell elements from tests by Chen et al. [36] 118
Figure 100 A typical section undergoing a combine failure mode 120
Figure 101 L-D curves for various corner radii, ITF-F (Shell)............................... 121
Figure 102 L-D curves for various corner radii, IOF (Shell)................................. 121
Figure 103 Bearing length location demonstration using ITF loading case (shown as N) 122
Figure 104 Demonstration of yield-arc failure mode.. 122
Figure 105 Demonstration of rolling post failure mode (bottom bearing plate omitted) 123
Figure 106 L-D curves for various bearing length, ITF-F (Shell) 123
Figure 107 L-D curves for various bearing length, IOF-F (Shell).......................... 124
Figure 108 L-D curves by changing the height, ITF-F-DEG0-N50 (Shell) 124
Figure 109 L - D curves by changing the height at minimum length, H90-L420, H120-L510 and H150-L600 (Shell)... 125
Figure 110 Definition of dimensions (Same as Figure 33) 126
Figure 111 L-D curves by changing the sloped angle of the web, ITF-F-H120-RIN3 (Solid element) 127
Figure 112 L-D curves by changing the sloped angle of the web, ITF-F-H120-RIN8 (Solid element) 128
Figure 113 L-D curves comparison between ETF-F (solid line) and ETF-UF (dot line)... 130

Figure 114 L-D curves comparison by changing top flange width, ITF-F-H120-DEG0-N50 131

Figure 115 L-D curves comparison between 1.5h (solid) method and 1.5H method (dash) 133

Figure 116 L-D curve comparison between 1.5H method (dash) and fix length method (solid) 134

Figure 117 Plastic mechanism model for hat sections: ITF-F and ETF-F loading cases 138

Figure 118 Plastic mechanism model for hat sections: ITF-UF and ETF-UF loading cases 138

Figure 119 Side view of general plastic mechanism model and detail of the slope 142

Figure 120 Plastic mechanism model for hat sections: IOF-F/UF loading cases 144

Figure 121 Plastic mechanism model for hat sections: EOF-F(a) and EOF-UF(b) loading cases 144

Figure 122 Eccentricity (e), internal corner radius (r_{in}) and centreline corner radius (r_c) 146

Figure 123 Preliminary DSM curve for hat sections, ITF fastened (L) and ETF fastened (R) 153

Figure 124 Preliminary DSM curve for hat sections, IOF fastened (L) and EOF fastened (R) 153

Figure 125 Preliminary DSM curve for hat sections, EOF unfastened 153

Figure 126 DSM curve for the IOF and EOF loading cases for C sections from Nguyen et al.[28] 154

Figure 127 Yield arc mechanism and rolling mechanism defined by Bakker and Stark [9] (Same as Figures 2 and 3) 155

Figure 128 The movement of the maximum horizontal displacement points on the webs as the loading process continues 156

Figure 129 Typical L-D curve for small-radius and large-radius sections in ITF load case 156

Figure 130 A typical rolling mechanism, the contact point (action point) is moving from A to B towards the orange dash line 157

Figure 131 Relation between eccentricity (e), internal corner radius (r_{in}) and centreline corner radius (r_c) (Same as Figure 122) 161

Figure 132 Relationship between e/t and RIN, DEG (t = 3 mm) 163

Figure 133 DSM design curve for the ITF-F loading case 166

Figure 134 DSM design curve for the ETF-F loading case 166

Figure 135 DSM design curve for the IOF-F loading case 167

Figure 136 DSM design curve for the EOF-F loading case 167

Figure 137 DSM design curve for the ITF-F loading case including ITF-UF test data 168

Figure 138 DSM design curve for the ETF-F loading case including ETF-UF test data 168

Figure 139 DSM design curve for the IOF-F loading case including IOF-UF test data 169

Figure 140 DSM design curve for the EOF-UF loading case including EOF-UF test data 169

Figure 141 ITF experimental and numerical data group by e/t range 172

Figure 142 ETF experimental and numerical data grouped by e/t range 172

Figure 143 IOF experimental and numerical data grouped by e/t range 173

Figure 144 EOF-F experimental and numerical data grouped by e/t range 173

Figure 145 ITF-UF experimental and numerical data grouped by e/t range 174

Figure 146 ETF-UF experimental and numerical data grouped by e/t range 174

Figure 147 IOF-UF experimental and numerical data grouped by e/t range 175

Figure 148 EOF-UF experimental and numerical data grouped by e/t range 175

Figure 149 DSM design curves for the ITF-F/UF loading cases (MDM) 178

Figure 150 DSM design curves for the ETF-F/UF loading cases (MDM) 179

Figure 151 DSM design curves for the IOF-F/UF loading cases (MDM) 179

Figure 152 DSM design curves for the EOF-F/UF loading case (MDM) 179

Figure 153 DSM design curves for the ITF-F/UF loading cases (STM) 180

Figure 154 DSM design curves for the ETF-F/UF loading cases (STM) 181

Figure 155 DSM design curves for the IOF-F/UF loading cases (STM) 181

Figure 156 DSM design curves for the EOF-F/UF loading case (STM) 181

Figure 157 Typical stress-strain curves of five sheet steels in Longitudinal tension given by Santaputra 186

Figure 158 Hat section cross-section dimensions for calculation example (Unit: mm) 198

Figure 159 Plastic mechanism model for a typical hat section: ITF loading case ... 200

Figure 160 Comparison of the experimental results ($PEXP$) against prediction results: AS4600 (PAS) and DSM design equations ($PDSM$), for vertical sections without safety factors 202

Figure 161 Comparison of Py using I-method (10 iterations) and Q-method 268

Figure 162 Comparison of Py using I-method (100 iterations) and Q-method 268

List of Tables

Table 1 Table 3.3.6.2(D) in AS/NZS 4600:2018 9
Table 2 Table 3.3.6.2(E) in AS/NZS 4600:2018 9
Table 3 Factors for plastic mechanism models presented by Nguyen 23
Table 4 DSM parameters proposed by Nguyen 24
Table 5 DSM equation Summary presented by Schafer and Glauz 25
Table 6 Typical node number allocation for hat sections with return lips 31
Table 7 Typical node number allocation for hat sections without return lips 31
Table 8 Loading cases and boundary conditions 32
Table 9 the AVE, StdDev and COV of $Pcr(FEM)/Pcr(FSM)$ 46
Table 10 A complete list of hat sections for use in Section 3.3.3 49
Table 11 Buckling load from THIN-WALL-PYTHON, ABAQUS (FRM) and ABAQUS (PRM) 50
Table 12 Collection of material property 57
Table 13 Nomenclature: Abbreviations, symbols and notes 62
Table 14 Number of tested specimens by loading cases and fastening conditions 62
Table 15 Numbering system for all tests 63
Table 16 Test results for all loading cases (Ultimate web crippling capacity at 10 mm displacement if maximum not reached) 72
Table 17 The selection of imperfection by various researchers 102
Table 18 List of FE models with imperfection and criteria 102
Table 19 AVE and StdDev of P_exp/P_solid and P_exp/P_shell 118
Table 20 FEM result comparison between 1.5h (solid) method and 1.5H method (dash) 134
Table 21 FE result comparison between 1.5H method (dash) and fix length method (solid) 134
Table 22 FE result comparison between 1.5H method and fix length method for H90 sections 135
Table 23 Summary of the exponents and factors for the Py model (TF) 142
Table 24 Summary of the exponents and factors for the Py model (OF) 145
Table 25 Summary of the exponents and factors for the Py model – location and length factors 150
Table 26 Summary of the exponents and factors for the Py model – rotation factors 150

Table 27 Summary of the exponents and factors for the Py model – yield line existence factors 150
Table 28 A summary of the exponent of DSM design equations (preliminary) 152
Table 29 Data groups with sources 162
Table 30 The calculation of the eccentricity and e/t of Chen's hat sections 163
Table 31 The base DSM design equations coefficients for fastened cases 165
Table 32 Comparison of the base DSM design equations coefficients between EOF-F and EOF-UF 169
Table 33 Coefficients for each design group using MDM 177
Table 34 Coefficient for each design group using STM 180
Table 35 Summary of AVE of Pexp/Pn (MDM) 183
Table 36 Summary of StdDev of Pexp/Pn (MDM) 183
Table 37 Summary of COV of Pexp/Pn (MDM) 183
Table 38 Summary of AVE of Pexp/Pn (STM) 184
Table 39 Summary of StdDev of Pexp/Pn (STM) 184
Table 40 Summary of COV of Pexp/Pn (STM) 184
Table 41 AVE, StdDev and COV of Pexp/Pn grouped by yield strength 185
Table 42 FEM result vs DSM design equation prediction using Minimum Design Method 186
Table 43 Limit of applicability for member design in Chapters E through H by the EWM and DSM 187
Table 44 Summary of material used by Santaputra 188
Table 45 Summary of AVE of Pexp/Pn (MDM) with 800MPa limit 189
Table 46 Summary of StdDev of Pexp/Pn (MDM) with 800MPa limit 189
Table 47 Summary of COV of Pexp/Pn (MDM) with 800MPa limit 189
Table 48 Summary of AVE of Pexp/Pn (STM) with 800MPa limit 190
Table 49 Summary of StdDev of Pexp/Pn (STM) with 800MPa limit 190
Table 50 Summary of COV of Pexp/Pn (STM) with 800MPa limit 190
Table 51 Table 3.3.6.2(D) in AS/NZS 4600:2018 (single hat sections) 191
Table 52 Table 3.3.6.2(E) in AS/NZS 4600:2018 (multiple-web deck sections) 191
Table 53 Comparison of AVE values of different design equations 193
Table 54 Comparison of StdDev values of different design equations 193
Table 55 Comparison of COV values of different design equations 193
Table 56 Statistical data for the determination of resistance factor (Table K2.1.1-1 in AISI S100-16) 196
Table 57 Reliability Analysis for DSM design equation using MDM 196
Table 58 Reliability Analysis for DSM design equation using STM 197

Table 59 Deviation analysis regarding $PEXP/PAS$ and $PEXP/PDSM$.................. 203

Chapter 1 Introduction

1.1 BACKGROUND

In recent years, cold-formed steel (CFS) members have become increasingly popular worldwide, used extensively in the construction industry both as structural and non-structural elements. Beyond construction, their applications span automotive manufacturing, storage solutions, railway coaches, highway products, and towers for transmission and telecommunication. Unlike hot-rolled steel, which is shaped at high temperatures mainly through rolling, CFS products are manufactured at near-room temperatures through cold-working processes such as rolling, pressing, stamping, and bending. This manufacturing approach enables the production of custom-made CFS products, accommodating a broader spectrum of requirements to meet diverse needs effectively.

The primary advantage of using cold-formed steel (CFS) in construction lies in its exceptional strength-to-weight ratio. The cold-rolling process allows for the production of materials with minimal thickness, down to 0.42 mm, while still achieving high strength levels of up to 550MPa. This significant strength-to-weight ratio brings numerous benefits, including, but not limited to: (1) reduced structural self-weight, (2) simplified fabrication and manufacturing processes, (3) streamlined transportation, erection, and installation, contributing to faster project completion, (4) resistance to termites, rot, and combustion, enhancing durability and safety, and (5) full recyclability, supporting sustainable construction practices. Together, these advantages can lead to considerable cost savings in the construction process.

Cold-formed steel members are typically shaped through bending processes. Common forms include channels, zeds, hats, and decking, along with specialized products like SupaCees, SupaZeds, Dimond Hi-Span (DHS), and built-up I and box sections. Due to their relatively thin profiles, cold-formed steel members exhibit failure modes and behaviours distinct from traditional hot-rolled steel sections. Additionally, the thin material of cold-formed steel members leads to unique structural responses to imperfections and residual stresses introduced during manufacturing. Consequently, design specifications and standards for cold-formed steel members are specifically tailored, differing from those applicable to hot-rolled steel.

1.2 SIGNIFICANCE OF STUDY

Cold-formed steel beams are subject to various types of failure, including compression, flexural (bending), shear, and combinations of these forces. Design rules for these failure types have been well developed and incorporated into current standards, such as AISI S100-16 [1] in North America and AS/NZS 4600:2018 [2] in Australia and New Zealand. There is a unique type of failure, namely web crippling, which is a form of localised failure that occurs at points of transverse concentrated loading or supports of thin-walled steel beams.

Members may serve as primary or secondary components in structures, where the contact area between primary and secondary members is typically small. Such concentrated loads over a small area are known as localised loading. While hot-rolled steel sections usually have sufficient thickness and robustness to withstand these loads without significant issues, cold-formed steel members are at a higher risk of web crippling failure when subjected to localised loading due to their unique structural characteristics – high depth to thickness ratio and eccentric load through the rounded corner. While there is a typical solution for hot rolled members like providing extra stiffeners and support for the web in certain area, it’s impossible and impractical to apply these amendments to cold formed steel members. Thus, a proper prediction of the localised loading capacity for cold-formed steel members is of great importance.

According to the standards and specifications, there are four different loading cases which are defined by the locations of the load: Interior One-Flange loading (IOF), End One-Flange loading (EOF), Interior Two-Flange loading (ITF) and End Two-Flange loading (ETF). Each of the loading cases corresponds to different failure mechanism.

Over the last few decades, researchers have made significant progress in identifying web crippling failure modes across various cold-formed steel (CFS) section types. Empirical equations for predicting localised loading capacity have been successfully developed and adopted in the design standards and specifications for channels (C), Z-sections, hat sections, and decking. A notable advancement in recent years has been the development of simplified and consistent design equations for localised loading on various channel sections, showcasing the feasibility of applying the Direct Strength Method (DSM) for localised loading predictions. Key inputs for DSM, namely as yield loads and buckling loads, are determined using plastic mechanism models and an enhanced version of the Semi-Analytical Finite Strip Method (SAFSM), respectively.

However, the design equations for hat sections have not been updated for some time and appear somewhat outdated. Existing empirical equations mainly cover hat sections with vertical webs, omitting the vast array of hat sections with sloped webs now prevalent in the market. In addition, those previously adopted empirical equations does not include any understanding of structural behaviour. Therefore, updating the design approach for localised loading to address these shortcomings and incorporate a broader spectrum of hat section geometries and behaviours is crucial.

1.3 OBJECTIVE OF STUDY

The objective of this study includes the following:

- To investigate the plastic mechanism behaviour of hat sections with different parameters subject to various types localised loading. This involves an extensive experimental study alongside the verification of a numerical model against experimental results.
- To develop suitable models and methods for the calculation of yield load (P_y) and buckling load (P_{cr}) in accordance with the DSM concept under different practical load cases. This objective includes exploring and comparing potential methods for accurately determining P_y and P_{cr}.
- To develop simplified and consistent DSM design equations for hat sections subject to localise loading. The new equations will be backed by calibration with a collection of relevant experimental data and supplemented with reliability analysis to ensure their applicability and accuracy.

1.4 RESEARCH METHODOLOGY

The methodology of this research is illustrated in Figure 1.

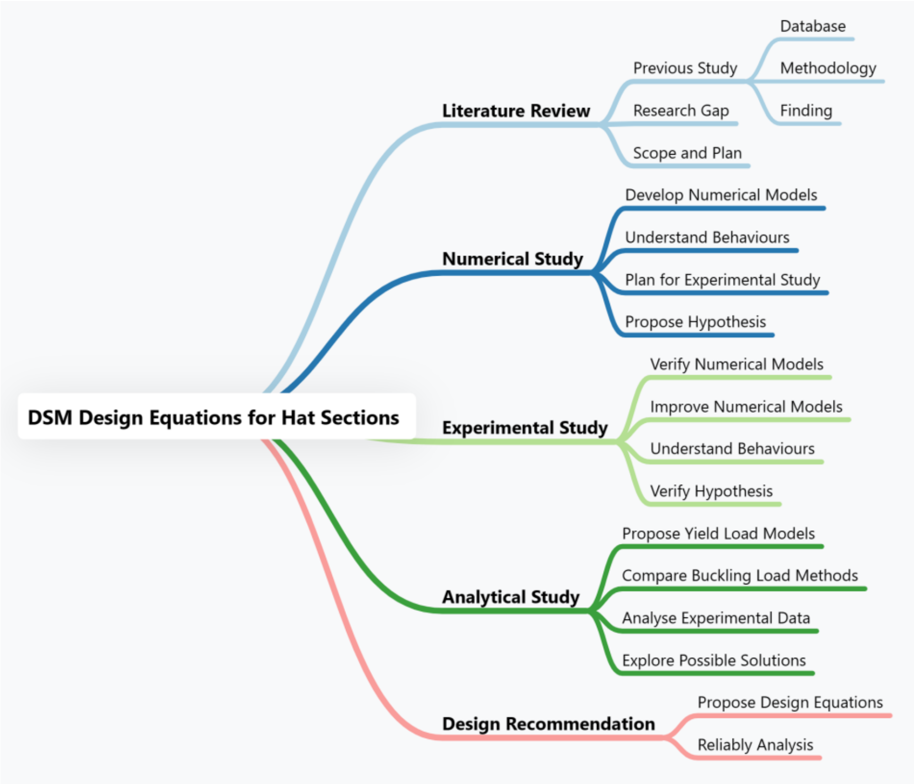

Figure 1 Research methodology

The initial phase involved an exhaustive literature review to establish a database of relevant existing studies. This review identified the research gaps, thus framing the scope and plan of the investigation. Particular focus was placed on previous studies that have developed models for hat sections and the findings that have emerged from these studies.

Following the literature review, numerical models were developed to understand the behaviour of hat sections under various load conditions. Due to the restrictions imposed by COVID-19, a preliminary stage of numerical analysis was performed to prepare for the experimental study once the restrictions were lifted. These models served as the foundation upon which the experimental study was planned, and subsequently, hypotheses were proposed as a reference for further study.

With the guidance of the numerical study, the experimental study was designed, and physical hat section specimens were then tested, allowing for an understanding of their behaviours in a controlled environment. Hypotheses proposed from the numerical models were verified and implemented during this time. The experimental data were collected, and numerical models were improved for parametric study.

In the next stage, an analytical study was conducted. Armed with data from both numerical and experimental studies, yield models were then proposed. Simultaneously, the results from different buckling load methods were compared to identify the best available options. This stage was crucial for exploring possible solutions and formulating design equations for hat sections.

In the final stage, the culmination of the research was the proposal of DSM design equations for hat sections, backed by a reliability analysis to ensure the practical application of the research findings. The aim was to contribute meaningful advancements in the field through these recommendations, supported by a rigorous validation process of the proposed equations.

1.5 THESIS OUTLINE

Chapter 1 provides an overview of the research project, including the context, significance of the study, objectives, and research methodologies employed.

Chapter 2 presents an in-depth literature review on relevant research into web crippling and the behaviour of hat sections subjected to localised loading. The methodologies and findings presented in previous studies are discussed and summarized to identify existing research gaps.

Chapter 3 offers a comprehensive discussion on buckling analyses using both the enhanced Finite Strip Method (FSM) and the Finite Element Method (FEM). The detailed Finite Element Method modelling process is also discussed. A comparison of both methods is carried out, demonstrating the validity of each approach.

Chapter 4 covers the comprehensive experimental program, including the design of the specimens, test configurations, results, and findings for all loading cases. For each loading case, sections with vertical webs and sloped webs are tested and compared. Additionally, this chapter addresses issues encountered during the experimental program.

Chapter 5 introduces the numerical study regarding the yielding behaviour of hat sections subjected to localised loading. In the first part, the detailed modelling method is presented, with both shell element and solid element models introduced. The second part includes a thorough discussion on the parametric study.

Chapter 6 first presents the plastic mechanism model used for calculating the yield load tailored for hat sections subjected to localised loading. A calculation example is also provided to demonstrate the calculation. Then, preliminary versions of the Direct Strength Method (DSM) design equations are proposed based on covering the minimum design value. Lastly, an explanation regarding the conservative prediction for large corner radius sections is discussed. Additionally, possible solutions for amending the DSM design equation for large corner radius sections are proposed.

Chapter 7 discusses two potential methods for improving the DSM design equations for various corner radii. A reliability analysis, along with a comparison between the newly proposed methods and the current standards listed in AS/NZS 4600, is also covered. Both FEM and experimental data are used in this chapter.

Chapter 8 presents the conclusions of the thesis and offers recommendations for future research.

Chapter 2 Literature Review

2.1 INTRODUCTION

This chapter aims to comprehensively review previous research related to the behaviour of hat sections under localised loading. This comprehensive overview seeks to bridge existing research gaps and contribute to the refinement of design practices for cold-formed steel sections under localised loading conditions.

Initially, the chapter introduces current design standards for predicting localised loading capacity, specifically web crippling capacity, in accordance with AISI S100-16 [1] and AS4600:2018 [2]. Following this, attention is turned to the historical analysis of localised loading on hat sections, with a particular focus on crushing behaviour under various loading cases. Subsequently, previous experimental investigations into hat sections under localised loading are meticulously reviewed. Relevant data from these studies are collected for the purpose of calibrating new equations. Finally, the chapter discusses recent advancements in Direct Strength Method (DSM) design equations. It covers empirical DSM design equations developed for channel sections under localised loading and explores a novel set of DSM design equations designed for members subjected to a variety of loading types.

2.2 CURRENT DESIGN STANDARD AND SPECIFICATIONS

The nominal localised loading capacity of hat sections can be calculated using either AS/NZS 4600:2018 [2], published by Standards Australia, or its similar counterpart, AISI S100-16 [1], published by the American Iron and Steel Institute. Note that AS/NZS 4600 calls it “Bearing Capacity” whereas AISI-S100 calls it “Web Crippling Strength”. For most of the commonly seen hat sections, the bearing capacity, or web crippling strength, are classified as design for bearing without holes. According to AS/NZS 4600:2018, Clause 3.3.6.2, the nominal capacity for concentrated load or reaction for one solid web connecting top flange and bottom flanges (R_b) shall be determined as follows:

$$R_b = C t_w^2 f_y \sin\theta \left(1 - C_r\sqrt{\frac{r_i}{t_w}}\right)\left(1 + C_l\sqrt{\frac{l_b}{t_w}}\right)\left(1 - C_w\sqrt{\frac{d_1}{t_w}}\right) \qquad (2\text{-}1)$$

where

C is the coefficient;

t_w is the thickness of the web;

θ is angle between the plane of the web and the plane of the bearing surface. θ shall be within the following limits: $90° \geq \theta \geq 45°$;

C_r is coefficient of inside bent radius;

r_i is inside bent radius;

C_l is coefficient of bearing length;

l_b is actual bearing length. For the case of two equal and opposite concentrated loads distributed over unequal bearing lengths, the smaller value of l_b shall be taken;

C_w is coefficient of web slenderness;

d_1 is the depth of the flat portion of the web measured along the plane of the web.

The standard also provides a definition for classification of one-flange and two-flange loading cases.

- One-Flange loading (IOF or EOF), or reaction occurs when the clear distance between the bearing edges of adjacent opposite concentrated actions or reactions is greater than $1.5d_1$.
- Two-Flange loading (ITF or ETF), or reaction occurs when the clear distance between the bearing edges of adjacent opposite concentrated actions or reactions is less than or equal to $1.5d_1$.
- End loading (EOF or ETF), or reaction occurs when the distance from the edge of the bearing to the end of the member is less than or equal to $1.5d_1$.
- Interior loading (IOF or EOF), or reaction occurs when the distance from the edge of the bearing to the end of the member is greater than $1.5d_1$.

It's important to note that AS/NZS 4600:2018 provides two calculation options applicable to multi-web sections. One option is to use the hat section table labelled as Table 3.3.6.2(D) as shown in Table 1, while the other is to use the multi-web decking table, referred to as Table 3.3.6.2(E) as shown in Table 2. Despite the title of Table

3.3.6.2(D) being "SINGLE HAT SECTIONS", there is a restriction in this table limiting the θ (theta) value to 90 degrees only. Consequently, Table 3.3.6.2(D) is not suitable for hat sections with sloped webs.

Table 1 Table 3.3.6.2(D) in AS/NZS 4600:2018

Load cases	C	C_r	C_l	C_w	ϕ_w	**Limits**
EOF-F	4	0.25	0.68	0.04	0.75	$r_i/t_w \leq 5$
IOF-F	17	0.13	0.13	0.04	0.80	$r_i/t_w \leq 10$
ETF-F	9	0.10	0.07	0.03	0.85	$r_i/t_w \leq 10$
ITF-F	10	0.14	0.22	0.02	0.85	$r_i/t_w \leq 10$
EOF-UF	4	0.25	0.68	0.04	0.75	$r_i/t_w \leq 4$
IOF-UF	17	0.13	0.13	0.04	0.90	$r_i/t_w \leq 4$

NOTE: The coefficient in this table apply if $d_1/t_w \leq 200$, $l_b/t_w \leq 200$, $l_b/d_1 \leq 2.0$ and $\theta = 90°$. "-F" denotes fastened and "-UF" denotes unfastened.

Table 2 Table 3.3.6.2(E) in AS/NZS 4600:2018

Load cases	C	C_r	C_l	C_w	ϕ_w	**Limits**
EOF-F	4	0.04	0.25	0.025	0.90	$r_i/t_w \leq 20$
IOF-F	8	0.10	0.17	0.004	0.85	$r_i/t_w \leq 10$
ETF-F	9	0.12	0.14	0.040	0.85	$r_i/t_w \leq 10$
ITF-F	10	0.11	0.21	0.020	0.85	$r_i/t_w \leq 10$
EOF-UF	3	0.04	0.29	0.028	0.60	$r_i/t_w \leq 20$
IOF-UF	8	0.10	0.17	0.004	0.85	$r_i/t_w \leq 20$
ETF-UF	6	0.16	0.15	0.050	0.90	$r_i/t_w \leq 5$
ITF-UF	17	0.10	0.10	0.046	0.90	$r_i/t_w \leq 5$

NOTE: The coefficient in this table apply if $d_1/t_w \leq 200$, $l_b/t_w \leq 210$, $l_b/d_1 \leq 3.0$ and $45° < \theta \leq 90°$. "-F" denotes fastened and "-UF" denotes unfastened.

A testing specification has been published by AISI named Testing Standards for Determining the Web crippling Strength of Cold-Formed Steel Flexural members, or known as AISI S909-17 [3]. This standard establishes procedures for conducting tests to determine the nominal web crippling strength [resistance] of cold-formed steel flexural members. This specification also highlights the minimum required length of the specimen in a similar expression. Based on in-place conditions, it is permitted to use a longer length; for example, L = 5.0 h. However, longer lengths for IOF and EOF loading are not recommended since they may result in premature failure resulting from combined bending and web crippling. Accordingly, the flexural capacity of the specimen needs to be controlled at the mid-span to ensure flexural failure will not occur prior to the web crippling failure at the ends or the mid-span throughout the test.

2.3 CRUSHING BEHAVIOUR OF HAT SECTIONS SUBJECT TO LOCALISED LOADING

2.3.1 Failure mechanism

While web crippling has been studied for decades since the 1940s, it was not until the 1990s that web crippling was qualitatively and systematically described by M.C.M. Bakker [4] in her PhD thesis, based on observations from a series of short-span three-point bending tests. Based on the mode of web deformation, two mechanisms can be distinguished: the rolling mechanism and the yield arc mechanism.

The term "rolling mechanism" was first used by Wierzbicki and Abramowicz [5], who pointed out that a yield line mechanism with moving fold lines is kinematically inadmissible. A kinematically admissible mechanism can be obtained by modelling the moving fold line with two moving yield lines. The first yield line bends the (web) plate into curvature, while the second straightens the (flange) plate again, as shown in Figure 2.

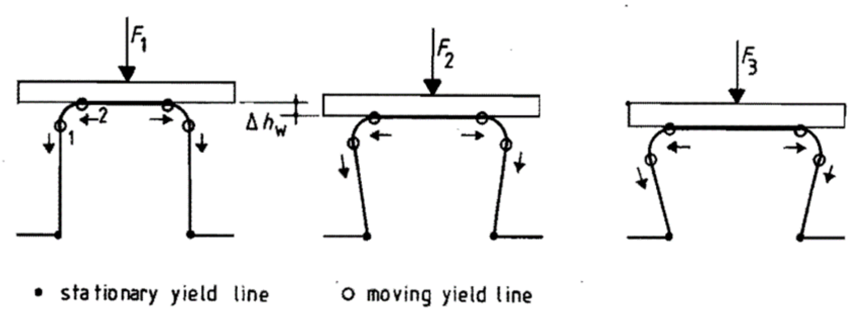

Figure 2 Rolling mechanism modelled with the moving yield lines presented in [4]

In a later study, Santaputra [6] described an overstressing failure, which is thought to be similar to the rolling mechanism. The definition of the overstressing failure is given as follows by Santaputra, Parks, and Yu [7]: "Failure of this type occurred just under the bearing plates, with relatively small lateral deformations of the webs of the hat sections. The applied load increased steadily up to the ultimate load and remained at that level for a long period of time while the bearing plate gradually penetrated into the web." Bakker selected the term "rolling mechanism" because it is believed that the member failed by a rolling process.

The yield arc mechanism was first described by Rockey, El-Gaaly and Bagchi [8]. However, their study did not include a discussion of the load-deformation behaviour. Later, Santaputra [6] described a web buckling failure, which is thought to be similar to the yield arc mechanism. Similarly, the Load-Displacement behaviour of this buckling failure was also described by Santaputra, Parks, and Yu [7]: "For this type of failure, the load increased steadily up to the ultimate load. At the ultimate load, the web became unstable, and the load dropped suddenly. There were relatively large lateral deformations of the webs of the hat sections even before failure." Bakker selected the term "yield arc mechanism" instead of "buckling failure", which is believed to better describe the failure behaviour, where a clear yield arc is formed in the web. A simplified model is presented to demonstrate the web deformations in the yield arc mechanism as shown in Figure 3.

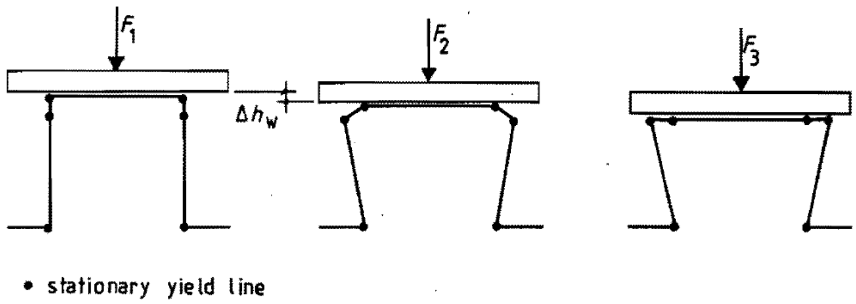

Figure 3 Web deformation in the yield arc mechanism

2.3.2 Plastic hinge mechanism

Bakker concluded that web crippling results in the formation of a plastic hinge mechanism, and hence the hinge mechanism is directly relevant for modelling web crippling behaviour. In the yield arc mechanism, the initiation of the hinge mechanism more or less corresponds to the attainment of the ultimate load. However, in the rolling mechanism, the hinge mechanism is formed before the ultimate load is reached, resulting in a clear change in the load-deformation behaviour. It is therefore proposed to define a mechanism initiation load as the concentrated load acting on the member corresponding to the initiation of the hinge mechanism.

The definition of the mechanism initiation load as the load corresponding to the initiation of the hinge mechanism suggests that there is a specific load at which this mechanism is formed. In reality, the hinge mechanism develops gradually. Yet, the mechanism initiation load was found to be a useful idealisation for analysing web crippling behaviour.

In this research, Bakker developed a similar theory for the determination of yield load used in the Direct Strength Method. The calculation of the yield load should be based on the yield line locations at the state of first yield, a state where the yield lines remain at their initial positions before significant movement occurs or a change in the mechanism takes place. The load at this state is found to be similar to the mechanism initiation load defined by Bakker. A typical figure for the determination of the experimental mechanism initiation load in members failing by the rolling mechanism is also given in Bakker's PhD thesis, as shown in Figure 4.

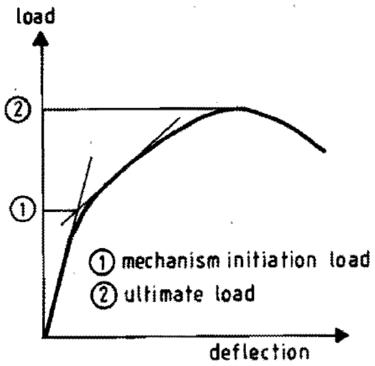

Figure 4 Determination of the experimental mechanism initiation load in members failing by the rolling mechanism presented in [4]

Bakker's PhD thesis described the finding of the research project on web crippling of cold formed flexural steel members. An analytical model for describing the load-deformation behaviour of members subjected to the combined action of a concentrated load and a bending moment was proposed. In this research project, a model for predicting the mechanism initiation load of member failing by the rolling mechanism is developed (which is somewhat similar to interior one flange loading case), and the comparison of the model with test results demonstrated a good alignment. The idealised yield line pattern in a member failing by the rolling mechanism is demonstrated as Figure 5. Constant-rolling-radius mechanism curves have also been derived for predicting the load deformation behaviour after the initiation of the mechanism.

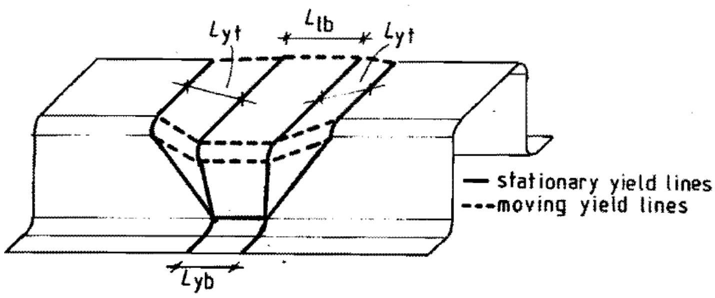

Figure 5 Idealised yield line pattern in a member failed by the rolling mechanism presented in [4]

In conclusion, Bakker's research is of great significance for the study of web crippling in cold-formed steel members, as it marks the starting point of using plastic mechanism models for design equation development instead of relying solely on empirical methods by performing curve fitting on experimental data without understanding the underlying behaviour. However, Bakker's research does not systematically cover all loading cases, and there is no mechanism model available for the yield arc mechanism failure mode, despite the presented model being considered relatively accurate for the rolling mechanism.

2.3.3 The use of Finite Element Method and Rigid Plastic Mechanism

After the last paper on web crippling of hat sections published by Bakker and Stark [9] as a summary of their work, there was a slow period of nearly a decade before research on this topic resumed. H. Hofmeyer performed a series of studies investigating the reasons behind the occurrence of specific yield line patterns. Two papers have been published by Hofmeyer regarding this study, with Part I [10] focusing on numerical modelling and Part II [11] on analytical modelling.

In the numerical part, Finite Element Models (FEM) were developed to simulate the crushing behaviour of very small strip sections of hat-sections under a concentrated load, focusing on the dynamics of moving yield lines. In this paper, Hofmeyer identified the transition in Load-Displacement curves by varying the rounded corner radii from 1 mm to 10 mm. He emphasized the importance of the number of integration points for accurately predicting the ultimate load for large radii. It was also found that the initial yield line's location and movement in a complete hat section can be effectively studied using only a 2D strip of the hat-section. However, the qualitative load-web crippling deformation behaviour is not equal for a complete hat section and a strip, particularly for large corner radii.

In the analytical part, Hofmeyer presented a considerably complex but detailed analytical model to explain why a yield line starts at a certain location. Additionally, the analytical model accurately predicted the rigid-plastic load-deformation behaviour for the strips with a corner radius between 1 and 10 mm but not for sections with larger corner radii.

Although Hofmeyer's research studied extreme conditions with simplifications, these papers combined offer a thorough investigation into the structural responses of hat-sections, highlighting the importance of corner radius in determining failure modes and emphasizing the need for models that can accurately capture the behaviour.

2.4 EXPERIMENTAL STUDY OF HAT SECTIONS SUBJECT TO LOCALISED LOADING

Experimental investigation of web crippling has been performed by many researchers. Interestingly, most of these research focus on single web sections – channels and zeds, and some of these researchers also include I- sections in their study. The experimental investigation of hat sections dates to early 1950s by Winter and included in AISI 1968. Baehre [12] performed the first study on single unreinforced web of multiple web sections with web inclination θ. Yu [13] in 1981 and Wing [14] in 1981 studied the web crippling and combined web crippling and bending of multi-web cold-formed steel sections in Missouri University of Science and Technology and University of Waterloo respectively. The experimental data presented in these papers were not collected as most of them were not directly relevant, unachievable, or the experimental program did not cover the full range of loading cases.

2.4.1 Santaputra and Yu

The first systematically designed experimental program regarding web crippling test in all of four loading cases complied with the AISI S909 testing specifications, "the design of automotive structural components using high strength sheeting steels: web crippling of cold-formed steel beams", was performed by Santaputra [6] in 1986. A separated report was presented by Santaputra and Yu [15] and a relevant paper was published in 1989 by Santaputra, Parks and Yu [7].

The main purpose of this portion of the investigation was to study the structural behaviour of very high strength cold-formed steel beams subjected primarily to web crippling and a combination of web crippling and bending moment. It was intended to use the research findings for a possible development of new and/or modified design criteria and to extend the use of materials having yield strengths exceeding the limitations presently included in the AISI Guide and Specification. The yield strengths of these sheet steels vary from 58 to 165 ksi (400 to 1137 MPa) as commonly used in the automotive industry, and also covers the range of the material currently used in Australia (G450 and G550). According to AS/NZS 4600, with a guaranteed minimum yield strength at 450 MPa and 550 MPa, and typically up to 680 – 740 MPa for G550.

In this experimental investigation program, 150 hat sections from five different types of sheet steels (80DK, 80XF, 100XF, 140XF and 140SK) were tested for IOF, EOF, ITF and ETF loading cases with only unfastened (UF) loading conditions. In addition, 18 test of hat sections were performed for transitions between the four basic loading conditions. The testing arrangements are shown in Figure 6. It's worth noting that for the IOF tests, half of the specimens (36) were loaded at mid-span with the clear distance between the opposite bearing plate (e_1 and e_2) of 1.5h, where h is the flat portion of the web, excluding the rounded corner, as defined by AISI S909. Those remaining 36 specimens were tested under unsymmetric loading. These unsymmetric loading cases were not used for DSM design curve calibration. For all tests, two 4-in. bearing plates were used at both ends and a 2-in. bearing plate was under the applied concentrated load. The specimens were braced to maintain the shape, and wood blocks were inserted in order to prevent undesired failure as required. Overall, 114 tests were collected for DSM design equation calibration later in this thesis: 30 for EOF, 24 for ETF, 36 for IOF, and 24 for ITF loading cases.

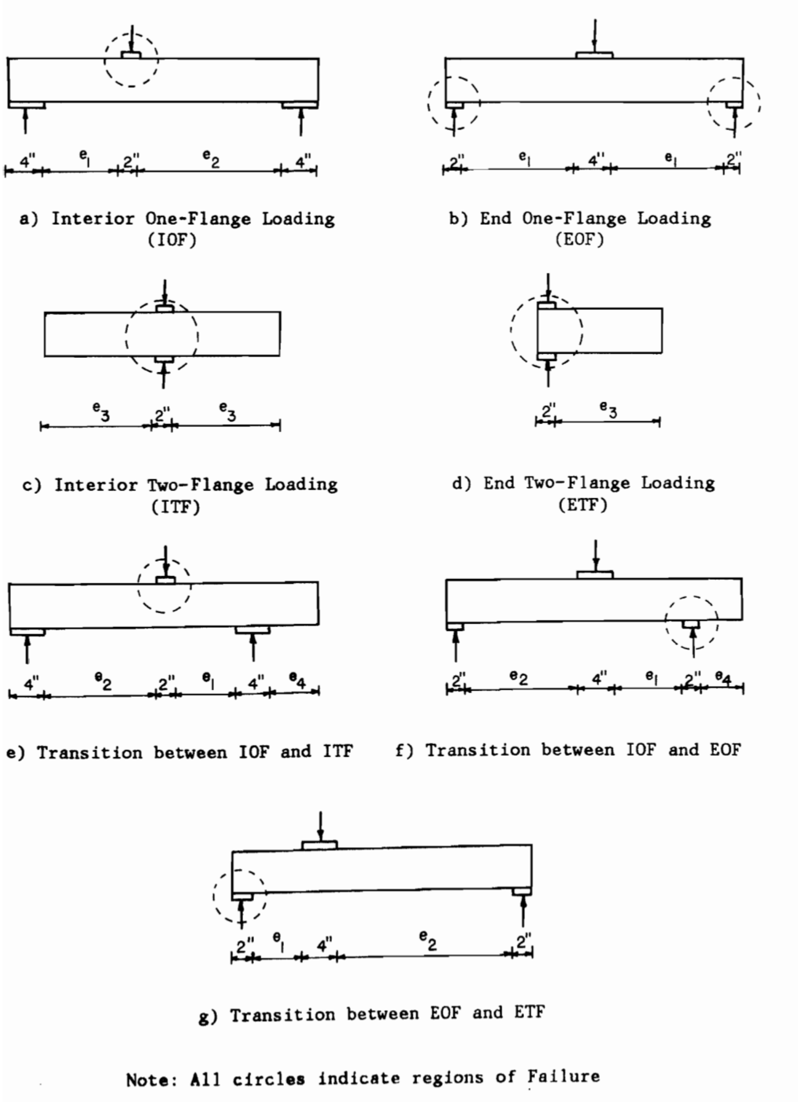

Figure 6 Testing arrangements reported in Santaputra and Yu [15]

While evaluating the fulfillment of Santaputra's original experimental objectives is beyond the scope of this thesis, the data provided in his report is invaluable for extending the Direct Strength Method (DSM) design equations to include unfastened (UF) loading cases not covered by the author's tests, enriching the database necessary for a broader application of DSM in the design of cold-formed steel hat sections. The dimensions, material properties and results collected for use in this thesis are attached in Appendix E.

2.4.2 Wu, Yu and LaBoube

Wu, Yu and LaBoube [16] carried out an experimental program regarding the strength of flexural members using structural grade 80 of A653 steel (web crippling test). The objectives of the project were to study the strength and structural performance of flexural members as affected by using the high strength, low-ductility Structural Grade 80 Steel and to develop appropriate design criteria based on the test programs.

Four loading conditions, namely End One-Flange (EOF), Interior One-Flange (IOF), End Two-Flange (ETF), and Interior Two-Flange (ITF) loading conditions, were considered in the web crippling tests. It is important to note that the IOF, ETF, and ITF loading cases were tested under fastened conditions, while the EOF loading case was tested without fastening. The web crippling test program included 136 single-rib and double-rib specimens having a hat-shaped section with sloped webs and 12 single-rib specimens having a hat-shaped section with vertical webs. Since double-rib specimens do not fall within the research scope of this thesis, the following discussion focuses on single-rib specimens only.

In the experimental program for the single-rib specimens, 6 different sloped-web hat sections with varying heights and rounded corner radii were tested for the TF loading cases, and 3 additional different vertical-web sections were tested for the IOF and EOF loading cases.

The length of the specimens was determined based on the width of the bearing plates, the minimum distance between two adjacent bearing plates (1.5h), and the minimum distance between a bearing plate and the end of a specimen (1.5h) as required for the EOF, IOF, ETF, and ITF loading conditions in the AISI Specifications. However, the length of the specimen for one-flange loading cases was intended to exceed the required minimum distance in the actual specimens to ensure the validity. The length of the specimen for EOF was short enough to avoid flexural failure in the middle of the specimen and the length of the specimen for IOF loading condition was short enough to reduce the effect of moment on the interaction between the moment and the web crippling load. However, the report did not provide the exact length of the specimens.

The test system consisted of a loading frame with top and bottom platens, various control panels, and a data acquisition system with a real time computer monitor and the detailed testing setup was included in the report. Interestingly, during the tests, the top platen was stationary, while the bottom platen was controlled by the system to move up and down as to apply load.

It should be highlighted that C-clamps were used to fasten the specimens in place. The reason for using C-clamps might be largely due to the relatively thin material used in these tests. As a result, C-clamps were able to provide sufficient hold-down forces to ensure that slippage was unlikely to occur. In other experimental programs, bolts and self-tapped screws were used. Given that the hat sections tested by the author which will be described in a later chapter in this thesis are considerably stockier, predrilled holes with high-strength bolts were used as the preferred fastening method. Additionally, applying C-clamps in restricted areas, especially for hat sections with returning lips on the bottom flanges, was found to be somewhat problematic.

The results presented in the report demonstrate good alignment with the finite element simulations performed by the author later in the thesis, which means these sections buckled before reaching the yielding point. Specifically, the deformed shapes were closer to the buckling mode because these test results fell in the high slenderness zone.

This experimental data provides strong support for the calibration of the DSM design, as they anchor the DSM design curves in the high slenderness zone. Overall, 62 tests were collected for the DSM design equation calibration: 18 for EOF-UF, 14 for ETF-F, 18 for IOF-F, and 12 for ITF loading cases. The collection of the experimental data for use in this thesis is included in Appendix E.

2.5 NUMERICAL STUDY

With the development of powerful computation methods and resources, numerical simulation is now becoming more important than ever. An increasing trend of using numerical study based on a small amount of testing data instead of performing large scale of experiments has been in place. Many researchers have been successfully using numerical method in their study regarding yield and/or buckling analysis.

2.5.1 Buckling analysis

A recent study published by Hancock, Chen, Xie and Pham [17] summarized the commonly used methods for elastic buckling analysis. Generally, elastic buckling analyses for localised loading are performed using one of three methods: the Finite Strip Method (FSM) [18], the Generalized Beam Theory (GBT) [19], or the Finite Element Method (FEM), as they are normally too complex for simple analytical expressions frequently used in compression, bending, and shear.

Hancock and Pham [20] pioneered the application of the Finite Strip Method (FSM) to localised loading cases. This method involves dividing the section into longitudinal strips, utilising longitudinal displacement functions (typically harmonic functions) and transverse displacement functions (generally polynomials). They introduced the Semi-Analytical Finite Strip Method (SAFSM) tailored for Simply Supported (SS) boundary conditions via a program called bfinst10.cpp. The SAFSM was then extended to other boundary conditions by Nguyen, Hancock and Pham [21,22]. A computer program named THIN-WALL-2, written by Nguyen [23], was subsequently developed. Later, the bfinst10.cpp was extended to bfinst10R.cpp in 2021 by Hancock and Pham [24] to cover more boundary conditions, including clamped ends and free ends.

In addition to the FSM, the FEM is also used as an alternative method for validating the buckling load. ANSYS and ABAQUS are two widely accepted software packages using FEM for analysing complex problems. In this discussion, ABAQUS is referenced for predicting the buckling load of sections under transverse load with rounded corners, as it is the software used in this thesis. A comparison of the FSM and FEM used for buckling analysis of hat sections is discussed in detail in a later chapter.

2.5.2 Yield analysis

The Finite Element Method (FEM) has been widely adopted by researchers as an efficient tool for conducting parametric studies in recent decades. The usage of FE simulations was first applied to web crippling studies by Sivakumaran [25] in 1989. In the past 25 years, more than 50 papers have been published regarding the use of FE simulations for web crippling studies. A publication by Degtyarev, Chen, Moen, Peterman, Schafer, Torabian and Zhou [26] offers a detailed insight into the finite element (FE) simulation of web crippling behaviours in cold-formed steel (CFS) members, with a focus on modelling techniques and parameters that contribute to the accuracy of these simulations.

The preference for ABAQUS by a majority of the studies (32 out of 48) over ANSYS (13 out of 48) underscores ABAQUS's capabilities in handling complex localised loading problems. The use of 4-node shell elements for CFS members and rigid shell elements for bearing plates, coupled with surface-to-surface contact, reflects a common approach to realistically simulate the physical interactions in FE models. All publications addressed the importance of fine meshing of the CFS members in the web crippling failure regions, especially for the rounded corners. The adoption of bilinear stress-strain curves, both with and without strain hardening, and multilinear stress-strain curves with von Mises isotropic hardening, indicates the diversity of material modelling approaches used to accurately represent the non-linear behaviour of steel under loading conditions leading to web crippling.

The findings regarding the use of "hard" contact in most cases, with some studies reporting improved Load-Displacement curve smoothness when "softened" contact with high stiffness was employed, suggest that the modelling of contact behaviour plays a significant role in simulating the actual physical response of CFS members under concentrated loads. In addition, the web crippling strength is relatively insensitive to the friction coefficient. The influence of initial geometric imperfections is found to be insignificant unless the magnitude of imperfections is comparable to the corner radius. The effect of the residual stresses on the web crippling strength was also found negligible.

Despite most FE simulations in this thesis being completed prior to the availability of Degtyarev et al.'s paper, an independent review conducted by the author in 2020 and 2021 aligns closely with the findings reported in 2023, affirming the conclusions drawn from earlier research on the application of FE simulations in localised loading and web crippling studies. New findings regarding the utilisation of solid elements and Implicit Static will be introduced in this thesis.

2.6 THE DETERMINATION OF PY – PLASTIC MECHANISM MODEL

Plastic mechanism models have been developed and adopted by Young and Hancock [27] for the estimation of yield load for unlipped channel sections under localised loading cases. The selected plastic mechanism models were derived from the observation of experimental and/or numerical results.

Expanding upon this foundational work, Nguyen [23] and Nguyen, Hancock and Pham [28] in subsequent research efforts, broadened the scope of application from unlipped channels to include a more diverse range of sections, such as lipped channels, SupaCee, and DHS sections. Nguyen [23] introduced a comprehensive series of simplified plastic mechanism models as shown in Figure 7 tailored for various loading cases and fastening conditions, facilitated by a unified set of generic formulas modifiable through specific factors. An extensive range of experimental data from

1995 to 2016 has been collected by Nguyen for the development of plastic mechanism models.

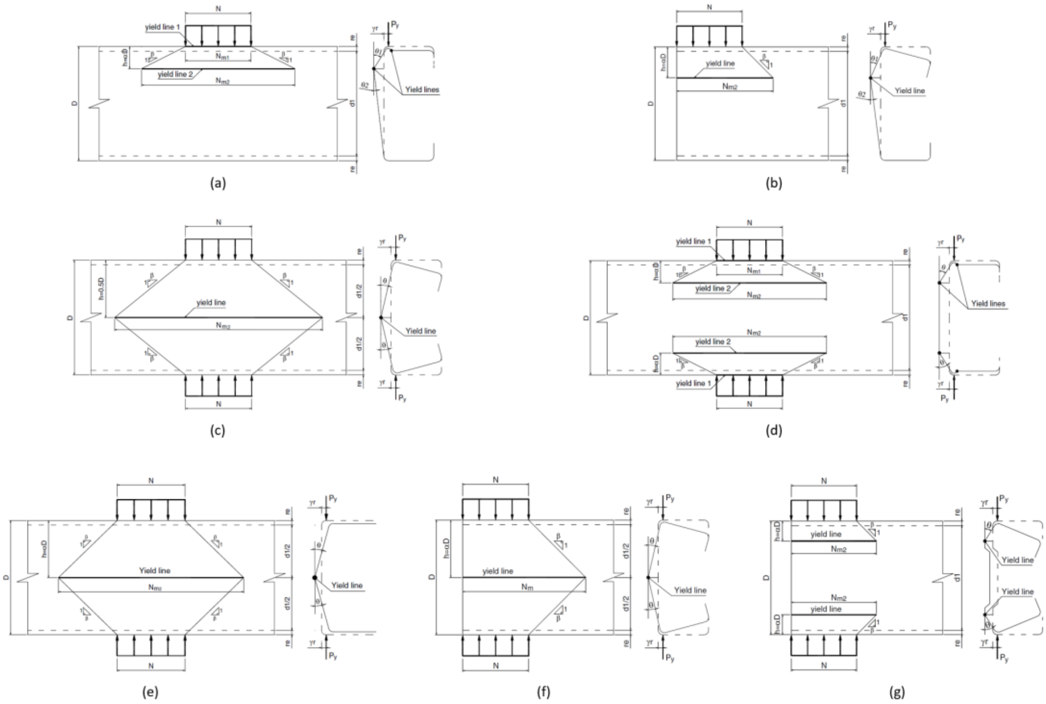

Figure 7 Plastic mechanism models for different loading cases and sections developed by Nguyen [23]

For equilibrium, the internal plastic energy of the structural member must be equal to the external energy of the applied loads. From this, the yield mechanism load is given as

$$P_y = \frac{M_p}{\gamma r}\left[a_1 N_{m1} + a_2 N_{m2}\right] \quad (2\text{-}2)$$

where γr = load eccentricity from the web center line; M_p = plastic moment per unit length of plate

$$M_p = \frac{f_y t^2}{4} \quad (2\text{-}3)$$

f_y = yield strength of steel

$$r = r_i + \frac{t}{2}, r_e = r_i + t \quad (2\text{-}4)$$

r_i, r, and r_e = interior, center, and outer radii, respectively

$$h = \alpha D \quad (2\text{-}5)$$

h = depth of the yield-line at the top and/or bottom of the web;

α = yield-line depth factor, given in Table 3 and t and D = section thickness and depth

$$N_{m1} = N \quad (2\text{-}6)$$

$$N_{m2} = N + a_3\beta h \quad (2\text{-}7)$$

N = bearing length; N_{m1}, N_{m2} = yield-line lengths on the flange and in the web of the section, respectively; a_1, a_2, and a_3 = yield-line length factors, given in Table 3; β = yield-line distribution slope factors

$$\beta = \beta_0\beta_1 \quad (2\text{-}8)$$

β_1 = slope factors, given in Table 3; β_0 = factor which depends on the bearing length ratio (N/D)

$$\frac{N}{D} = 0.15, \beta_0 = 1.6 \quad (2\text{-}9)$$

$$\frac{N}{D} = 0.5, \beta_0 = 1.0 \quad (2\text{-}10)$$

$$\frac{N}{D} \geq 1.0, \beta_0 = 0 \quad (2\text{-}11)$$

For other values of N/D, β = interpolated or extrapolated linearly. The β_0 value reflects the fact that the yield-lines are shorter relative to the bearing length for longer bearing length

$$\gamma = \frac{1}{\gamma_0} \quad (2\text{-}12)$$

$$\frac{r_i}{t} = 2.5, \gamma_0 = 1.0 \quad (2\text{-}13)$$

$$\frac{r_i}{t} = 1.5, \gamma_0 = 0.8 \quad (2\text{-}14)$$

γ = factor which depends on the radius ratio ($r_i = t$); for other values of $r_i = t$, γo = interpolated or extrapolated linearly. Smaller $r_i = t$ ratios lead to smaller γ_0 and hence larger γ.

For different loading cases, the corresponding plastic mechanism model is attached in Figure 7.

Table 3 Factors for plastic mechanism models presented by Nguyen

Sections	Load cases	Plastic hinge factors		Yield line length factors		
		α	β_1	a_1	a_2	a_3
Unlipped plain-C	IOF	0.350	1.0	0	b	2
	EOF	0.250	1.0	0	b	1
	ITF-U	0.500	1.5	0	1	2
	ITF-F	0.350	1.0	0	1	2
	ETF	0.500	1.0	0	1	1
lipped plain-C and SupaCee	IOF	0.125	2.0	1	b	2
	EOF	0.250	1.0	0	b	1
	ITF-U	0.500	1.5	0	1	2
	ITF-F	0.125	2.0	1	1	2
	ETF	0.500	1.0	0	1	1
DHS	IOF	0.070	2.0	1	b	2
	EOF	0.250	1.0	0	b	1
	ITF-U	0.500	1.5	0	1	2
	ITF-F	0.125	2.0	1	1	2
	ETF	0.500	1.0	0	1	1

2.7 DIRECT STRENGTH METHOD

V.V. Nguyen [23] successfully proposed a consistent and simplified Direct Strength Method for the design of cold-formed steel sections under localised loading in his PhD thesis. A relevant paper has been published by Nguyen et al. [28] in 2020. These equations were built up based on the buckling load (P_{cr}) obtained from the THIN-WALL-2 V2.0 program developed by Nguyen and presented by Nguyen Hancock and Pham [29], while the yield load (P_y) models were introduced in the same thesis. The general form of DSM design equations are given as

$$\frac{P_n}{P_y} = \left[1 + \left(1 - \frac{\lambda}{\lambda_0}\right)(k_4 - 1)\right] \text{ for } \lambda \leq \lambda_0 \tag{2-15}$$

$$\frac{P_n}{P_y} = k_1\left[1 - k_2\left(\frac{P_{cr}}{P_y}\right)\right] \text{ for } \lambda > \lambda_0 \tag{2-16}$$

where

P_{cr} = elastic buckling load;

P_y = yield load;

λ = nondimensional section slenderness, $\lambda = \sqrt{P_y/P_{cr}}$;

and λ_0 = value of λ when $P_n/P_y = 1$.

The coefficient and exponents k_1 k_2, and k_3 were originally developed by fitting the set of ratios $P_{exp} = P_y$ on the right-hand side of Equation (2-16), proposed previously by Natário, Silverstre and Camotim [30]. Different coefficients and exponents are employed for the four loading cases as given in Table 4.

Table 4 DSM parameters proposed by Nguyen

Load cases	**Coefficient and exponents**				**Section Slenderness**
	$\boldsymbol{k_1}$	$\boldsymbol{k_2}$	$\boldsymbol{k_3}$	$\boldsymbol{k_4}$	$(\boldsymbol{\lambda_0})$
IOF	1.00	0.15	0.40	1.80	0.776
EOF	1.00	0.15	0.40	1.80	0.776
ITF	1.00	0.15	0.60	1.80	0.844
ETF	1.00	0.15	1.00	1.80	0.707

When $\lambda \leq \lambda_0$, the nominal inelastic capacity based on Equation (2-17) has been evolved from the inelastic reserve equation for beams in the AISI S100-16 Specification (Sections F3.2.3 and F4.3). On this basis, Equation (2-15) was developed to predict the nominal inelastic capacity of structural members under localised loading

$$P_n = P_y + \left(1 - \frac{1}{C_y^2}\right)\left(k_4 P_y - P_y\right) \tag{2-17}$$

where

$C_y = \sqrt{\lambda_0/\lambda}$;

and k_4 = mechanism strengthening effect coefficient ($k_4 = 1.8$ has been selected in Table 4).

According to the thesis, a reasonable empirical trend line for the IOF (excluding the unlipped plain-C sections), EOF (excluding the unlipped plain-C sections), and ETF has been provided by the factor. It is low for the ITF-F load case excluding the unlipped plain-C sections. The unlipped plain-C sections are more difficult to categorize and so a mean fit to the results has been used.

Although Nguyen's thesis [23] does not provide a flawless solution for all loading cases, the initial effort to apply a comprehensive and simplified equation across the channel family is a significant step forward.

2.8 A UNIFIED FORM OF DSM DESIGN EQUATIONS ACROSS DIFFERENT TYPES OF LOADINGS

Glauz and Schafer have recently made significant contributions to the application of DSM with the publication of two papers [31,32]. These papers focus on the application of a new form of DSM design equations in various types of loading in structural engineering, including cases involving axial compression, as well as flexural and shear forces.

According to these papers, the new form of DSM design equation is written as Equation (2-18). A series of DSM design equations for selected scenarios are developed with featured modifications.

$$\frac{R_n}{R_m} = \frac{1+a\lambda^2}{1+b\lambda^2} = \frac{R_{cr}+aR_y}{R_{cr}+bR_y} \tag{2-18}$$

A paper written by Schafer and Glauz [33] presenting in 2023 summarizes work to date on this novel functional form for the application of the Direct Strength Method in cold-formed steel design. The summary of the application includes the prediction of the loading capacity of flexural members, compression members, shear strength, etc. At the end of the paper, the author provides a table of summary of DSM equation for comparison as shown in Table 5 demonstrating a potential to expand the usage of same format of DSM design equations for localised loading capacity prediction.

Table 5 DSM equation Summary presented by Schafer and Glauz

R_n	R_m	λ^2	a	b
$P_{n\ell}$	$1.2P_{ne}$	$P_{ne}/P_{cr\ell}$	0.10	0.55
P_{nd}	$1.2P_y$	P_y/P_{crd}	0.05	0.67
$M_{n\ell}$	k_sM_{ne}	$M_{ne}/M_{cr\ell}$	$0.10\alpha_s$	$0.55\beta_s$
M_{nd}	M_p	M_y/M_{crd}	$0.17\alpha_s$	$0.60\beta_s$
$\beta_{n\ell}$	$(1.2 \to k_s)\beta_{ne}$	$\beta_{ne}/\beta_{cr\ell}$	$0.10 \to 0.10\alpha_s$	$0.10 \to 0.10\alpha_s$
β_{nd}	$(1.2 \to k_s)\beta_y$	β_y/β_{crd}	$0.05 \to 0.07\alpha_s$	$0.67 \to 0.60\alpha_s$
V_n	$1.2V_y$	V_y/V_{cr}	0	0.57
V_n^*	$1.2V_y$	V_y/V_{cr}	0.05	0.45
$B_{n\ell}$	B_p	$B_y/B_{cr\ell}$	0.094	0.23
B_{nd}	B_p	B_y/B_{crd}	0	1.11

* with transverse web stiffeners

It's important to note that in the application of the DSM (Direct Strength Method) as described by Glauz and Schafer, there is a deviation from the typical DSM general equation format as presented in Equation (2-18), particularly in the way the k_p factor is incorporated. In their approach, the k_p factor is embedded within the Rm value. According to Table 5, the k_p factor is set at 1.2 for the design equation of compression members and shear members. However, for flexural members, k_p factor is set at 1.0 instead of 1.2. This exclusion could be attributed to the inclusion of M_p in the design equation for flexural members. M_p represents the plastic moment capacity of the section, which inherently accounts for plasticity considerations in the member's behaviour.

Thus, a hypothesis is posited that the inclusion of a k_p factor of 1.2 might be unnecessary for solely accounting for the plastic behaviour in the selection process for the k_p value in localised loading equations, particularly due to the incorporation of M_p in the P_y calculation process. However, an adjustment factor greater than 1.0 could be beneficial concerning the rolling mechanism for the sections with large e/t value as discussed later in the thesis.

2.9 SUMMARY OF LITERATURE REVIEW

This chapter has reviewed existing literature, offering insights into the behaviour of hat sections under localised loading and previous efforts to develop localised loading design equations for various sections. Prior research highlights the significant role of cold-formed steel (CFS) sections as both structural and non-structural elements, attributed to their high strength-to-weight ratio. However, the application of CFS, particularly hat sections, remains somewhat constrained by certain structural behaviours that are not fully understood. Although AISI S100-16 addresses localised loading for hat sections, the design equations appear outdated and do not comprehensively cover the range of products currently available in the market. Hence, further experimental and theoretical investigations are highly recommended to enhance our understanding of hat sections under localised loading. This chapter also outlines the groundwork for extending both experimental and numerical studies to hat sections, alongside presenting the latest developments in the Direct Strength Method (DSM) design.

Chapter 3 Numerical study – buckling

3.1 INTRODUCTION

The development of the Direct Strength Method (DSM) requires the calculation of the buckling load (P_{cr}) as a fundamental component of the web crippling design process. A comprehensive overview of different tools and methodologies for calculating P_{cr} under various loading conditions was recently presented by Hancock et al. [17] at ICTWS 2023. According to their publication, a range of tools have been developed specifically for the determination of P_{cr} in localised loading scenarios. The most commonly used software tools for buckling load analysis typically employ either the Finite Element Method (FEM) or the Finite Strip Method (FSM).

Regarding FEM, several software options are available for calculating buckling load under localised loading. ANSYS and ABAQUS stand out as widely recognized tools for tackling complex analyses using FEM. This thesis utilises ABAQUS [34], a well-established and broadly accepted FEM software, which has been validated as an effective tool for obtaining buckling loads in various research studies. In these research studies, the application of ABAQUS is particularly aimed at accurately predicting the buckling load of sections under transverse loads, especially those with rounded corners.

As with the FSM developed by Cheung [18], there was no application for use in buckling analysis under localised loading until 2015 [20], when bfinst10.cpp was developed by Hancock based on the evolution of the Semi-Analytical Finite Strip Method (SAFSM) for thin-walled sections under local loading. The bfinst10.cpp program has been successfully benchmarked against the Spline Finite Strip Method (SFSM) use previously by Pham and Hancock [35]. The application of bfinst10.cpp was firstly used in the program THIN-WALL-2 written by Nguyen [29] containing a version of bfinst10.cpp that is restricted to simply supported ends. The theory of buckling analysis and the convergence studies have been carried out by Nguyen and discussed in Chapter 4 in his PhD thesis. Later, the bfinst10.cpp was extended to bfinst10R.cpp in 2021 to cover more boundary conditions including clamped ends and free ends by Hancock and Pham [24].

THIN-WALL-2 was initially written in MATLAB and designed for buckling analysis under localised loading for channel sections only. In early 2020, a new version of THIN-WALL, called THIN-WALL-PYTHON, was developed by Hancock using Python 3 for the simplification of the buckling analysis for channel sections.

In this chapter, the author proposes a new version of THIN-WALL-PYTHON using the improved bfinst10R.cpp for applying the SAFSM to the buckling analysis of localised loading for hat sections. In Section 3.2, there is a brief introduction to the graphical user interface (GUI) of THIN-WALL-PYTHON, followed by an extensive guide detailing the critical aspects of modelling for various loading cases. This section also includes the methodology for calculating the buckling load (P_{cr}), along with practical calculation examples. Section 3.3 introduces the methodology for conducting buckling analysis using the Finite Element Method (FEM), specifically employing ABAQUS software. A detailed discussion of the processes and parameters involved in FEM analysis for this purpose. Also, the result obtained from THIN-WALL-PYTHON is benchmarked against those derived from the FEM analysis using ABAQUS.

3.2 BUCKLING ANALYSIS USING THIN-WALL-PYTHON

The initial purpose of developing THIN-WALL-PYTHON was to develop a mini-program to generate the input file for bfinst10.cpp and bfinst10R.cpp, as an alternative to THIN-WALL-2. However, as the project progressed, several advantages of using Python as the primary programming language emerged, particularly when compared to MATLAB.

Firstly, Python's versatility allows for easy maintenance and modification to suit a variety of needs. This includes adjusting the shape and dimensions of sections, various loading cases, and buckling analysis settings, all within a single user interface. This flexibility significantly enhances the program's adaptability to different sections and loading cases in further research.

Secondly, the advancement of Python modules, such as *matplotlib* and *openpyxl*, has expanded Python's capabilities in data visualization and integration. These modules enable Python to produce various plots, including stress distribution and buckling shapes in both 2D and 3D. Furthermore, the integration with Excel through *openpyxl* allows for the batch calculation of P_{cr}, streamlining the analysis process.

3.2.1 The GUI of the program

The main window of the GUI is shown in as Figure 8.

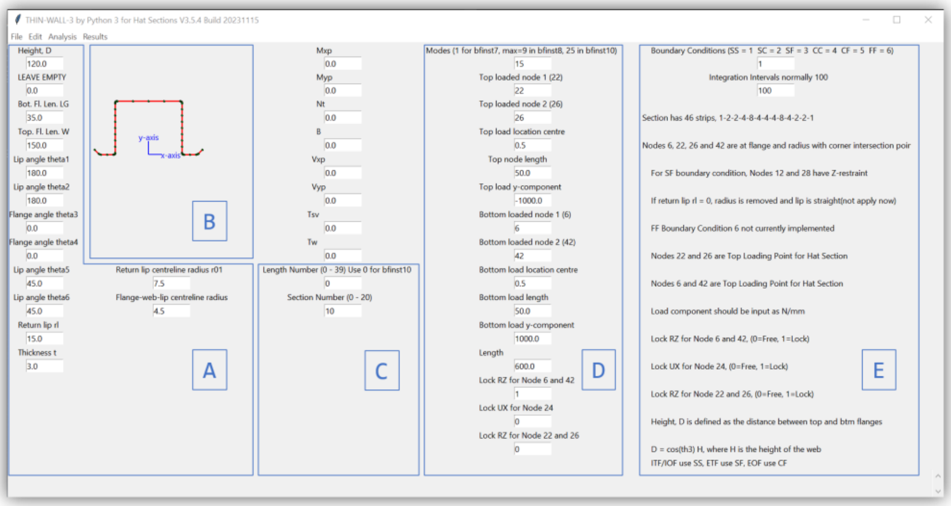

Figure 8 Main window of the THIN-WALL-PYTHON

In the graphical user interface (GUI) of the software or program being described, the layout is organized into distinct zones, each serving a specific purpose:

Zone A: This area is dedicated to the input of cross-sectional dimensions. Users can enter the measurements and geometrical details of the section they are analysing or designing.

Zone B: This zone functions as a graphical interface for generating the cross-section illustration. It transforms the dimensions input in Zone A into a visual format, presenting users with a two-dimensional model of the cross-section’s geometry.

Zone C: Designated for the input of length number and plotting section control parameter. These include the selection of bfinst10R.cpp, and the options that affect which cross-section is displayed on the canvas in Zone B when demonstrating the result.

Zone D: Reserved for inputting data related to loading and member-specific dimensions. This could involve the specification of load types, magnitudes, locations, as well as dimensions that are related to the structural member under analysis. The fastening setting is also included in this zone.

Zone E: Employed for entering boundary conditions and intervals. It also provides space for offering a description of the GUI's functionality and usage guidelines.

3.2.2 An introduction to the node allocation

In the latest version of the THIN-WALL-PYTHON software, a typical hat section is made up with 46 strips by connecting 47 nodes. The software accommodates two types of hat sections - one with return lips and one without. For the hat sections with return lips shown on the left side of Figure 9, five strips are distributed as follows: one strip in the return lip, two in the edge rounded corner, and two in the bottom flange. For those hat sections without return lips shown on the right side of Figure 9, five strips are evenly distributed in the bottom flange.

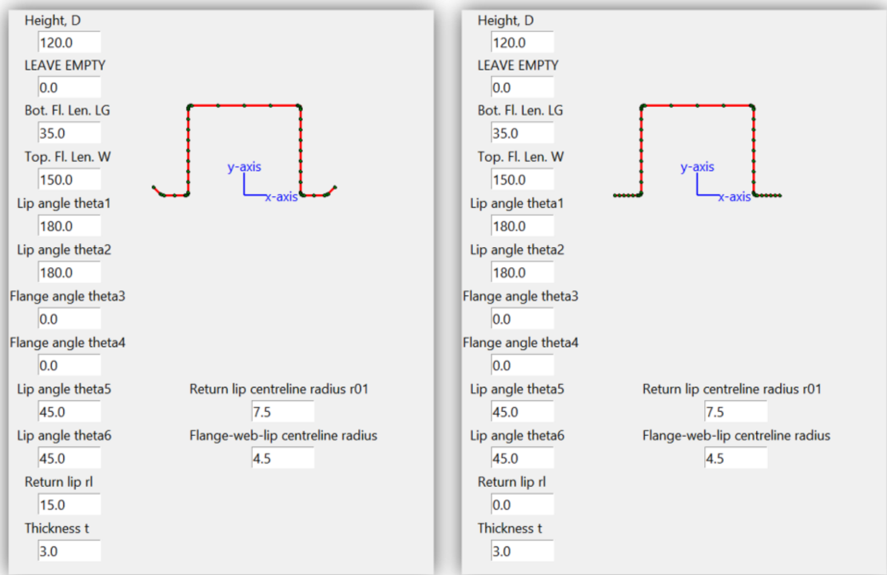

Figure 9 Hat sections with return lips (L) and without return lips (R)

Table 6 and Table 7 provide the detail of the node number allocations for the two types of hat sections respectively. It's important to note that these tables only show the node allocation on the left side of each section. The nodes are symmetrically arranged about the Y-axis, meaning the node distribution on the right-side mirrors that on the left. Figure 10 and Figure 11 demonstrate the corresponding drawing of Table 6 and Table 7.

Table 6 Typical node number allocation for hat sections with return lips

Node ID (Start)	Node ID (End)	Node counts	Strip counts	Note
1	2	2	1	Return lip
2	4	3	2	Lip rounded corner
4	6	3	2	Flat part of bottom flange
6	10	5	4	Bottom rounded corner
10	18	9	8	Flat part of the web
18	22	5	4	Top rounded corner
22	24	3	2	Half of top flange

Note: the mirror of Nodes 6 and 22 are Nodes 42 and 26 respectively.

Table 7 Typical node number allocation for hat sections without return lips

Node ID (Start)	Node ID (End)	Node counts	Strip counts	Note
1	6	6	5	Flat part of bottom flange
6	10	5	4	Bottom rounded corner
10	18	9	8	Flat part of the web
18	22	5	4	Top rounded corner
22	24	3	2	Half of top flange

Note: the mirror of Nodes 6 and 22 are Nodes 42 and 26 respectively.

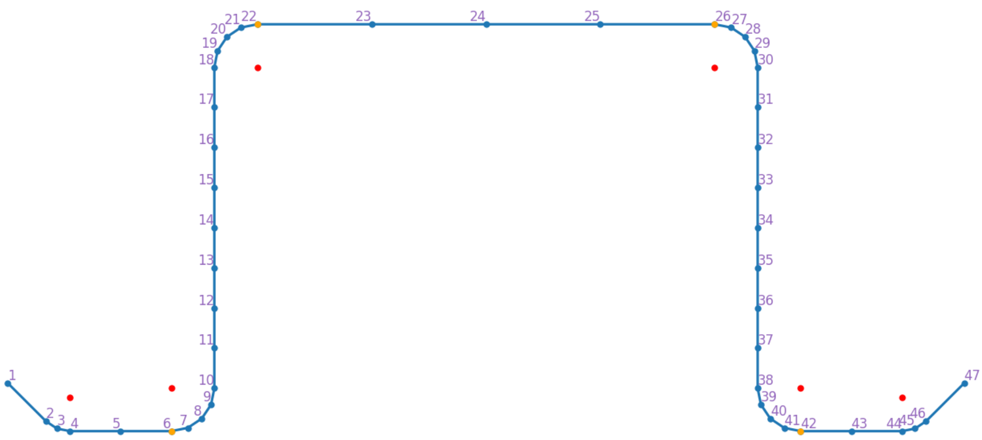

Figure 10 Node allocation of typical hat sections with lips

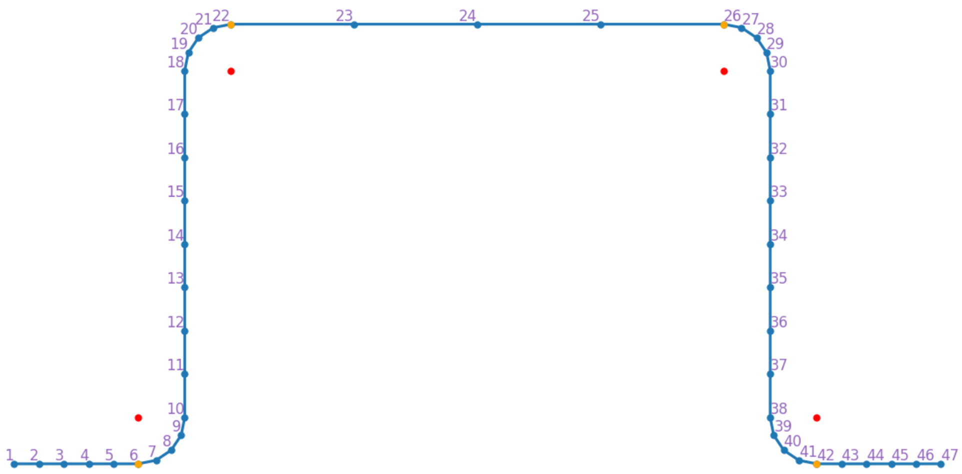

Figure 11 Node allocation of typical hat sections without lips

3.2.3 Loading cases and boundary conditions

The boundary conditions are crucial components that define how a model interacts with the environment. In localised loading problems, the boundary conditions can be broadly categorised into two parts:

- *Constraints at both end of the specimen*: This part involves defining how the ends of the structural member or specimen are restrained or supported. These constraints might simulate real-world support conditions like fixed (clamped), pinned (simply supported), or free ends.
- *Constraints related to the fastening condition*: This aspect pertains to the simulation of how the specimen is fastened or connected to the support in accordance with specific loading condition. In FSM, the constraints related to the fastening condition is applied to relevant nodal lines from the typical cross section and it is applied to the whole length of the member.

3.2.3.1 Constraints at both end of the specimen

The THIN-WALL-PYTHON program has been developed to accommodate six different boundary conditions (BC). These specific boundary conditions are selected by entering the corresponding BC number, as outlined in Table 8 along with the suitable loading cases.

Table 8 Loading cases and boundary conditions

BC Num. & BC	BC – near (z = 0)	BC – far (z = L)	Loading case
1 – SS	Simply supported	Simply supported	ITF/IOF
2 – SC	Simply supported	Clamped	

BC Num. & BC	BC – near (z = 0)	BC – far (z = L)	Loading case
3 – SF	Simply supported	Free	ETF
4 – CC	Clamped	Clamped	
5 – CF	Clamped	Free	EOF
6 – FF	Free	Free	

3.2.3.2 Constraints related to the interaction and fastening condition

The constraints related to interaction and fastening conditions in the model simulate how the hat sections interact with other objects (like bearing or loading plates) and the application of fasteners. In the context of localised loading on hat sections, the contact points are critically selected at the junctions where the rounded corners meet the flanges. This choice is based on the observed loading behaviour of hat sections, where these points typically are the touching points after initial displacement. Consequently, in simulations and analyses, the external load should be applied to these specific nodes on the relevant cross-sections.

For the hat sections as described, the loading points on the top flange are at Node 22 and Node 26, while for the bottom flanges, the loading points are at Node 6 and Node 42. To adhere to the standards specified in AISI S909-17 [3], particularly Clause 8.1, it is essential that the test specimen maintains both lateral and torsional stability. In line with this requirement, the horizontal movement (UX) at Node 6 and Node 42 is restrained in all cases to ensure stability against lateral shifting and splaying.

The fastening condition is also controlled by the constraint at the junction between the bottom rounded corners and flanges (Node 6 and 42). In typical scenarios where a fastener is installed, the rotation about the longitudinal direction (RZ) is restrained as shown in Figure 12. A standalone input option is provided for controlling the rotation about the longitudinal direction (Z axis) at the junction between the bottom rounded corners and bottom flanges.

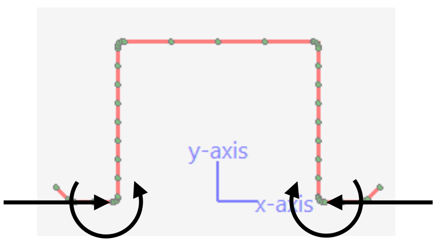

Figure 12 Boundary condition demonstration for a typical hat section with fastened condition

3.2.4 Load input

The loading input includes two key values: the **magnitude** of loading and the **location.**

3.2.4.1 Magnitude of the load

To accurately define a specific load for the hat section in the model, the magnitude of the load is determined using two critical inputs: the unit load and the width of the load. This approach allows for a precise and customizable load application based on the specific loading cases.

- *Unit Load*: This input defines the intensity of the load per unit length (N/mm) along the section. Both positive and negative values are required to represent the load's direction. A positive value indicates that the direction of the load is the same as the Y-axis direction in the model. Conversely, a negative value would imply the load is in the opposite direction.
- *Width of the Load*: This input corresponds to the bearing length at the specific location where the load is applied. It should match the actual or intended bearing length of the load in the physical scenario being modelled.

The total load applied to a single web is then calculated by multiplying the load per unit length by the length of the load along the section.

3.2.4.2 Location of the load

In the model, the location of the applied load is determined by inputting a ratio that defines the position of the load's centre relative to the total length of the specimen as input.

For ITF and IOF loading cases, the load should be centrally located on the specimen. Therefore, the input ratio for the load location is set at 0.5, positioning the loading point in the middle of the specimen.

For ETF and EOF loading cases, the load location is defined in relation to the simply supported or clamped end of the specimen (z = 0). The input ratio for these cases is calculated as 1 minus the quotient of half of the end-bearing length and the input length. For example, for a load length of 100 mm on a 1000 mm long section, the ratio would be $1 - \frac{100}{1000} \times 0.5 = 0.95$.

The method for determining the input total length varies based on the type of loading case:

- *Two-Flange (TF) loading cases*: The input length should be the total length of the specimen as shown in Figure 13.
- *IOF loading cases*: The input length in this loading case is calculated as the total length of the specimen minus the lengths of the two end bearings as shown in Figure 14.
- *EOF loading cases*: In this case, only half of the specimen is analysed. This is due to the stiffening effect at the middle of the specimen, which acts like a clamped boundary condition. The input length for EOF cases is determined by taking the total specimen length, subtracting the length of the mid-bearing plate, and then dividing the result by two, as shown in Figure 15.

The following three figures illustrate how the input length varies across different loading cases.

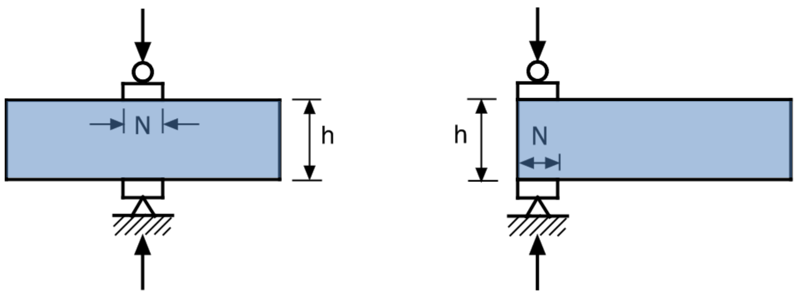

Figure 13 Input length for ITF and ETF loading cases

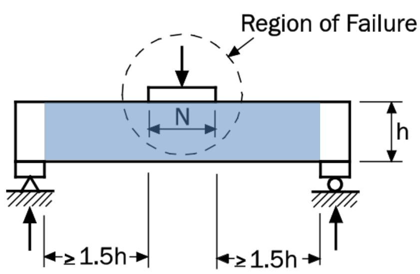

Figure 14 Input length for IOF loading case

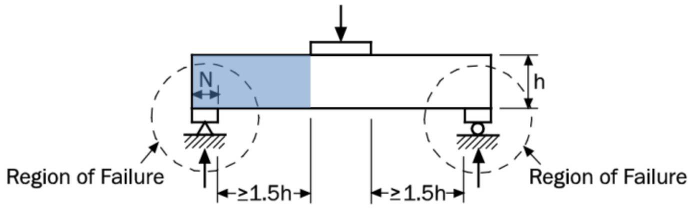

Figure 15 Input length for EOF loading case

3.2.5 Example of using THIN-WALL-PYTHON

Figures 16 - 20 illustrate the setup of a typical hat section in THIN-WALL-PYTHON for analysis. The hat section for use as an example is labelled as “H120-RIN3-DEG0-N50-L600.” Figure 21 displays the cross-section dimensions of this hat section. Using the ITF-F loading case in Figure 16 as an example, the resulting eigenvalue from the buckling analysis is shown in Figure 22.

The buckling load equals to the load applied (as N/mm) times the bearing length times the eigenvalue, which is calculated as

$$2.559 \times 50 \times 2 = 255900\ N = 255.9\ kN \tag{3-1}$$

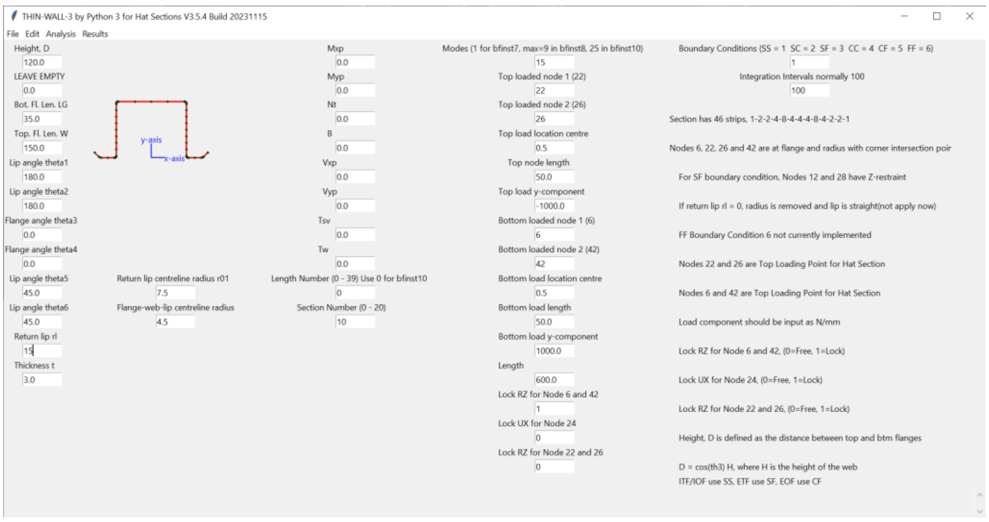

Figure 16 Typical setup of THIN-WALL-PYTHON for ITF-F loading case

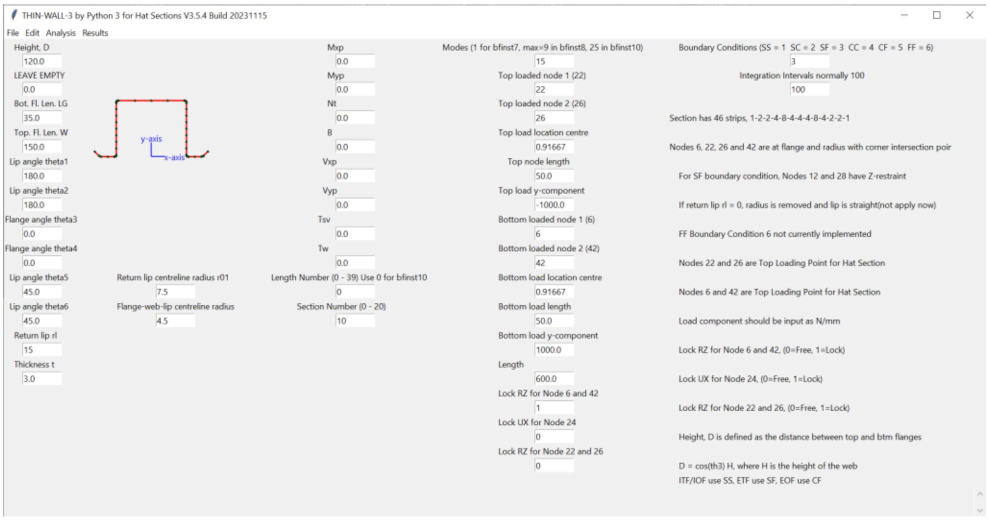

Figure 17 Typical setup of THIN-WALL-PYTHON for ETF-F loading case

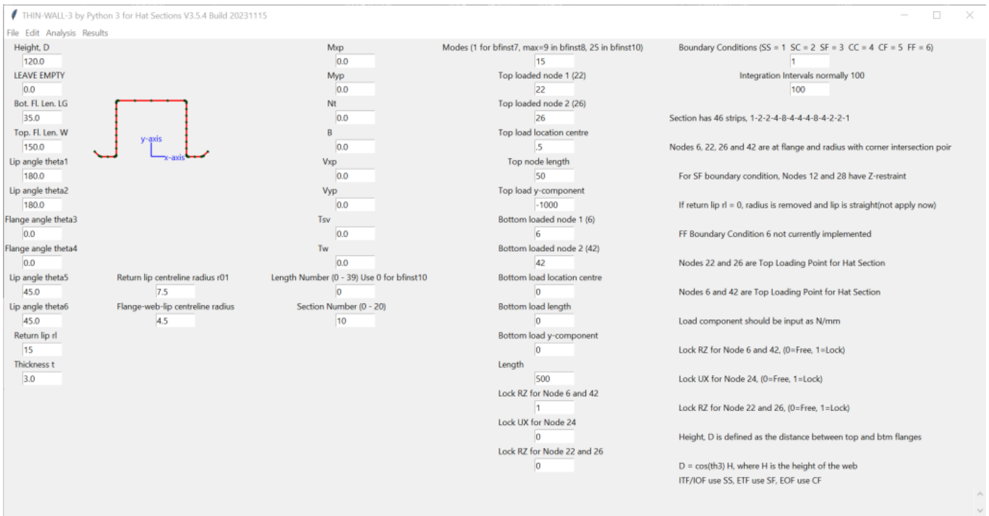

Figure 18 Typical setup of THIN-WALL-PYTHON for IOF-F loading case

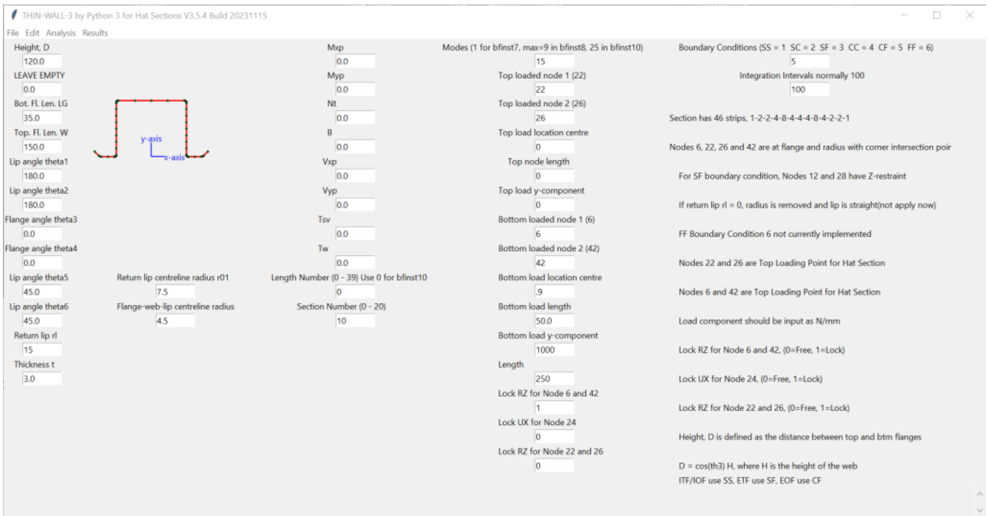

Figure 19 Typical setup of THIN-WALL-PYTHON for EOF-F loading case

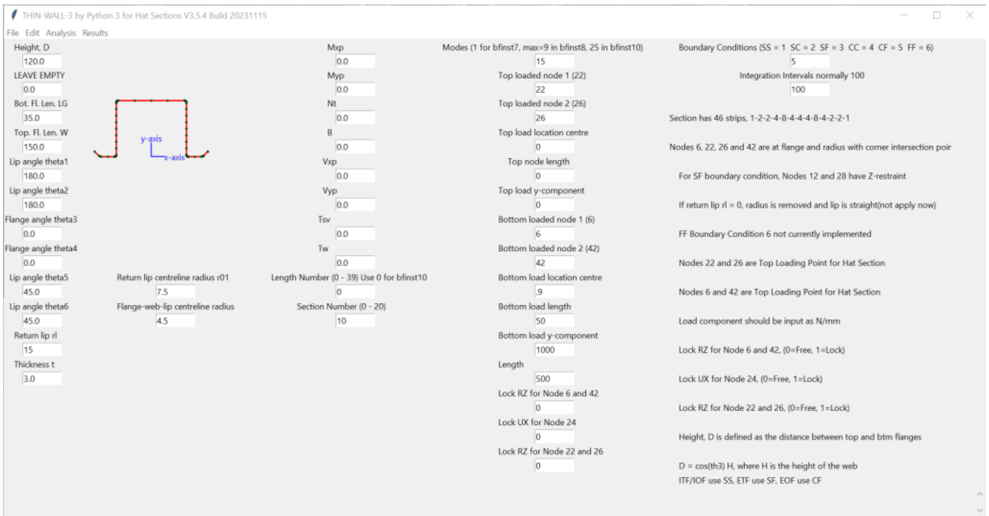

Figure 20 Typical setup of THIN-WALL-PYTHON for EOF-UF loading case

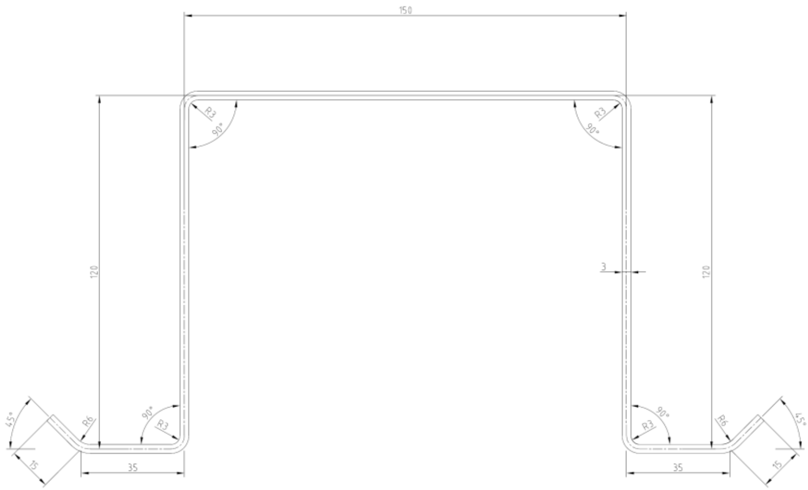

Figure 21 Hat section cross section dimension, H120-RIN3-DEG0

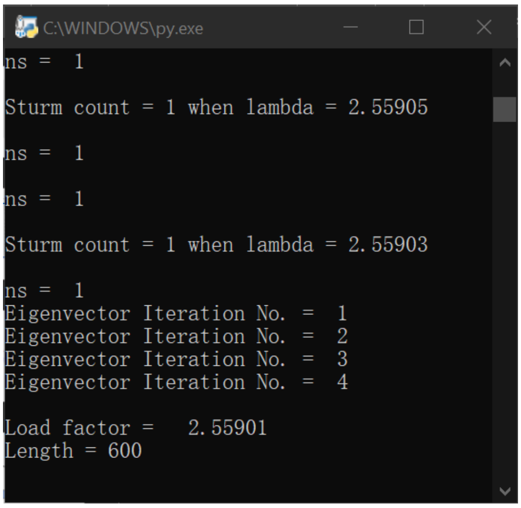

Figure 22 Typical result page from THIN-WALL-PYTHON

3.2.6 Result from THIN-WALL-PYTHON

Other than calculating the eigenvalue of buckling load, the THIN-WALL-PYTHON program can be used to performing further calculations: (1) single buckling mode at specific cross section, and (2) 3D buckling mode for the whole member.

3.2.6.1 Buckling mode

After completing the analysis in THIN-WALL-PYTHON, the buckling mode for various sections of the specimen can be obtained. In this software, each specimen is represented by 21 sets of nodes that are evenly distributed along the longitudinal direction. Each set of these nodes is associated with a specific section number, which corresponds to the out-of-plane buckling mode. This association of nodes with specific section numbers for buckling analysis can be defined in Zone C, as detailed in Section 3.2.1 in this chapter. The IOF-F buckling mode for the data in Figure 16 and the output in Figure 22 is shown in Figure 23 at the central (loaded) cross-section.

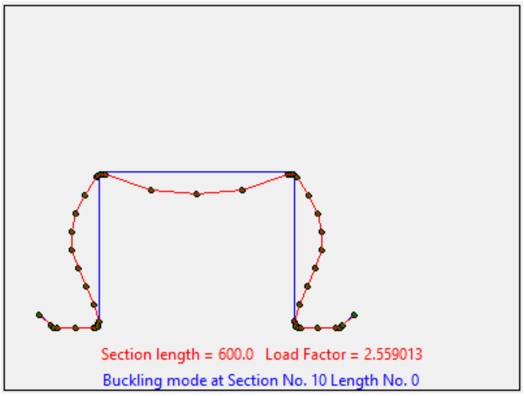

Figure 23 Buckling shape for ITF-F-H120-RIN3-DEG0-N50 at Section No. 10

3.2.6.2 3D buckling mode

THIN-WALL-PYTHON offers advanced visualization capabilities beyond the 2D buckling shape at selected sections. It includes two types of 3D representations for the buckling mode of the entire structural member as shown in Figure 24 and Figure 25:

- 3D Wireframe Plot: This representation shows the buckling mode in a three-dimensional wireframe format, enabling viewers to observe the structure's buckling pattern in detail (e.g. Figure 24).

- 3D Surface Filled with Colour Contour: This form of visualization presents the buckling mode as a 3D surface, where the contours are filled with colours. The colour contouring adds an additional layer of information, representing varying degrees of across the specimen (e.g. Figure 25).

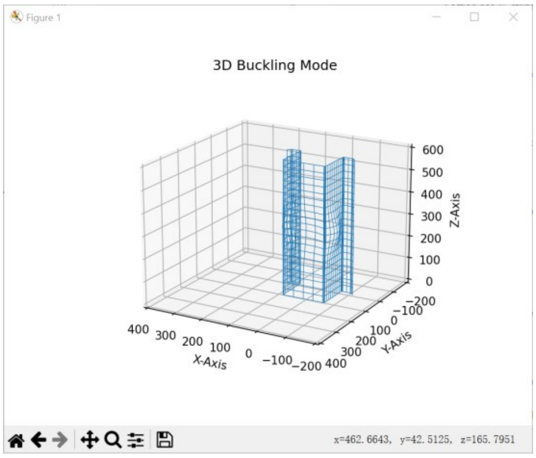

Figure 24 Typical 3D Wireframe Plot in ITF-F loading condition (3D buckling mode)

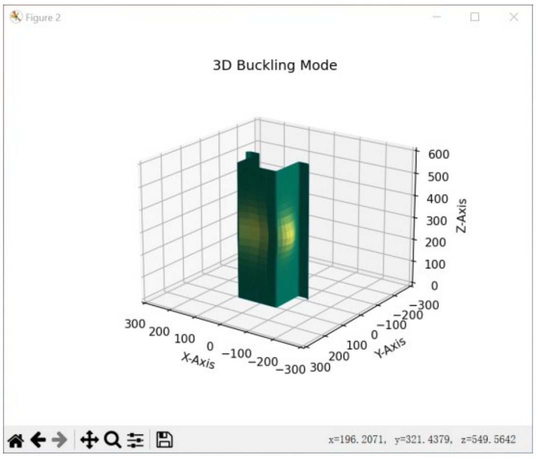

Figure 25 Typical 3D Surface Filled with Colour Contour in ITF-F loading condition (3D buckling mode)

Both types of 3D visualization in THIN-WALL-PYTHON enrich the analysis by offering a more comprehensive view of the structural behaviour under buckling conditions. These tools are invaluable for structural engineers and researchers, facilitating a deeper understanding of the buckling behaviours.

3.3 BUCKLING ANALYSIS USING ABAQUS

In the previous section, the development, capabilities, and usage of THIN-WALL-PYTHON, based on the Finite Strip Method (FSM), were extensively discussed. This provided valuable insights into how the tool simplifies and effectively calculates the buckling load of hat sections under various localised loading conditions.

In this section, the use of ABAQUS [34], a Finite Element Method (FEM) based software, for the buckling analysis of hat sections under localised loading is detailed. The section is structured to provide a comprehensive introduction of the buckling analysis using ABAQUS. Section 3.3.1 covers a detailed discussion of the modelling process for various loading cases. Section 3.3.2 provides examples of critical buckling load (P_{cr}) calculations in ITF and EOF loading cases. Section 3.3.3 concludes by benchmarking THIN-WALL-PYTHON's buckling load results against those obtained from ABAQUS, evaluating the accuracy and applicability of THIN-WALL-PYTHON in the context of an established FEM tool. Finally, an exploration of alternative modelling methods using ABAQUS follows, including a comparative analysis of their results in Section 3.3.4.

3.3.1 Modelling Using ABAQUS

The Finite Element Method (FEM) is a powerful and versatile solution for structural analysis. It has been widely used as an effective tool to perform buckling analysis under localised loading by researchers worldwide. While its use for buckling analysis in C sections, Z sections, and their variations is well-documented, the application to hat sections has seldom been mentioned in previous publications. In this section, the key points to develop a suitable model for buckling analysis are discussed in detail with following five contexts: parts, assembly, load, boundary condition (BC) and mesh.

3.3.1.1 Parts

For buckling analysis, the use of shell elements aligns well with the Finite Strip Method (FSM) theory. Shell elements are preferred in such analyses because they efficiently model the behaviour of thin-walled structures.

In the context of using ABAQUS for buckling analysis, an important consideration highlighted in the ABAQUS manual is that the contact conditions cannot change during a linear perturbation analysis; they remain as they were defined in the base state. This rule implies that modelling of physical contact elements, such as bearing plates, or defining contact interactions, is not necessary for this buckling analysis.

As a result, to simulate the effects of loading and restraint that would typically be provided by physical contact with elements like bearing plates, equivalent loads and boundary conditions are applied instead. The specifics of how these equivalent load applications and boundary conditions are implemented in the ABAQUS model will be elaborated upon in the later sections.

3.3.1.2 Assembly

In buckling analysis, the load exerted by the bearing plate is replicated by applying a line load along the contact line situated at the junction between the flanges and the rounded corners as for the Finite Strip Method (FSM). This method effectively simulates the bearing plate's load distribution on the hat section. During the assembly process, the specimen is carefully partitioned using a set of datum planes. These datum planes are strategically positioned to facilitate the precise application of load.

Typically, it is recommended that there should be a set of six (6) datum plates as a minimum to create at least six (6) nodes for applying point load to simulate a line load.

3.3.1.3 Load

In ABAQUS, the absence of a direct option for applying line loads necessitates an alternative approach. This is achieved by replacing the line load with a series of equivalent point loads, a method that allows for the simulation of the effect of distributed loads along a line.

Using the minimum required number of datum plates specified in the previous section as an example, the loading zone is divided in to five (5) strips using six (6) datum plates for each web. At each intermediate point between these strips, a point load of 100 Newtons is applied. At the first and last points, a reduced load of 50 Newtons is applied to simulate the distribution of the load along the length. As a result, the total load on the specimen is calibrated to sum up to 1 kN. This calibration is crucial because it ensures that the resulting eigenvalue from the analysis corresponds accurately to the actual P_{cr} allowing for an accurate and direct output when performing batch calculation.

Figure 26 demonstrates the distribution of the datum plates and the application of point loads.

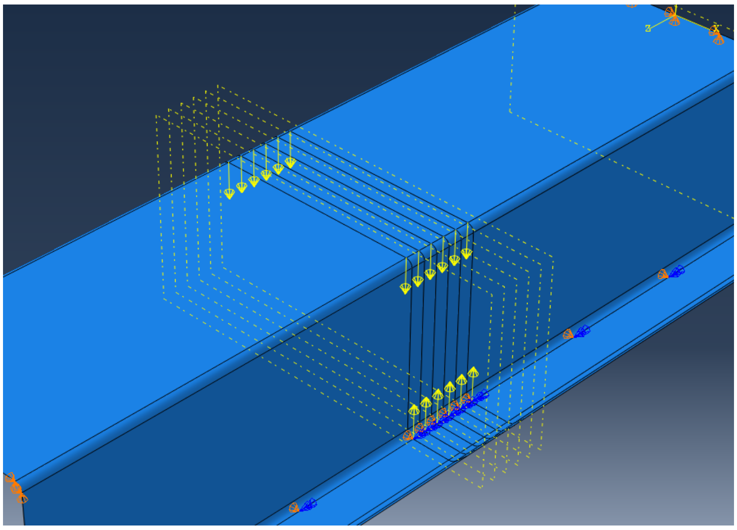

Figure 26 Distribution of datum plates and application of point loads

3.3.1.4 BC

To ensure the validity of results obtained from ABAQUS, it is critical to align the boundary conditions with those applied in THIN-WALL-PYTHON. This alignment is crucial for achieving comparable results and validating the accuracy of the analyses conducted using THIN-WALL-PYTHON. In this section, the end boundary conditions, and the bottom loading point boundary conditions are discussed separately.

In terms of the end boundary conditions, "S" (simply supported) and "C" (clamped) conditions in THIN-WALL-PYTHON require further attention in ABAQUS modelling. For "S" condition, the boundary conditions are set such that both horizontal movements in the X and Y directions (UX and UY) are restricted to 0, allowing the section to rotate freely but not to translate. For "C" condition, translation in all directions and rotation about all axes are set to 0.

As per the bottom loading point boundary conditions, the constraint setup is determined by the fastening condition. For unfastened (UF) loading cases, a constraint of UX = 0 is applied at the two junctions between the bottom flanges and the rounded corners on the web along the length of the specimen. Horizontal movement along this line is restricted for keep the shape of the cross section. For fastened loading cases, in addition to the UX = 0 constraint, a rotational constraint of RZ = 0 is applied along the length of the specimen. This replicates the effect of the fastener holding the bottom flange to the bearing plate.

It is worth noting that for ETF loading cases, an additional constraint of UZ = 0 should be applied for stability purposes. This restriction ensures that the specimen remains at its original position and does not move along the Z direction during the loading process.

3.3.1.5 Mesh

Numerous studies in the literature have underscored the significance of mesh size in achieving accurate computational results. Despite this acknowledgment, precise guidelines for determining the optimal mesh size remain elusive. It is generally recognised that finer mesh sizes tend to yield more precise outcomes, albeit at the expense of increased computational complexity and, consequently, extended calculation durations.

For buckling analysis, it is recommended to use a minimum of 20 elements per circle to ensure sufficient detail and accuracy. However, when conducting nonlinear numerical analysis involving a bearing plate, a higher number of elements may be necessary to obtain a smooth Load – Displacement (L-D) curve.

An assignment of global seeds is required to create the mesh on a specific object. According to the ABAQUS User's Manual, seeds are markers that you place along the edges of a region to specify the target mesh density in that region. Both the mesh density along the boundary of the region and the mesh density in the interior of the region are determined by the seeds along the edges of the region.

In this study, the approximate global size is set to 2.5 in the global seed setting, which means that the distance between two seeds is approximately 2.5 units of standard length (in this study the default unit is mm).

To implement curvature control in the meshing process of a part or part instance, ensuring that small holes or regions of high curvature are accurately represented, a parameter called the "Maximum deviation factor" is utilised. The deviation factor is a measure of how much the element edges deviate from the original geometry. In Abaqus/CAE, upon specifying this setting, the software illustrates the number of elements it would generate around a circle, based on the provided deviation factor. This feature aids in achieving a mesh that closely approximates the geometry's curvature, enhancing the accuracy of the simulation results.

In this study, the curvature control is set to 0.02, with an approximate number of elements per circle equals to 39 as shown in Figure 27.

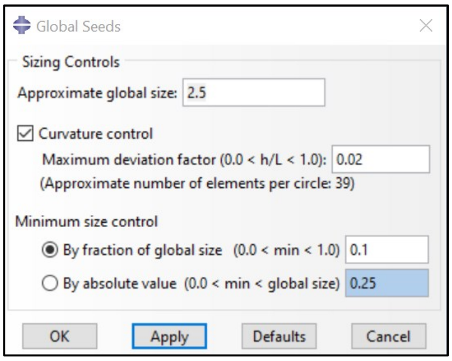

Figure 27 Global seeds setting in buckling analysis

3.3.2 Pcr calculation using ABAQUS

An example of the P_{cr} calculation is provided using the section given in Section 3.2.5. The buckling load calculated from ABAQUS is given as 254.33 kN, which has a <1% difference from the result provided by THIN-WALL-PYTHON with a value at 255.9 kN. The buckling mode and the buckling load result from the ABAQUS are demonstrated in Figure 28.

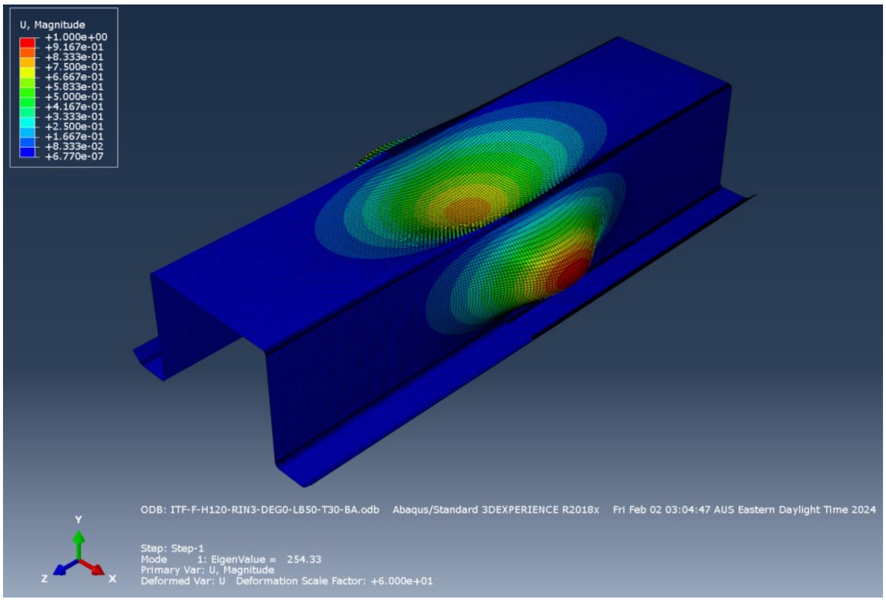

Figure 28 Buckling analysis result from ABAQUS for specimen ITF-F-H120-RIN3-DEG0-N50 (first buckling mode)

3.3.3 Comparison between ABAQUS and THIN-WALL-PYTHON

The prediction results obtained from the Finite Element Method (FEM) using ABAQUS are compared to those obtained from the Finite Strip Method (FSM) using THIN-WALL-PYTHON. The sections selected for this study are derived from those examined in the research conducted by Chen, Pham and Hancock [36] listed as Table 11.

Figure 29 illustrates the discrepancies between FEM and FSM predictions. In this figure, each data point, identified by coordinates (X, Y), where X and Y correspond to the prediction result from FEM and FSM respectively. Data points that lie closer to the dash line indicate a smaller difference between FEM and FSM predictions. Table 9 presents the Average (AVE), Standard Variation (StdDev) and Coefficient of Variation (COV) of $P_{cr_{(FEM)}}/P_{cr_{(FSM)}}$ corresponding to the result demonstrating in Figure 29. The results presented confirm a strong correlation between the FEM and FSM approaches. Consequently, FEM is validated as a suitable and accurate alternative for predicting the buckling load of hat sections subjected to transverse load.

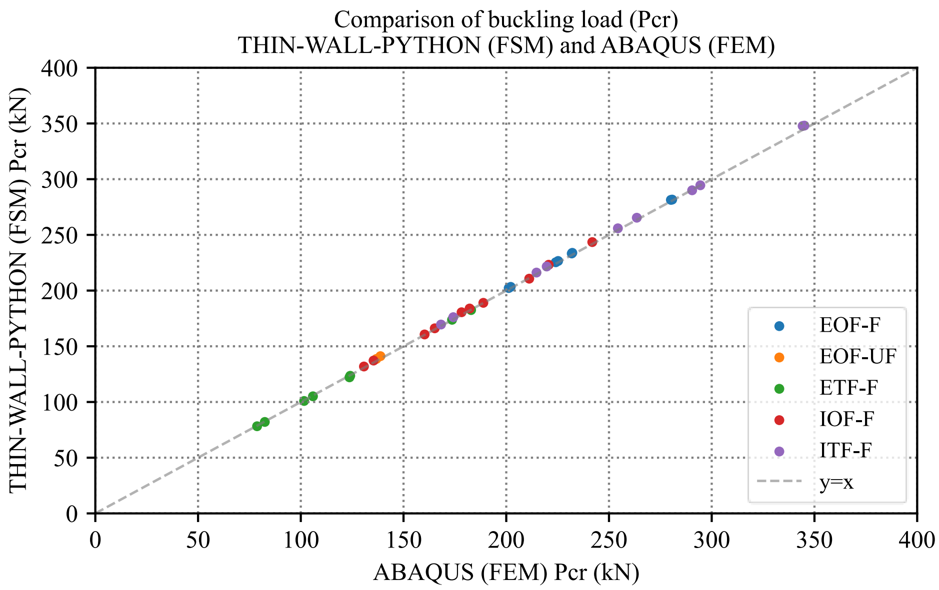

Figure 29 Comparison of buckling load between ABAQUS (FEM) and THIN-WALL-PYTHON (FSM)

Table 9 the AVE, StdDev and COV of $P_{cr_{(FEM)}}/P_{cr_{(FSM)}}$

Load case	Average	StdDev	COV
EOF-F	0.994	0.001	0.001
EOF-UF	0.985	0.002	0.003
ETF-F	1.006	0.004	0.004
IOF-F	0.993	0.005	0.005
ITF-F	0.994	0.004	0.004
Grand Total	0.996	0.007	0.007

3.3.4 Alternative boundary conditions setup in ABAQUS

A comprehensive study of the buckling analysis using Finite Strip Method (FSM) with THIN-WALL-PYTHON has been presented and verified with ABAQUS in Sections 3.3.2 and 3.3.3 respectively. It has been proved that the FSM and corresponding FEM models provide a consistent result across all loading cases with less than 2% difference.

However, inherent to the Finite Strip Method's design, constraints placed on cross-section nodes affect the entire length of the specimen, a practice known as the Full Restraint Method (FRM). This approach often results in an over-constrained model relative to common loading conditions, where restraints on the flanges occur only at specific points (often at the bearing zone), referred to as the Partially Restraint Method (PRM).

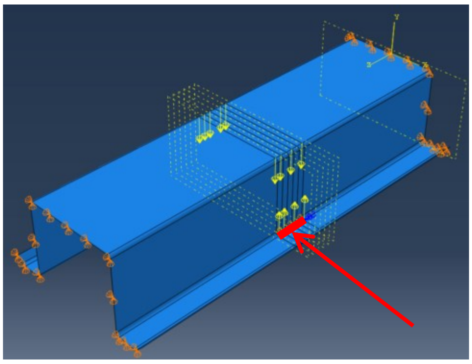

Figure 30 Typical BC setup in ABAQUS using PRM (restraint only apply within bearing length)

In view of these considerations, comprehensive research has been conducted to examine the disparities in critical load predictions between the full restraint and partially restraint methods. This exploration aims to refine the accuracy of buckling load predictions by aligning the modelling constraints more closely with the real-world conditions of structural components under load.

A new series of buckling models has been created utilising the Partially Restrained Method (PRM) approach. Figure 30 illustrates the standard configuration of an ABAQUS model employing PRM. Based on the cross-section dimensions described in Section 3.3.3, the buckling load was recalculated with the PRM model. With Figure 29 serving as the reference, the buckling load determined through the

PRM approach is superimposed on Figure 29 for comparative analysis and replotted as Figure 31.

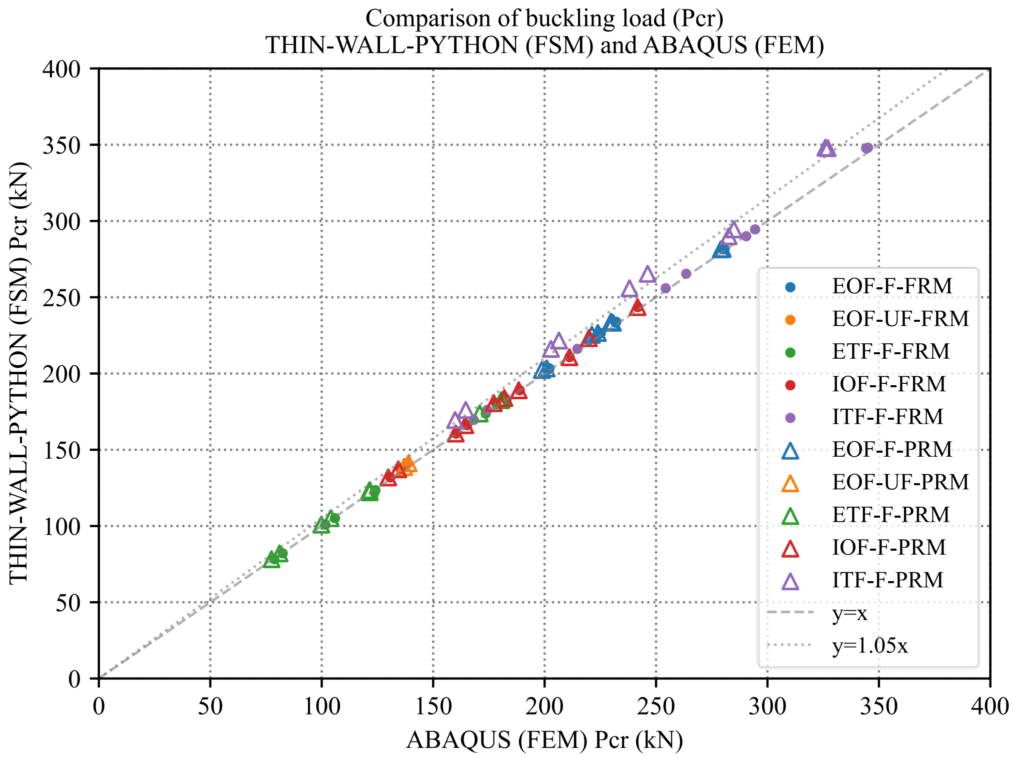

Figure 31 Comparison of buckling load between THIN-WALL-PYTHON and ABAQUS with different methods

According to this figure, while most of the loading cases have negligible differences between these two methods, a noticeable but not significant difference (5% maximum) is found between the buckling load results from FRM and PRM in ITF-F loading cases only.

Despite that there is a 5% difference between the FRM and PRM methods, Clause 8.7 in S909-17 [3] clarified that it's permitted to be laterally restrained by rigid elements at the open side of the section that might subject to splaying effect. Consequently, additional strips may be necessary in practical applications, nudging the condition closer to FRM rather than PRM. Based on this, using the buckling load calculated from FRM is considered permissible.

Table 10 A complete list of hat sections for use in Section 3.3.3

SEQ	LC	FC	H (mm)	RIN (mm)	DEG (deg)	N (mm)
1	EOF	F	120	3	0	50
2	EOF	F	120	3	15	50
3	EOF	F	120	3	30	50
4	EOF	F	120	8	0	50
5	EOF	F	120	8	15	50
6	EOF	F	120	8	30	50
7	EOF	F	90	3	0	50
8	EOF	F	90	8	0	50
9	EOF	UF	120	3	0	50
10	EOF	UF	120	8	0	50
11	ETF	F	120	3	0	50
12	ETF	F	120	3	15	50
13	ETF	F	120	3	30	50
14	ETF	F	120	8	0	50
15	ETF	F	120	8	15	50
16	ETF	F	120	8	30	50
17	ETF	F	90	3	0	50
18	ETF	F	90	8	0	50
19	IOF	F	120	3	0	100
20	IOF	F	120	3	0	50
21	IOF	F	120	3	15	50
22	IOF	F	120	3	30	50
23	IOF	F	120	8	0	100
24	IOF	F	120	8	0	50
25	IOF	F	120	8	15	50
26	IOF	F	120	8	30	50
27	IOF	F	90	3	0	50
28	IOF	F	90	8	0	50
29	ITF	F	120	3	0	100
30	ITF	F	120	3	0	50
31	ITF	F	120	3	15	50
32	ITF	F	120	3	30	50
33	ITF	F	120	8	0	100
34	ITF	F	120	8	0	50
35	ITF	F	120	8	15	50
36	ITF	F	120	8	30	50
37	ITF	F	90	3	0	50
38	ITF	F	90	8	0	50

Table 11 Buckling load from THIN-WALL-PYTHON, ABAQUS (FRM) and ABAQUS (PRM)

SEQ	SECTION CODE	TWP (kN)	FRM (kN)	PRM (kN)	FRM/TWP	PRM/TWP
1	EOF-F-H120-RIN3-DEG0-N50	233.30	231.87	230.64	0.994	0.989
2	EOF-F-H120-RIN3-DEG15-N50	226.58	225.24	223.90	0.994	0.988
3	EOF-F-H120-RIN3-DEG30-N50	203.33	202.17	200.94	0.994	0.988
4	EOF-F-H120-RIN8-DEG0-N50	233.88	232.15	229.77	0.993	0.982
5	EOF-F-H120-RIN8-DEG15-N50	225.41	224.09	221.19	0.994	0.981
6	EOF-F-H120-RIN8-DEG30-N50	202.28	201.20	198.77	0.995	0.983
7	EOF-F-H90-RIN3-DEG0-N50	281.67	280.75	279.94	0.997	0.994
8	EOF-F-H90-RIN8-DEG0-N50	281.42	280.13	279.05	0.995	0.992
9	EOF-UF-H120-RIN3-DEG0-N50	141.14	138.76	138.94	0.983	0.984
10	EOF-UF-H120-RIN8-DEG0-N50	138.62	136.77	137.01	0.987	0.988
11	ETF-F-H120-RIN3-DEG0-N50	122.12	123.69	121.47	1.013	0.995
12	ETF-F-H120-RIN3-DEG15-N50	105.10	105.92	104.02	1.008	0.990
13	ETF-F-H120-RIN3-DEG30-N50	82.09	82.48	81.10	1.005	0.988
14	ETF-F-H120-RIN8-DEG0-N50	123.52	124.06	121.47	1.004	0.983
15	ETF-F-H120-RIN8-DEG15-N50	100.91	101.61	99.81	1.007	0.989
16	ETF-F-H120-RIN8-DEG30-N50	78.23	78.73	77.48	1.006	0.990
17	ETF-F-H90-RIN3-DEG0-N50	182.51	182.89	180.55	1.002	0.989
18	ETF-F-H90-RIN8-DEG0-N50	173.79	173.62	170.88	0.999	0.983
19	IOF-F-H120-RIN3-DEG0-N100	243.53	241.87	241.74	0.993	0.993
20	IOF-F-H120-RIN3-DEG0-N50	223.19	220.65	219.87	0.989	0.985
21	IOF-F-H120-RIN3-DEG15-N50	180.56	178.25	177.19	0.987	0.981
22	IOF-F-H120-RIN3-DEG30-N50	137.18	135.42	134.35	0.987	0.979
23	IOF-F-H120-RIN8-DEG0-N100	210.69	211.18	211.12	1.002	1.002
24	IOF-F-H120-RIN8-DEG0-N50	189.01	188.85	188.41	0.999	0.997
25	IOF-F-H120-RIN8-DEG15-N50	166.12	165.19	164.43	0.994	0.990
26	IOF-F-H120-RIN8-DEG30-N50	131.86	130.73	129.85	0.991	0.985
27	IOF-F-H90-RIN3-DEG0-N50	183.90	182.16	181.96	0.991	0.989
28	IOF-F-H90-RIN8-DEG0-N50	160.62	160.25	160.13	0.998	0.997
29	ITF-F-H120-RIN3-DEG0-N100	290.02	290.47	282.58	1.002	0.974
30	ITF-F-H120-RIN3-DEG0-N50	255.90	254.33	238.10	0.994	0.930
31	ITF-F-H120-RIN3-DEG15-N50	221.63	219.69	206.45	0.991	0.932
32	ITF-F-H120-RIN3-DEG30-N50	176.14	174.23	164.63	0.989	0.935
33	ITF-F-H120-RIN8-DEG0-N100	294.51	294.45	284.92	1.000	0.967
34	ITF-F-H120-RIN8-DEG0-N50	265.40	263.54	246.23	0.993	0.928
35	ITF-F-H120-RIN8-DEG15-N50	216.17	214.72	202.83	0.993	0.938
36	ITF-F-H120-RIN8-DEG30-N50	169.53	168.23	159.85	0.992	0.943
37	ITF-F-H90-RIN3-DEG0-N50	347.76	344.26	327.04	0.990	0.940
38	ITF-F-H90-RIN8-DEG0-N50	348.08	345.11	325.96	0.991	0.936

Note:
TWP: Buckling load from THIN-WALL-PYTHON.
FRM: Buckling load from ABAQUS using Fully Restraint Method.
PRM: Buckling load from ABAQUS using Partially Restraint Method.

3.4 CONCLUSION

The comprehensive analysis undertaken in this study demonstrates the effectiveness and accuracy of the Finite Strip Method when applied with THIN-WALL-PYTHON and validated against ABAQUS simulations for buckling analysis.

While the FRM used in these analyses may not perfectly capture real-world conditions in every instance, comparisons between ABAQUS simulations using both FRM and the PRM show that the buckling load results are closely aligned for most loading cases. Despite observing up to a 5% difference in ITF-F loading case, the AISI S909-17 standards endorse the use of lateral restraints. This approach effectively brings the boundary conditions closer to those of FRM. It is considered appropriate to use buckling load calculations derived from FRM for its efficiency, convenience, and user-friendliness.

This page intentionally left blank.

Chapter 4 Experimental study on failure modes of cold formed steel sections

4.1 INTRODUCTION

In the past few decades, few researchers have systematically conducted web crippling tests regarding hat sections. Santaputra [6] performed a comprehensive range of hat sections subject to unfastened loading cases. The purpose of the investigation was to study the structural behaviour of high strength cold-formed steel beams subjected primarily to web crippling and a combination of web crippling and bending moment. Wu et al. [16] conducted a series of tests regarding single and double ribs hat sections as shown in Figure 32. However, that research was mainly directed at improving the empirical equations. Only slender sections were tested by Wu et al. and there is no recent detailed test for the web crippling of hat sections under localised loading for use in the DSM, especially in the range of stocky sections.

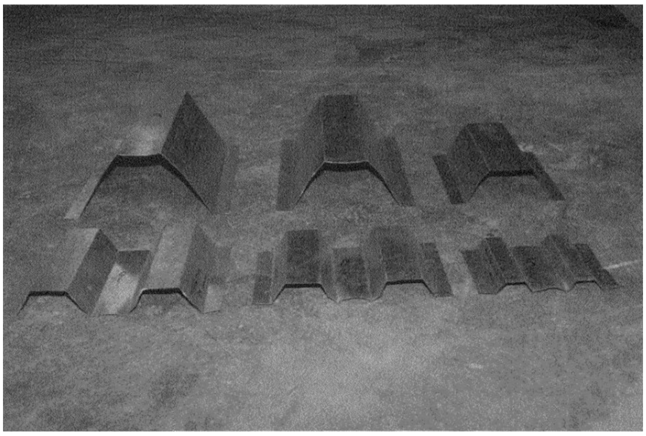

Figure 32 single and double ribs hat sections tested by Wu et al. [16]

This chapter presents a comprehensive report on the experimental study investigating the web crippling capacity of hat sections under various practical loading cases. In this experimental programme, ninety experiments were conducted, utilising HA250 Grade Cold-Formed Steel (CFS) plates conforming to the Australian Standard AS1594 [37], which have a guaranteed minimum yield strength of 250 MPa. The nominal thickness of the steel sheet was 3 mm and the nominal internal corner radii for two different corner radii were 3 mm and 8 mm. Grade 12.9 bolts were used to ensure the fastened conditions were met throughout the tests. The test results are used in this thesis to calibrate the DSM for the design of CFS hat sections under localised loading, as well as to validate an FEM model used separately to conduct parametric studies.

In this chapter, Section 4.2 discusses the detailed experimental program. The general design of the specimens is first introduced, followed by a detailed discussion of the test configurations for the Two-Flange (TF) and One-Flange (OF) loading cases, respectively. Section 4.3 presents and discusses the experimental results and findings, categorized by different loading cases. For each loading case, sections with vertical webs and sloped webs are analysed and compared. Additionally, this chapter covers issues encountered during the experimental program.

4.2 EXPERIMENTAL PROGRAM

4.2.1 Test specimen design

The dimensions of the test specimens were selected accounting for the following factors. In general, the size should be practical and based on hat sections available in the market. Hat sections from the BlueScope Lysaght catalogue [38] were selected as a reference. Since the specimens were manufactured by brake-press folding instead of cold-rolling, manufacturing limitations were taken into account. Furthermore, stocky sections were selected to specifically investigate the yield load and yielding behaviour of the sections as well as the plastic mechanism models developed, as there is a lack of experimental data for stocky sections. Both vertical and sloped web configurations were tested. It should be noted that due to the nature of hat sections, splaying of the sloped webs should be properly controlled during the tests. In the previous research conducted by Wu et al. [16], C-clamps were used to control the splaying of the sloped webs, whereas in this research program, fasteners were used instead of C-clamps. Two different corner radii were also selected to fully identify the different structural behaviours with small and large corner radii.

4.2.1.1 Dimension of cross sections

In this test series, eight different sections were selected for the localised loading research. The major dimensions are the height of the web (H), width of the top flange (W), internal corner radius (r_{in}) between flange and webs, and the slope angle of the webs relative to the vertical direction (α) as shown in Figure 33.

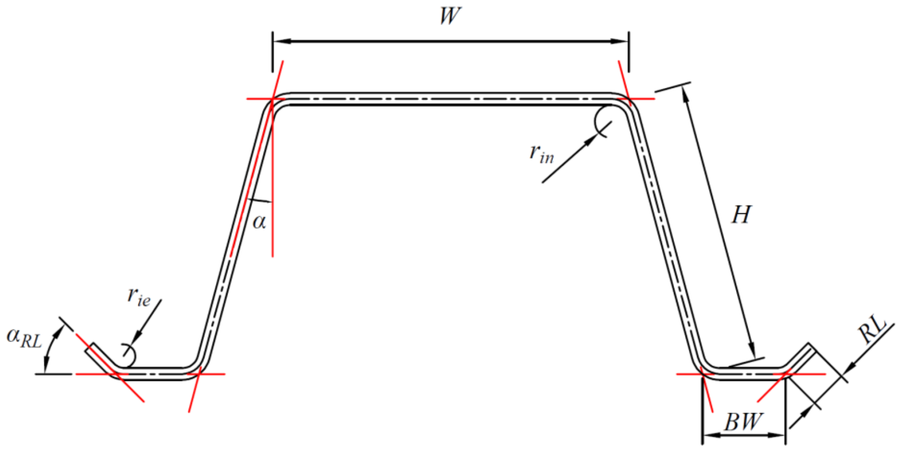

Figure 33 Detail of dimension

The heights of the web (H) were selected as 90 mm and 120 mm, and the width of the hat section (W) was fixed at 150 mm for all sections due to the manufacturer's advice based on the method of manufacture. An electrical vernier scale and micrometer were used to measure and confirm the actual thickness (t) of the sheet metal. The internal corner radii (r_{in}) were pre-determined based on the failure behaviours described by Bakker [39] and were selected as 3 mm and 8 mm to cover both the rolling and yield-arc post-failure modes respectively discussed by Bakker. A radius gauge was used to measure both the internal and external corner radii between the flanges and webs. The inclination of the webs (α) was selected as 0, 15 and 30 degrees as shown in Figure 33. A bevel protractor was used to determine the actual slope angles. For all sections, the width of the bottom flanges (BW) was set at 35 mm, the return lips (RL) at 15 mm, and the angle of the return lips relative to the horizontal (α_{RL}) was set at 45 degrees.

It is important to note that the internal corner radius between the return lip and the bottom flange (r_{ie}) was set at 6 mm, which is different from the internal corner radius between the bottom flange and the web. The internal corner radius between the bottom flange and the web was set to be the same as the internal corner radius between the top flange and the web.

Given that the width of the hat section (W) and the height of the web (H) are defined as the centreline lengths as shown in Figure 33 and cannot be measured directly, alternative dimensions were measured for back calculating the centreline parameters. Three parameters were measured for calculating the width of the hat section (W) and the height of the section (H). They are the angle between bottom flange and the web (θ_L, θ_R where L and R means the web on the left and right), the width of the flat part of the top flange (W_{TF}) and the heights of the section (D_{EL}, D_{ER}), measured from the top of the top flange to the bottom of the bottom flange regarding left and right webs respectively. With these three parameters plus the internal corner radii (r_{in}) and the thickness (t), the dimension of the sections can be back calculated. Detailed measured dimensions are given in Appendix B.

According to the dimensional deviation study, the as-manufactured specimens were found to be within the acceptable manufacturing tolerances (±1.5 mm or, 0.0125 rad or 0.716° equivalent for 120 mm cantilever plate, as specified by the manufacturer) and were therefore deemed adequate for the experimental testing.

4.2.1.2 Material properties

The material used for manufacturing the specimens was carefully selected for a better understanding of the effect of the yielding behaviour of the hat sections. In this study, TRU-SPEC coil plate steel from BlueScope [37], complying with AS/NZS 1594 – HA250, was selected for manufacturing the specimens for the following reasons. Firstly, mild steel with normal strength has a typical stress – strain curve with a clear yield plateau. The yield strength can be simply determined by taking the stress at the yield plateau instead of using 0.2% strain offset strength as for high strength steel. Secondly, thanks to the relatively low yield stress (nominally 300 MPa to 330 MPa), it is easier for the specimen to achieve the yielding point while keeping the buckling load at a high level. In order to better understand the yielding behaviour of hat sections under localised loading, the thickness of the plate was selected as 3 mm so that the section is relatively stocky for yielding to occur first before local buckling.

Eight coupons from two batch of materials were taken from the sheet plates which were used to manufacture the specimens. Four of the coupons were taken longitudinally and four were taken transversely. Previous research [40] suggests using enhanced material properties within 2t distance from corners. However, the enhanced strength zone comprises a relatively small portion of the overall section, with limited strength enhancement (<20%) in these regions. Consequently, material properties from flat portions were selected to represent overall section properties. As a conservative approach, no coupon tests were conducted in the strength-enhanced zones.

Because the sheet steel is mild steel and the thickness of the steel sheet is 3 mm, the tensile behaviour from both directions is expected to be similar with minimal difference. The tensile coupon dimensions conformed to the Australian Standard AS 1391 for the tensile testing of metals using 12.5-mm-wide coupons with a gauge length of 50 mm. The coupon tests were performed using the using the MTS Sintech 65/G testing machine operated in a displacement control mode. The detailed testing data is converted to stress – strain curves and attached in Appendix A.

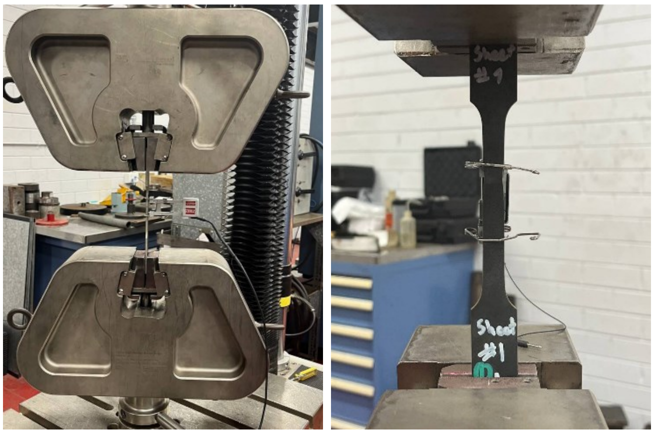

Figure 34 Typical coupon test setup

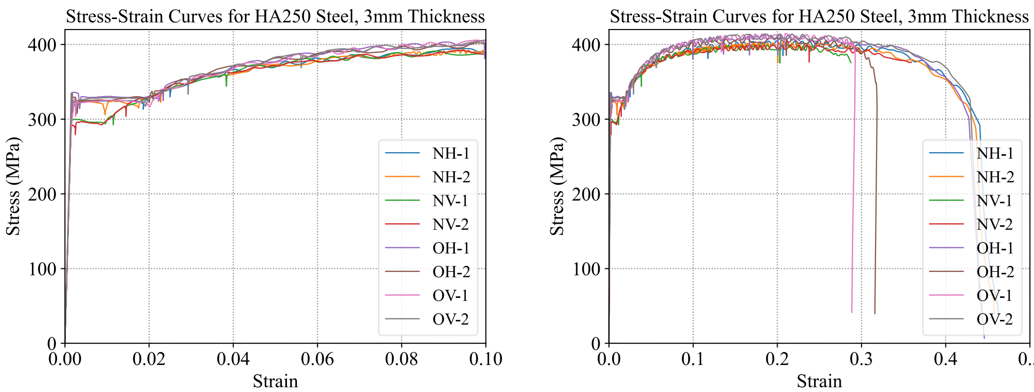

Figure 35 Typical stress – strain curve for HA250, 3 mm, strain = 0 - 0.1 (L) and 0 - 0.5 (R)

Table 12 Collection of material property

SEQ	BATCH	DIRECTION	NUM	f_y (MPa)	f_u (MPa)
1	O	V	1	323	414.7
2	O	V	2	323	414.0
3	O	H	1	333	412.8
4	O	H	2	327	408.4
5	N	V	1	300	404.8
6	N	V	2	297	403.2
7	N	H	1	323	399.3

SEQ	BATCH	DIRECTION	NUM	f_y (MPa)	f_u (MPa)
8	N	H	2	325	399.1

Figure 35 demonstrates the stress-strain curves from all eight coupon tests, and the yield stress and ultimate strength values have been collected in Table 12. According to the coupon test results, there is a noticeable but minimal difference between the yield stresses of the two batches of materials. Thus, it is important to identify the material direction (longitudinal or transverse) of each specimen and ensure that the corresponding yield stress value is selected for future analyses. To avoid ambiguity regarding the material and specimen directions, the following definitions are used:

- **V & H** are used to define the direction of the raw material, where V is the rolling direction of the steel coil, and H is the direction perpendicular to the rolling direction of the steel coil.
- **Longitudinal & Transverse** are used to define the direction of the specimen. The capacity of the specimen is taken as the strength of the coupon cut from the transverse direction.
- The material used in this experiment study are from two different batches. The first batch of specimens refers to **batch O**. The second batch of specimens refers to **batch N**.
- For the **first** batch of specimen, the **transverse** direction of the specimen is the same as the **V direction** of coil steel **(batch O)**.
- For the **second** batch of specimen, the **transverse** direction of the specimen is the same as the **H direction** of coil steel **(batch N)**.

Figure 36 is used to demonstrate the relationship between the directions of the specimens and the coil steel. It is not meant to indicate that these two batches of specimens were cut from the same steel coil.

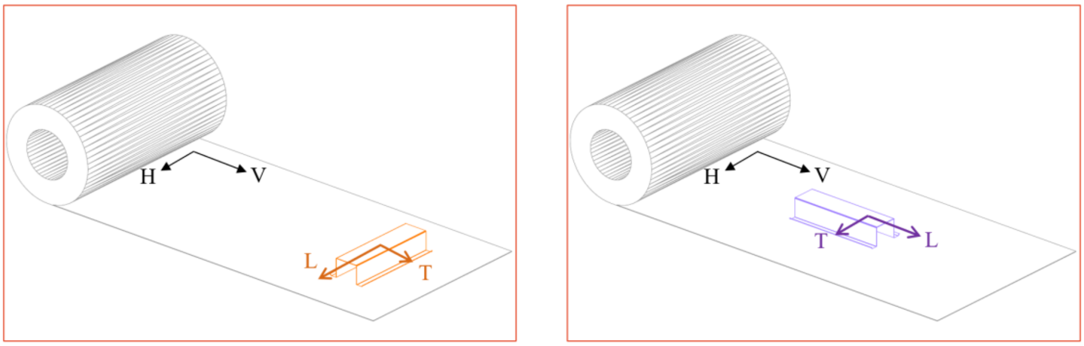

Batch Code: O
ITFs and ETFs

Batch Code: N
IOFs and EOFs

Figure 36 Correlation between specimen direction and material direction

Based on this correlation and referring to the coupon test results presented in Figure 35 and Table 12, the yield strength value of 323 MPa, corresponding to the transverse (H or V) direction of the material, is selected for further analyses involving these test specimens.

4.2.1.3 Bearing plate length

For interior loading cases, the bearing length (N) was selected as 50 and 100 mm to investigate the effect of different load distributions through the web. It is believed that the bearing plate length should be less than the height of the section to be considered as localised loading instead of a type of uniformly distributed load (UDL).

For end loading cases, the bearing length was selected as 50 mm only.

The locations of critical bearing plate, which is also referred to the bearing plates at the region of failure, has been defined by S909-17 and to be discussed in later section 4.2.3.2.

4.2.1.4 Specimen length

According to the or Clause 8.8 in AISI Standard S909-17 [3], the length of the specimen should be at least three (3) times the depth of flat portion of web element along the plane of web (h), plus the bearing plate lengths if applicable. For ITF loading cases, it is permitted to use a longer length, for example, 5.0 h.

In this study, for the two-flange loading cases, given that the bearing plate length is selected as 50 mm and 100 mm, the length of the specimen was selected as 600 mm to ensure the web crippling requirement is fulfilled.

For one-flange (OF) loading cases, the referenced test standard does not recommend employing excessively long specimen lengths, as these may promote early failure via the simultaneous action of bending and web crippling prior to pure web crippling becoming the dominant failure mode. Thus, in this study, similar to the previous study performed by Wu et al. [16], the length of specimen was purposefully greater than the minimum required length to guarantee the validity of the one flange loading condition.

It's important to note that slightly exceeding the minimum length requirements offers additional leeway to accommodate experimental uncertainties. This approach does not conflict with the principle that specimens for One-Flange (OF) loading should not be overly long to prevent bending failures because they must not be so short as to compromise the validity of OF loading conditions simultaneously. Despite taking extra precautions, manufacturing and specimen preparation processes inevitably introduce imperfections. For instance, the actual height of the specimen might slightly exceed the nominal value, fastener holes are made 2 mm larger than the diameter of the fasteners, and the middle bearing plate might be slightly off-centre due to alignment errors or slippage. If a specimen were cut exactly to the nominal desired length, any of these factors could compromise the minimum clear distance specified by the standards.

Consequently, the clear distance of the bearing plate was intentionally designed to exceed the minimum required distance by a reasonable margin. Supported by a numerical study prior to testing, the length of the specimen used in the one-flange loading cases was thus set at 600 mm.

It should be noted that for the section with a 120 mm height, the minimum required length subject to a 50 mm bearing length is 510 mm, and the minimum required spacing between the middle and end bearing plates (3.0h) is 360 mm. In this study, when the length of the specimen is selected as 600 mm, the clearance is calculated as 450 mm, which is 25% more than the minimum required distance. A separate study regarding the difference of the capacity is discussed in section 5.3.7.

Similarly, for the section with a 90 mm height, the minimum required length subject to a 50 mm bearing length is 420 mm, and the minimum required clearance (3.0 h) is 270 mm. Thus, a 450 mm clearance distance means that there is 66.7% more than the minimum required distance.

4.2.1.5 Nomenclatures

A nomenclature system was developed based on the loading cases, fastening conditions, dimensions and test number for a given section configuration. Table 13 is used to demonstrate the abbreviation and its meaning. It should be noted that the equivalent height of hat sections is defined as the height of the section when the webs are vertical, that is, for sections with the same height of webs, the "H" dimension is identical regardless of the slope angle of the webs. The number of the tested specimens is presented as shown in Table 14.

In certain circumstances, alongside the detailed nomenclature, a separate numbering system is implemented to abbreviate each specimen's name. This numbering system utilises three-digit numbers, where the first digit distinguishes the loading cases, while the second and third digits are assigned sequentially. Full detail of the numbering system is given in Table 15. The detail of definitions marked with symbols is shown in Figure 33.

Table 13 Nomenclature: Abbreviations, symbols and notes

Abbreviation as prefix	Symbol	Note
ITF/ETF/IOF/EOF		Loading cases
F		Fastening conditions - [F] for fastened
UF		Fastening conditions - [UF] for unfastened
H	H	Equivalent height of the section
W	W	Width of top flange
RIN	r_{in}	Internal corner radius
DEG	α	Slope angle
N	N	Bearing length
T		Thickness
L		Length of specimen

Note 1: When any of the dimensions are not important, they can be omitted to avoid overlength. For example, T and L might be omitted when the presented tests have identical value regards the thickness and length.
Note 2: A unique ID number is assigned to each specimen at the end of the full name of specimen when the tests are repeated. For example, for ITF-F-H120-RIN3-DEG0-N50-1, the last number "1" is the first test of ITF-F-H120-RIN3-DEG0-N50
Note 3: "FTF" means fastened top flange.
Note 4: "LB" written on the specimen in the figures are identical to the "N" used in this thesis.

Table 14 Number of tested specimens by loading cases and fastening conditions

LC-FC	SPECIMEN COUNTS
ITF-F	23
ETF-F	18
IOF-F	20
EOF-F	20
EOF-UF	5
ITF-F-FTF	2
IOF-UF	2

Table 15 Numbering system for all tests

		N50 H120 DEG0	N50 H120 DEG15	N50 H120 DEG30	N50 H90 DEG0	N100 H120 DEG0
ITF-F	**RIN3**	103 104 105[1]	106 107	108 109 110	122 123	101 102
ITF-F	**RIN8**	114 115 116[1]	117 118	119 120 121	124 125	111 112 113
ETF-F	**RIN3**	201[2] 202 203	204[2] 205 206	207[2] 208 209	218 219	
ETF-F	**RIN8**	210 211	212 213 214	215 216 217	220 221	
IOF-F	**RIN3**	303[2] 304 305	306 307	308 309	318 319	301 302
IOF-F	**RIN8**	312 313	314 315	316 317	320 321	310 311
IOF-UF	**RIN3**		322			
IOF-UF	**RIN8**		323			
EOF-F	**RIN3**	401 402	403 404	405 406 407	415 416 417	
EOF-F	**RIN8**	408 409	410 411	412 413 414	418 419 420	
EOF-UF	**RIN3**	421 422 423				
EOF-UF	**RIN8**	424 425				

Note 1: 201, 204, 207, 303 were dummy test for specific load cases.
Note 2: Example: For a specific section, ITF-F-H120-RIN3-DEG0-N50 has two tests: 103 and 104.

[1] Top flange was fastened to the bearing plate (FTF).
[2] Dummy test, data not included.

4.2.2 Fasteners

Two types of fasteners namely M10 hex head bolts and socket head cap screws in Grades 10.9 and 12.9 respectively were used in the experiments. There was no significant behaviour difference between these fasteners in the experiments. Socket head cap screws were the preferred option when the working space was limited. Metal Tek self-tapping screws (Buildex® 12-24 Hex Head Series 500® Teks® Screw) were used for fixing the stiffened plate to the specimen in the EOF loading cases.

4.2.3 Test configuration for two-flange (TF) loading cases

4.2.3.1 TF Loading cases and control

A total of 46 specimens were tested to study the web crippling behaviour of the hat sections under TF loading cases with fastened bottom flanges. Among these specimens with valid results, 25 of them were tested with the ITF loading case and 18 with the ETF loading cases. The width of the loading plates used was 50 mm and 100 mm. All specimens were tested under displacement control with the minimum displacement set at 100 mm to ensure significant deformation had occurred.

4.2.3.2 TF test setup and procedure

The tests were conducted in the J.W. Roderick Structural Laboratory of the School of Civil Engineering, the University of Sydney. MTS Sintech 65/G was used for the web crippling tests. A digital data recorder was also used during the tests to record the load and displacement using the MTS control system and two sets of Linear Voltage Displacement Transducer (LVDT) respectively. During the tests, the load was applied by a controlled displacement of the top loading cell while the bottom bearing plate sat on a half round fixed to the base plate as shown in Figure 37.

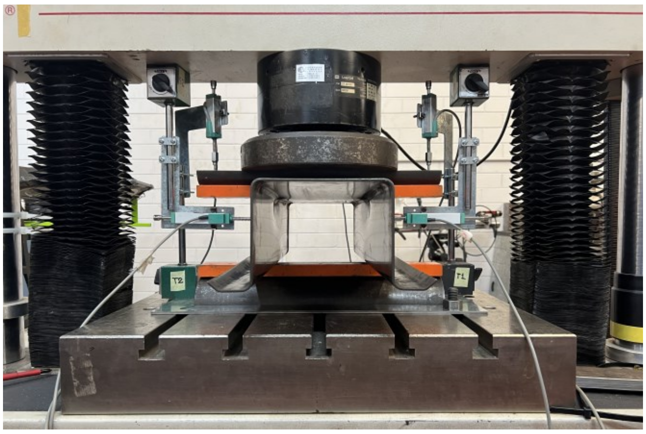

Figure 37 End view of two flange loading test setup in MTS Machine

The setup of the test rig for two flange loading is shown in Figure 37 and was designed to meet the criteria described in Figures 38 and 39 taken from AISI Standard S909-17 for the ITF and ETF loading respectively.

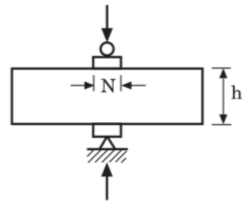

Figure 38 Interior Two-Flange Loading (ITF) in AISI S909-17

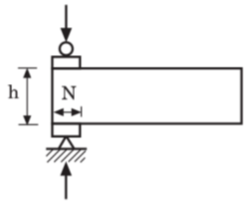

Figure 39 End Two-Flange Loading (ETF) in AISI S909-17

For the ITF load case, the specimen was fastened to a bearing plate with thickness of 20 mm by using high strength bolts through the predrilled holes in the bottom flanges. The specimen together with the fastened bottom bearing plate was placed on a half round fixed on the base plate of the testing machine. A top bearing plate, with the same dimensions as the bottom bearing plate, was placed on the top flange and carefully aligned with the bottom plate. After the specimen was adjusted to a horizontal position with the help of a bubble level and timber blocks, the top half round was carefully placed on the top of the bearing plate so that the centre of the loading line for the whole system was aligned through the specimen. Once the initial load was applied, after installing and initializing the LVDTs for recording the displacement data, all timber blocks used to maintain the horizontal position were removed. An example of the ITF loading condition setup is shown in Figure 40 including the bolts attaching the bottom flanges for the sloping web case.

Figure 40 ITF loading case setup

For the ETF load case, the test setup was similar to the ITF case, except that the bearing plates were installed at one end of the specimen. Timber blocks and a hydraulic scissor lift trolley were used as temporary supports to hold the horizon position of the specimen at the unsupported end as shown in Figure 41.

During the tests, two sets of LVDTs were used to monitor the displacements. The first set of LVDTs was mounted on the base plate so that the vertical displacement of the top bearing plate was measured. The data was extracted for further analysis of the Load-Displacement curves. The second set of LVDTs was mounted on the moving loading bar of the MTS testing system and the purpose of this set of LVDTs was to monitor the deformation of the web to ensure the deformations remained symmetric indicating equal loading on both webs.

Figure 41 ETF loading case setup (view from the unsupported end)

The specimens were prepared in advance by drawing grids on the outer sides of the web, either in the middle or at the end of the web, respectively, for alignment and better demonstration of deformations. After the assembly of the bearing plates and specimens the assembling was placed on the half-round and carefully aligned with the centreline of the loading cell. The MTS loading cell was zeroed. An initial load (less than 1 kN) was applied to the specimen to ensure that the whole loading system was secured in place. Then the timber blocks and other supporting objects were removed, and LVDTs were carefully installed and calibrated. Once the digital data recorder started recording, the loading process was started. The loading process was set to 0.5 mm per minute. Once the displacement reached 12 mm or significant capacity drop was observed, the data recording was stopped, and the loading system was reset.

4.2.4 Test configuration for one-flange (OF) loading cases

4.2.4.1 OF loading cases and control

A total of 48 specimens were tested to study the web crippling behaviour of the hat sections under OF loading cases. Among these specimens with valid results, 22 of them were tested under IOF loading and 25 of them were tested under EOF loading. The width of the loading plates used were 50 mm and 100 mm. All specimens were tested under displacement control with the minimum displacement set at 100 mm to ensure significant deformation had occurred. Some of the tests were stopped before 100 mm displacement when two conditions were met:

- an obvious peak load was observed; or
- the L-D curve was on a stable decreasing trend.

The limited scope of unfastened specimens in the experimental programme reflects practical considerations. Hat sections with inclined webs demonstrate superior stability, assembly efficiency, and stackability. While these sloped web sections exhibit fundamentally different behaviour from channel sections, introducing splaying effects that typically require mechanical restraint in practice. Since hat sections are rarely used without fasteners in practical applications, research resources were focused on investigating loading conditions most relevant to contemporary industry needs. As EOF-UF cases have been tested and reported by Wu, Yu and LaBoube, nine unfastened tests were conducted specifically in the EOF configuration with vertical web sections for comparison.

4.2.4.2 OF test setup and procedure

As a second series test of the whole experimental study, the one-flange tests were conducted in the J.W. Roderick Structural Laboratory of the School of Civil

Engineering, the University of Sydney. MTS Sintech 65/G was used for both web crippling tests and coupon tests to obtain the material properties. The machine setup for one-flange web crippling test was similar to the two-flange loading test.

In order to perform a one-flange loading test using the MTS Sintech 65/G machine, a specially designed test rig was required to extend the testing platform. The test rig was made of two parallel-placed 125 PFC (Parallel Flange Channels) of 800 mm length. These two PFCs were placed face to face at 260 mm distance as shown in Figure 42.Two angles were welded at the bottom of the PFCs for securing them to the base plate of the testing machine. Two 20 mm thick bearing plates with 25 mm radius half rounds on top were secured on the top of the PFCs by specially designed clips with a 500 mm internal clear distance so that a 600 mm specimen could be placed on the top.

An FEM numerical analysis was performed prior to experimental testing to verify the rigidity of the test fixture and confirm that deformations introduced by the test frame itself would be negligible. Additionally, this preliminary numerical study validated that any variation in specimen length (25% extra space equivalent) beyond the minimum requirement would have a minor influence on the results. A detailed discussion is presented in a later Section 5.3.7.

Stiffening blocks and plates as shown in yellow in Figure 43 were employed in the one flange loading cases for enforcing the required failure mode. Four sets of stiffening blocks were made of steel plates. Each set of stiffening blocks were carefully made to match the height of the corresponding hat section so that the top flange of the hat section was supported by the stiffening block. In this way, the loads at relevant locations were carried by the stiffening block instead of the web, forcing the web crippling failure to occur at the desired locations. The stiffening blocks were fastened to the bearing plates.

For the EOF loading case, in order to prevent the failure occurring under the middle bearing plate, stiffening plates with a thickness at 6 mm were applied to the external side of both webs of the specimen as shown in Figure 44. The size of the stiffening plates was carefully selected to maintain the minimum required clearance distance from the edge of the stiffening plate to the near edge of the external bearing plate. Self-tapping screws were used to fasten the stiffening plates to the specimen.

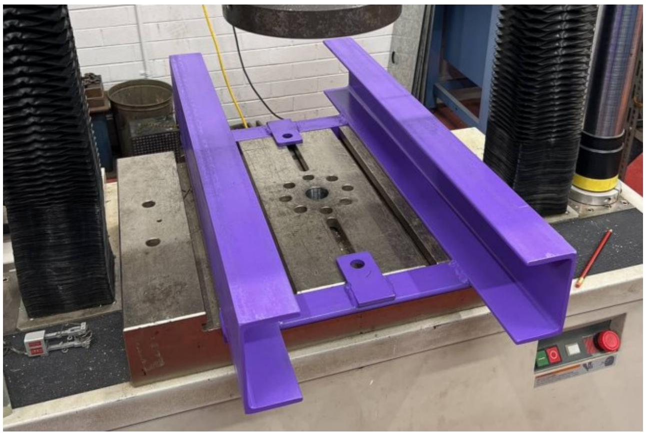

Figure 42 Test rig for OF loading cases

Figure 43 Assembly with bearing plates (IOF loading case) including half rounds and specimen

Figure 44 Stiffening plate for EOF loading cases (painted orange) bolted to the side of the web

The setup of the test rig was designed to meet the criteria described the AISI S909-17 Specification as shown in Figures 45 and 46 for the IOF and EOF loading cases respectively.

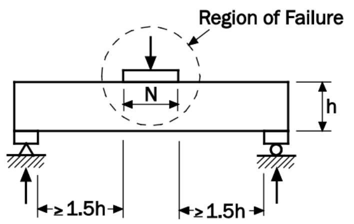

Figure 45 Interior One-Flange Loading (IOF) in AISI S909-17

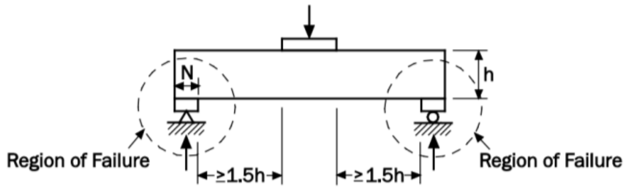

Figure 46 End One-Flange Loading (EOF) in AISI S909-17

To install the full OF loading test rig, the purple frame shown in Figure 42 was fixed to the base plate with two T bolts. The frame was carefully positioned and aligned to the centre of the base plate. Then two of the 25 mm – radius half rounds were carefully positioned and fastened at marked position. It should be noted that two of the 20 mm bearing plate were placed underneath the half rounds to provide sufficient room for vertical movement of the specimen.

For IOF loading case, two stiffening blocks were installed at both end of the specimen. Then the bearing plates were carefully aligned with the marks on the half rounds. Similar to ITF loading cases, the top bearing plate, top half rounds were installed and aligned. The bottom strap in the mid stan was also installed for keeping the hat section's shape at this time. A preload (<1 kN) was given. Once the initial load was applied, after installing and initializing the LVDTs for recording the displacement data, the test was ready to be performed. A typical IOF test setup is presented in Figure 43.

For EOF loading case, two stiffening plates were firstly installed to the mid span of the webs. Self-tapping screws were used to fasten the stiffening plate into position. Then one stiffening block was installed in the middle of the specimen. The end bearing plates were installed with fasteners and the specimen was aligned to the test rig. Based on the fastening condition of the test, the fasteners on the end bearing plates were carefully removed accordingly when testing EOF-UF loading cases. After installing the top bearing plate, half round and given an initial load to hold everything in position, the LVDT for monitoring the vertical displacement can be installed and the test was ready to start. A typical EOF test setup is presented in Figure 44.

4.3 TEST RESULT AND DISCUSSION

The determination of specimen failure loads follows a systematic approach. A 12 mm displacement, corresponding to 10% of the specimen's total height, is applied to the top bearing plate. Web crippling resistance is defined as the maximum load achieved within the first 10 mm of displacement. This methodology was adopted considering two practical factors: commercial hat sections typically do not exceed 120 mm in height, and predictions should extend beyond serviceability limits while maintaining reasonable deformation bounds.

The maximum test loads and displacements are given in Table 16. All EOF loading cases results are given by half of the load recorded from the load cell. For each hat section variant, a minimum of two specimens were tested, with the outcomes showing remarkable consistency across similar configurations. However, in cases where the experimental Load-Displacement (L-D) curve demonstrated a significant disagreement with other test results, or an accident occurred during the testing, a third specimen was then tested.

In specimens featuring a smaller corner radius of 3 mm, all exhibited a notable decline in their Load-Displacement (L-D) curves post the formation of plastic hinges. The displacements recorded at peak load for these specimens are denoted as $[\boldsymbol{Disp_1}, \boldsymbol{Disp_2}, \boldsymbol{Disp_3}]$ in the results. Conversely, sections with a larger corner radius of 8 mm did not display a significant drop in their L-D curves, even at relatively large displacements. For these specimens, the load levels attained within the initial 10 mm of displacement are specifically noted (as presented in Table 16). In both the small-radius and large-radius specimens, the top flange began to exhibit slight downward bending shortly after the commencement of loading, while the bottom flange, held stationary by fasteners, did not exhibit such movement. Simultaneously, both longitudinal edges of the specimen were observed to move downwards initially. Following this initial phase, the response of the 3 mm and 8 mm corner radius sections began to diverge, indicating different structural behaviours attributable to the variance in corner radii.

Table 16 Test results for all loading cases (Ultimate web crippling capacity at 10 mm displacement if maximum not reached)

	P_{max_1} kN	$Disp_1$ mm	P_{max_2} kN	$Disp_2$ mm	P_{max_3} kN	$Disp_3$ mm
ITF-F-H120-RIN3-DEG0-N100	99.689	3.096	99.176	3.105		
ITF-F-H120-RIN3-DEG0-N50	76.085	6.066	77.348	6.427	79.290*	6.332*
ITF-F-H120-RIN3-DEG15-N50	79.656	4.851	79.418	4.066		
ITF-F-H120-RIN3-DEG30-N50	72.404	5.273	72.020	4.568	75.023	4.496
ITF-F-H120-RIN8-DEG0-N100	75.664	9.988	75.700	9.984	75.609	9.958
ITF-F-H120-RIN8-DEG0-N50	59.311	9.998	58.780	9.982	58.854*	9.981*
ITF-F-H120-RIN8-DEG15-N50	63.541	9.999	64.109	9.998		
ITF-F-H120-RIN8-DEG30-N50	64.274	7.068	63.908	8.001	63.468	8.906
ITF-F-H90-RIN3-DEG0-N50	80.004	6.079	80.681	6.070		
ITF-F-H90-RIN8-DEG0-N50	60.850	9.972	60.740	9.991		
ETF-F-H120-RIN3-DEG0-N50	-	-	41.128	3.161	41.787	2.999
ETF-F-H120-RIN3-DEG15-N50	-	-	41.879	2.573	42.153	2.461
ETF-F-H120-RIN3-DEG30-N50	-	-	36.660	2.384	37.154	1.631
ETF-F-H120-RIN8-DEG0-N50	30.544	9.414	30.526	9.886		
ETF-F-H120-RIN8-DEG15-N50	29.720	5.105	32.650	6.250	31.295	5.347
ETF-F-H120-RIN8-DEG30-N50	32.686	2.857	32.448	4.456	30.983	4.785
ETF-F-H90-RIN3-DEG0-N50	42.538	2.930	42.996	2.770		
ETF-F-H90-RIN8-DEG0-N50	31.844	9.983	32.869	9.950		
IOF-F-H120-RIN3-DEG0-N100	80.205	4.444	80.425	4.383		
IOF-F-H120-RIN3-DEG0-N50	-	-	62.608	4.113	63.761	4.528
IOF-F-H120-RIN3-DEG15-N50	61.802	4.900	60.886	5.318		
IOF-F-H120-RIN3-DEG30-N50	61.491	5.755	61.619	4.675		
IOF-F-H120-RIN8-DEG0-N100	64.567	8.399	63.578	8.408		
IOF-F-H120-RIN8-DEG0-N50	50.082	9.993	50.339	9.769		
IOF-F-H120-RIN8-DEG15-N50	50.815	8.455	50.870	8.453		
IOF-F-H120-RIN8-DEG30-N50	49.167	6.916	49.368	7.013		
IOF-F-H90-RIN3-DEG0-N50	59.330	4.503	58.286	4.368		
IOF-F-H90-RIN8-DEG0-N50	46.365	8.484	45.816	7.881		
IOF-UF-H120-RIN3-DEG15-N50	62.571	4.980				
IOF-UF-H120-RIN8-DEG15-N50	51.547	7.706				
EOF-F-H120-RIN3-DEG0-N50	43.609	7.130	47.125	5.951		
EOF-F-H120-RIN3-DEG15-N50	46.704	6.353	45.532	5.949		
EOF-F-H120-RIN3-DEG30-N50	46.264	9.975	47.088	4.951	46.924	5.000
EOF-F-H120-RIN8-DEG0-N50	34.380	9.973	35.552	9.989		
EOF-F-H120-RIN8-DEG15-N50	35.552	7.939	35.900	7.406		
EOF-F-H120-RIN8-DEG30-N50	35.909	8.851	36.266	6.621	36.257	6.614
EOF-F-H90-RIN3-DEG0-N50	48.846	5.384	49.414	4.859	48.132	5.402
EOF-F-H90-RIN8-DEG0-N50	36.715	9.984	37.658	9.086	36.724	8.009
EOF-UF-H120-RIN3-DEG0-N50	39.315	5.085	41.421	6.652	40.689	4.803
EOF-UF-H120-RIN8-DEG0-N50	30.077	8.264	29.509	8.367		

Note:
All EOF loading cases results are given by half of the load recorded from the load cell.
Value marked with * indicates that they are FTF case value.
- indicates that the specimen was used for dummy test.

4.3.1 Test result for TF loading cases

4.3.1.1 Test results for ITF-F loading case (vertical web sections)

For the 3 mm radius sections, as the loading continued, the top flange stopped bending downwards when the corners began to rotate. The top half of the webs bent outwards away from the centreline of the cross-section, while the bottom half bent inwards towards the centre line of the cross-section as shown in Figure 14. In the next stage, plastic hinges formed on both the top and bottom half of the webs near the flanges at approximately ¼ of the height of the webs. Then the hinges moved slightly towards the rounded corner adjacent to the closest flanges respectively. The lengths of the hinges extended slightly outside the width of the bearing plates regardless of the width as shown in Figure 47. It should be also noted that in the final stage, due to imperfection and uncertainty, the hinges did not develop evenly between the top and bottom. However, the maximum load difference between two identical specimens was found to be negligible. A yield-arc post-failure mode as described by Bakker [39] was observed in the small-radius sections.

For the 8 mm radius sections, as the bearing plate continued loading, the top flange stopped bending downwards further when the corners began to rotate. Both the top rounded corners continued rolling away from the vertical symmetric axis, while both of the bottom rounded corners continued rolling in the opposite direction as shown in Figure 48 There were no obvious plastic hinges formed in the webs, however the rolling behaviour of the corners was only limited to the surrounding area of the bearing width. As a result, a knee point occurred on the Load-Displacement curve, but the load continued to increase along with the increased displacement. The test results for the two sections with the same configuration showed good alignment with each other, so that the imperfection of the specimen was not a sensitive variable in the large-radius section. Load-displacement curves are shown in Figure 49 for Specimens 103, 104 with 3 mm radius, and 114 and 115 with 8 mm radius.

Figure 47 Out-of-plane bending for ITF loading case, 3mm radius section

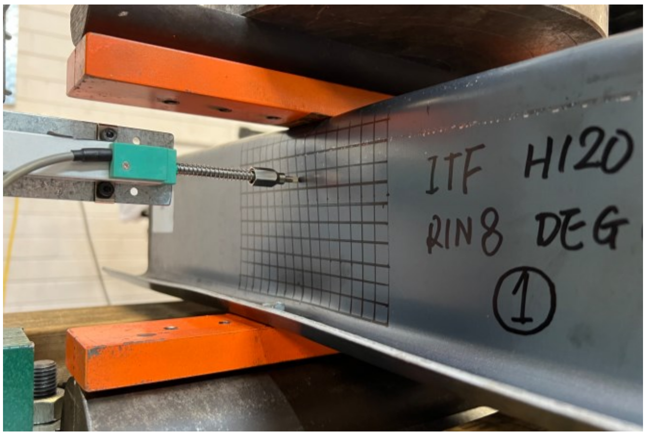

Figure 48 Out-of-plane bending for ITF loading case, 8 mm radius section

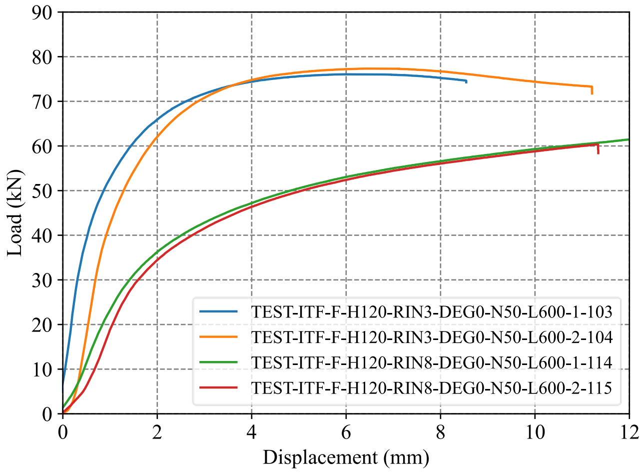

Figure 49 Typical L-D curve for small-radius and large-radius sections in ITF load case

4.3.1.2 Test results for ITF-F loading case (sloped web sections)

For the Interior Two-Flange (ITF-F) loading case, especially with hat sections featuring sloped webs, the presence of fasteners in the bottom flange plays a crucial role in counteracting the splaying effect induced by the load. With an increase in the slope angle, the horizontal force counteracted by the fasteners is expected to rise. Notably, two phenomena were observed during these tests: bolt slip and bolt-in-shear fracture.

The slip between the specimen and bearing plate is common because the diameter of the predrilled hole was 2 mm larger than the diameter of the fasteners to allow assembly. Thus, before the load reached to a specific value, the horizontal force from the splaying effect was resisted by the friction between the specimen and bearing plate. When the horizontal force exceeds the friction force from the bolts, the bottom flanges slipped and the bolts touched the edge of the fastener hole on the specimen, resulting in a bump on the L-D curve. Since the change in geometry is minimal, the ultimate load difference is also considered negligible.

An example of this phenomenon is section ITF-F-H120-RIN3-DEG30-N50 (Specimen 108). The L-D curve for this specimen exhibits a slip displacement followed by bolt fracture near the ultimate load. Following this initial test, two additional tests (Specimens 109 and 110) were carried out using two M10 bolts per flange inserted into 10 mm holes. When comparing the data from all three tests, it was evident that while the slip altered the shape of the L-D curve, the ultimate load remained unaffected. This finding was consistent across tests, as demonstrated by Specimens 119, 120, and 121 for sections with an 8 mm radius, which exhibited similar slip behaviour, albeit without the occurrence of fracture.

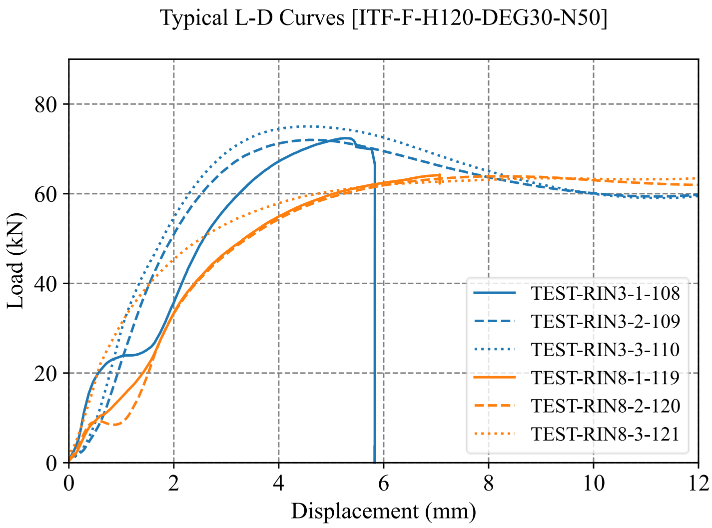

Figure 50 L - D curve, ITF-F-H120-DEG30-N50

The bolt in shear failure was only observed in the first test of ITF-F-H120-RIN3-DEG30-N50 (Specimen 108 in Figure 50) because only one (1) single M8 Grade 8.8 bolt on each bottom flange was used. In later tests, larger capacity bolts, e.g. M10 and M12 with Grade 12.9, were used.

4.3.1.3 Test result for ETF-F loading case (vertical web sections)

The loading process and the behaviour on the L-D curve was similar to the ITF-fastened loading cases. Initially, for each section, two specimens were tested. If the difference of the load capacity was greater than 5%, a third test was conducted.

For both the small-radius and large-radius sections, shortly after the loading started, on the loaded end, the top flange started to bend slightly downwards while the bottom flange remained in the same position due to the fasteners. The free unloaded end to moved downwards during the whole loading process. It should be noted that the diverging behaviour after the initial loading was similar to the ITF-F loading conditions for both small-radius and large radius sections. In addition, the bearing plates for both the top and the bottom rotated about the longitudinal direction of the bearing plate during the loading process as shown in Figure 51 due to the asymmetry at the end.

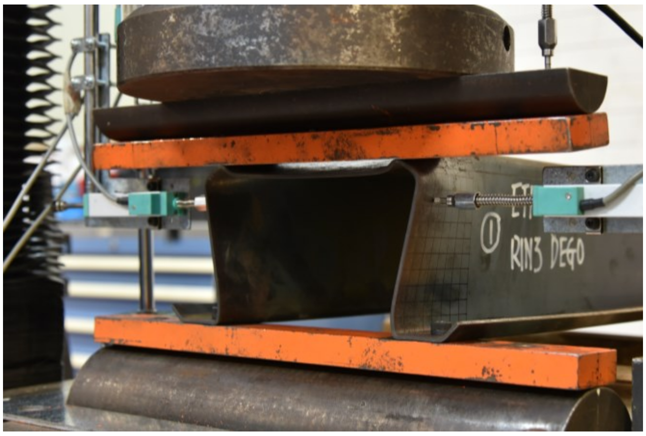

Figure 51 Bearing plate rotation for ETF-F

4.3.1.4 Test result for ETF-F loading case (sloped web sections)

For the section with sloping webs, although the yield-arc and rolling post-failure mechanism were observed on small and large corner radii respectively, plastic hinges formed in the webs regardless of the size of radius. After the loading process started, plastic hinges started to form in the webs of the small corner radius sections and rolling mechanism behaviour occurred in large corner radius sections, which was similar to the vertical web sections respectively. As the loading process continued, besides the rolling behaviour, two hinges started to form approximately at the hinge locations corresponding to the small radius sections. Figure 52 demonstrates the rolling and hinge forming processes for a typical ETF-F sloped web section.

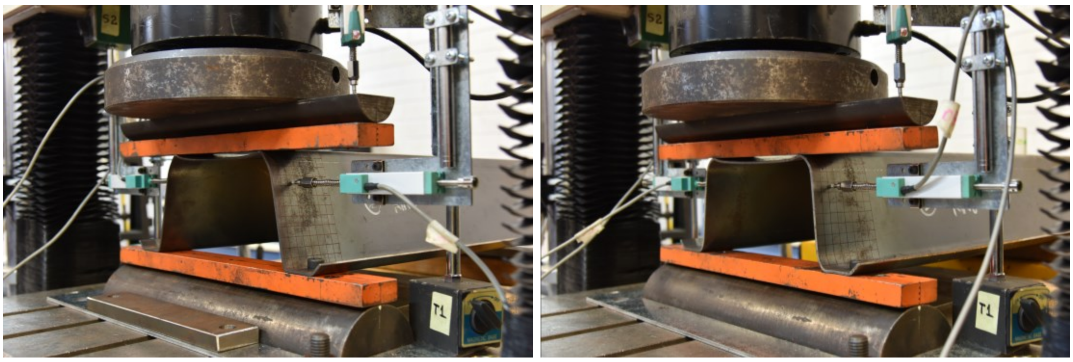

Figure 52 ETF-F plastic hinge for small (L) and large (R) corner radii

The behaviour shown on the L-D curve for large corner radius was similar to the L-D curve corresponding to pure rolling mechanism initially. As the hinge started to form, the slope of the L-D curve began to reduce and eventually the L-D curve reached a peak. The larger the slope angle, the earlier the L-D curve reached its peak, as shown in Figure 53.

It should be noted that for a slope angle section with 30 degrees (Specimen 209), the ultimate load on shown on the L-D curve was found to be significantly lower than the 15 degrees and vertical web sections. This phenomenon may be attributed to the load composition at the corner, where the vertical load is a combination of forces acting along the web and horizontally on the bolt. In sections with larger slope angles, a smaller vertical load can produce the same magnitude of force along the web. Consequently, it is expected that sections with large-angle sloped webs may exhibit lower ultimate capacities compared to vertical web sections or those with small-angle sloped webs.

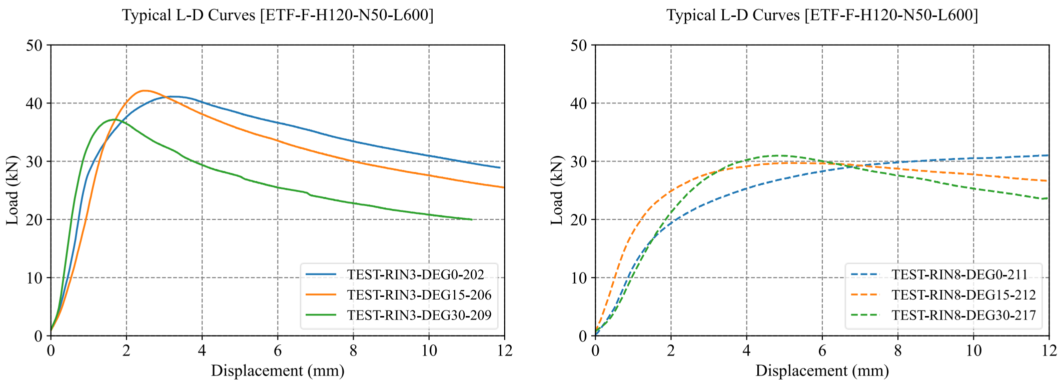

Figure 53 L - D curve comparison between vertical web and sloped web sections, ETF-F

4.3.2 Test results for OF loading cases

4.3.2.1 Test result for IOF-F loading case (vertical web sections)

For the sections with vertical webs under IOF-F loading conditions, the yield-arc and rolling mechanisms were observed in the small and large corner radii sections respectively as for the ITF cases.

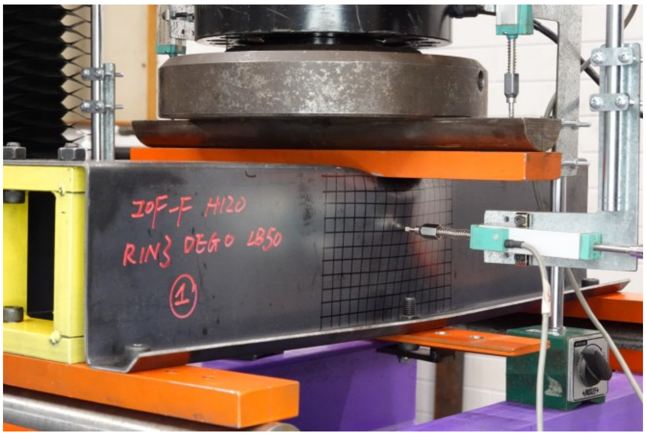

Figure 54 Figure of IOF-F-H120-RIN3-DEG0-N50

For small corner radius sections, two plastic hinges formed near the junctions of the rounded corners and the webs just underneath the bearing plate, and two hinges formed at the junction between the top flange and the rounded corners. Plastic hinges were not found in the bottom half of the section. Figure 54 demonstrates a typical vertical web hat sections with small corner radius under IOF-F loading case.

For the large corner radius sections, at the first stage of loading no plastic hinge formed. However, a rolling mechanism was observed at the top rounded corners. At a later stage, two plastic hinges began to form near the top rounded corners of the webs along with the rolling mechanism. As shown in Figure 55, these two photos were taken by the same camera on a tripod as the loading process continues. A set arrow and line coloured in yellow has been added to indicate the separation point of the specimen at the bearing plate before loading. Another set of arrow and line coloured in green has also been added to indicate the separation point of the specimen at the bearing plate in a later stage. A virtual ruler was placed at the same position (13.5 unit-length from the end of the bearing plate) so that the rolling behaviour could be observed. In the end, after the plastic hinges formed as shown in Figure 56, the specimen started to collapse.

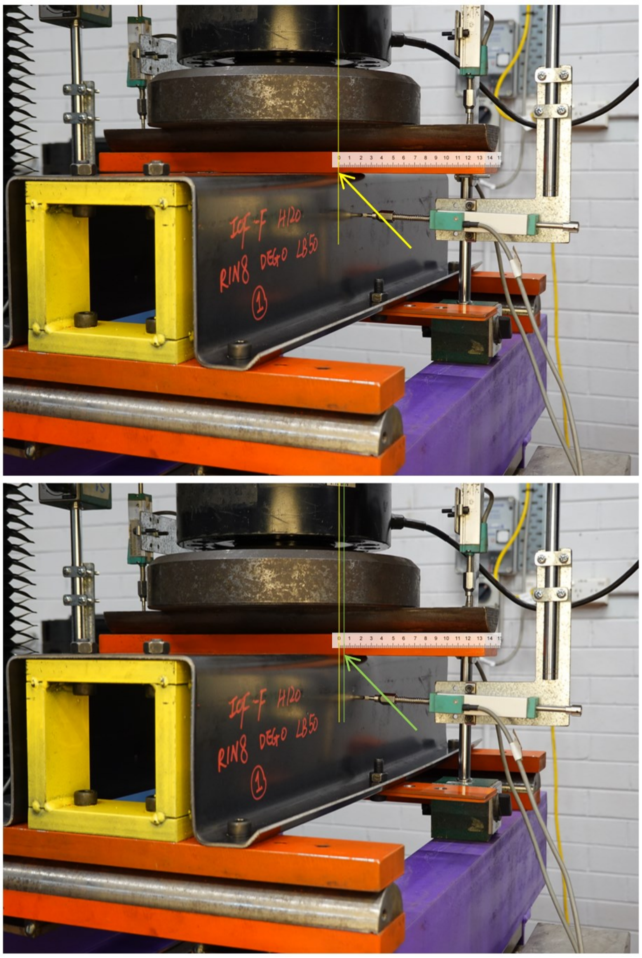

Figure 55 IOF-F loading case typical initial rolling mechanism at lower deformation

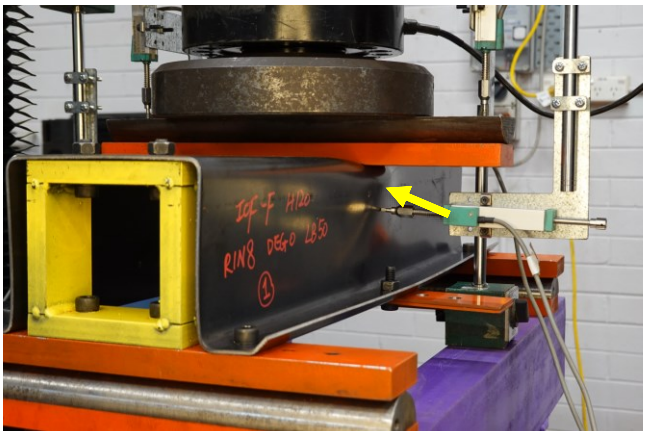

Figure 56 Hinge formation (indicated by yellow arrow) on the web for large corner radius section under IOF-F loading case

4.3.2.2 Test result for IOF-F loading case (sloped web sections)

The mechanism for sloping web sections was similar to that of the vertical web sections under IOF-F loading with good consistency. Hinges were observed regardless of the dimensions of the corner radii. It was found that within the same web inclination angle, the larger corner radius section required more deformation to form the hinges. A comparison of the L-D curve between the vertical web sections and sloped web sections is shown in Figure 57. As for the TF loading cases, the small radius sections had a distinct maximum load at a lower deformation, whereas the large radius sections tended not to have a maximum or a maximum at a large deformation.

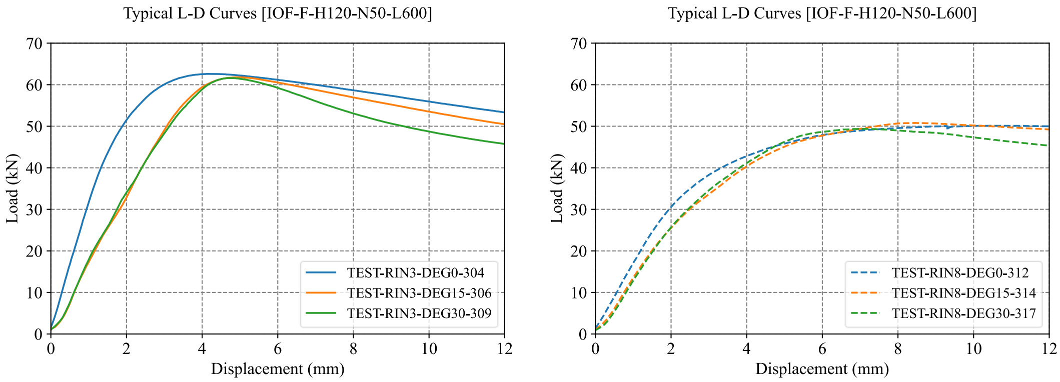

Figure 57 Comparison of L - D curves between vertical web sections and sloped web sections, IOF-F for small and large corner radii

4.3.2.3 Test result for EOF-F loading case (vertical web sections)

Figures 58 and 59 demonstrate the failure mode of vertical web sections under EOF-F loading case.

For the small corner radius sections, plastic hinges formed on the web near the bottom rounded corners, and the hinges in the webs were not found to be parallel to the flange. For the fastened (F) condition, two additional plastic hinges were observed at the intersection of the rounded corners and the lower flanges. During the loading process, a yield-arc mechanism was observed. After the hinges were fully developed in the webs, the section collapsed rapidly with increasing deformation. The lower bearing plates also rotated towards the centre of the specimen during loading as would be expected due to the longitudinal asymmetry.

For the large radius sections, the plastic hinges on the web did not form at the beginning. Instead, the rolling mechanism behaviour on the bottom rounded corner dominated the behaviour. As the rolling behaviour continued, the plastic hinges formed in the web gradually and the location of the hinges were identical to the small radius section's hinge locations. In terms of the rolling mechanism, at the beginning of the loading process, the plastic hinges on the flange moved towards the centre of the flange (symmetric axis of the cross section). At a later stage, the movement of the plastic hinges stopped when the plastic hinge on the webs formed.

As per the overall behaviour, initially, both webs of the specimen were deformed evenly. Due to the combination of several imperfections, including imperfections from manufacturing, assembling and loading, the deformations started to become asymmetric between the webs.

Figure 60 demonstrates a typical hat section exhibiting asymmetrical deformation under the EOF-F loading case. Test results have indicated that, despite the asymmetrical deformation observed between the two ends of the specimen, this variation does not substantially influence the ultimate web crippling load. A plausible explanation for this phenomenon is that the plastic hinge formation at both ends of the specimen precedes the occurrence of asymmetric deformation. Consequently, the ultimate loading capacity is effectively determined before any significant asymmetry develops. To ensure reliability, all specimens within this loading scenario were subjected to at least two tests. Comparative analysis of the results from specimens with symmetric versus asymmetric deformation revealed negligible differences. This finding further undermines the minimal impact of asymmetrical deformation on the localised loading capacity.

Figure 58 Typical failure mode of vertical web sections with small RIN for EOF-F loading case

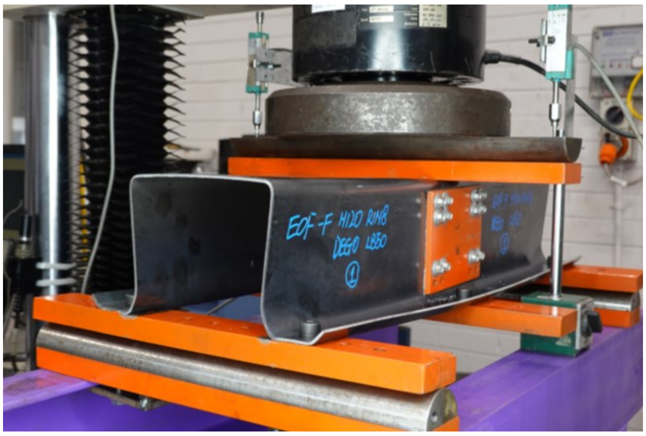

Figure 59 Typical failure mode of vertical web sections with large RIN for EOF-F loading case

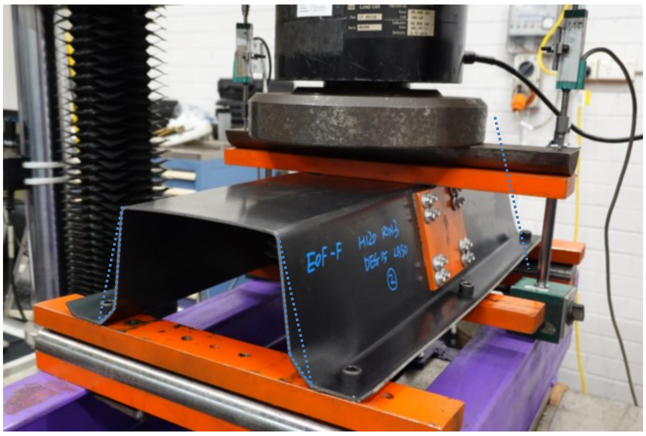

Figure 60 Typical asymmetric deformation for EOF-F loading case

4.3.2.4 Test result for EOF-F loading case (sloping web sections)

The behaviour of sloping web sections for the EOF-F loading case was found to be vary significantly with different web angles.

For the sections with small slope angles, the behaviour was found to be similar to the vertical web sections, while the only difference from the corresponding vertical web section with same corner radius was that a smaller vertical displacement was required to achieve the ultimate load capacity.

For the large slope angle sections (for example, H120-DEG30), the length of the specimen needed to be carefully selected since using the same length as the vertical web sections (H120-DEG0) does not necessarily guarantee a successful EOF-F web crippling test as desired. Two test specimens with different corner radii under the EOF-F loading case for H120-DEG30 sections were conducted. The bearing length for the end bearing plates and middle bearing plate were initially selected as 50 mm. It was found that for the small corner radius sections, flexural failure was captured first and then immediately follow by web crippling failure. Flexural failure is defined as major deformation occurring in the midspan of the specimen before web crippling occurring. Figure 61 is demonstrating a typical flexural failure in web crippling tests [EOF-F-H120-RIN3-DEG30-N50]. For the large corner radius section, although no flexural failure was observed before the web collapsed on one side, flexural behaviour was still captured before the web crippling occurred.

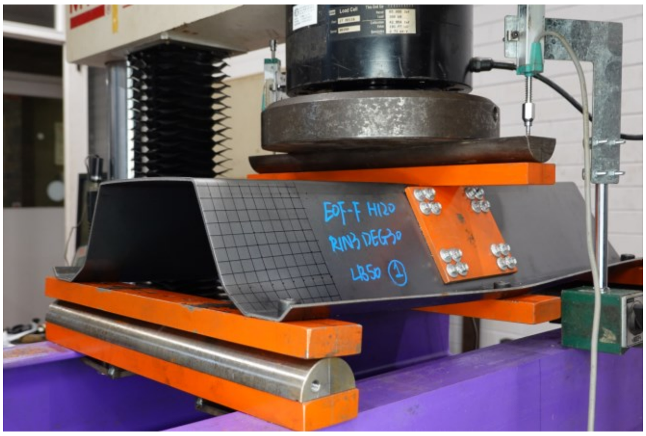

Figure 61 flexural failure followed by web crippling

As an alternative other than reducing the length of the specimen, the bearing length of the middle bearing plate (noted as MB) was increased to 100 mm so that the clear distances between the middle bearing plate and end bearing plates were reduced. The comparison of the L-D curves is plotted in Figure 63 for Specimens 405, 406, 407 with the 3 mm radius corners, and 412, 413, 414 with the 8 mm radius corners. The specimens with the 50 mm middle bearing plate are plotted with a dash line. It was found that the L-D curves were affected by the flexural failure or flexural behaviour. However, as long as the web crippling eventually occurred, the ultimate capacity was not significantly affected. Adjusting the middle bearing plate was also found to be practical as an alternative to reducing the minimum required clearances for the EOF loading cases.

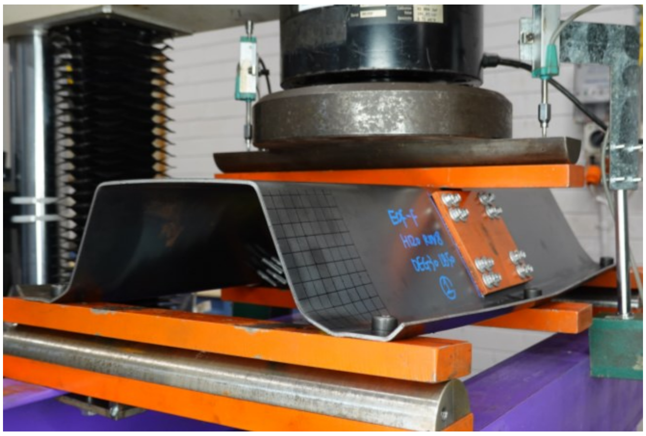

Figure 62 EOF-F-H120-RIN8-DEG30-N50, with 50 mm middle bearing plate

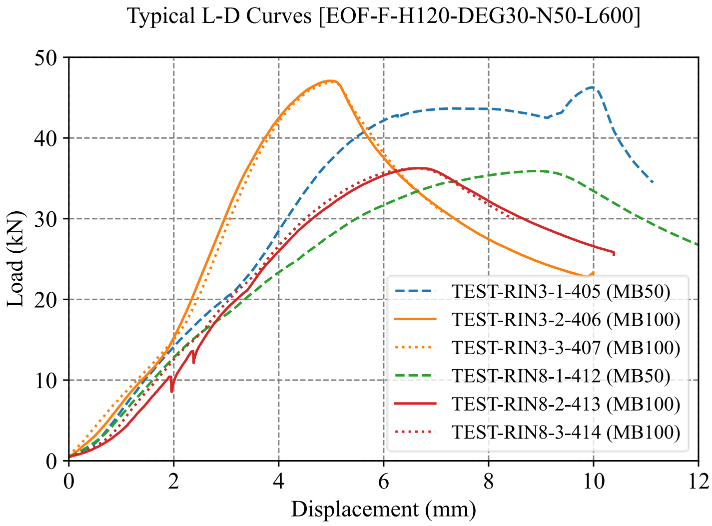

Figure 63 comparison of L-D curves between 50 mm mid bearing plate (MB50, dash line) and 100 mm mid bearing plate (MB100, solid/dotted line)

4.3.2.5 Test result for EOF-UF loading case (vertical web sections)

As a practical loading cases alternative in the EOF family, only vertical web sections were tested because the splaying of the web under load makes the sloping web sections subject to EOF-UF loading case not practical.

Compared to the EOF-UF load case with vertical webs, the most significant difference is the rolling effect of the bottom flange as shown in Figure 64. In the absence of the fastener that attaches the bottom flange to the bearing plate, only two plastic hinges were formed: one on each side near the rounded corner. Regardless of the corner radius, plastic hinges were formed on the web and extended diagonally to the bottom flanges. Thus, the ultimate load capacity was slightly lower than the same section with fastened bottom flanges as shown in Figure 65.

Figure 64 Typical photo of curling of bottom flange

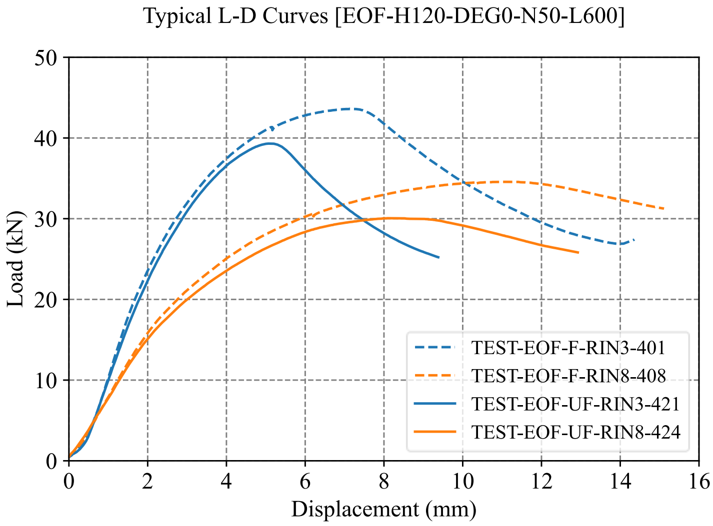

Figure 65 Comparison of the L-D curves regard EOF-F and EOF-UF

4.4 SUMMARY

An experimental program has been conducted on hat sections subjected to localised loading, with the aim of understanding their yielding behaviours under common practical loading cases. This experimental study involved a total of ninety specimens, encompassing a variety of dimensions, including rounded corner radii, web heights, and web sloping angles. Furthermore, the variables investigated in the tests include the bearing length and fastening conditions.

Based on the results obtained from this experimental study, the major findings can be summarized as follows:

1. The typical failure modes (yield-arc failure and rolling failure) for hat sections described by previous researchers for IOF loading case can be extended to all loading cases listed in current standards. The Load – Displacement curves for hat sections failed by enlisted failure mode shows a similar pattern against previous research.
2. For the two-flange (TF) loading cases, the Load-Displacement (L-D) curves for the small corner radius sections, which exhibit a yield-arc failure mode, demonstrate a rapid increase in load. After reaching the peak load, the L-D curve shows a descending trend. Conversely, the L-D curves for the large corner radius sections, which feature a rolling failure mode, typically show an indefinite increasing trend in the first 10 mm of controlled-displacement loading.
3. For the one-flange (OF) loading cases, the L-D curves for the small corner radius sections demonstrate a similar pattern to the TF loading cases. For the large corner radius sections, the typical characteristics of the rolling mechanism can be observed in the initial stage of loading. In a later stage, a higher chance of reaching a peak load value is observed, which marks the difference between the TF and OF loading cases in the behaviour of the L-D curves.
4. Regardless of the failure mode and loading cases, increasing the sloping angle of the web results in reaching to the maximum of localised loading earlier. However, the web sloping angle's influence on the overall load capacity was found to be minimal.
5. Some accidental events were observed during the experimental study. In most cases, the slippage between the bearing plate and the specimen did not have a significant impact on the overall load capacity, but it did result in fluctuations in the L-D curves. For the fastened loading cases on the sloped web sections, the splaying effect could generally be well-managed by the fasteners. However, in some instances, the strength of the fasteners and the diameter of the pre-drilled holes should be carefully selected and prepared to minimize the splaying effect.

Chapter 5 Numerical study – nonlinearities

5.1 INTRODUCTION

Finite element method (FEM) has been developed for over 50 years and has been become of the most powerful tools for research purposes. FEM analysis has been considered as a feasible alternative to physical testing in various loading conditions for cold-formed steel members, especially when appropriate modelling techniques are used. With the substantial growth of high-performance computation, the FEM models for analysing web crippling behaviour have transitioned from 2D to 3D analysis, as well as from strip models to full 3D models. A recent review of 48 publications by V. Degtyarev et al. [26] published in 2023, provides modelling recommendations based on best practices to provide guidance for FE modelling of web crippling behaviour in cold-formed steel members. Whilst the recommendations cover all aspects of modelling and analysis for various sections, including channels, zeds, decks and hollow sections, there is currently no publication that provides a proper recommendation for modelling the web crippling of hat sections. This gap indicates an area for potential research and development to extend the applicability of FEM analysis further in the study of cold-formed steel structures.

It should be noted that the principle of simulation work is not to create a completely identical 3D model in FEM software. Instead, the aim is to simplify the model as much as possible while preserving the essential information and behaviours of the real system, thereby drastically reducing computation time and resource usage.

Whilst the previous chapter introduced the numerical analysis concerning the buckling load, this chapter offers an in-depth discussion on numerical analysis with a focus on yielding behaviours. The discussion in this chapter consists of two main parts. The first part, presented in Section 5.2, includes the details of the FEM for modelling the web crippling of hat sections. A validated method specific to hat sections is presented based on successful applications from several publications.

The second part, presented in Section 5.3, describes an extensive parametric study aimed at understanding the impact of variations in hat section dimensions on structural behaviours. This in-depth investigation seeks to elucidate how changes in key dimensional attributes affect the hat section's yielding response, thereby providing valuable insights to guide the design of commercial hat sections for mass production.

5.2 FEM MODELLING OF HAT SECTIONS

5.2.1 General discussion of FE modelling options

5.2.1.1 Software

This study utilised ABAQUS 2018 [34], a widely used finite element analysis package, to provide a comprehensive and detailed analysis of the subject matter. A variety of analysis and modelling techniques were applied and investigated in this numerical study. Similar modelling and analysis techniques were also recommended in the latest publication before the recommendation was available to the public. The computer programming language Python was employed as a tool to enhance the efficiency of the modelling process and facilitate data generation and processing tasks. It should be noted that ABAQUS 2016 was used in part of the study when the University of Sydney's High Performance Computation cluster, Artemis, was used.

5.2.1.2 Analysis type

Implicit Static (IS), Implicit Dynamic (quasi-static) (ID), and Explicit Dynamic (ED) are three typical analysis types utilised by various researchers to study web crippling behaviours. Numerous studies have indicated that the IS encounters convergence challenges, particularly with nonlinear analyses involving complex models with multiple contacts and large displacements. In order to overcome the convergence problem, an artificial damping factor or energy input might be required and has to be verified by experimental data. In this case, most of the researchers selected their analysis type as ID or ED for easier convergence. Sundararajah [41] has provided with a detailed methodology and recommendations regarding quasi-static analysis using a contact model. Extension controls exclusively for quasi-static analysis, including energy balance, load rate, mass scaling and noise reduction, were also discussed in his PhD thesis.

In this study, an IS approach was initially proposed and employed. The advancement in computational power has mitigated previously encountered convergence issues and the need for extensive iterations to solve large sets of linear equations. Additionally, this study benefited from the computational resources provided by the University of Sydney's High Performance Computation cluster, Artemis. The use of Artemis provided a significant advantage in terms of computational resources, enabling complex simulations and the concurrent execution of multiple simulation jobs. In this research, Implicit Static was chosen as the preferred method for this numerical analysis.

5.2.1.3 Ideal model vs contact model

The ideal finite element model has been widely used to study web crippling behaviour, as the most important idealisation feature is that the loads are simplified as line loads rather than as a pressure distribution. This approach has been widely adopted not only for buckling analysis in thin-walled series programs based on the Finite Strip Method (FSM), but also in the commercial software package ABAQUS, which is based on the Finite Element Method (FEM). The difference in the buckling loads using these two methods with ideal models has been proven to be insignificant.

However, in the process of attempting to adopt an ideal model for load case analysis with large deformations, a significant shortcoming was discovered. The idealisation concept with a fixed line load position does not reflect the actual loading condition, which constantly changes as the section deforms instead of loading at a stationary position. As a result, the load positions can be observed beyond the initial contact point between the specimen and the bearing plate. In this case, the ideal model does not reflect the rolling mechanism induced by the bearing plate. Although the ideal model was found to reduce the simulation time significantly, the failure shape does not match with that of the tests, and the rolling mechanism forced by the bearing plate cannot be properly modelled, making the ideal model inappropriate for this specific study.

Compared to the ideal model, the contact model is more complex and computationally intensive. However, the contact model preserves the most critical components during the loading process and allows the rolling mechanism to be captured to the maximum extent possible. In conclusion, the ideal model is only adopted for the buckling analyses and the contact model is used for yield mechanism analysis.

5.2.1.4 Loading cases

The purpose of the numerical study is to create a reliable finite element (FE) model that can be used for a comprehensive parametric study based on practical loading cases. In order to use the experimental data to validate the FE models, the development of the models strictly follows the details of the experimental study, with reasonable simplifications. Load cases were divided into two groups such as one flange (OF) and two flange (TF) and they are discussed separately.

5.2.1.5 Element type and parts

Shell elements are commonly accepted as the preferred types of elements for modelling thin-walled structures. According to the ABAQUS modelling recommendations given by V. Degtyarev et al. [26], indicate shell elements are suitable for structures where length significantly exceeds thickness. Other than shell elements, the recommendations also provided with a strong support for using solid elements because shell elements are simplifications of solid elements, although shell elements were used in all reviewed publications.

In this study, the 4-node general-purpose shell with reduced integration with hourglass control and finite membrane strains (S4R) is initially selected for modelling the hat sections for better computation efficiency without compromising accuracy.

However, in later numerical research, it was found that using shell element for modelling stocky hat sections with sloped webs is not appropriate as it often provides overestimated values even though the result is similar for hat sections with vertical webs. Thus, an extensive numerical study using solid elements is conducted with similar modelling process. The detailed comparison of shell element model and solid model is discussed in a later section. In this chapter, the model description applies to both shell and solid based models unless specified.

In terms of element type used for the bearing plate, both shell and solid elements were used by previous researchers. Most of the bearing plates were defined as rigid bodies because the deformation and stress distribution in the bearing plates were found insignificant. In this study, a rigid solid element is used for modelling the bearing plates. According to the ABAQUS manual, calculations on the element level are not carried out for elements that are part of a rigid body. Thus, unnecessary calculation can be minimised for better efficiency.

5.2.2 Modelling details for TF loading cases

5.2.2.1 Material

Material coupon tests were carried out using the same batch of sheet steel used to fabricate the specimens. Coupons cut from the longitudinal direction of the web (perpendicular to the longitudinal direction of the specimen) were selected. After noise filtering, an average stress-strain curve was calculated for use in the simulation. From the data collected, the Young's modulus (E) and Poisson's ratio (ν) of the material were taken as nominal values of 200 GPa and 0.30 respectively. According to the previous section, AS/NZS 1594 HA250 steel [37] was used for manufacturing the specimens, the type of steel is considered as a hot-rolled mild steel and the yield strength difference between the longitudinal and transverse directions is negligible. When the material properties were input into ABAQUS, it is considered as an isotropic material.

In the plastic range of the stress – strain curve, engineering stress and strain were converted into true stress and strain respectively as recommended by multiple researchers for numerical analysis using the EN 1993-1-5 (2006) equations. The equations are given as Equations (5-1) and (5-2).

$$\varepsilon_t = \ln(1 + \varepsilon_e) \tag{5-1}$$

$$\sigma_t = \sigma_e(1 + \varepsilon_e) \tag{5-2}$$

where

ε_t and ε_e are true strain and engineering strain.

σ_t and σ_e are true stress and engineering stress.

5.2.2.2 Assembly

The models are assembled following the geometry of the test setup as shown in Figures 66 and 67 for ITF and ETF respectively. The use of half rounds in the experimental tests was to ensure that the load from the bearing plate was applied as a line load and distributed evenly. In the numerical analysis, these half rounds can effectively be substituted with equivalent boundary conditions, and hence, are excluded from this study.

Given the use of shell elements for modelling the specimen, a clearance equal to half the thickness of the specimen was introduced between the bearing plate and the specimen. This step was taken to avoid any initial contact interference. Such clearance is deemed unnecessary when employing solid element models.

In order to minimise the unnecessary contact area between the bearing plate and the specimen, partitions were created on the specimen as needed. The literature review indicates a lack of clarity on whether these partitions should be created in the parts module or assembly module. In this research, it was found that either method is acceptable for numerical analysis, whilst the order of the nodes is not essential. When the sequence number of the nodes is sensitive, for example, when the displacement of nodes is required for further analysis, partitions are recommended to be finished in the parts module with extra attention in the mesh procedure.

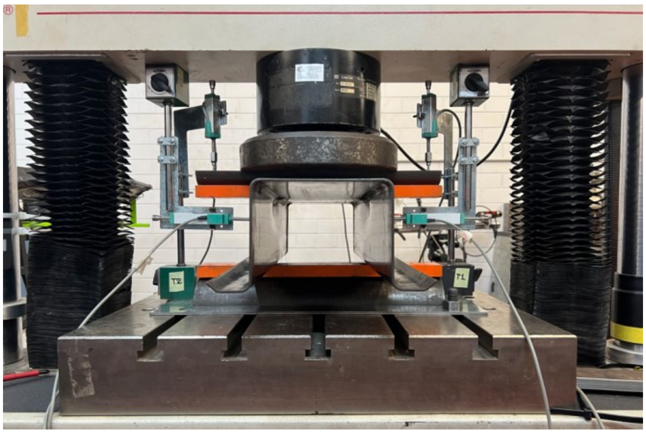

Figure 66 Typical experimental setup for ITF loading case

Figure 67 Typical experimental setup for ETF loading case

5.2.2.3 Contact

In order to reduce the complexity of the model, only possible contact areas were selected for contact pairs. To define a contact, the contact property is required prior to the definition of contact pairs. Two contact property options were defined: “tangential behaviour” and “normal behaviour” as defined in the ABAQUS manual.

In terms of the tangential behaviour, according to the literature, the friction coefficient between the steel-and-steel surface varies based on the surface conditions. The friction formulation “penalty” was generally adopted, and the range of the friction coefficient was selected ranging from 0 to 0.4. In this study, the bearing plates were painted with spray painting for better demonstration in photos in related experimental research. The friction coefficient is set to 0.4 based on Sundararajah’s research [42] and the recommendations given by V. Degtyarev et al. [26].

Normal behaviour is used for specifying the contact pressure-overclosure relationship that governs the motion of the surfaces in a mechanical contact analysis. The options of “hard” contact and “softened” contact with a “linear” feature were predominantly used in reviewed publications. According to the ABAQUS Manual, the “hard” contact refers to a relationship which minimises the penetration of the slave surface into the master surface at the constraint locations and does not allow the transfer of tensile stress across the interface; while a “softened contact with linear” pressure-overclosure refers to a relationship in which the contact pressure is a linear function of the clearance between the surfaces.

A publication has been proposed by Natario et al. [43] with an equation for calculating the contact stiffness for linear pressure-overclosure. Contact stiffness can be calculated by using the bearing plate’s Young’s modulus divided by the thickness of the bearing plate. However, the contact stiffness should also include the system stiffness. Thus, different contact stiffness (K) values were also attempted for the benchmark section of test ITF-F-H120-RIN3-DEG0-N50. The different Load – Displacement curves (L-D curves) are plotted together for understanding the difference between different k value.

In Figure 68, the curve representing “hard contact” is labelled as “HARD”, and it is plotted alongside curves for “softened contact with linear” for K values of 2000, 5000, and 10000. The graph illustrates that the Load-displacement (L-D) curves exhibit a smoother transition, particularly in the phase of plastic deformation, when "softened contact" is applied. Although curves associated with higher K values show a tendency toward slightly increased capacity, the variance in the maximum web crippling capacities across the different K values is minor and can be deemed negligible. Furthermore, the analysis indicates no substantial difference for K values of 4000 N/mm and above.

In scenarios where "softened contact" is employed within this study, the effective thickness for calculating the contact stiffness (K value) is considered to be twice that of a single bearing plate. A similar trend was observed when shell elements are used. Consequently, based on the outcomes of the analysis for both solid and shell element models, a contact stiffness of 5000 N/mm has been selected.

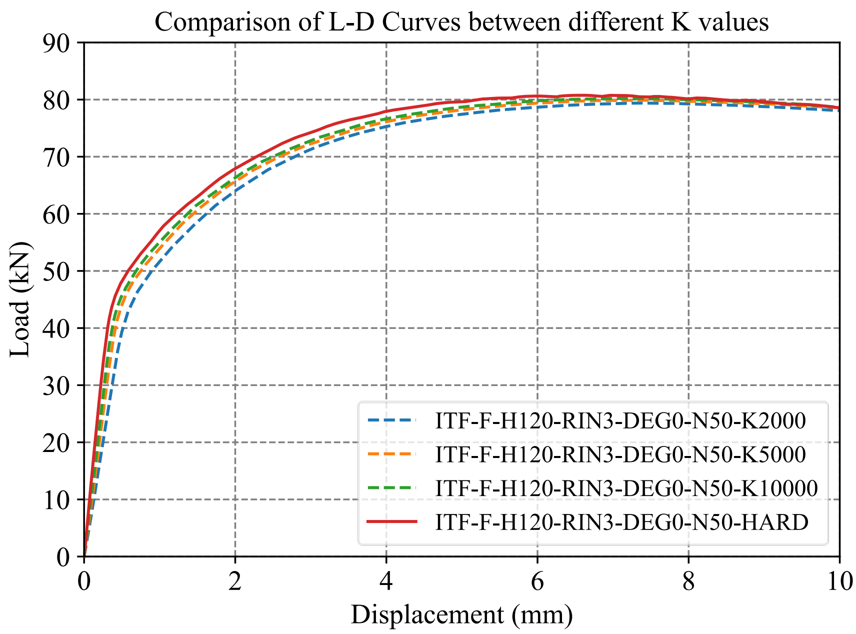

Figure 68 L - D curve comparison between "hard" contact and "linear" contact with k = 5000

In this study, surface-to-surface contact was used to define the contact, as recommended by most of the publications reviewed. In each contact pair, the surface of the bearing plate was defined as the master surface, while the contact surface of the specimen was defined as the slave surface as shown in Figure 69. In this figure, the master surfaces coloured in **red** are located on the under and side surfaces of the top bearing plate; the slave surface coloured in **magenta** are in the middle of the specimen on top and side surfaces.

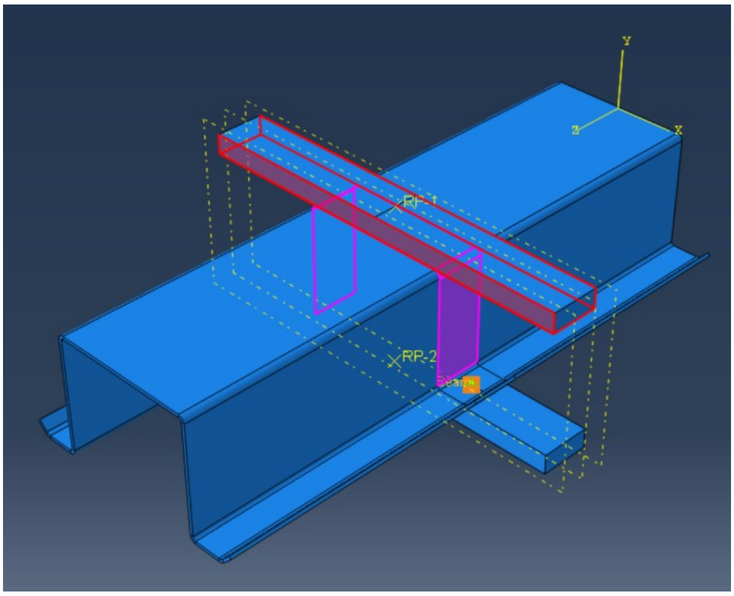

Figure 69 Typical master and slave surface in contact setting

5.2.2.4 Constraint

According to multiple publications, the top and bottom bearing plate can be safely considered as a rigid body for simplification as the deformation compared to the size is negligible. In ABAQUS, a rigid body can be generated and constrained to a reference point. For each bearing plate, a reference point is established to enable the application of the "rigid body" constraint. Typically, the reference point is positioned at the centre of the bearing plate's surface shown in Figure 70. The location of the reference point for "rigid body" is carefully selected for the best effect for omitting the half round. Similarly, the reference point at the bottom bearing plate is selected at the centre of bottom surface. All the boundary conditions are applied to ese reference points and are discussed in a later section.

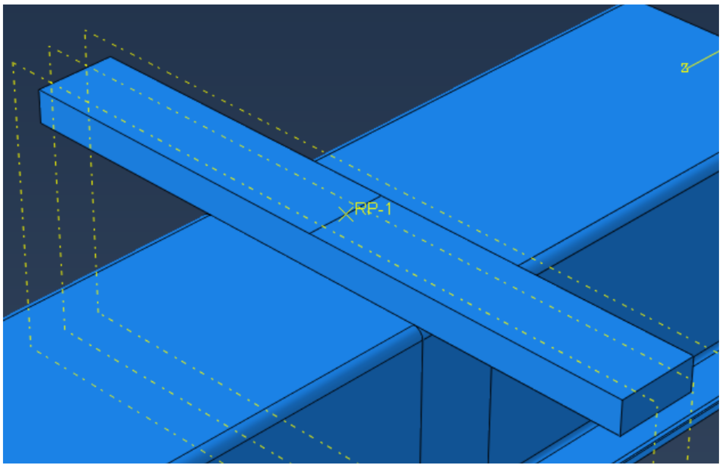

Figure 70 Typical example of reference point location referencing to the bearing plate

5.2.2.5 Fasteners

In the context of fastened loading cases, Sundararajah's work did not include any simulations regarding such scenarios, whereas Natario and al. [30] in 2017 applied the "tie constraints" to simulate the fasteners of the built-up I-sections. Similarly, He and Young's publications [44,45] in 2022 also reported the use of solid elements for modelling screws connecting channel webs in built-up I-sections.

It is important to acknowledge that fastener holes were not directly modelled in the FEM analysis. During the loading of test specimens, the splaying effect, stemming from the tolerance in bolt holes and the sloping webs, caused horizontal movement of the bottom flange. As a result, additional displacement was necessary to reach the same load capacity which can be observed in the Load-displacement (L-D) curves. This specific behaviour was not replicated in the FEM simulations.

Fasteners were modelled using ABAQUS's integrated fastener module. The experimental setups employed high-strength Grade 10.9 or 12.9 bolts. Numerical analysis of horizontal forces induced by vertical loads on sloped web sections indicated that bolt failure was highly improbable.

Initial attempts at modelling with explicit holes resulted in irregular mesh shapes around the holes, increasing computational time. To avoid unnecessary contact issues between the shell (hat section) and fasteners, this study utilised ABAQUS's internal fastener function. The attachment type was set as "beam element" with an impact radius of 5 mm, corresponding to the bolt diameter used in experiments.

5.2.2.6 Steps

For a typical model in the ITF and ETF loading cases, two steps are required in one model. "Initial step" is used to define the base state of all the components, including contact, constraint, and fasteners, which was discussed in the previous sections. For the "simulation step" to define the boundary conditions, "General" procedure type with "Static, General" was adopted in this research.

In the configuration phase, the "Nlgeom" option, which accounts for non-linear geometry, is enabled to refine the outcome of simulations, particularly in instances characterised by extensive deformations. This practice aligns with the common approaches observed in numerous studies focusing on numerical analysis for web crippling, where a damping factor is integrated within the automatic stabilization settings, defaulting to 0.0002. In the increment setting page, the initial increment size was carefully selected based on experience. A suitable initial increment size not only expedites the calculation process but also contributes significantly to accuracy. Furthermore, the feature for automatic incrementation is activated to optimize the simulation's efficiency.

5.2.2.7 Boundary Conditions

The boundary conditions of the FE models, particularly for the bearing plates, were applied while simulating those in the experimental study. While some of the papers reviewed, for example Schafer's paper [46] for the deck and Hofmeyer's paper [10] for the hat sections modelled half of the model to reduce the computational time, this study predominantly analysed full models to align with the experimental study, unless stated otherwise. As in most previous studies over the last few decades, the loading was applied by vertical displacement on the bearing plate, similar to the physical test setup.

5.2.2.8 Mesh control

Mesh size has been acknowledged to be critical for FEM analysis to produce satisfactory results by many researchers. An appropriate mesh size is required to balance the need for accuracy with computational limitations. In general, a finer mesh model can provide a better representation of reality but at the cost of increased computational demand due to a higher number of degrees of freedom. Conversely, a coarser mesh reduces computational load but may oversimplify the model, potentially failing to capture the actual behaviour.

The discussion of mesh size can be separated into two parts: flat portion and corner radius portion. For the flat portion, according to the publications recently reviewed by Degtyarev et al. [26], the members were modelled with 1 to 15 mm elements near the load or reaction and 2.5 to 22 mm elements away from the load. Researchers have employed both uniform and non-uniform mesh distributions, with finer meshes in regions subjected to loading and coarser meshes elsewhere. For bearing plates, mesh sizes varied from fine (as small as 2 mm) to coarse (ranging from 5 mm to 10 mm).

In this research, for the section modelled with shell elements, 2.5 mm and 5 mm meshes were attempted for both the flat portion of the specimen and bearing plate. In order to see the difference between two options, “hard” contact was utilised for clearer result demonstration. It was observed that the finer mesh model produced a smoother Load-displacement curve with fewer fluctuations in the non-linear phase of loading. Given privileged access to the High Performance Computing (HPC) facility “Artemis” [47] provided by the University of Sydney, a 2.5 mm mesh was chosen to enhance accuracy, except where otherwise noted.

In solid element models, the mesh size is primarily governed by the material’s thickness. To fully exploit the advantages conferred by solid elements, it’s crucial that the thickness direction of the material incorporates at least two layers. Consequently, for a hat section with a thickness of 3 mm, the mesh size is selected as 1.5 mm. This specification ensures that the model adequately represents the material’s physical properties and behaviours under load. An example of the mesh size and the setup for the specimen is demonstrated in Figure 71.

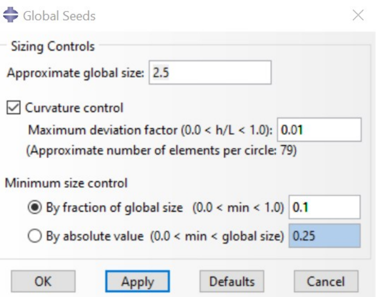

Figure 71 Typical mesh size setup for the specimen

Degtyarev et al. [25]’s recommendation underscores the critical role of the corner radius in web crippling studies. This highlights the consensus among researchers that significant non-linear deformation typically occurs around the hinge near the loading zone. Researchers have approached the definition of corner mesh in different ways: some have used a segment-based approach involving 7 to 20 elements, while others prefer specifying mesh size directly, ranging from 0.5 to 1 mm.

In this research, multiple mesh configurations for corners and bearing plates were explored in pairs to identify the best possible setups. It was discovered that the mesh size discrepancy between the bearing plate (modelled as a solid body) and the corner portions should be minimised to mitigate convergence problems. Consequently, corners were modelled using segments, with approximately 20 elements per quarter-circle.

In the mesh settings within ABAQUS, “global seeds” were applied to the instance. For shell elements, the approximate global size was set at 2.5 (1.5 for solid elements), and the maximum deviation factor in curvature control was adjusted to 0.01. This setting achieves an approximate number of 79 elements per circle for all models, unless otherwise noted.

Regarding the bearing plate’s mesh, an initial decision matched its size with that of the hat section to prevent convergence issues, based on the recommendation that the master surface’s (bearing plate) mesh size should not exceed that of the slave surface (specimen). However, subsequent parametric studies revealed that the bearing plate’s mesh size could be increased to twice that of the specimen’s mesh without problems. Thus, mesh sizes were adjusted as needed, allowing for flexibility in mesh size selection based on specific study requirements.

5.2.2.9 Imperfection

Initial imperfections are a critical consideration in the FEM modelling of cold-formed steel (CFS) members. This necessity arises from their high slenderness ratios and susceptibility to instability effects. Imperfections can be introduced during the manufacturing and transportation processes, introducing variations in the structural integrity of the members. Generally, the post-buckling behaviour is adopted for the most critical condition and used as the initial geometric imperfection. However, most researchers have found that the impact of imperfections on the load-bearing capacity of cold-formed steel (CFS) members under localised loading conditions is minimal. This insignificance holds unless the magnitude of these imperfections approaches the size of the corner radius.

Pastor, Casafont, Bonada and Roure [48] provided a collection of imperfection amplitudes in 2014. Sundararajah [42] chose $d_1/150$, where d_1 is the length of the flat part of the web. Pham and Hancock [49] in 2010 used $0.15t$ given by Camotim and Silvestre [50] in 2004 and $0.64t$ given by Schafer and Peköz [51]. For multiple webs and hollow sections, He and Young [45] in 2022 reported that the local imperfection of the specimen was not taken into account in the numerical modelling. It has been shown that the effect of local imperfection is generally negligible for web crippling because the load eccentricity due to the presence of corner radii overrides the influence of local imperfections. Hofmeyer , Geers, Snijder and Schafer [46] in 2022 cited another paper by Kanthasamy et al. [52] in 2022 and indicated that the imperfection was not considered because it was not relevant to the load-bearing capacity. A table of the authors and the selected value is listed as below.

Table 17 The selection of imperfection by various researchers

Author	Imperfection value selected
Sundararajah [42]	$d_1/150$
Camotim and Silvestre [50]	0.15t
Schafer and Peköz [51]	0.64t
He and Young [45]	The presence of corner radii overrides the influence
Kanthasamy et al. [52]	not considered because it was not relevant

Given the lack of existing research on imperfections for hat sections and sloped web sections, a numerical investigation was performed on the ITF-F-H120-DEG0-N50 section with internal corner radius equal to 3 mm and 8 mm respectively. The thickness of the material is 3 mm, which is identical to the material tested by the author. Initially, a buckling analysis using an "ideal model" determined the buckling shapes, with nodal displacements recorded and saved as a .fil file for further usage. This file contains unit nodal displacement data with a maximum value of 1.0.

To introduce initial imperfections to the model, an amplitude factor along with specified signs (positive or negative) was utilised to apply initial nodal displacements to specific meshes. The amplitude factor is listed in Table 18. Noted that the value of $d_1/150 = (120 - 4.5 \times 2)/150 = 0.74\,mm$ for $r_{in} = 3\,mm$ sections, and $d_1/150 = 0.67\,mm$ for $r_{in} = 8\,mm$ sections, are smaller than 0.34t. Consequently, to ensure clarity and enable a direct comparison across various criteria based on thickness, the simulation results for these specific scenarios have been excluded from this presentation.

Table 18 List of FE models with imperfection and criteria

MODEL	CRITERIA	Max imperfection (mm)
IMP-101	0.10t	0.30
IMP-102	0.15t	0.45
IMP-105	0.34t	1.02
IMP-106	0.50t	1.50
IMP-107	0.64t	1.92

Note: t is the thickness of the material.

Simultaneously, a perfect contact model was developed to capture the initial deformation shape under a minor load. The result from this perfect model served as a benchmark, allowing for comparison with results from models incorporating designated imperfections. The buckling mode that closely replicated the initial deformation shape was then chosen as the foundational model for inputting imperfections. Various amplitude factors were applied, and the directions of the imperfections were meticulously aligned with the observed deformation shape. Models incorporating these imperfections underwent analysis, and the resulting Load-displacement (L-D) curves were recorded and plotted on the same graph, as illustrated in Figure 72.

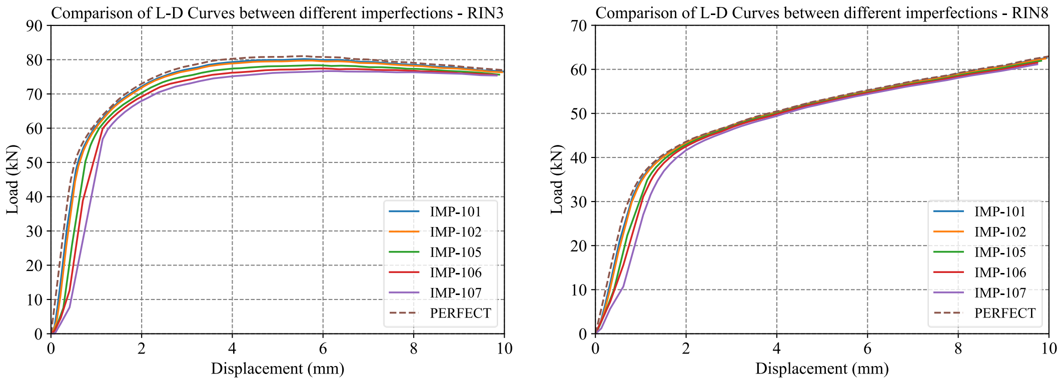

Figure 72 L - D curves with imperfections (L: RIN = 3 mm, R: RIN = 8 mm)

According to the simulation results, the effect of employing the initial imperfection aligned with the initial deformation shape on the loading capacity can be considered as marginal. This observation is consistent for both sloped web sections and sections with a larger corner radius which have a rolling post-failure mechanism. Simulations reveal that increased imperfection magnitude tends to result in a greater loss of capacity, though this reduction is still considered minor. Specifically, an imperfection of 0.5t, visually noticeable and deemed significant, leads to a capacity loss of 4.6% and 2.3% for sections with 3 mm and 8 mm corner radii respectively. Additionally, it was observed that sections with a larger corner radius, which feature a rolling post-failure mechanism, tend to be less affected by imperfections compared to those with a smaller corner radius.

The test sections analysed are characterised as stocky, which implies that buckling, and consequently, the effects of imperfections, are not significant factors in their structural response. This contrasts with more slender sections, such as those examined by Wu et al. [16] in 1997, where imperfections might play a more critical role in influencing the structural behaviour.

Therefore, in view of the marginal effect that imperfections have on loading capacity, imperfections are not included in the analysis in this numerical study. This decision is based on the understanding that, for the types of sections under consideration, the presence of imperfections does not substantially alter the overall results, or the conclusions drawn regarding the load-bearing capacity and structural integrity of the sections.

5.2.3 Modelling details for OF loading cases

In modelling one-flange (OF) loading cases, the techniques used for two-flange (TF) loading cases largely remain applicable. Special attention should be paid to modelling the stiffener blocks and plates attached to the specimen at specific locations in order to force the buckling to occur in specific locations. It is also noted that the specialised test rig designed for OF loading cases as shown in Figure 42 is not fully replicated in the numerical model, under the assumption that it is integrated within the testing machine. The typical experimental setup for IOF and EOF loading cases are shown in Figures 73 and 74, respectively.

In order to reduce the complexity and the size of the numerical model, several simplifications are applied to the models to minimise unnecessary calculation. Efforts to simulate the stiffener blocks included different strategies:

- Modelling the blocks and plates for stiffening the specimen as shown in experimental study;
- Increasing the thickness in targeted areas;
- Assigning stiffer material properties to selected regions;
- Applying “rigid body” constraint at particular locations.

After comparative analysis revealed minimal differences in outcomes across these approaches, the “rigid body” constraint was chosen for its simplicity and effectiveness. This method is applied consistently across all one-flange (OF) loading cases, except where otherwise noted. Figure 75 illustrates the regions to be set as “rigid body” for IOF and EOF loading cases respectively. The “rigid body” regions include the flanges, webs and rounded corners.

Noting that stiffener blocks and plates, being made of steel, do not exhibit absolute rigidity. Thus, if “rigid body” was assigned to the stiffened area, the numerical model might be over-stiffened. Given that using "rigid body" for insignificant components and reasonably overestimation in numerical simulation are common in previous publications, this simplification is believed to be acceptable in this numerical study.

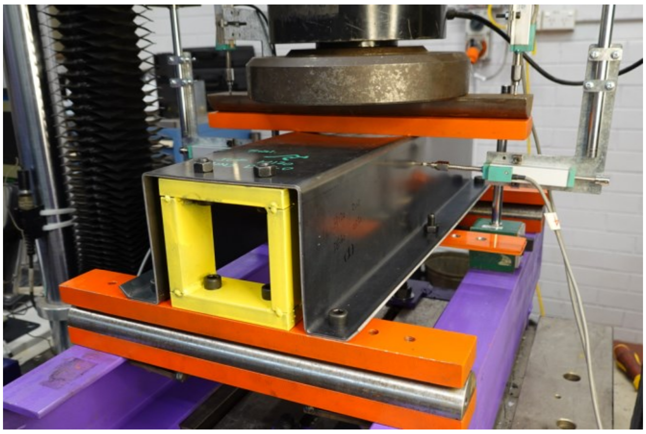

Figure 73 Typical experimental setup for IOF loading case

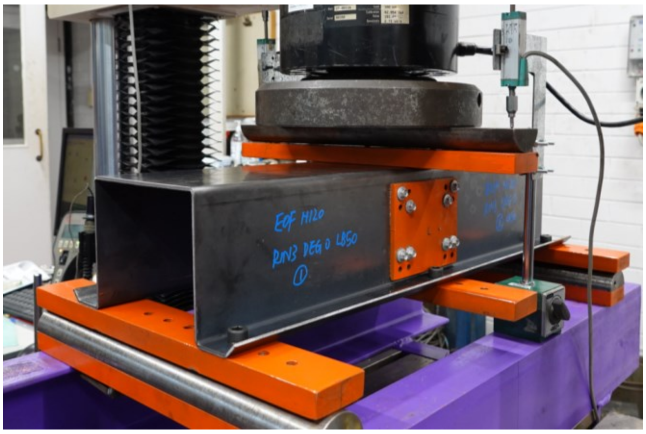

Figure 74 Typical experimental setup for IOF loading case

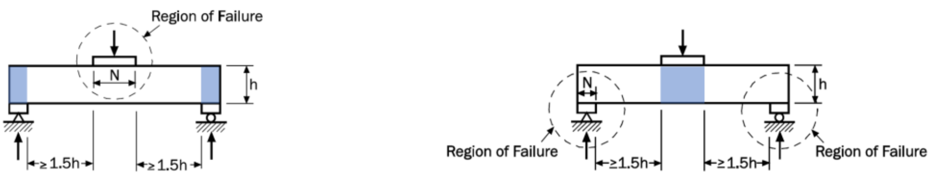

Figure 75 IOF & EOF "rigid body" setup locations

5.2.4 Validation

To validate the numerical models, both shell and solid element models undergo a two-step validation process against corresponding experimental tests. The initial step involves a visual comparison of the mechanism behaviour between the numerical models and experimental tests. Following this visual inspection, the second step entails a numerical comparison of the Load – Displacement (L-D) curves generated from the numerical models against those derived from experimental test data. This comparison offers a direct and quantifiable measure of the models' validity, providing a clear indication of how well the numerical simulations align with the physical testing outcomes.

5.2.4.1 Failure mode comparison

The validation of the numerical model against relevant experimental tests is illustrated through Figures 76 to 85. It is important to clarify that the chosen photographs do not necessarily present the point of maximum load due to the variability in how maximum loading capacity is achieved. Specifically, the peak load might occur at an early stage with minimal displacement, or, in instances of failure by the rolling mechanism, the load capacity may continue to increase without a definitive peak within the experiment loading range.

Consequently, for each loading case, a photograph that best represents the observed failure mechanism is carefully selected for demonstration purposes. Alongside these photographs, the corresponding numerical models at the same stage of deformation captured in the photos are displayed, providing a visual comparison that underscores the accuracy of the numerical simulations in reflecting the observed experimental behaviours.

The analysis of the photographs concludes that the numerical results obtained from both the shell element model and the solid element model qualitatively replicate the mechanical behaviour observed in the experimental tests. This finding substantiates the suitability of these numerical models for conducting parametric studies. By accurately mirroring the experimental outcomes, these models provide a reliable basis for exploring various parameters and their impacts on structural behaviour, thereby extending the scope of research beyond the constraints of physical testing.

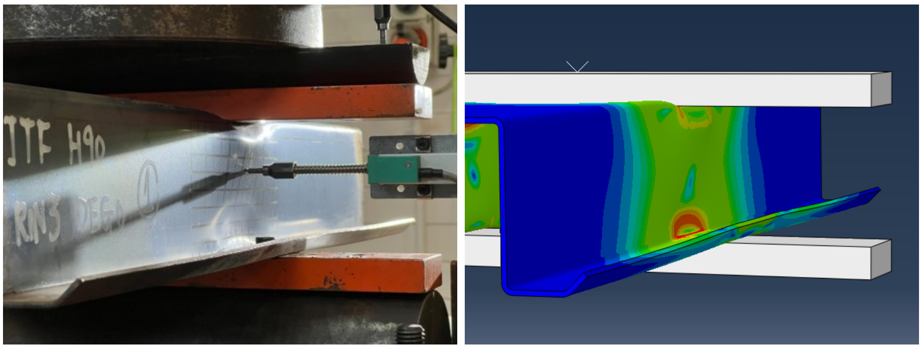

Figure 76 ITF-F-RIN3

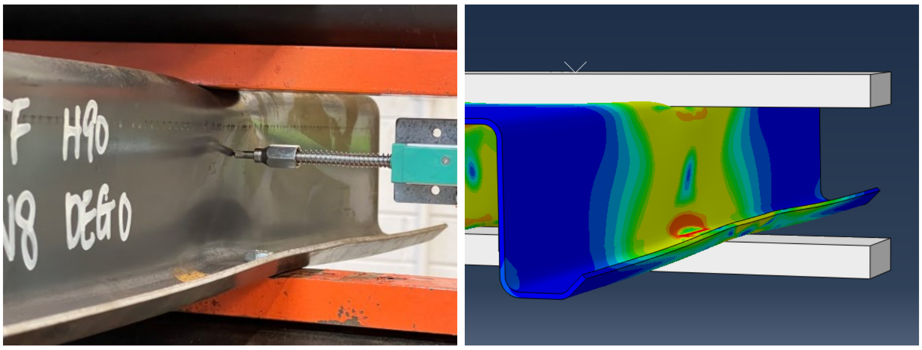

Figure 77 ITF-F-RIN8

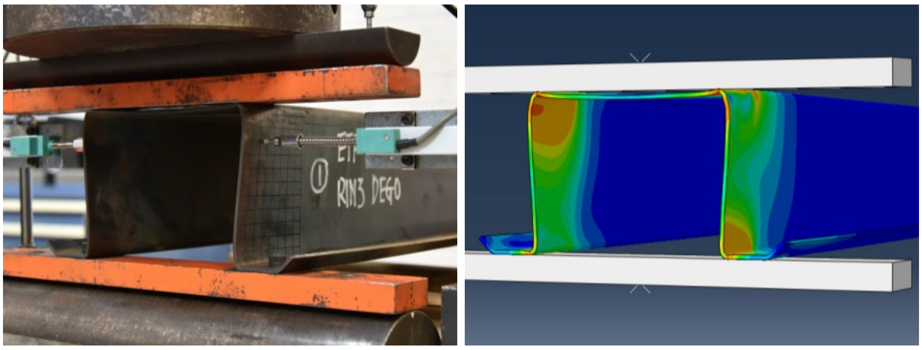

Figure 78 ETF-F-RIN3

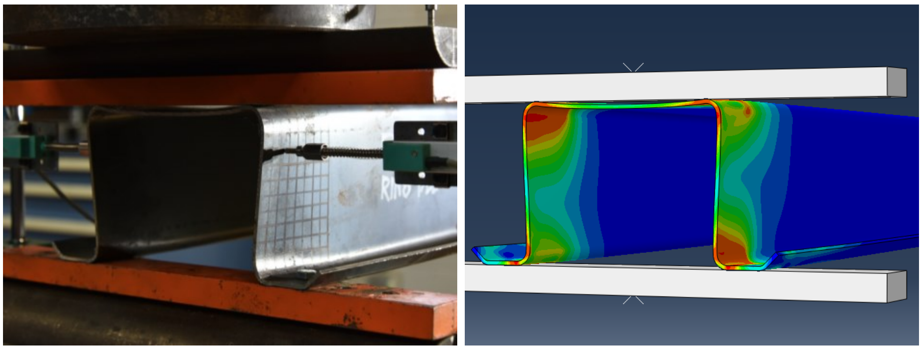

Figure 79 ETF-F-RIN8

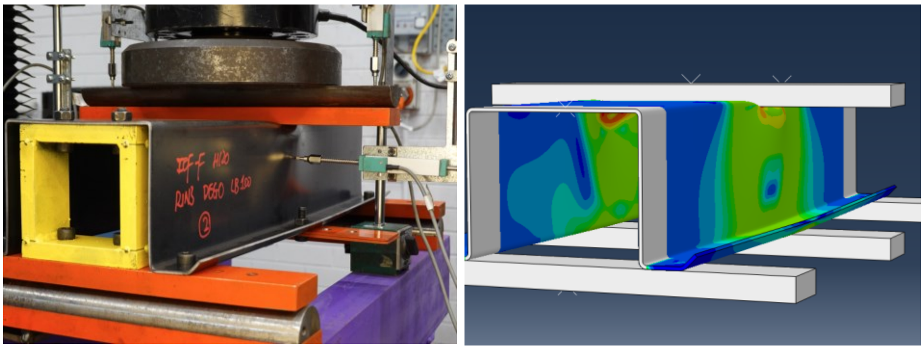

Figure 80 IOF-F-RIN3

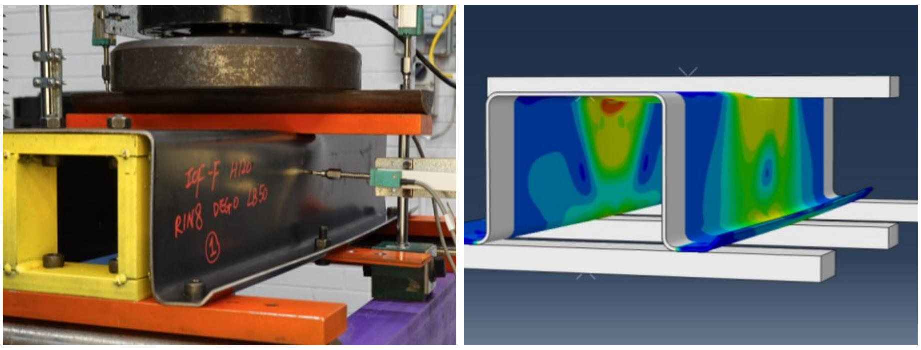

Figure 81 IOF-F-RIN8

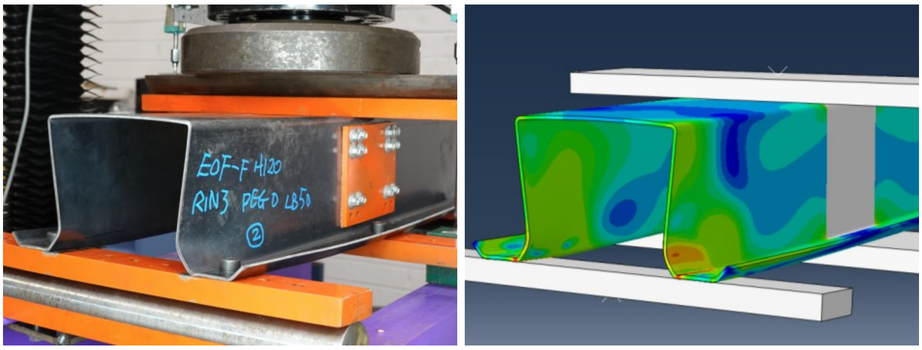

Figure 82 EOF-F-RIN3

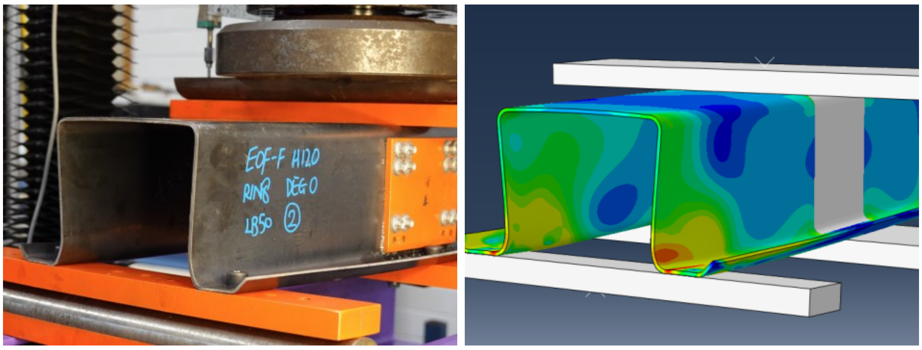

Figure 83 EOF-F-RIN8

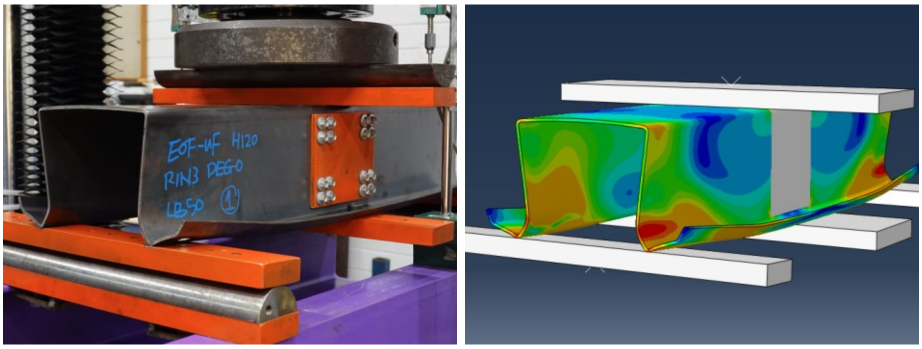

Figure 84 EOF-UF-RIN3

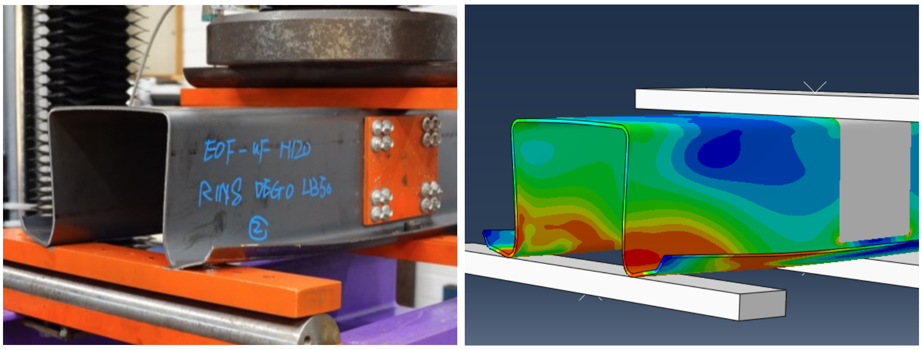

Figure 85 EOF-UF-RIN8

5.2.4.2 L-D curve comparison

The comparison of Load – Displacement (L-D) curves between experimental and simulation results plays a crucial role in validating the Finite Element Method's (FEM) capability to accurately predict loading capacity. For selective typical cross sections being tested, L-D curves collected from experimental tests are plotted alongside those exported from both shell and solid element models as shown in Figures 86 to 94. It's worth noting that for EOF loading cases, the load recorded by the load cell is two times the localised loading capacity. In order to be consistent with other loading cases, the load L-D curves are presented using half of the load captured by the load cell.

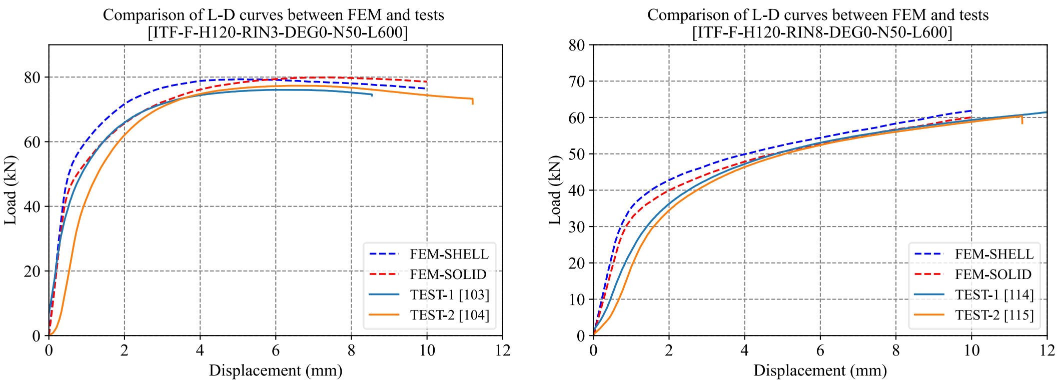

Figure 86 ITF-F-H120-DEG0-N50 (L: RIN=3, R: RIN=8)

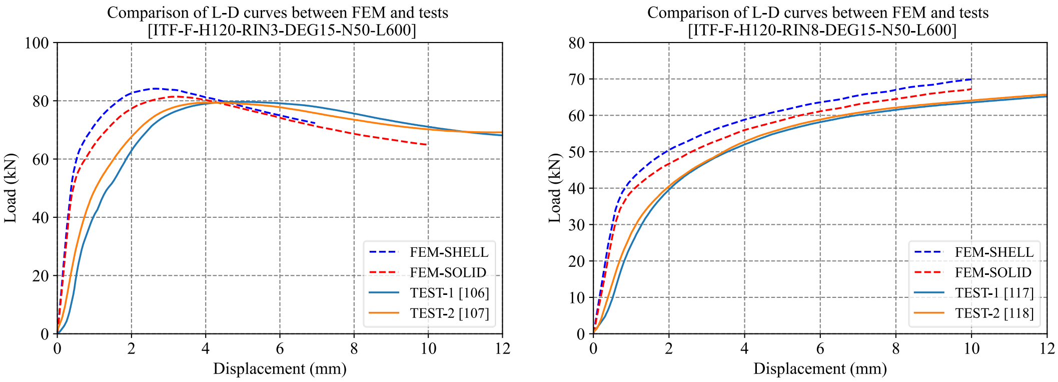

Figure 87 ITF-F-H120-DEG15-N50 (L: RIN=3, R: RIN=8)

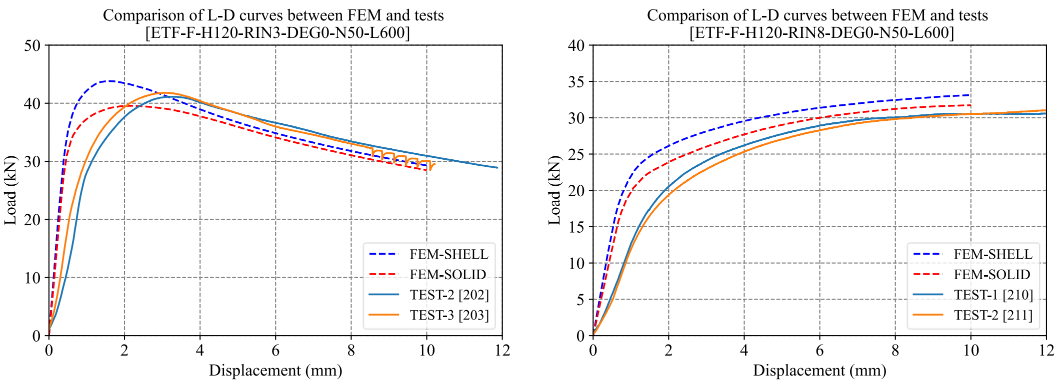

Figure 88 ETF-F-H120-DEG0-N50 (L: RIN=3, R: RIN=8)

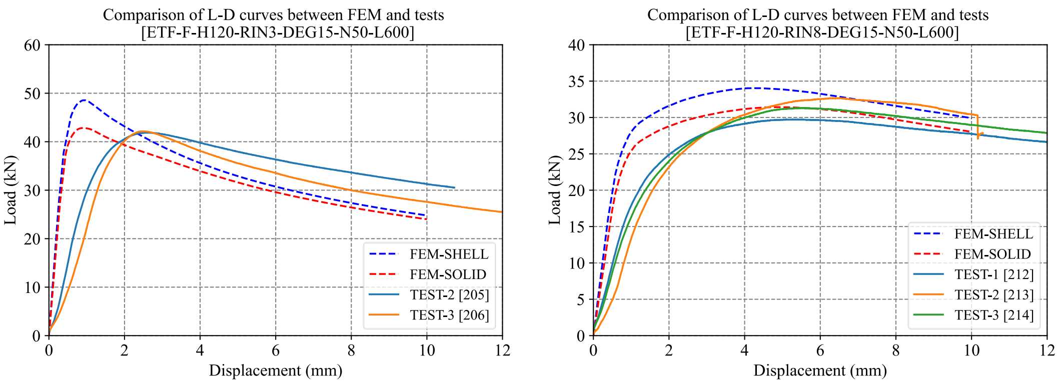

Figure 89 ETF-F-H120-DEG15-N50 (L: RIN=3, R: RIN=8)

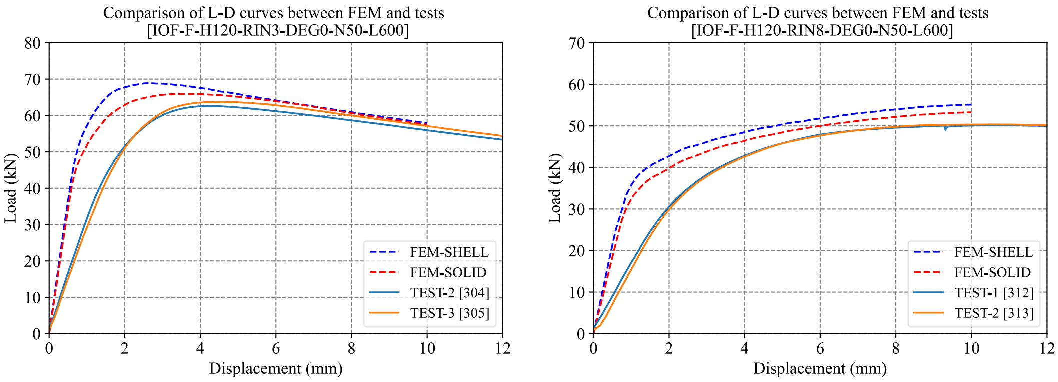

Figure 90 IOF-F-H120-DEG0-N50-L600 (L: RIN=3, R: RIN=8)

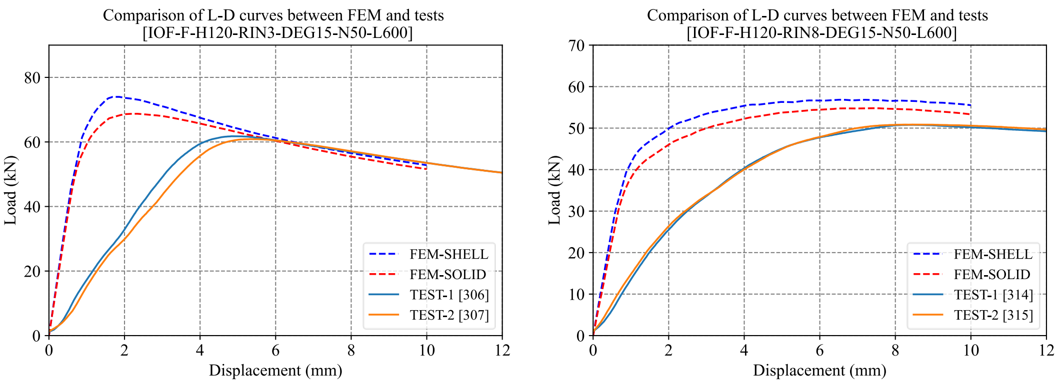

Figure 91 IOF-F-H120-DEG15-N50-L600 (L: RIN=3, R: RIN=8)

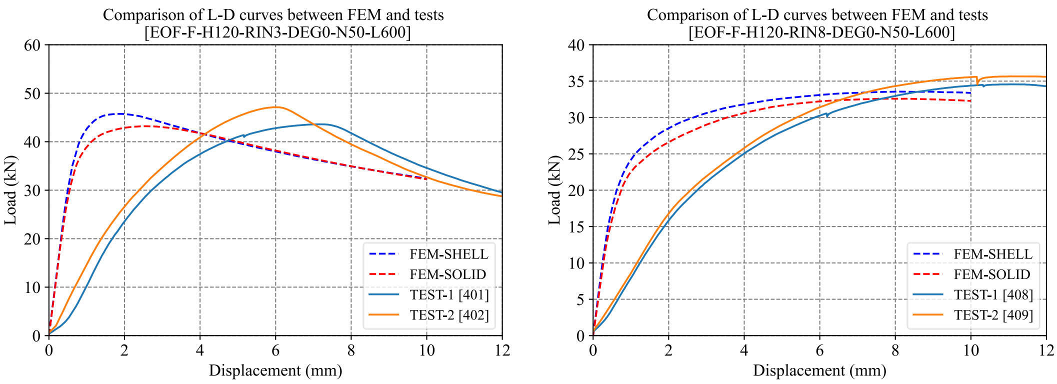

Figure 92 EOF-F-H120-DEG0-N50-600 (L: RIN=3, R: RIN=8)

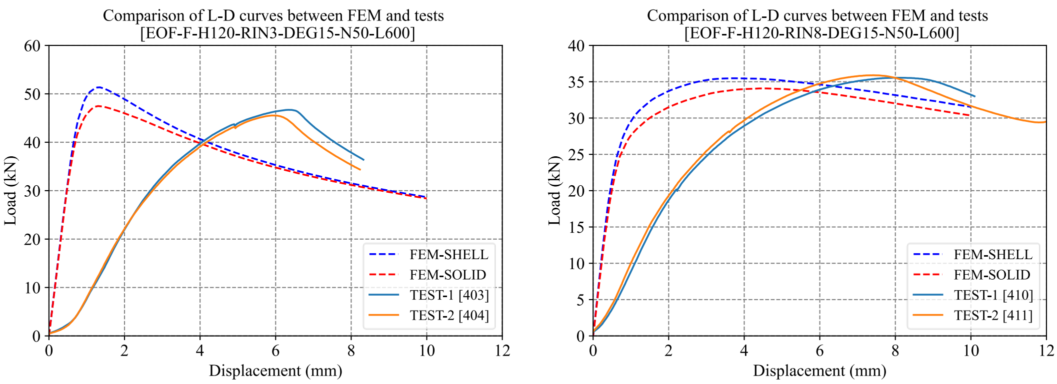

Figure 93 EOF-F-H120-DEG15-N50-L600 (L: RIN=3, R: RIN=8)

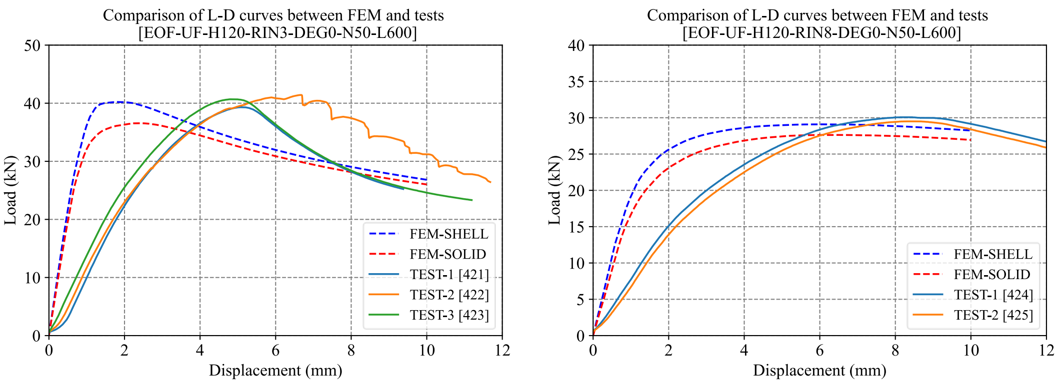

Figure 94 EOF-UF-H120-DEG0-N50-L600 (L: RIN=3, R: RIN=8)

The analysis of the provided figures leads to the conclusion that for most sections with vertical webs, both shell and solid element models yield accurate estimations regarding ultimate capacity and the profile of the Load – Displacement (L-D) curves. In the case of inclined web sections, shell element models tend to slightly overestimate results, whereas solid element models deliver more precise capacity predictions. A plausible explanation for this discrepancy is that shell elements may not adequately capture the behaviour of thick materials. Details are discussed in Section 5.2.5.

A notable observation for EOF loading cases is the absence of asymmetric behaviour between the two longitudinal ends in the FE simulations, owing to the models being configured with perfect symmetry. In the experimental tests, asymmetric failure was observed in most of the tests due to inherent assembly imperfection.

In the ideal conditions, the top bearing plate in the middle of the sections does not have any rotations. In this case, the interior top flange loading is acting at the perfect middle position of the specimen resulting in a perfect symmetric failure at two end as shown in Figures 95 and 96. However, in more common scenarios, a variety of factors including but not limit to manufacturing, assembly, and systemic errors, can introduce imperfections that disrupt this perfect symmetry. Such imperfections can accumulate, leading to asymmetric loading and, consequently, failure at one end of the specimen beyond the bifurcation point, as illustrated in Figures 97 and 98.

Interestingly, despite the occurrence of both symmetric and asymmetric failures in the tests, the web crippling capacities recorded from the load cell closely match the results from FE simulations. This agreement between two sets of results suggests that the experimental setup is fundamentally sound and that any discrepancies caused by asymmetry in the experimental studies are minor.

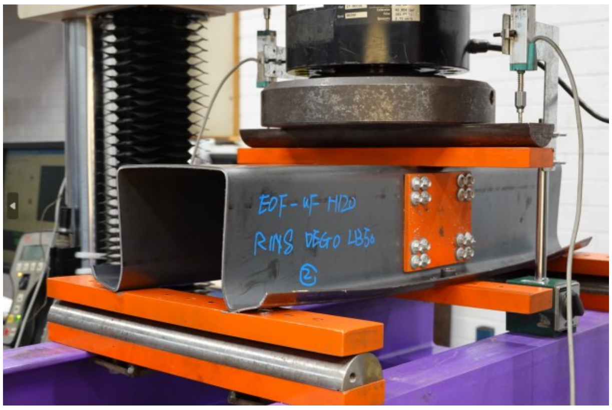

Figure 95 Symmetric failure at two ends for EOF loading case, experimental study photo

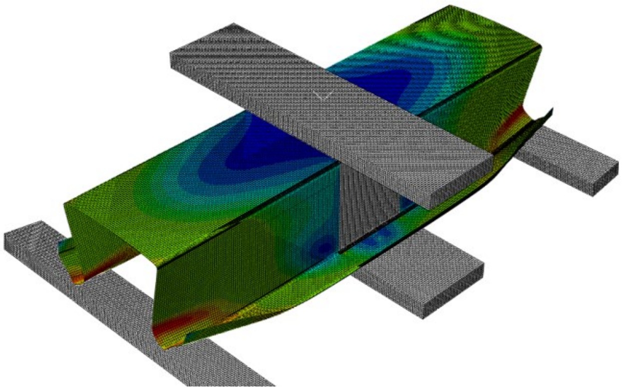

Figure 96 ABAQUS simulation – symmetric failure

Figure 97 Asymmetric failure at two ends for EOF loading case, experimental study photo

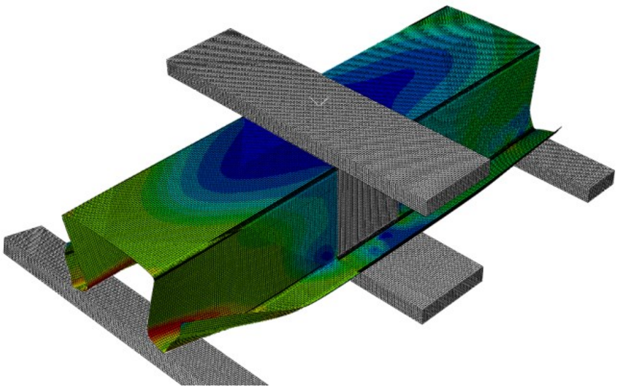

Figure 98 ABAQUS simulation – asymmetric failure

In many L-D curves, a significant difference in elastic stiffness between experimental results and FE simulations is evident. This phenomenon can be attributed to two factors.

The primary explanation for this discrepancy is the presence of minor gaps between components due to manufacturing imperfections. These inevitable contact imperfections, combined with slight irregularities between the two legs, accumulate and require substantial displacement to close, resulting in Load-Displacement curves with lower initial slopes compared to idealised models.

A secondary explanation is the flexibility of the test rig, which is captured in experimental displacement measurements but not incorporated into the finite element simulations. Heurkens, Hofmeyer, Mahendran and Snijder [53] proposed a simple equation to explain this issue in 2018. Similar to the spring in series, the relationship of the system stiffness of the experiment k_{test}, stiffness of the specimen k_{sp} and the stiffness of the test rig k_{rig} can be expressed as

$$k_{test}^{-1} = k_{sp}^{-1} + k_{rig}^{-1} \tag{5-3}$$

This equation indicates that the absence of the test rig in modelling lead to a difference between the specimen's stiffness k_{sp} and the system's experimental stiffness k_{test}. However, it's important to note that this additional observed flexibility in experiments does not significantly influence the maximum loads or the overall profile of the L-D curves. Consequently, considering the research does not primarily focus on stiffness differences, the discrepancy in stiffness between experimental and numerical simulation results can be regarded as negligible.

5.2.5 Theoretical basis for both element types for FE analyses

In previous sections, a comprehensive discussion of using both types of elements for FE analyses shows that solid elements seem to be a preferable method for future studies, especially for stock sections and sloped web sections.

The differences in the definition between solid and shell elements could provide a plausible explanation for the observed discrepancies. According to the ABAQUS Manual, shell elements are 2D elements that are used to model thin 3D structures. Whilst these elements include a thickness setting, their nodes are dimensionally positioned on the mid-surface. Conversely, solid elements are 3D elements with nodes extending through the thickness direction.

Conventional shell elements are essentially treated as a special category of solid elements with a reduced degree of freedom in the thickness direction. This reduction simplifies the model by generally excluding transverse shear deformation and changes in thickness, whilst assuming stress through the thickness to be negligible.

Furthermore, stress variations across different control layers within the thickness are determined via interpolation.

These simplifications, whilst beneficial for certain applications, could lead to inaccuracies in scenarios involving large deflections and rotations, or substantial strains. This issue becomes more pronounced when dealing with thick sheet materials where the stress distribution deviates from the idealized uniformity assumed by shell element models.

Although shell element modelling proves unconservative for stocky sections, it demonstrates good accuracy for slender sections, validating its application within specific contexts. This finding is substantiated by the author's numerical study for the tests conducted by Wu et al. [16] presented in a later chapter and also in Appendix J, which shows strong correlation between the experimental and FE results in the slender range.

Analysis indicates that solid element modelling requires a minimum of two mesh layers to achieve accuracy levels comparable to shell element modelling. This requirement significantly increases computational demands. A typical shell element analysis of web crippling in hat sections requires 15-20 minutes on a 32-core high-performance computing (HPC) node, consuming 1.5 GB of storage. In contrast, the equivalent solid element analysis requires 3-4 hours on the same HPC node, contingent on model convergence, and occupies 8-10 GB of storage.

Given the research focus on stocky sections, where a 3 mm thick plate is used, solid elements are the preferred choice. Nevertheless, for studies involving thinner sections when ensuring two layers of mesh or securing ample computational resources might be challenging, shell elements with appropriate modifications are advisable.

In addition, previous numerical research predominantly employed shell elements with Implicit Dynamic (ID) and Explicit Dynamic (ED) methods, yielding comparable results. However, these methods often require significant calibration, indicating the need for a simplified and consistent web crippling simulation methodology. The increasing availability of high-performance computing (HPC) facilities enables the analysis of more complex, yet accurate models within reasonable timeframes. This technological advancement has been utilised in the present study to develop a simplified, consistent approach for efficient and accurate web crippling simulation.

A comprehensive comparison between shell element and solid element modelling approaches, supported by quantitative data, is presented in the following section.

5.2.6 Comparison between shell elements and solid elements

Initial investigations into optimal element types for numerical analyses revealed significant differences between solid and shell element results for thicker sections, with diminishing variations for thinner sections. Of particular significance, shell element models demonstrated increasing web crippling capacity variations with increased web slope compared to solid element models. This observation is particularly intriguing since it is a phenomenon unique to shell element sections, which has not been previously documented in previous research. The absence of prior discussions or analyses on this matter likely based on the fact that the majority of studied sections do not feature sloping webs. Among those sections with vertical webs, the difference in performance between solid and shell elements is found to be minimal. Thus, extensive research was conducted for further understanding the difference between shell and solid elements for web crippling simulations, especially for hat sections.

A comparative analysis was conducted for not only clarifying the differences in employing shell versus solid elements, but also providing a form of reliability analysis. The discrepancies in outcomes between solid and shell elements in comparison to experimental data gathered from this thesis's is presented in Figure 99. For each experimental data, two values were calculated as part of the comparison: P_{exp}/P_{solid} were plotted on the Y axis and P_{exp}/P_{shell} were presented on the X-axis, where P_{exp}, P_{solid} and P_{shell} represent the web crippling capacities as determined through experimental observation, simulation using solid elements, and simulation using shell elements, respectively. The data points were categorised by different loading cases and the webs' sloping angles. A static analysis was conducted for calculating the average (AVE) values and standard deviations (StdDev) for both P_{exp}/P_{solid} and P_{exp}/P_{shell} ratios, as meticulously compiled in Table 19.

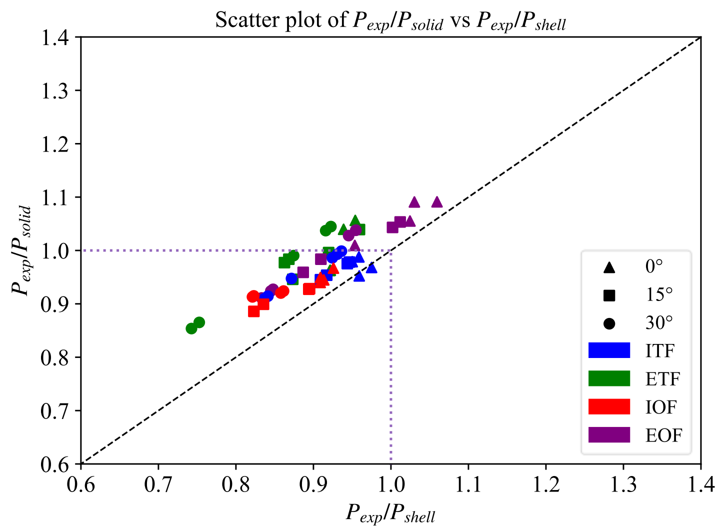

Figure 99 Comparison of experimental results and numerical results using solid and shell elements from tests by Chen et al. [36]

Table 19 AVE and StdDev of P_exp/P_solid and P_exp/P_shell

	AVE of EXP/SOLID	AVE of EXP/SHELL	StdDev of EXP/SOLID	StdDev of EXP/SHELL
EOF	1.011	0.947	0.060	0.074
ETF	0.982	0.888	0.063	0.067
IOF	0.926	0.872	0.022	0.040
ITF	0.964	0.921	0.028	0.043
Grand Total	**0.972**	**0.908**	**0.055**	**0.064**

According to the data presented in Figure 99 and Table 19, the simulations employing solid elements yield more accurate predictions, with an average P_{exp}/P_{solid} value of 0.972. Although the simulation result is slightly unconservative, this close correspondence with experimental results suggests that the differences are minimal and acceptable. However, for the simulations using shell elements, the P_{exp}/P_{shell} value has an average of 0.908, which means these results tend to provide more unconservative predictions. This distinction underscores the greater reliability of solid elements in accurately predicting the behaviour of web crippling for hat section stocky sections. Interestingly, the discrepancy between solid and shell element predictions is smallest for sections with a 0° sloping angle (vertical web) for each loading cases.

In summary, the numerical models developed using solid elements have proven to be reliable and are sufficiently accurate for conducting further parametric studies. On the other hand, models employing shell elements were found to be slightly unconservative, especially in ETF and IOF loading cases. This finding suggests the need for additional adjustments to the result obtained from shell element models before they can be utilised for precise equation calibration purposes.

The observed 10% deviation in shell element results does not invalidate their application in numerical studies. The substantial reduction in computational time when employing shell elements for parametric studies, particularly for slender sections with vertical webs, justifies their use where solid element analysis proves impractical. This approach is substantiated by evidence demonstrating reduced variation between experimental and simulation results with increasing section slenderness. Thus, shell element models remain valuable for analysing general trends and behaviour patterns within the Direct Strength Method (DSM) design equations, specifically in the mid-to-high slenderness ratio range.

5.3 PARAMETRIC STUDY: EFFECT OF SECTION PARAMETERS

Following the validation of both shell and solid element models, a comprehensive parametric study was conducted to identify the primary factors influencing the behaviour of hat sections. This section of the research involved systematic variations in several parameters to explore the intricate relationships between the dimensions of the hat sections and their localised loading capacities. It's noteworthy that the dimension of the hat sections not only includes the cross-section dimension, but also includes the exploration of the length of the specimen particularly for one-flange loading cases.

As established previously, sections with vertical webs exhibit minimal discrepancy between solid and shell element simulation results. Shell element simulations thus provide sufficient accuracy for analysing behavioural patterns in vertical-webbed sections. The analyses in this section primarily employ shell element models, except where explicitly stated. For investigations involving web sloping angles, solid elements are used exclusively due to identified discrepancies in shell element performance with sloped web sections.

5.3.1 Corner radius

Both shell and solid elements models were used in this study.

The influence of corner radius on both the load capacity and mechanical behaviours of structural sections has been a topic of extensive research. In this study, corner radii ranging from 3 mm to 8 mm, with 1 mm increments, were modelled and analysed to understand their impact, with the experimental studies using 3 mm and 8 mm radii as boundary values. The sections under consideration were specified with dimensions of height (H) = 120 mm, thickness (t) = 3 mm, width (W) = 150 mm, and web slope (DEG) = 0°.

The FE results from the 3D model analyses demonstrate distinct failure modes associated with different corner radii. For an internal rounded corner radius of 3 mm, the failure mode is yield-arc post-failure mechanism, where a yield arch forms in the web near the rounded corner. Conversely, for a radius of 8 mm, the failure mode is observed as rolling post-failure mechanism, where no clear yield line is evident. Between these two extremes, a mixture of rolling mechanisms and yield-arc mechanisms is observed, starting with rolling mechanism at small loads which transitions into yield-arc formation as loading increases, subsequently slowing the rate of load capacity growth. Figure 100 shows a section with a combined failure mode, demonstrating both a rolling mechanism and the formation of a yield-arc simultaneously.

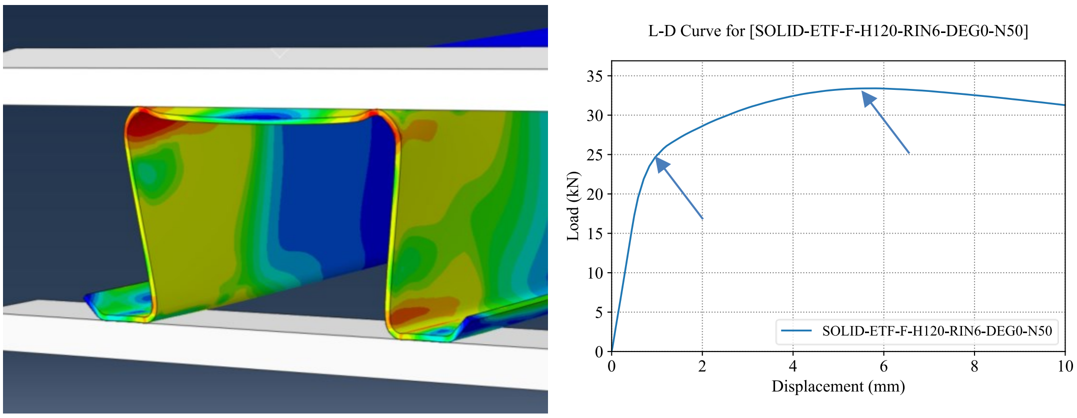

Figure 100 A typical section undergoing a combine failure mode

The following two figures demonstrate two Load-Displacement (L-D) curves for different sections, varying only in corner radii, are plotted on the same graph for ITF-F (Figure 101) and IOF-F (Figure 102) loading cases respectively. The L-D curve of a section failing purely by rolling mechanism exhibits a continuous growth until nearly the end of the loading range, while the pure yield-arc mechanism shows a sharp increase in load capacity followed by a rapid post-peak decline. Sections exhibiting combined failure modes display two distinct slope changes on their L-D curves, indicative of the transition between mechanisms.

This pattern of behaviour is consistent across all four basic load cases, irrespective of the fastening condition. It emphasises the critical role that corner radius plays in determining the structural performance and load-bearing capacity of sections under different loading conditions.

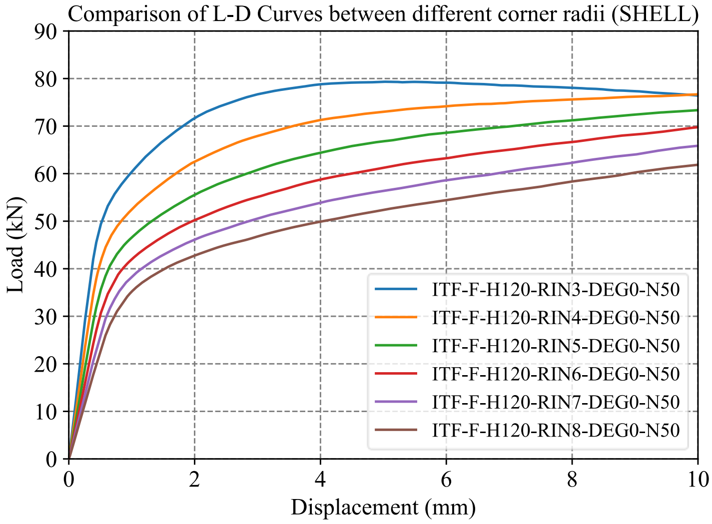

Figure 101 L-D curves for various corner radii, ITF-F (Shell)

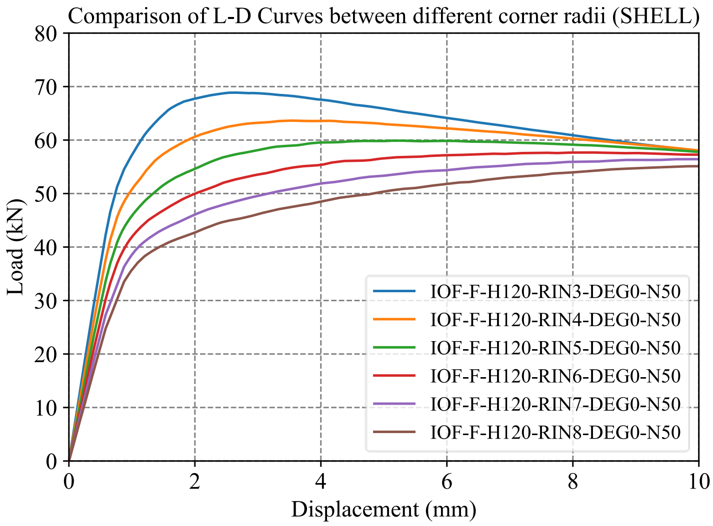

Figure 102 L-D curves for various corner radii, IOF (Shell)

5.3.2 Bearing length

Shell elements models were employed in this study.

In order to understand the influence of changing bearing length, ITF-F loading case is taken as an example for further investigation. In the experimental study, hat sections were tested with both 50 mm and 100 mm widths of bearing length, shown as N in Figure 103. To further investigate the impact of changing the bearing length, a parametric study was carried out for the ITF loading cases with bearing lengths ranging from 50 mm to 125 mm in 25 mm increments.

Finite Element Method (FEM) results highlight distinctive structural behaviours in 3D models for sections with large and small corner radii. Regardless of the bearing length within the range indicated above, the phenomena of rolling and yield-arc post-failure mechanisms are consistent with previously established understandings for large and small corner radius sections, respectively. Figures 104 and 105 demonstrates the cross-section behaviours of yield-arc post failure mode and rolling post failure mode respectively.

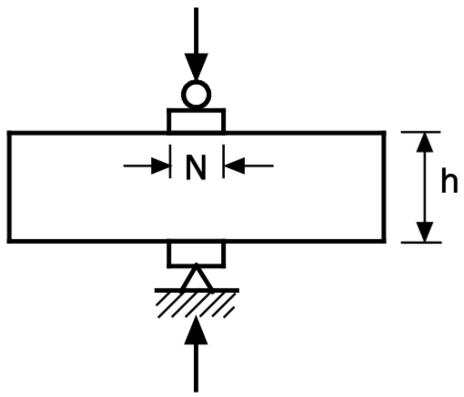

Figure 103 Bearing length location demonstration using ITF loading case (shown as N)

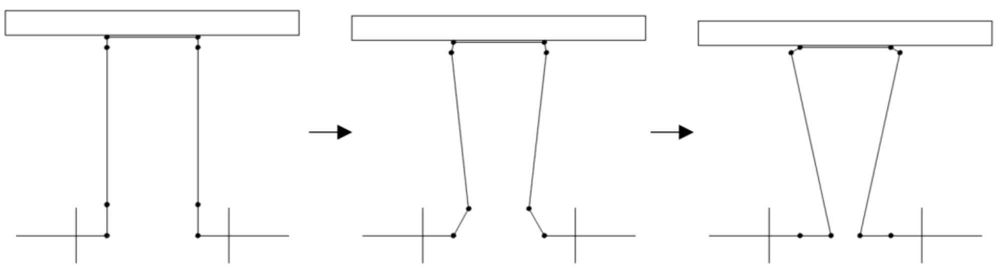

Figure 104 Demonstration of yield-arc failure mode

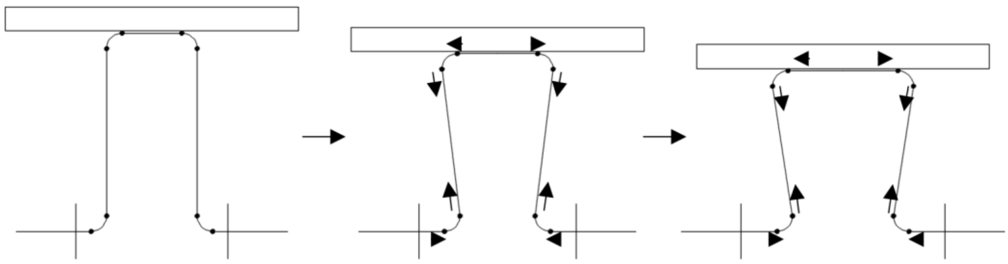

Figure 105 Demonstration of rolling post failure mode (bottom bearing plate omitted)

Moreover, an increase in bearing length influences the positioning of plastic hinge formation on the web beneath the bearing plate, shifting it further from the radius-web intersection. Conversely, narrower bearing plates result in plastic hinge development closer to this intersection. This observation suggests a minimum width requirement for bearing plates to ensure the formation of a plastic hinge on the web. This requirement is crucial to prevent scenarios similar to concentrated loads, where the failure mode diverges from typical web crippling conditions.

In accordance with the L-D curves in Figure 106, for sections with both 3 mm and 8 mm corner radii, an increase in bearing length leads to a corresponding increase in web crippling capacity. This capacity can be conceptualized as a combination of two components: one attributable to the capacity directly under the bearing length and another to the capacity from the diffusion width outside the bearing area, as visually demonstrated in Figure 107.

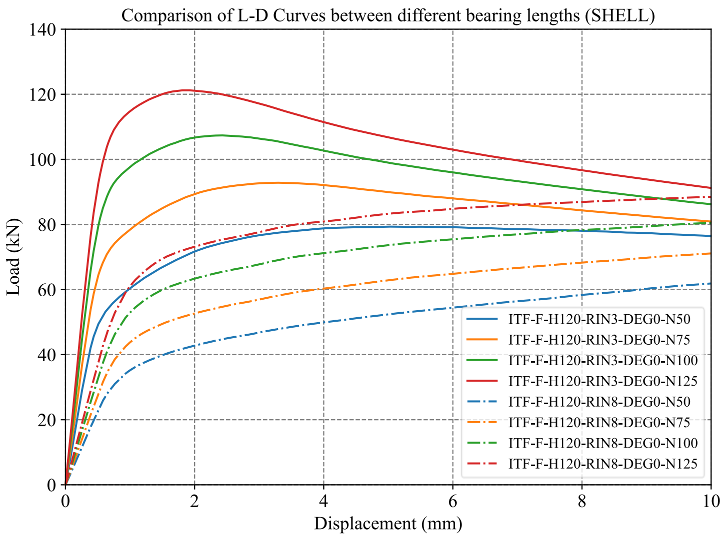

Figure 106 L-D curves for various bearing length, ITF-F (Shell)

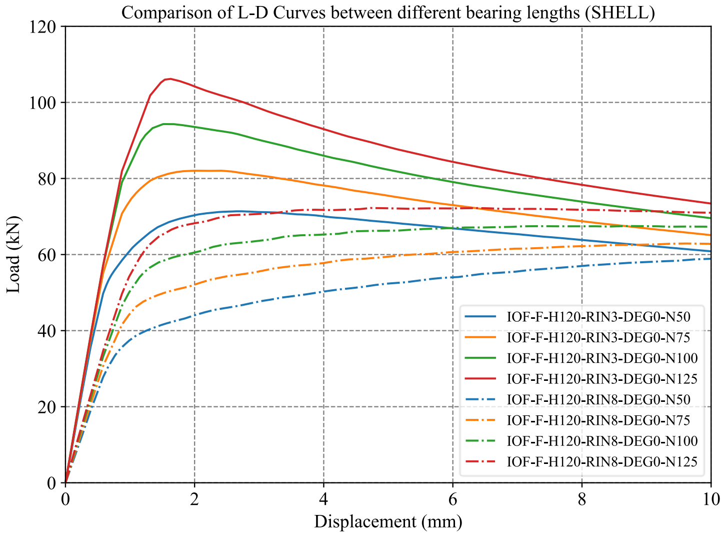

Figure 107 L-D curves for various bearing length, IOF-F (Shell)

5.3.3 Height

Shell elements models were used in this study.

For Two Flange (TF) loading cases, an observed trend in the data is that increasing the height of hat sections slightly reduces their bearing capacity, as shown in Figure 108. A plausible explanation for this behaviour is that a taller section height leads to increased slenderness of the web. This increased slenderness, in turn, results in a lower buckling load, adversely affecting the overall capacity, despite the sections primarily failing due to yielding. This observation suggests that, for TF loading cases, the web crippling capacity exhibits minimal sensitivity to changes in section height.

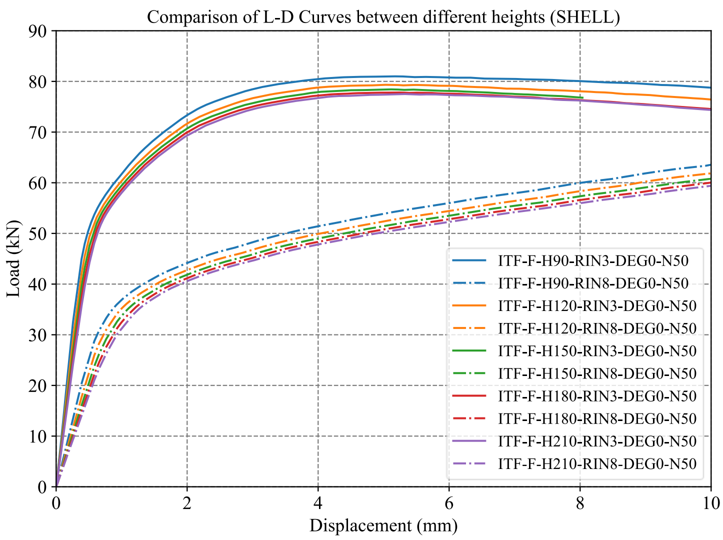

Figure 108 L-D curves by changing the height, ITF-F-DEG0-N50 (Shell)

In the context of One Flange (OF) loading conditions, a targeted parametric study was conducted to discover how variations in the height of hat sections affect their web crippling capacity. Hat sections with web heights of 90 mm, 120 mm, 150 mm, 180 mm, and 210 mm were selected for this study, each with internal corner radii of 3 mm and 8 mm.

It's important to clarify that the length used in this analysis does not adhere strictly to the minimum required length as recommended in testing specification S909-17, where the clearance between two bearing plates is calculated using the formula $1.5h$ (h being the length of the flat portion of the web). Instead, the lengths chosen for this study are slightly over the minimum required length, calculated as $1.5H$ (where H represents the total height of the web, including the rounded corner). This modification is considered as a general adaptation to ensure the validity of OF loading cases during the experimental studies, which has been used by Wu, Yu and LaBoube[16] and Young and Hancock [27,54].

The L-D curves shown in Figure 109 provide a significant finding: when specimens maintain a consistent bearing length and an adjusted reasonable minimum length across varying section heights, the web crippling capacity shows minimal variation with respect to the section's height. A separated section regarding the OF loading cases on the influence of the length of specimen is also discussed in a later section.

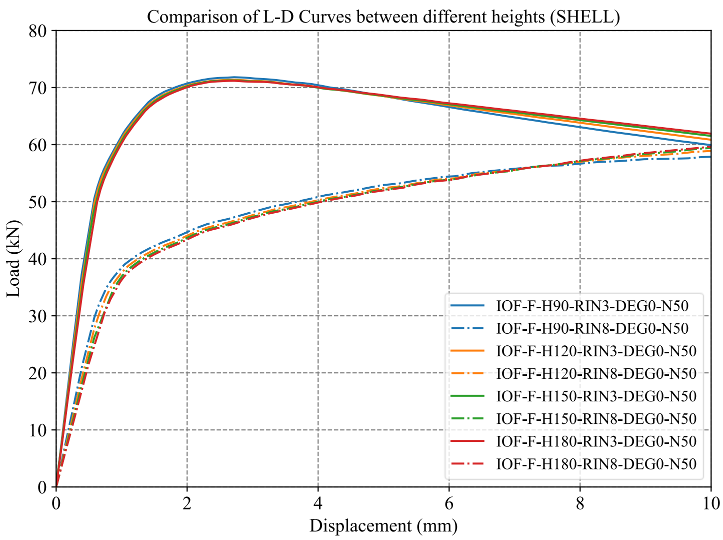

Figure 109 L - D curves by changing the height at minimum length, H90-L420, H120-L510 and H150-L600 (Shell)

5.3.4 Inclination of web

Solid elements models were used in this study.

Given the inclusion of sections with sloped webs in this study, solid elements were selected for use in this series of simulations. To investigate the effects of sloped webs, a parametric study using ITF loading case as an example was conducted using the solid element model. The web' s inclination angle, denoted as α, was varied from 0 degrees to 30 degrees in 5-degree increments, as illustrated in Figure 110. The sections under consideration were specified with dimensions of height (H) = 120 mm, thickness (t) = 3 mm, width (W) = 150 mm, and bearing length (N) = 50 mm.

Figures 111 and 112 demonstrate the influence of changing the slope angle of the web for small and large corner radii sections respectively.

For small corner radius sections, modifications to the web's slope angle exhibited minimal influence on the ultimate capacity for angles up to 20 degrees. Beyond this point, as the slope angle surpasses 20 degrees, a small but noticeable reduction in web crippling capacity is observed as shown in Figure 111. Concurrently, from 0 degrees to 30 degrees, the increment in the slope angle results in a reduction in the displacement necessary to achieve maximum load capacity.

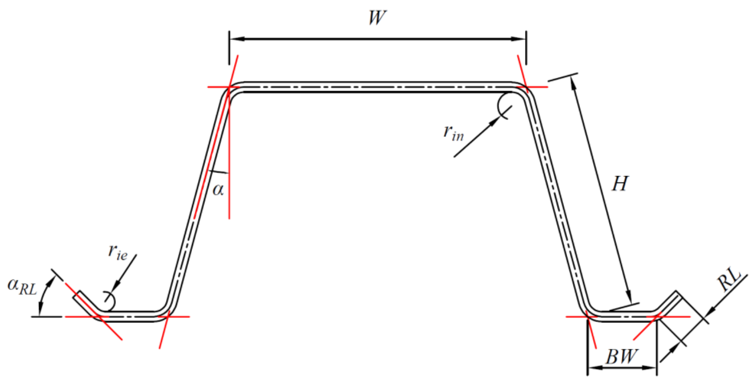

Figure 110 Definition of dimensions (Same as Figure 33)

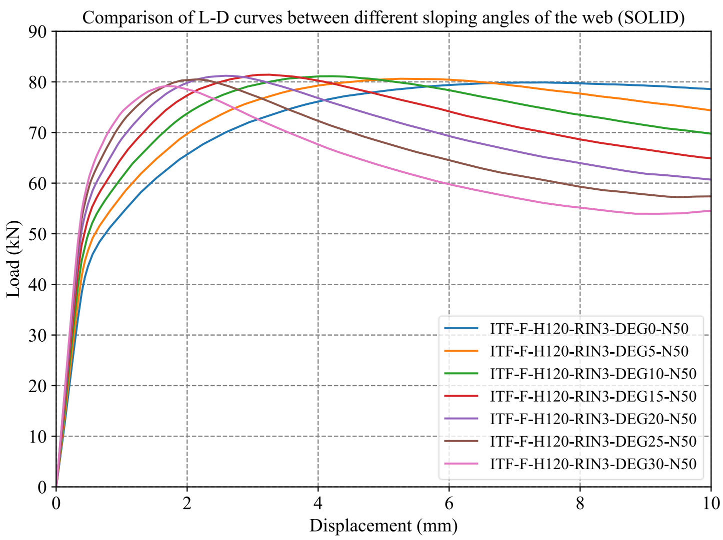

Figure 111 L-D curves by changing the sloped angle of the web, ITF-F-H120-RIN3 (Solid element)

For large corner radius sections, within 10 mm displacement range the behaviour as shown in Figure 112 is different between 0 to 20 deg and from 20 deg onwards. A continuous increasing trend is shown on the L-D curves when the slope angle of the web is up to 20 deg. From 20 deg onwards, a peak of capacity is observed follow by a capacity decrease. The ultimate capacity within the simulation range decreases when the sloped of the web is over 20 deg. This behaviour is consistent with the small corner radius sections.

For sections with large corner radii, the behaviour within a 10 mm displacement range varies based on the slope angle of the web as demonstrated in Figure 112. Up to a slope angle of 20 degrees, the L-D curves exhibit a continuous increasing trend. However, beyond a 20-degree slope, a distinct peak in load capacity is followed by a decrease in capacity. This pattern indicates that the ultimate capacity within the simulation range reduces when the web's slope exceeds 20 degrees, a finding that corresponds with observations made for sections with smaller corner radii. Despite the simulations only extending to the initial 10 mm of displacement, which represents 8.3% of an equivalent height, the observed patterns suggest a general principle for both small and large corner radius sections: increasing the slope angle up to 20 degrees tends to reduce the deformation required to reach peak capacity.

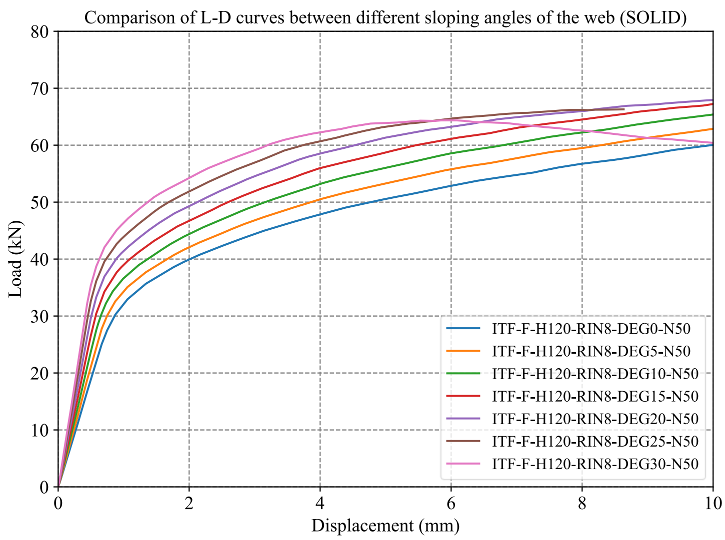

Figure 112 L-D curves by changing the sloped angle of the web, ITF-F-H120-RIN8 (Solid element)

In conclusion, sections with smaller corner radii and larger slope angles exhibit a notable advantage by reaching maximum load capacity more rapidly, by the meaning of less displacement is required, compared to sections with smaller slope angles. This principle could be instrumental in optimising hat section designs for mass production and commercial applications, where efficiency and performance are paramount.

For sections characterised by larger corner radii, the adoption of smaller slope angles initiates a rolling post-failure mode, allowing the section to progressively approach its maximum capacity. Conversely, when larger slope angles are adopted, a transition in failure modes is observed, where, after the initial rolling behaviour, a yield-arc mechanism becomes evident in some cases.

It should be noted that the radius of the rounded corner has a minimum requirement due to limitations in the manufacturing process. Consequently, a careful consideration regarding the selection of a proper corner radius to maximize the performance of a hat section is required.

5.3.5 Fastening condition

Shell elements models were use in this study.

Fastening conditions have demonstrated a tangible impact on the loading capacity, particularly evidenced in the EOF-F and EOF-UF experimental series. While fastening conditions are typically not considered a direct attribute of the hat section geometry, they do play a critical role as part of the loading case setup. In practical applications, fasteners are predominantly applied to the bottom flanges, facilitating a categorization of loading cases into two primary groups based on their application points: ITF and IOF represent middle-loaded cases, whereas ETF and EOF represent end-loaded cases. This categorization forms the basis for the exploration into the effects of fastening on the web crippling capacity.

For this analysis, a variety of hat sections with internal corner radii ranging from 3 mm to 8 mm were subjected to simulations across the aforementioned loading cases. Each loading cases within this series generated two distinct datasets—one incorporating fasteners and the other without. These datasets were subsequently plotted within the same figure, as indicated in Figure 113.

According to the L-D curves, for interior loading cases (ITF and IOF), the presence of fasteners does not significantly affect the web crippling capacity. This is attributed to the section’s ability to retain its shape due to restraints on both sides. In contrast, a notable difference was observed for the end loading cases (ETF and EOF). The absence of restraint on one end in these cases means that fasteners play a crucial role in preventing the bottom flanges from curling, thereby enhancing the web crippling capacity.

It’s worth noting that sloped web sections are excluded from the UF fastening condition study. Simulation has demonstrated that hat sections with sloped webs might spread out, or splay, when their bottom flanges are not fastened. It’s observed that sections exhibiting sufficient stockiness or where friction between the bottom flanges and the bearing plate counteracts the splaying effect can exhibit behaviour similar to that of vertical web sections without fasteners. However, this observation does not eliminate the potential for splaying, given the variability in contact surface conditions that could complicate the effect’s predictability. As a result, UF fastening conditions is generally considered not practical and they are excluded from the discussion in this section.

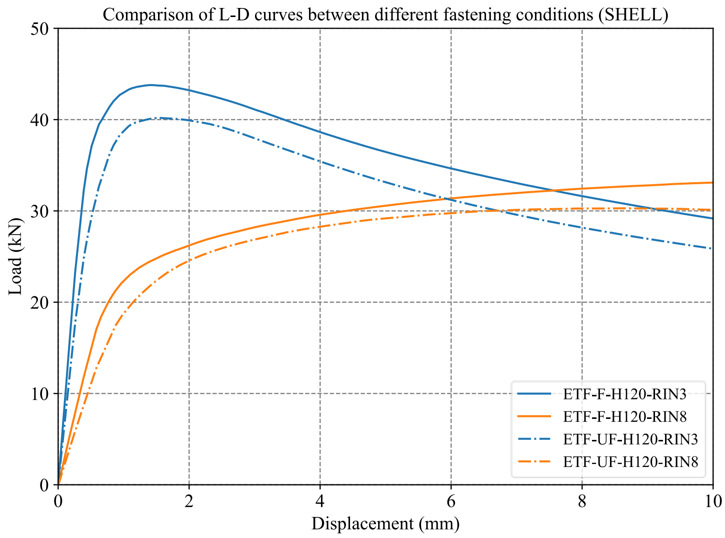

Figure 113 L-D curves comparison between ETF-F (solid line) and ETF-UF (dot line)

5.3.6 Width of top flange of hat sections

A parametric study using ITF-F loading case as an example was conducted by varying the width of the top bearing plate from 100 mm to 200 mm in increments of 50 mm. The sections under consideration were specified with dimensions of height (H) = 120 mm, thickness (t) = 3 mm, sloped angle of the web (DEG) = 0°, and bearing length (N) = 50 mm. The width of the top flange of the hat sections is denoted as W, as illustrated in Figure 110.

Analysis of the L-D curves, presented in Figure 114, reveals that variations in the width of the top flange have a minimal impact on the web crippling capacity of the sections. This influence remains insignificant across a reasonable range of flange widths encountered in standard design practices. Therefore, the width of the top flange is deemed to have a negligible effect on localised loading capacity, suggesting it is not a critical factor in the design considerations for typical hat section configurations.

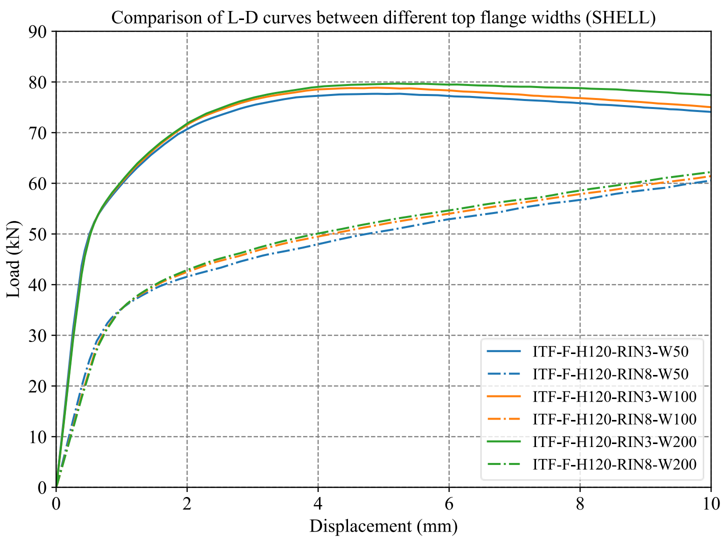

Figure 114 L-D curves comparison by changing top flange width, ITF-F-H120-DEG0-N50

5.3.7 Length of the specimen for OF loading cases

According to the testing specification AISI S909-17 [3], the way in which the web crippling capacity is tested for OF loading cases is similar to a three-point bending tests. Consequently, the load capacity includes both the web crippling capacity of the section and the bending capacity of the member. It is important to note that the bending capacity cannot be excluded entirely but can only be minimised. The testing specification has defined a **Minimum Clear Distance** (MCD) between the edge of bearing plates ($1.5h$ where the h is the height of the web of the flat portion), to ensure the validity of OF loading cases while recommending specimen lengths short enough to minimise bending effects.

Historically, the MCD has been calculated in different ways by various authors. Santaputra [15] and Sundararajah [41] have adopted the $1.5h$ where h is the flat portion of the web. Young and Hancock have acknowledged the MCD calculated as $1.5h$, but in general, 1.5 times the overall depth of the web was adopted. Macdonald et al. [55] and Macdonald and Heiyantuduwa [56] did not specify the calculation of MCD but opted for a standardized specimen length of 600 mm across all one-flange loading tests. The height of the web measured by the flat portion is ranging from 69.2 to 101.0 mm and internal radius value is ranging between 1.25 and 4.5 mm, which is deemed to satisfy the MCD calculated by AISI S909-17. For testing sections with sloped webs, Wu et al. adapted AISI's minimum length criteria but with certain modifications to exceed the minimum required distance in their specimens to ensure the validity of each one-flange loading condition was maintained.

Considering the critical role of rounded corners in the load transfer within the plastic mechanism model, the conventional practice of using only the flat portion of the web (h) to calculate the MCD for OF loading cases is reassessed. This approach has been refined to incorporate the entire web, including the rounded corners, acknowledging their contribution to the overall structural integrity. Thus, the MCD is recalculated based on 1.5 times the full height of the web (H), where H spans from the rotation centre at the top rounded corner to the rotation centre at the bottom rounded corner. The rotation centre of a rounded corner is identified as the point where the central lines of the web and flange converge.

For experimental studies, specimen lengths were carefully chosen to exceed the MCD defined by AISI S909-17 and further discussions, thereby ensuring the authenticity of OF loading conditions while providing allowances for experimental variances. A subsequent parametric study validated this approach by recalculating web crippling capacities considering the MCD.

A comprehensive parametric study was undertaken on hat sections to assess the impact of specimen length under IOF-F loading cases. This investigation was structured around three distinct series to explore the influence of MCD and overall specimen length:

- 1.5h method - MCD calculated as specified in AISI S909-17, given as $1.5h$.
- 1.5H method - MCD calculated by newly proposed method, given as $1.5H$.
- A fixed length of 600 mm for all tests.

For the first two series, the specimen length was derived from adding twice the MCD to the sum of the middle and end bearing lengths. Using a hat section denoted as H120-RIN3-DEG0 with 50 mm bearing plates as an exemplar, the specimen length based on the AISI S909-17 method equates to $2 \times 50 + 1 \times 50 + 2 \times 1.5 \times (120 - 4.5 \times 2) = 483\ mm$. Conversely, the specimen length utilising the newly proposed MCD method calculates to $2 \times 50 + 1 \times 50 + 2 \times 1.5 \times 120 = 510\ mm$.

For each set of the hat sections, the internal corner radius is ranging from 3 mm to 8 mm at 1 mm increment. The L-D curves are presented as below.

Figure 115 shows a comparison of the Load-Displacement (L-D) curves between the traditional 1.5h method (marked with "-F") and the newly proposed 1.5H (marked with "-H") method for determining the Minimum Clear Distance (MCD) in one-flange loading cases. Throughout the range of simulations conducted, the differences between the two methods are found to be minimal. However, the 1.5H method consistently yields slightly more conservative results. Given that there is a reasonable reason to use 1.5H method instead of the traditional 1.5h method, it is considered appropriate to adopt the 1.5H method as the standard for MCD calculation in these scenarios for further comparisons. The web crippling capacity comparison is presented in Table 20.

Figure 116 demonstrates a comparison of the Load-Displacement (L-D) curves between the newly proposed 1.5H method and the fixed length, examining the impact of extending specimen length on web crippling capacity. The results show a capacity decrease of 3.6% to 6.3% when the clear distance of the bearing plate is extended by 25% beyond the MCD. This extension provides ample allowance for mitigating errors due to manufacturing and assembly processes, with an average capacity reduction of less than 5%. Therefore, a conclusion can be drawn that the fixed length method used during the experimental study is validated as sufficiently accurate, provided that the clear distance between the edge of two bearing plate does not exceed 25% of the minimum clear distance. Thus, the data from the experimental study can be used for calibration without adjustment. The web crippling capacity comparison is presented in Table 21.

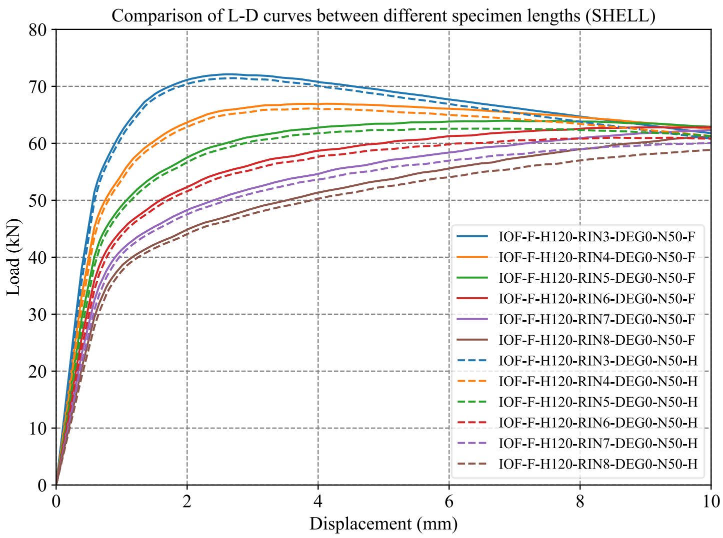

Figure 115 L-D curves comparison between 1.5h (solid) method and 1.5H method (dash)

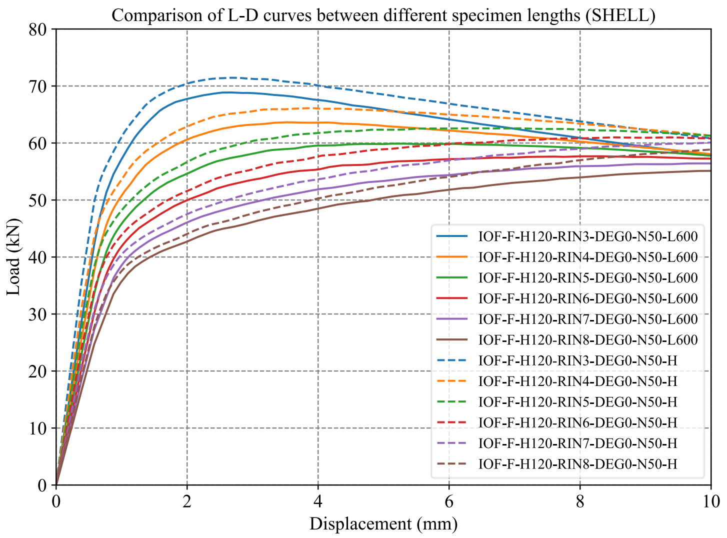

Figure 116 L-D curve comparison between 1.5H method (dash) and fix length method (solid)

Table 20 FEM result comparison between 1.5h (solid) method and 1.5H method (dash)

RIN	1.5h (mm)	P_h (kN)	1.5H (mm)	P_H (kN)	$1.5H/1.5h$	P_H/P_h
3	166.5	72.124	180	71.441	108.1%	99.1%
4	163.5	66.942	180	66.108	110.1%	98.8%
5	160.5	63.970	180	62.579	112.1%	97.8%
6	157.5	62.830	180	60.992	114.3%	97.1%
7	154.5	62.287	180	60.079	116.5%	96.5%
8	151.5	61.191	180	58.853	118.8%	96.2%

Table 21 FE result comparison between 1.5H method (dash) and fix length method (solid)

RIN	1.5H (mm)	P_H (kN)	CD (mm)	P_{FIX} (kN)	$CD/1.5H$	P_{FIX}/P_H
3	180	71.441	225	68.870	125.0%	96.4%
4	180	66.108	225	63.637	125.0%	96.3%
5	180	62.579	225	59.887	125.0%	95.7%
6	180	60.992	225	57.676	125.0%	94.6%
7	180	60.079	225	56.427	125.0%	93.9%
8	180	58.853	225	55.115	125.0%	93.6%

Simultaneously, H90 sections with internal corner radii (RIN) of 3 mm and 8 mm were modelled using similar settings to those previously described. For these sections, the specimen length determined by the 1.5H method is calculated as 420 mm, whereas for the fixed length method, the specimen length remains unchanged at 600 mm. Consequently, the clear distance for the fixed length method is calculated as 225 mm, which exceeds the Minimum Clear Distance (MCD) of 135 mm by 66.7%. This significant extension in length resulted in simulation outcomes indicating capacity losses of 11.7% for sections with a 3 mm internal corner radius and 16.7% for those with an 8 mm radius, respectively. Therefore, the experimental data for IOF-F loading cases with a specimen length of 600 mm may need to be considered overly conservative due to this observed capacity loss. The simulation result is demonstrated in Table 22.

Table 22 FE result comparison between 1.5H method and fix length method for H90 sections

RIN	1.5H (mm)	P_H (kN)	CD (mm)	P_{FIX} (kN)	CD/1.5H	P_{FIX}/P_H
3	135	71.815	225	63.418	166.7%	88.3%
8	135	57.879	225	48.241	166.7%	83.3%

Note: CD is the abbreviation of “Clear Distance”.

5.4 CONCLUSION

This chapter presents an in-depth analysis of the modelling techniques employed for simulating hat sections under localised loading conditions using ABAQUS, as part of the numerical investigation. It compares current modelling approaches to previous studies, detailing the process and rationale behind the chosen methods. A significant portion of the chapter is dedicated to a comprehensive parametric study, aimed at explaining the relationship between dimensional variations of hat sections and their web crippling capacity. Additionally, an investigation into the appropriate specimen length for testing is included, offering insights into how specimen dimensions influence experimental and simulation results. The main finding is listed as follows.

1. The implicit static (IS) approach has been successfully employed for numerical analyses related to web crippling studies. This method stands out from the more commonly used quasi-static or explicit dynamic approaches by offering a simpler modelling process while still delivering accurate predictions. Unlike the extension controls required for quasi-static and explicit dynamic methods, the implicit static approach simplifies the process by utilising automatic stabilization, thereby simplifying the modelling procedure.

2. Solid elements were introduced for the first time in web crippling analyses of thin-walled structures. Comparative analysis between solid and shell element simulations revealed that solid elements provide superior predictive accuracy, particularly for stockier sections and those with sloped webs. Shell element simulations consistently produced results approximately 10% above experimental values across various loading cases, indicating overestimated predictions. However, shell elements remain viable for slender sections with vertical webs, supported by evidence based on FE simulations on previous study, and for behavioural analyses in numerical simulations where computational resources are constrained.
3. A refined approach for calculating the Minimum Clear Distance (MCD) in one-flange (OF) loading cases has been proposed. This method acknowledges the crucial role of rounded corners in contributing to the web crippling capacity of hat sections. By incorporating the entire height of the web, this approach offers a uniform methodology applicable across sections with same web height but different rounded corner radii and sloping angles.

Chapter 6 Plastic mechanism models and preliminary DSM design

6.1 INTRODUCTION

The thesis has described an extensive range of experimental studies to investigate the yielding and plastic mechanism formation of different hat section configurations. These experimental efforts are thoroughly detailed in Chapter 4. To complement this exploration, corresponding numerical models have been created, providing a deeper understanding of the yielding and plastic mechanism formation behaviours, with a detailed discussion presented in Chapter 5.

Building upon the findings from these experiments and numerical analyses, as well as the buckling load calculations outlined in Chapter 3, a comprehensive plastic mechanism model has been developed. This model is based on the observed plastic mechanisms, offering a systematic approach to predicting and understanding the structural responses of hat sections under various loading conditions.

6.2 THE DEVELOPMENT OF PLASTIC MECHANISM MODEL

General plastic mechanism models are proposed based on the yielding behaviour and plastic mechanism formation observed from experiments and various FEM simulation models in Chapters 4 and 5. These general plastic mechanism models can be used for the 4 different load cases provided that different parameters are selected for the length and location of the hinge lines.

The development of a general plastic mechanism model begins with a discussion of vertical web sections under two-flange (TF) loading cases. This initial model serves as the foundation for further analysis. Following this, the model is refined and adapted to address one-flange (OF) loading cases, demonstrating the versatility and adaptability of the approach. The exploration then extends to include sloped web sections, leveraging the foundational principles defined for vertical web configurations.

6.2.1 General plastic mechanism model for vertical web sections (TF)

Figure 117 demonstrates the general plastic mechanism model for hat sections subjected to localised loading for the ITF-F and ETF-F loading cases where the "-F" refers to the fastening condition of the bottom flanges.

The proposed yield load P_y is given by

$$P_y = k_w F_{sw} \tag{6-1}$$

where

k_w is the number of webs in the section. For Hat sections, k_w = 2;

F_{SW} is the load calculated for a single web.

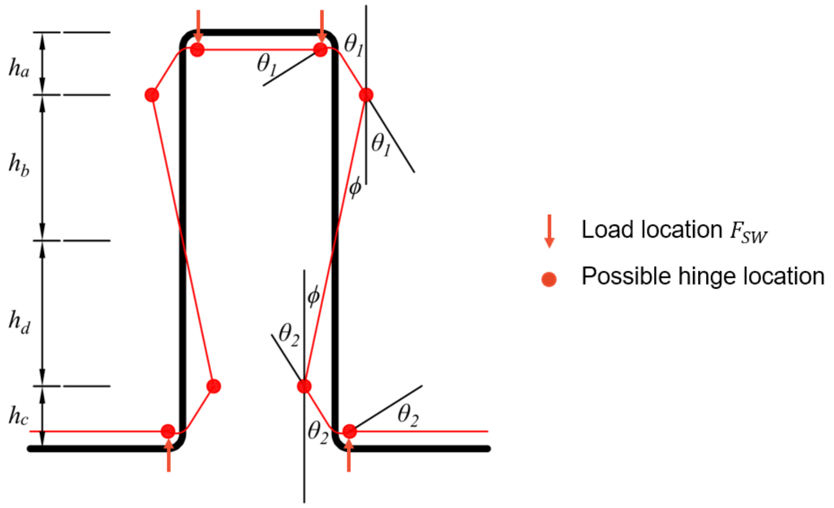

Figure 117 Plastic mechanism model for hat sections: ITF-F and ETF-F loading cases

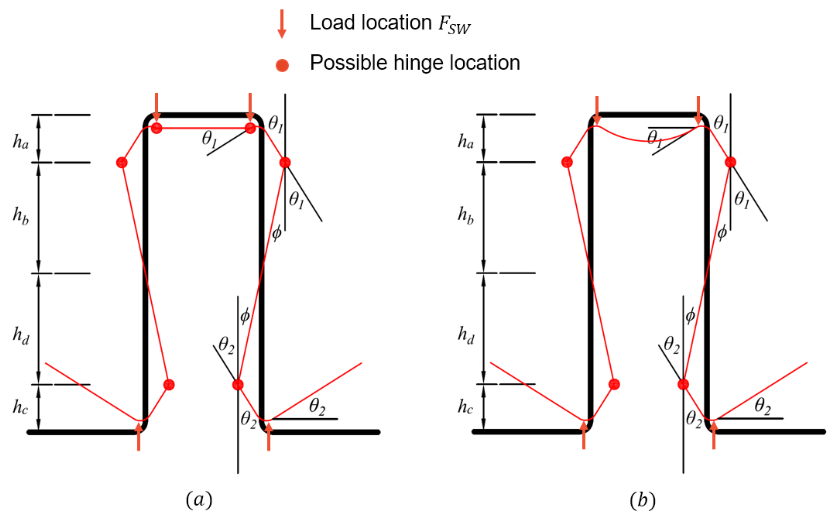

Figure 118 Plastic mechanism model for hat sections: ITF-UF and ETF-UF loading cases

For equilibrium using the virtual work principle, the external energy of the load acting on the loading plate must be equal to the internal plastic energy in the hinges. The energy equation for a single web can be therefore written as

$$F_{SW} \times (r_c\theta_1 + r_c\theta_2) = M_p \times \sum_{i=1}^{n} \omega_i L_i \quad (6\text{-}2)$$

$$M_p = \frac{f_y t^2}{4} \quad (6\text{-}3)$$

where the summation n is taken over a single web and

θ_1 is the rotation for the top corner.

θ_2 is the rotation of the bottom corner.

ω_i is the rotation angle at each plastic hinge.

M_p is the plastic moment per unit length of plate.

L_i is the length of each yield line, which is discussed in detail in the next section.

r_c is the centreline corner radius. The calculation of r_c is given as $r_c = r_{in} + 0.5t = r_{ext} - 0.5t$, where r_{in} is the inside corner radius, r_{ext} is the external corner radius and t is the thickness of the section.

Thus F_{SW} can be rewritten as

$$F_{SW} = \frac{M_p}{(\theta_1 r_c + \theta_2 r_c)} \times \sum_{i=1}^{n} \omega_i L_i \quad (6\text{-}4)$$

The plastic energy for each hinge is determined by two values: the rotation angle of the hinge and the yield line length.

Similarly, for the ITF-UF and ETF-UF loading cases, the general plastic mechanism model is demonstrated in Figure 118, where the "-UF" refers to the unfastened condition.

6.2.1.1 The hinge location and rotation angles

For a single web, four plastic hinges are defined with rotation angles as $\omega_1, \omega_2, \omega_3$ and ω_4 respectively. From the top to the bottom, ω_i $(i = 1,2,3,4)$ are calculated as follows:

$$\omega_1 = \theta_1 \quad (6\text{-}5)$$

$$\omega_2 = \theta_1 + \phi \quad (6\text{-}6)$$

$$\omega_3 = \theta_2 + \phi \quad (6\text{-}7)$$

$$\omega_4 = \theta_2 \tag{6-8}$$

$$\phi = \frac{\theta_1 h_a + \theta_2 h_c}{h_b + h_d} \tag{6-9}$$

Where $h_a, h_b, h_c \; and \; h_d$ are the heights given in Figure 117.

Thus, F_{sw} can be rewritten as

$$F_{SW} = \frac{M_p}{(\theta_1 r_c + \theta_2 r_c)} \times [\theta_1 \times L_{TF} + \theta_2 \times L_{BF}$$

$$+(\theta_1 + \phi) \times L_{TW} + (\theta_2 + \phi) \times L_{BW}] \tag{6-10}$$

L_{TF} and L_{BF} are the length of the yield lines in the top and bottom flanges respectively as shown in Figure 119.

L_{TW} and L_{BW} are the length of the yield lines in the top and bottom of the web respectively as shown in Figure 119.

In order to simplify the plastic mechanism model, for two flange loading cases, the assumptions listed below are based on observations from the FE model:

- The hinge locations on the webs are symmetrical between the top and bottom. Thus,

$$h_a = h_d, h_b = h_c, h_a + h_c = H/2 \tag{6-11}$$

- The rotation angle at the top and bottom of the web are identical. Thus,

$$\theta = \theta_1 = \theta_2 \tag{6-12}$$

Consequently,

$$\omega_1 = \omega_4 = \theta_1 = \theta \tag{6-13}$$

$$\omega_2 = \omega_3 = \theta_1 \times \left(1 + \frac{h_a}{h_b}\right) = \theta\left(1 + \frac{h_a}{h_b}\right) \tag{6-14}$$

In this case, when the θ is a non-zero value, the θ value can be eliminated using the equations listed above. Thus, k_θ and k_{ω_i} are introduced as two factors and for a hat section subject to TF loading case, the general equation for the capacity of a single web for hat sections under localised loading is given as

$$F_{SW} = \frac{M_p}{k_\theta r_c} \times \sum_{i=1}^{n} k_{\omega_i} L_i \tag{6-15}$$

where

k_θ is a factor for the number of loaded flanges, for two-flange loading cases, $k_\theta = 2$; and

k_{ω_i} is a factor representing the relative rotation angle at each plastic hinge. Table 26 with k_{ω_i} values for all loading cases is given at the end of this section for further calculation**.**

6.2.1.2 The length of the yield lines

A numerical FEM model and testing have been used for the determination of the yield line lengths L_{TF}, L_{BF}, L_{TW} and L_{BW}. The methodology for yield line length prediction is similar to the method proposed for tubular sections by Zhao and Hancock [57], which has been included in the Australian Standards AS4100 [58]. According to the assumptions in previous sections, the location of the yield lines on the top and bottom of the web are assumed to be symmetric about the half-height of the web and the length of the yield line is assumed to be identical between the top and the bottom. Thus, only L_{TF} and L_{TW} need to be calculated.

The length of the yield line on the top of flange (L_{TF}) and top of the web (L_{TW}) are calculated according to Equations:

$$L_{TF} = L_w + 2t \tag{6-16}$$

$$L_{CT} = L_{TF} + k_s \times k_{dc} \times r_c \tag{6-17}$$

$$L_{TW} = L_{CT} + k_s \times k_{dw} \times (h_a - r_c) \tag{6-18}$$

where

L_w is the bearing length of the bearing plate, also known as N;

L_{CT} is the length at the intersection between the top corner and the web;

k_s is the number of sides that has the diffusion, for interior loading cases $k_s = 2$ and for end loading cases, $k_s = 1$;

$k_{dc} = \frac{1}{\tan \gamma_1}$ where γ_1 is the diffusion angle in the corner as shown in Figure 119;

$k_{dw} = \frac{1}{\tan \gamma_2}$ where γ_2 is the diffusion angle in the corner as shown in Figure 119.

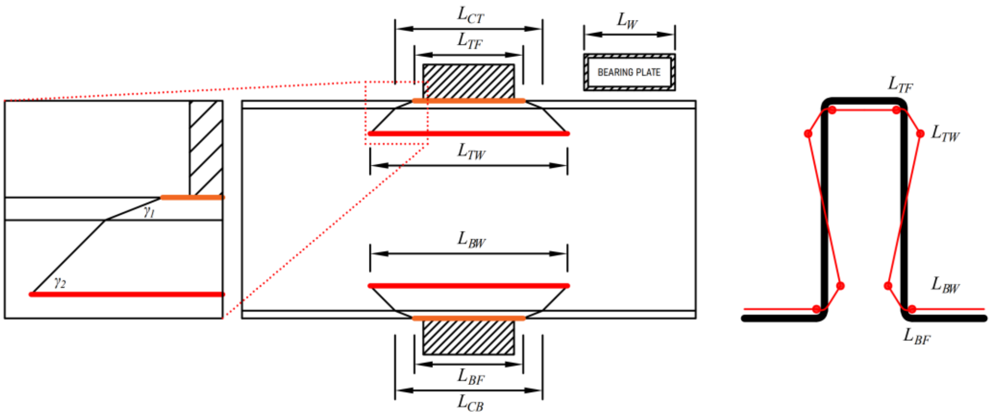

Figure 119 Side view of general plastic mechanism model and detail of the slope

6.2.1.3 *Summary of the exponent and factor for the Py model for TF loading cases*

The factors of the P_y models are based on the initial yield line locations before significant position shifting, also known as first yield location in accordance with observation from the verified FE analysis. A summary of the exponents and factors for the P_y model of the hat sections for both the TF fastened and unfastened loading cases is given in Table 23, where LC stands for loading cases and FC stands for the fastening condition.

Table 23 Summary of the exponents and factors for the Py model (TF)

LC	FC	k_θ	k_H	k_{dc}	k_{dw}	$\exists L_{TF}$	$\exists L_{TW}$	$\exists L_{BW}$	$\exists L_{BF}$
ITF	F	2	1/4	2.5	2	1	1	1	1
ETF	F	2	1/4	2.5	2	1	1	1	1
ITF	UF	2	1/4	2.5	2	1	1	1	0
ETF	UF	2	1/4	2.5	2	0	1	1	0

Note:
$\exists L_{TF}$ marks the existence of specific yield line noted as "1" and absence of specific yield line as "0".
k_H is equal to h_a/H or h_c/H.

For instance, in the case of ITF-F loading case, all four yield lines are present as detailed in Table 23. Consequently, the factors k_{ω_i} and L_i must account for all four yield lines. Similarly, when the section undergoes an ETF-UF loading case, only L_{TW} and L_{BW} are necessary according to Table 23. Therefore, the computation of F_{SW} should exclusively consider those yield lines that actually exist in the given loading case.

6.2.2 General plastic mechanism model for vertical web sections (OF)

The general equation for a single web of a hat section in one-flange loading cases is the same as that used for two-flange loading cases as shown in Equation (6-15). In this context, the factor for the number of loaded flanges, known as the coefficient $k_\theta = 1$ is assigned for one-flange loading cases, written as

$$F_{SW} = \frac{M_p}{1 \times r_c} \times \sum_{i=1}^{n} k_{\omega_i} L_i \tag{6-19}$$

It's important to recognise that depending on the specific loading conditions, certain yield lines present in the generic model may not manifest, leading to the obsolescence of some values within the generic framework. Based on the observation from the FE model, assumptions are made specifically for each of the OF loading cases for simplification.

6.2.2.1 The hinge location and rotation angles

For the OF loading cases, since the hat section is loaded from either the top flange or the bottom flanges, the yield lines are only formed near the loaded flanges as follows:

In the IOF loading case where the load is on the top flange,

$$h_a + h_b = H, h_c = h_d = 0, \theta_2 = 0 \tag{6-20}$$

In EOF loading case where the load is on the lips, regardless of the fastening condition,

$$h_c + h_d = H, h_a = h_b = 0, \theta_1 = 0 \tag{6-21}$$

Based on these simplifications and observations, the plastic mechanism models for the OF loading cases are redrawn as Figure 120 for IOF-F/UF loading cases, and Figure 121 for EOF-F and EOF-UF loading cases respectively. According to the availability of the yield lines and the h_a/H or h_c/H ratio, the k_{ω_i} value can be calculated accordingly.

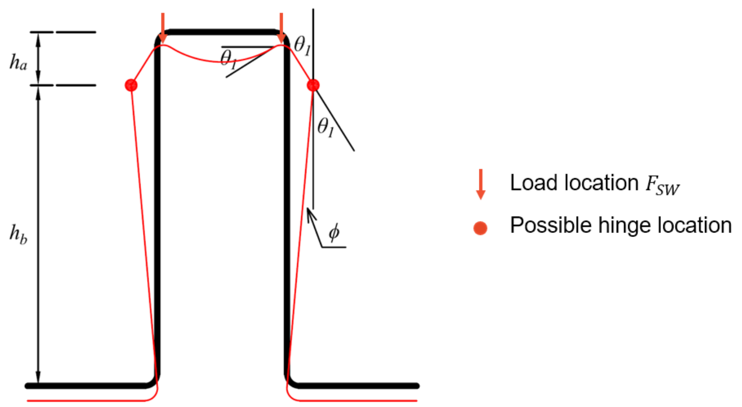

Figure 120 Plastic mechanism model for hat sections: IOF-F/UF loading cases

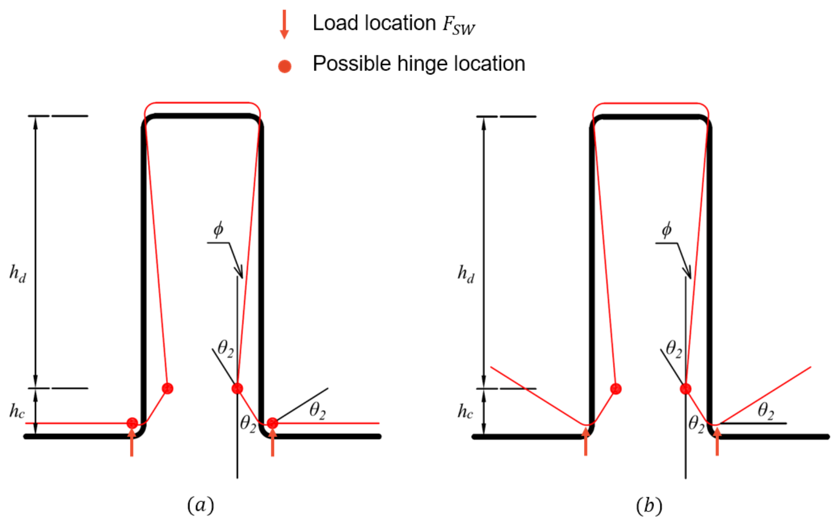

Figure 121 Plastic mechanism model for hat sections: EOF-F(a) and EOF-UF(b) loading cases

6.2.2.2 The length of the yield line

Similar to the Two Flange (TF) loading cases, the methodology for predicting yield line length is similar to the method proposed for tubular sections by Zhao and Hancock [59], which has been included in the Australian Standard AS4100[58].Using Figures 119 and 120 to guide the fastened cases, two yield lines need to be included in the yield load calculation, while only one yield line in the web needs to be considered for unfastened cases.

By taking the IOF-F loading case as an example and use the same symbol as Equations (6-16) to (6-18), the lengths of the yield line on the top of flange (L_{TF}) and top of the web (L_{TW}) are calculated with $k_s = 2$.

For the EOF-F loading case, using the Equations (6-16) to (6-18), the lengths of the yield line L_{BF} and L_{BW} are calculated by applying following changes: $k_s = 1$, and h_a is replaced by h_c, respectively.

6.2.2.3 Summary of the exponent and factor for the Py model for TF loading cases

Similar to the TF loading cases, a summary of the exponents and factors for the P_y model of the hat sections for both the OF fastened and unfastened loading cases is given in Table 24.

Table 24 Summary of the exponents and factors for the Py model (OF)

LC	FC	k_θ	k_H	k_{dc}	k_{dw}	$\exists L_{TF}$	$\exists L_{TW}$	$\exists L_{BW}$	$\exists L_{BF}$
IOF	F	2	1/3	2.5	2	0	1	0	0
EOF	F	2	1/3	2.5	2	0	0	1	1
IOF	UF	2	1/3	2.5	2	0	1	0	0
EOF	UF	2	1/3	2.5	2	0	0	1	0

Note:
$\exists L_{TF}$ marks the existence of specific yield line noted as "1" and absence of specific yield line as "0".
k_H is equal to h_a/H or h_c/H.

6.2.3 Special considerations

6.2.3.1 Amendments for sloped web sections

To accommodate sections with sloping webs, the basic P_y equation, which initially only accounts for sections with vertical webs, requires further modification. This adjustment is necessary because the eccentricity of the load—from the point of application to the centre of rotation—differs in sections with sloping webs compared to those with vertical webs.

Figure 122 demonstrate the relationship between eccentricity of the load (e), internal corner radius (r_{in}) and centreline corner radius (r_c). Noted that for sloping webs, the eccentricity e is less than the centreline corner radius. In this figure, Point O is assumed to be the rotation centre of the corner when vertical load is applied to point A. Thus,

$$\beta = \frac{180° - (90° + \alpha)}{2} = \frac{90° - \alpha}{2} \tag{6-22}$$

$$e = OA = OB = r_c \tan \beta \tag{6-23}$$

$$OA = OA' \approx OA'', OB = OB', OD = OD' \approx OD' \tag{6-24}$$

$$BD = OD - OB = a - r_c \tan \beta \tag{6-25}$$

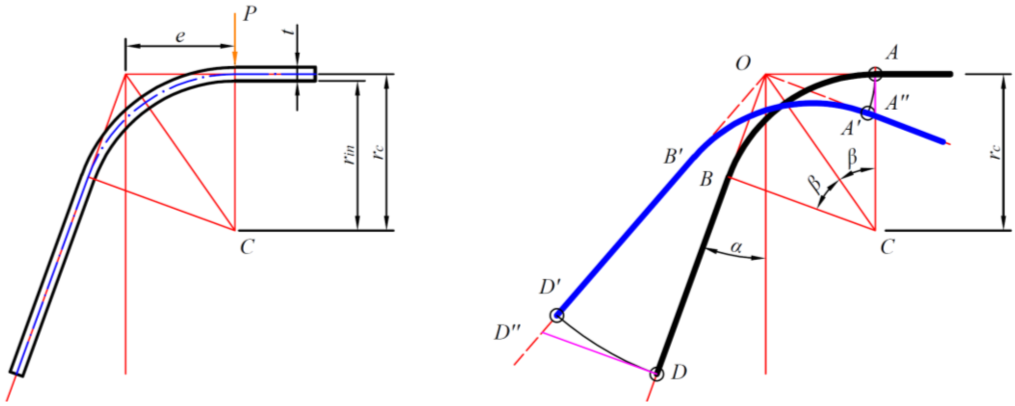

Figure 122 Eccentricity (e), internal corner radius (r_{in}) and centreline corner radius (r_c)

In conclusion, the P_y equation can be converted to accommodate the sloped web sections by replacing the $[r_c]$ with $[r_c \tan\beta]$. Thus, the energy equation for a single web can be rewritten as

$$F_{SW} \times (r_c \tan\beta \cdot \theta_1 + r_c \tan\beta \cdot \theta_2) = M_p \times \sum_{i=1}^{n} \omega_i L_i \tag{6-26}$$

The general F_{SW} equation can be rewritten as

$$F_{SW} = \frac{M_p}{k_\theta r_c \tan\beta} \times \sum_{i=1}^{n} k_{\omega_i} L_i \tag{6-27}$$

Incorporating adjustments for sloped web sections into the plastic mechanism model is crucial for accurately representing the dimensions of rounded corners and calculating load eccentricity. This adjustment underscores the importance of load eccentricity as a key factor influencing failure mechanism behaviour, rather than solely on the radius of the rounded corners.

For sections with vertical webs, the inclination angle (α) is typically zero hence $\tan 45° = 1$, leading to the eccentricity (e) coincides with the radius of the rounded corner (r_c). The dimension of the rounded corner is acknowledged by numerous researchers as a significant factor affecting web crippling behaviour, largely due to the fact that the majority of previously studied sections do not feature sloped webs. Consequently, earlier research often confuses the radius of the rounded corner with eccentricity and ignores the distinction between these two values.

In contrast, sections with sloped webs feature a non-zero α value. Consequently, the eccentricity of the load (e) should be less than r_c considering $\tan\beta < 1$. Therefore, when analysing the behaviour of sections with sloped webs, it becomes more critical to consider the value of e rather than r_c because the eccentricity of the load can truly reflect the actual behaviour for a sloped web section. Alternatively, regarding the non-dimensional value, the ratio of e/t should be used instead of r_c/t.

Noted that according to Equation (6-16) to (6-18), the length of the yield line is a function of r_c. As a result, these values need to be adjusted accordingly.

6.2.3.2 Reduction in the plastic moment capacity for axial compression

The research conducted by Zhao and Hancock [59,60] demonstrated that the plastic moment capacity of a yield line subjected to axial forces should be adjusted downwards to accurately reflect its reduced capacity under such conditions. As a result, a modified plastic moment capacity per unit length (M'_p) is used, incorporating the findings from Zhao and Hancock's study.

The basic formula for the plastic moment capacity per unit length, M_p, is:

$$M_p = \frac{f_y t^2}{4} \tag{6-28}$$

where:

f_y is the yield stress.

t is the thickness of the plate.

According to Zhao and Hancock, the plastic moment capacity considering an axial load P in the yield line, is modified to:

$$M'_p = \frac{f_y t^2}{4}\left[1 - \left(\frac{P}{f_y b t}\right)^2\right] \tag{6-29}$$

where:

P is the compressive load in the yield line.

b is the length corresponding to the relevant yield line.

This modification accounts for the reduction in moment capacity due to the axial load P. Thus, the equation based on the virtual work principle for a web subjected to localised loading can be written as:

$$F_{sw} k_\theta r_c \tan\beta = \sum_{i=1}^{4}\left(M'_{pi} k_{\omega_i} L_i\right) \tag{6-30}$$

where:

F_{SW} is the localised load per web.

k_θ is the flange loading factor.

r_c is the radius at the centreline of the rounded corner.

k_{ω_i} is the rotation factor for each yield line segment L_i.

By substituting M'_p from equation (6-29) into the virtual work principle:

$$F_{SW}\frac{k_\theta r_c \tan\beta}{M_p} = \sum_{i=1}^{4}\left[k_{\omega_i}L_i - k_{\omega_i}L_i\left(\frac{P_i}{f_y L_i t}\right)^2\right] \quad (6\text{-}31)$$

Define:

$$C_1 = \frac{k_\theta r_c \tan\beta}{M_p} \quad (6\text{-}32)$$

$$C_2 = \frac{1}{f_y^2 t^2} \quad (6\text{-}33)$$

$$u_i = k_{\omega_i}L_i \quad (6\text{-}34)$$

Equation (6-31) can be rearranged as

$$F_{SW}C_1 = \sum_{i=1}^{4}\left[u_i - \frac{C_2 u_i}{L_i^2}P_i^2\right] \quad (6\text{-}35)$$

where:

P_i is the axial force corresponding to u_i.

Using ITF-F loading case as an example, L_1 to L_4 are corresponding to $L_{TF}, L_{TW}, L_{BW}, L_{BF}$ respectively. Thus, P_1 and P_4 are the loads on the flanges, while P_2 and P_3 are the loads on the web. According to the force decomposition rules,

$$P_1 = P_4 = F_{SW} \times \tan\alpha\,, P_2 = P_3 = F_{SW} \times \frac{1}{\cos\alpha} \quad (6\text{-}36)$$

Define $v_1 = v_4 = \tan\alpha$, $v_2 = v_3 = \frac{1}{\cos\alpha}$, the resulting equation is:

$$F_{SW}C_1 = \sum_{i=1}^{4}\left[u_i - C_2\frac{u_i v_i^2}{L_i^2}F_{SW}^2\right] \quad (6\text{-}37)$$

Or rearranged as

$$AF_{SW}^2 + BF_{SW} + C = 0 \quad (6\text{-}38)$$

where:

$$A = \sum_{i=1}^{4}\left[C_2\frac{u_i v_i^2}{L_i^2}\right] \quad (6\text{-}39)$$

$$B = C_1 \tag{6-40}$$

$$C = -\sum_{i=1}^{4}[u_i] \tag{6-41}$$

The F_{SW} with reduced plastic moment capacity included can be calculated by solving the quadratic equation and taking the positive root.

In order to speed up the solving of this quadratic equation, a specific calculation preparation order is recommended as below:

Step 1: Identify known factors: k_θ, k_{ω_i}

Step 2: Identify known dimensions: r_c, α, t, L_i

Step 3: Calculate constants: u_i, v_i, C_1, C_2

Step 4: Calculate coefficients: A, B, C.

Step 5: Solve the quadratic equation and keep the positive value as F_{SW}.

It’s worth noting that only the locations with yield lines should be included in the summation for A and C. For example, according to the P_y model, the EOF-F loading case does not have yield lines on the top half of the section. Consequently, only i=3 and 4 are required to calculate A and C in that case.

6.2.4 The recommendation of Py calculation process

A standardised calculation procedure is designed to offer engineers a clear and coherent guideline for calculations. The objective is to facilitate a more efficient and user-friendly approach to calculating plastic mechanism loads, thereby enhancing the overall efficiency and accuracy of engineering analyses. The key steps of the calculation are listed as below.

Step 1: Calculate the required dimensions and factors, including r_c, β, M_p and e, using the given dimensions of the cross section.

Step 2: Calculate the yield line lengths (L_i) and locations (h_a, h_b, h_d, h_c) based on the bearing length L_w and the factors listed as Table 25.

Step 3: Calculate the rotation factors (k_{ω_i}) based on the rotation angles (ω_i) using the geometry relation and the factors given in Table 25. Alternatively, find the k_{ω_i} based on the table calculated as Table 26.

Step 4: Following the specific calculation preparation order, calculate the plastic mechanism capacity for a single web (F_{SW}) by solving the quadratic equation based on the existence of yield line table listed as Table 27. In this table, "1" stands for the existence of the specific yield line and "0" mean the designated yield line does not exist in this loading case.

Table 25 Summary of the exponents and factors for the Py model – location and length factors

LC	FC	k_θ	k_H	k_{dc}	k_{dw}
ITF	F	2	1/4	2.5	2
ETF	F	2	1/4	2.5	2
ITF	UF	2	1/4	2.5	2
ETF	UF	2	1/4	2.5	2
IOF	F	1	1/3	2.5	2
EOF	F	1	1/3	2.5	2
IOF	UF	1	1/3	2.5	2
EOF	UF	1	1/3	2.5	2

Table 26 Summary of the exponents and factors for the Py model – rotation factors

LC	FC	k_{ω_1}	k_{ω_2}	k_{ω_3}	k_{ω_4}
ITF	F	1	2	2	1
ETF	F	1	2	2	1
ITF	UF	1	2	2	-
ETF	UF	-	2	2	-
IOF	F	-	1.5	-	-
EOF	F	-	-	1.5	1
IOF	UF	-	1.5	-	-
EOF	UF	-	-	1.5	-

Table 27 Summary of the exponents and factors for the Py model – yield line existence factors

LC	FC	$\exists\ L_1(L_{TF})$	$\exists\ L_2(L_{TW})$	$\exists\ L_3(L_{BW})$	$\exists\ L_4(L_{BF})$
ITF	F	1	1	1	1
ETF	F	1	1	1	1
ITF	UF	1	1	1	0
ETF	UF	0	1	1	0
IOF	F	0	1	0	0
EOF	F	0	0	1	1
IOF	UF	0	1	0	0
EOF	UF	0	0	1	0

Note: $\exists\ L_1(L_{TF})$ means "there exists L_1 which is also known as L_{TF}".

6.3 THE PRELIMINARY PROPOSAL OF DSM DESIGN EQUATIONS

A preliminary version of Direct Strength Method (DSM) design equation has been developed, deviating from the standard format originally proposed by Glauz and Schafer. This new equation incorporates adjustments guided by a selected collection of the experimental data from Chen and Wu, particularly in the selection of constants. The primary objective of this preliminary proposition is to offer insights into the DSM design curve for localised loading using the new and consistent format.

It is worth noting that this preliminary design equation aims to use a single Direct Strength Method (DSM) design curve to estimate the web crippling capacity for each loading case that has been tested by Chen so far. Santaputra's test data were not included in this initial analysis, mainly for two reasons. Firstly, the ITF-UF, ETF-UF, and IOF-UF loading cases tested by Santaputra were not considered as practical loading scenarios for certain cross-section profiles. Secondly, most of Santaputra's test specimens did not fall within the small corner radius range. Similarly, the large corner radius range data from Wu's IOF and EOF loading cases were excluded at this initial stage of the analysis. These data are to be included in the enhancement of the DSM design equation section in Chapter 7.

Given that there is no experimental data available for the EOF-F loading cases, sections from Wu's EOF-UF tests have been selected for performing finite element method (FEM) simulations under the EOF-F loading cases. The results from these simulations have been included for the purpose of anchoring the DSM design curve in the high slenderness region.

The basic format of the equation is written as

$$\frac{P_n}{P_y} = k_p \frac{1+a\lambda^c}{1+b\lambda^d} \tag{6-42}$$

where

P_n is the nominal load capacity for localised loading;

P_y is the yield load, calculated with the plastic mechanism model proposed in this chapter;

λ is the slenderness, calculated using following equation:

$$\lambda = \sqrt{P_y/P_{cr}} \quad (6\text{-}43)$$

where

P_{cr} is the buckling load, calculated with the programme THIN-WALL-PYTHON, which has been introduced in Chapter 3 in detail.

The DSM design equation coefficients are carefully selected to alter the curve to approach the data point from the conservative side. A summary of the factors and exponents a, b, c, d and k_p is listed as shown in Table 28.

Table 28 A summary of the exponent of DSM design equations (preliminary)

LC	FC	a	b	c	d	k_p
ITF	F	0.14	1.50	2	2	1
ETF	F	0.08	1.68	2	2	1
IOF	F	0.14	1.50	2	2	1
EOF	F	0.12	2.28	2	2	1
EOF	UF	0.12	1.60	2	2	1

6.4 INITIAL FINDINGS FROM THE PRELIMINARY DSM DESIGN EQUATIONS

6.4.1 The conservative prediction outcome for large e/t sections

Figures 123 - 125 demonstrate the preliminary DSM design equation against the experimental and numerical data. According to these figures, regardless of the loading cases, the data for the smaller (3 mm) corner radius sections show good alignment with the DSM design curve predictions. In contrast, the predictions for the larger (8 mm) corner radius sections using the DSM curves appear to be more conservative.

Similar trends can also be observed for the channel sections according to Nguyen, Hancock and Pham [28] as shown in Figure 126 marked by the orange dash line. In previous research focused on channel sections, these discrepancies were considered as variations or errors, leading to no adjustments being made at that time.

Given this consistent trend, it is imperative to recognize these behaviours as a phenomenon rather than mere variable discrepancies. Consequently, this issue requires proper examination and justification to ensure the DSM design curves provide accurate prediction and further discussed in Chapter 7.

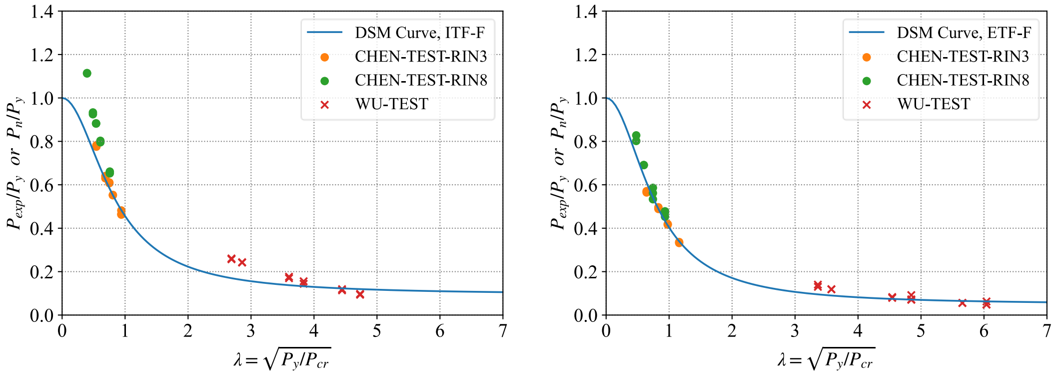

Figure 123 Preliminary DSM curve for hat sections, ITF fastened (L) and ETF fastened (R)

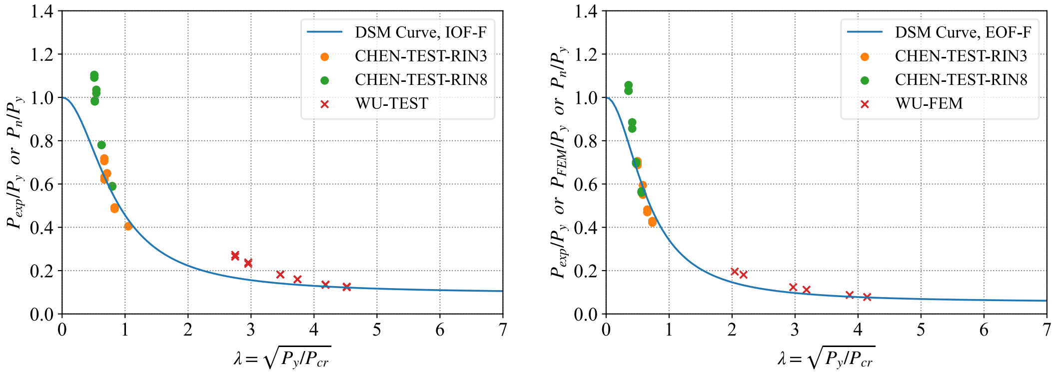

Figure 124 Preliminary DSM curve for hat sections, IOF fastened (L) and EOF fastened (R)

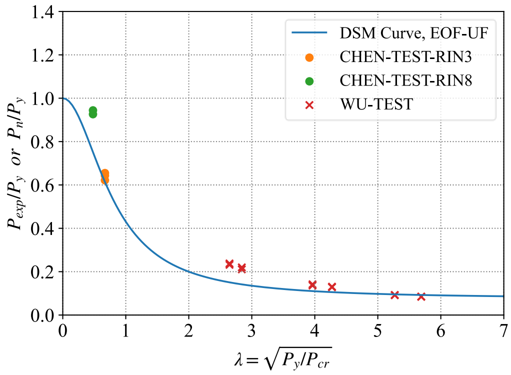

Figure 125 Preliminary DSM curve for hat sections, EOF unfastened

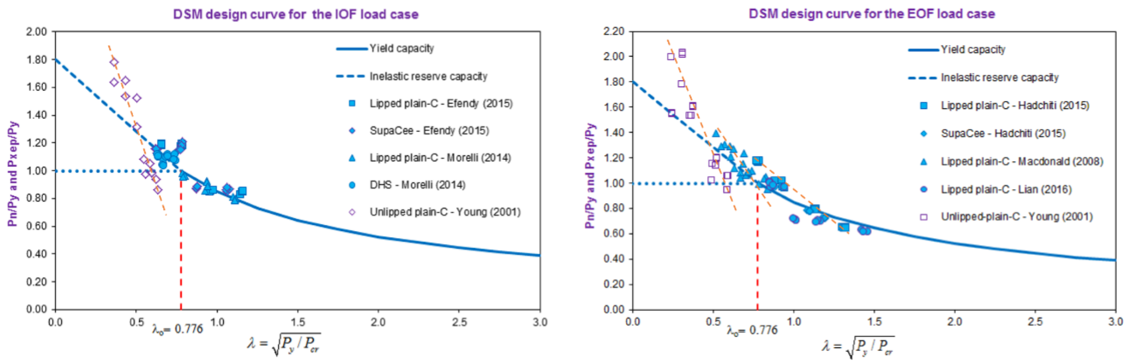

Figure 126 DSM curve for the IOF and EOF loading cases for C sections from Nguyen et al.[28]

6.4.2 Possible explanations

Given that the preliminary DSM proposal is consistently demonstrating a good alignment with the section failing by yield-arc mechanism but conservative for the sections failed by rolling mechanism, the possible explanation for the conservative prediction in the large corner radius sections is most likely due to the difference in failure modes.

Bakker and Stark [9] have observed two types of web crippling failure modes for hat section: yield arc mechanism and rolling mechanism from short span three-point bending tests as shown in Figure 127. Their research revealed that the specific mechanism leading to failure is determined by the corner radius: yield arc mechanism is commonly seen on small corner radii sections, whereas rolling mechanism is commonly seen on large corner radii sections. These two mechanisms can be differentiated by the method through which web deformation is enabled. For the yield arc mechanism, the web deformation is enabled by the formation of a yield arc. For the rolling mechanism, the web deformation is enabled by the rolling down of the corner radius through the web.

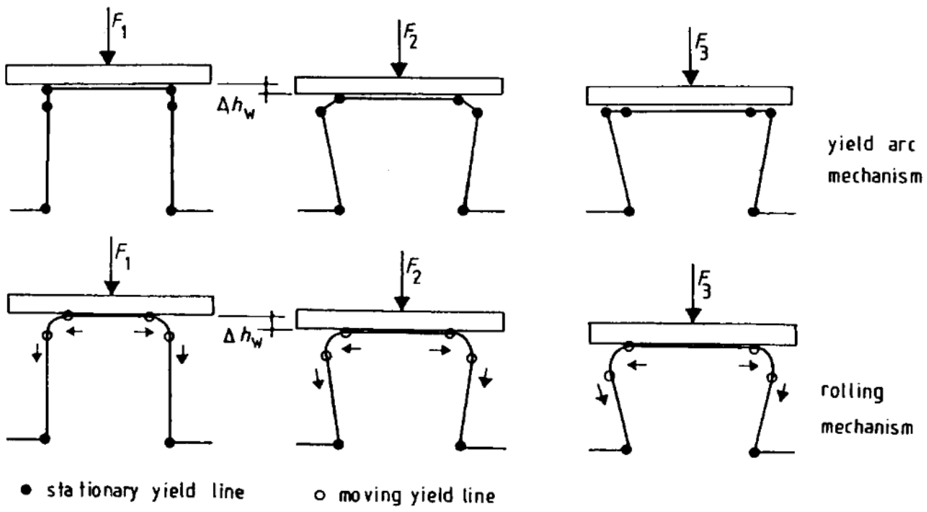

Figure 127 Yield arc mechanism and rolling mechanism defined by Bakker and Stark [9] (Same as Figures 2 and 3)

While the number and the initial location of the yield lines are similar, the key difference between these two mechanisms is whether the yield lines are in a stationary position as the loading continues. In the case of the yield arc mechanism, the yield lines are established and maintain a fixed position throughout the loading process before the load reaches to the localised loading capacity. Conversely, in the rolling mechanism, the yield lines in the vicinity of the loaded flanges exhibit movement.

As discussed in Section 6.2, the plastic mechanism was developed based on the status that first yield occurred in the web, as in the suggestion given by Bakker and Stark stating that the design rules should be based on the mechanism initiation load instead of the ultimate load. At that point, the maximum bending moment locations which coincide with the maximum horizontal displacement points (MHDP) start to shift away from the initial position (¼H for two flange loading cases or ⅓H for one flange loading cases where H is the height of the web), indicating the occurrence of significant mechanism change. A verified FE model is used to demonstrate the change of the mechanism as shown in Figure 128, where the mechanism initiation stage is in the transition between the first and the second image.

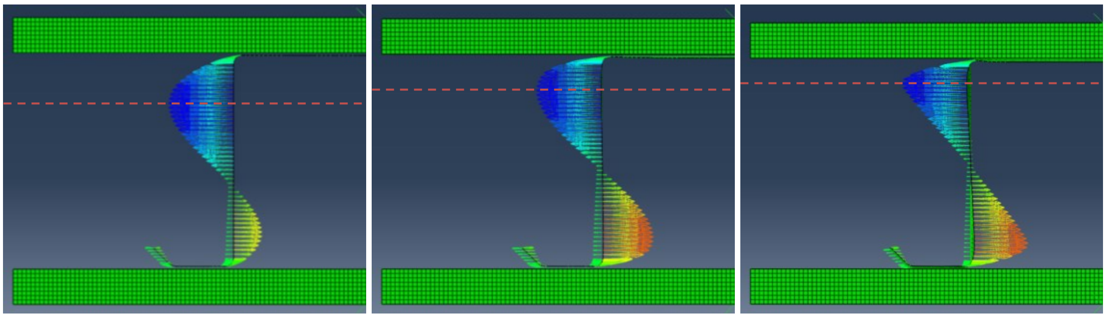

Figure 128 The movement of the maximum horizontal displacement points on the webs as the loading process continues

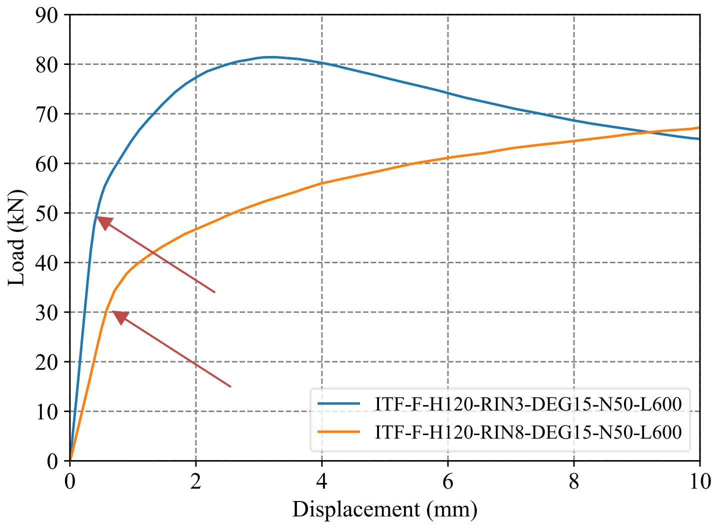

Figure 129 Typical L-D curve for small-radius and large-radius sections in ITF load case

In addition to the failure mechanism behaviours, the mechanism initiation can be observed form the L-D curve. Figure 129 presents two L-D curves for hat-shaped sections subjected to the ITF-F loading cases, differing in their rounded corner radii. In this figure, the section with a smaller corner radius, which exhibits a typical yield-arc failure mechanism, is plotted in blue. In contrast, the section with a larger corner radius is represented by the curve plotted in orange.

The initial load at which the mechanism begins for the smaller corner radius section is approximately 55 kN, whereas for the rolling mechanism, it starts at 35 kN as demonstrated by the arrows. From the initiation load to the ultimate load capacity, the increase for the section with a small corner radius is about 45% (from 55 to 80 kN), whereas for the section with a large corner radius, the ultimate capacity nearly doubles (from 35 to 65 kN). This observation suggests that sections with larger corner radii are likely to exhibit a significant increase in loading capacity during the rolling mechanism phase following mechanism initiation. Consequently, relying solely on the mechanism initiation state to calculate P_y might not fully account for the capacity contributed by the rolling mechanism.

Furthermore, a phenomenon is observed during the rolling mechanism process and might be associated with the increasing of localised loading capacity. Figure 130 displays the detailed view of a rounded corner undergoing a typical rolling mechanism. In this illustration produced by an FEM analysis, the load is applied to the specimen through a bearing plate, coloured in grey. Initially, before the application of any load, the contact point between the bearing plate and the specimen is conventionally recognized as the junction between the top flange and the rounded corner, identified as Point A. As the loading progresses, this contact point shifts from Point A towards Point B, moving leftward relative to its original position. This shift results in a decrease in eccentricity, which may also contribute to the observed increase in localised loading capacity.

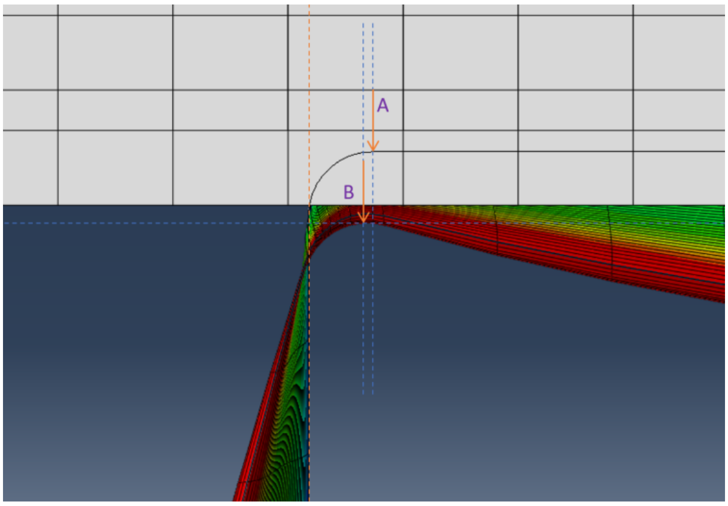

Figure 130 A typical rolling mechanism, the contact point (action point) is moving from A to B towards the orange dash line

6.5 CONCLUSION

A plastic mechanism model has been developed to predict the localised loading capacity based on the initiation of the hinge mechanism before significant change of the hinge position. This new yield load (P_y) equation successfully provides a consistent calculation model across all loading cases, but also extends the support to hat sections featuring both vertical and sloped webs. This equation incorporates adjustments for plastic moment capacity reduction due to axial load, enhancing load capacity prediction accuracy.

A preliminary version of DSM design equations has been developed based on the standard format originally proposed by Glauz and Schafer in recent years. This new set of DSM design equation provide strong supports for the new format regarding the localised loading capacity calculation for the first time.

As this study represents the first development of DSM design equations for hat sections under localised loading, no existing benchmark exists for direct yield load (P_y) comparison. Within the DSM framework, after validating critical buckling load (P_{cr}) values, the yield load (P_y) serves as the primary input parameter. The yield load (P_y) calculation accuracy was evaluated through a holistic approach examining relationships between non-dimensional values, including slenderness ratio (λ), experimental-to-yield load ratio (P_{exp}/P_y), and nominal-to-yield strength ratio (P_n/P_y). The plastic mechanism model demonstrates reliable prediction capabilities for both failure mechanisms.

By comparing the prediction result against the ultimate loading capacity from the experimental study, it's deemed accurate for sections failing by the yield arc mechanism but conservative for sections failing from the rolling mechanism.

For the sections failing by yield arc mechanism, the prediction of localised loading capacity is close to the ultimate loading capacity from the tests because the maximum load is recorded soon after the initiation of the hinge mechanism. This is not the case for the sections failing by the rolling mechanism. The conservatism is due to the capacity development difference between the rolling and yield arc mechanisms.

A few reasons listed below have contributed to the development of capacity for rolling-mechanism failure:

- It is easier to reach to the initiation of mechanism for larger corner radii sections because the initiation load is lower.
- The development of the capacity for rolling-mechanism failure requires continuous movement of yield lines.
- The eccentricity of the load to the web reduces during the loading process, which results in loading capacity increasing.

A hypothesis is made that there is a transition between the yield arc mechanism and the rolling mechanism when the corner radii of the section drop in between. A solution by combining the results from both mechanisms might be plausible, but the calculation process might be complex and lengthy, which does not suit the need for use by engineers.

As a practical alternative, a simplified method for facilitating this issue is proposed by using multiple DSM curves to facilitate the sections with various e/t values in the following Chapter 7.

This page intentionally left blank.

Chapter 7 Advanced DSM design equations for hat sections under localised loading

7.1 INTRODUCTION

The main objective of this chapter is to develop new DSM design curves for localised loading of hat sections.

In the previous chapter, the significance of the difference in the strength between failures by the yield arc mechanism and rolling mechanism which is dependent on the corner radius and hence the loading eccentricity which governs the e/t ratio was emphasized, highlighting the need to develop DSM curves based on this value in addition to the non-dimensional slenderness. This chapter presents an extensive parametric study using varied data sources to facilitate e/t value variations. Figure 131 demonstrates the relationship between eccentricity of the load (e), internal corner radius (r_{in}) and centreline corner radius (r_c), noting that for sloping webs, the eccentricity e is less than the centreline corner radius.

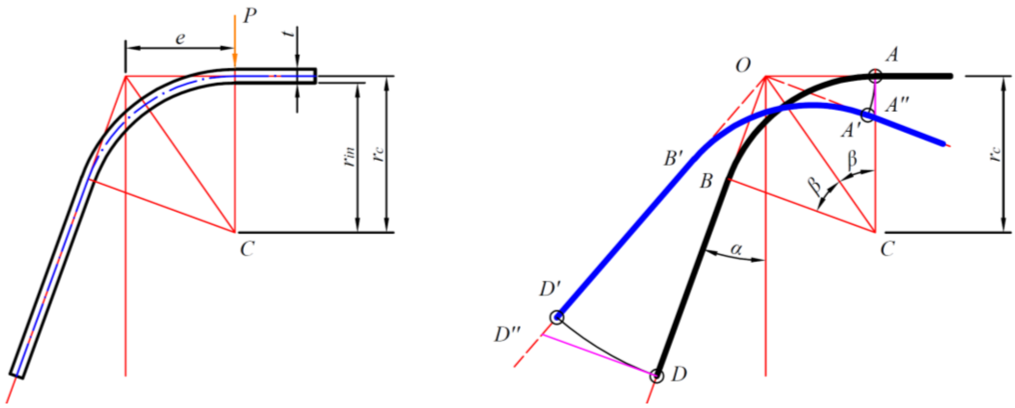

Figure 131 Relation between eccentricity (e), internal corner radius (r_{in}) and centreline corner radius (r_c) (Same as Figure 122)

This chapter is structured to provide a thorough exploration of the DSM design curves and their application. In Section 7.2, the chapter delves into a detailed discussion of the key findings derived from the DSM curves, with a particular focus on how they are differentiated by e/t values. Section 7.3 provides a comprehensive analysis of the process involved in selecting the appropriate DSM curves. This part of the chapter is essential for comprehending the criteria and considerations that guide the selection of DSM curves for different structural scenarios in a consistent manner. In Section 7.4, the chapter presents a comparison between the newly developed DSM design equations and the current standards as outlined in AS/NZS 4600:2018 [2] or its similar counterpart (only for localised loading), AISI S100-16 [1], published by the American Iron and Steel Institute. Note that AISI-S100 calls it "web crippling strength" and AS/NZS 4600 calls it "bearing capacity" even though the equations are the same. This comparative analysis is critical for evaluating the effectiveness and relevance of the new DSM equations in the context of existing structural design standards. Reliability analyses regarding the newly developed design equations are presented in Section 7.5. In addition, a demonstration example is included in Section 7.6.

The data groups used in the analysis include various experimental and numerical data. Table 29 describes all the data groups to be used in the analysis. All the numerical data are listed in Appendix G.

Table 29 Data groups with sources

Group ID	Strength (MPa)	Thickness (mm)	Element types or Test	Note
1	Various	Various	Test	All Experiments by Chen, Wu and Santaputra
2	323	3	Shell	Numerical analysis using ABAQUS
3 & 13	323	3	Solid	Numerical analysis using ABAQUS
4	323	Various	Shell	Numerical analysis (selected dimension)
6	323	3	Shell	Numerical analysis DEG varying
7	323	3	Solid	Numerical analysis DEG varying
8	717	0.7366	Shell	Numerical analysis using Wu's section
9	323	3	Solid	Numerical analysis RIN varying
11	717	0.7366	Shell	Wu's section under EOF-F loading case

Note: Groups 5, 10, and 12 have been omitted as they fall outside the scope of this discussion.

7.2 EXPLORATION OF THE DSM DESIGN EQUATION OPTIONS

7.2.1 Base curve selection criteria

As suggested in the preceding Chapter 6, the selection of coefficients for the DSM (Direct Strength Method) curves must also consider the influence of the e/t (load eccentricity/thickness) ratio. Table 30 outlines the calculation of the e/t values for Chen's specimens in Chapter 4 and later in a separated publication [36], incorporating several key parameters:

- RIN (internal corner radius in mm): This denotes the internal corner radius of the steel sections.

- DEG (degree): This represents the angle of the web's slope, measured from the vertical position.
- t (thickness in mm): This is the thickness of the steel sheeting.
- e (eccentricity in mm): This refers to the eccentricity of the load, specifically its distance from the rotation centre O at the corner.

Examples of the e/t values for Chen's tests in Chapter 4 which are crucial for the appropriate selection of DSM curve coefficients, are given in Table 30. In particular, RIN of 3 mm and 8 mm are used to demonstrate the effect on e/t.

Table 30 The calculation of the eccentricity and e/t of Chen's hat sections

RIN (mm)	DEG (degree)	t (mm)	e (mm)	e/t
3	30	3	2.598	0.866
3	15	3	3.453	1.151
3	0	3	4.500	1.500
8	30	3	5.485	1.828
8	15	3	7.290	2.430
8	0	3	9.500	3.167

In addition to the test data listed in Table 30 shown with triangle markers in Figure 132, the e/t values are also calculated with RIN ranging from 4 to 7 (included) and DEG ranging from 5 to 25 (included) with round markers. A selected range of parameters is used in the parametric studies. The full set of results are tabulated in Appendix D.

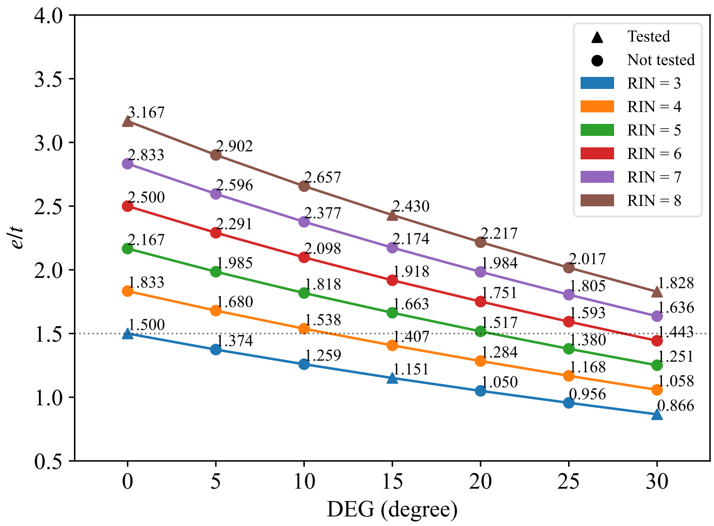

Figure 132 Relationship between e/t and RIN, DEG (t = 3 mm)

In the manufacture of cold-formed steel sections, the minimum internal corner radius typically equals the material thickness, leading to a minimum e/t (web depth-to-thickness) ratio of 1.5 for sections without a sloping web. However, for sections with sloping webs, this minimum e/t ratio can be reduced by increasing the slope of the web within a practical range. While sections with a lower e/t ratio generally demonstrate enhanced serviceability performance, characterised by achieving localised loading capacity with smaller displacement, it has been observed in the parametric studies that sections with an e/t ratio less than 1.5 do not exhibit a significant performance improvement compared to those with an e/t ratio of 1.5.

Additionally, there is a concern regarding potential cracking due to cold work in sections with smaller corner radii. This risk hinders the production of sections with very small e/t ratios. Given these considerations, it is reasonable to adopt the minimum internal corner radius with a 0-degree web angle as the reference point for the base curve in DSM (Direct Strength Method) designs. This approach balances the benefits of lower e/t ratios with the practical limitations of manufacturing and structural integrity. In the lower e/t ratio range, Chen's test results in Chapter 4 have been selected to control the DSM curves and hence give the lower bounds as discussed in Chapter 6. In the high slenderness range of the curve, the e/t value becomes insignificant on the strength due to the nature of the buckling effect. Wu's test results were selected to control the selection of the DSM curves in the high slenderness range as discussed in Chapter 6.

Considering the reasons listed above, the base e/t ratio is selected as 1.5. The base DSM equation coefficients, namely the preliminary version, were thus developed and the chosen values are given in Table 28 in Chapter 6.

7.2.2 Insight of DSM design curves

The general form of DSM equation by Glauz and Schafer [31,32] is written as

$$\frac{P_n}{P_y} = k_p \frac{1+a\lambda^c}{1+b\lambda^d} \tag{7-1}$$

where

P_n is the nominal load capacity for localised loading;

P_y is the yield load;

λ is the slenderness, calculated using following equation:

$$\lambda = \sqrt{P_y/P_{cr}} \tag{7-2}$$

where

P_{cr} is the buckling load.

The parameters k_p, a, b, c and d are selected coefficients and exponents.

In order to gain a comprehensive understanding of how the base design curve performs, the full set of experimental and finite element method (FEM) results from the parametric studies are systematically compared with the base Direct Strength Method (DSM) design curves developed in Chapter 6.

The comparison is conducted in two stages:

- Fastened loading cases only, as given in Section 7.2.2.1;
- Fastened loading cases together with unfastened experimental data, as given in Section 7.2.2.2.

7.2.2.1 Fastened loading cases

The full set of experimental and FEM results from the parametric studies are systematically compared with the base DSM design curves developed in Chapter 6. for the four distinct loading cases in Figures 133 to 136. The coefficients used in Equation (7-1) for the base curves are detailed in Table 31 and were derived in [61,62] and also listed in Table 28. Note that the full range of e/t values varying from <1.5 to >4.5 are included in Figures 133 to 136 and will be presented in the following Section 7.2.4.

It's worth noting that only fastened loading cases are included at this stage. The unfastened cases are discussed in the next section.

Table 31 The base DSM design equations coefficients for fastened cases

LC	FC	a	b	c	d	k_p
ITF	F	0.14	1.50	2	2	1
ETF	F	0.08	1.68	2	2	1
IOF	F	0.14	1.50	2	2	1
EOF	F	0.12	2.28	2	2	1

For each data point on these plots, the ratio P_{exp}/P_y (experimental load capacity to yield load) or P_{FEM}/P_y (numerical load capacity to yield load) is plotted on the Y-axis, while λ, representing the non-dimensional slenderness parameter, is plotted on the X-axis. The experimental and FEM data points in the DSM (Direct Strength Method) design curve comparisons are represented as follows:

- Experimental data points are plotted as solid dots '●'.
- FEM results using solid elements are plotted as solid triangles '▲'.
- FEM results using shell elements are plotted as '+'.

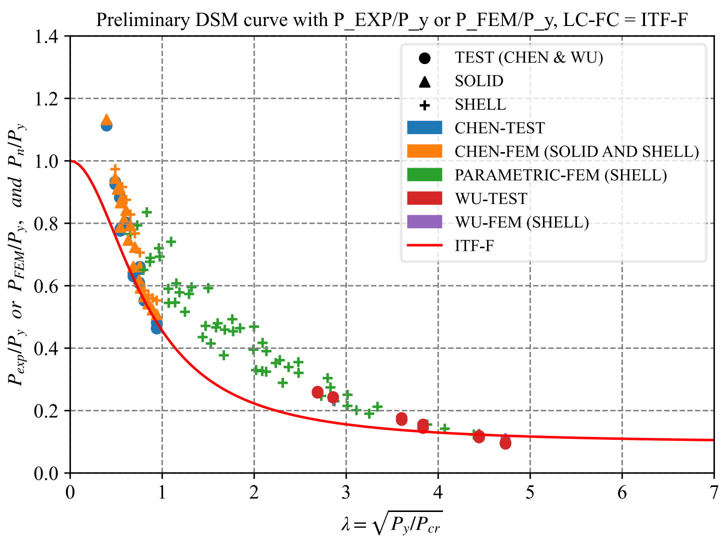

Figure 133 DSM design curve for the ITF-F loading case

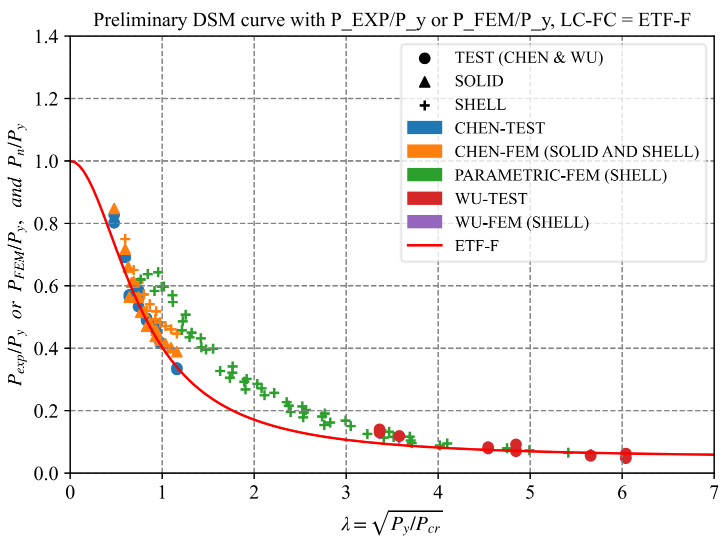

Figure 134 DSM design curve for the ETF-F loading case

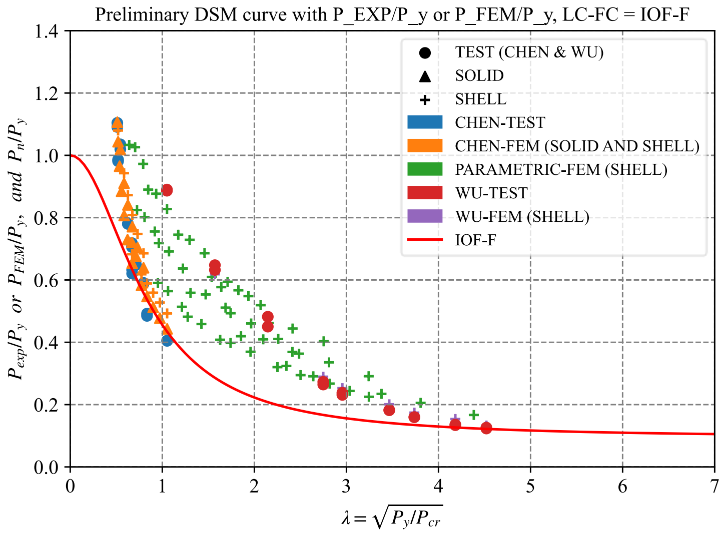

Figure 135 DSM design curve for the IOF-F loading case

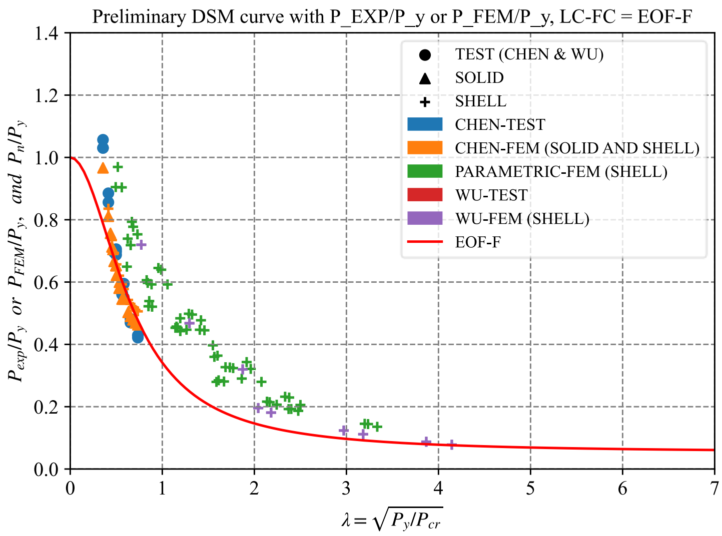

Figure 136 DSM design curve for the EOF-F loading case

It should be noted that in ITF-F and ETF-F loading cases, data points from WU-FEM (SHELL) demonstrate a good alignment with WU-TEST. Supplementary figures are provided in Appendix J for further elucidation.

7.2.2.2 *Unfastened loading cases*

The Santaputra test data in [15] related to unfastened loading cases are plotted in Figures 137 to 139, marked with 'x' symbols overlaid on the graphs previously shown in Figures 133 to 135. Figures 137 to 139 aim to provide a side-by-side comparison, highlighting differences between unfastened and fastened loading scenarios.

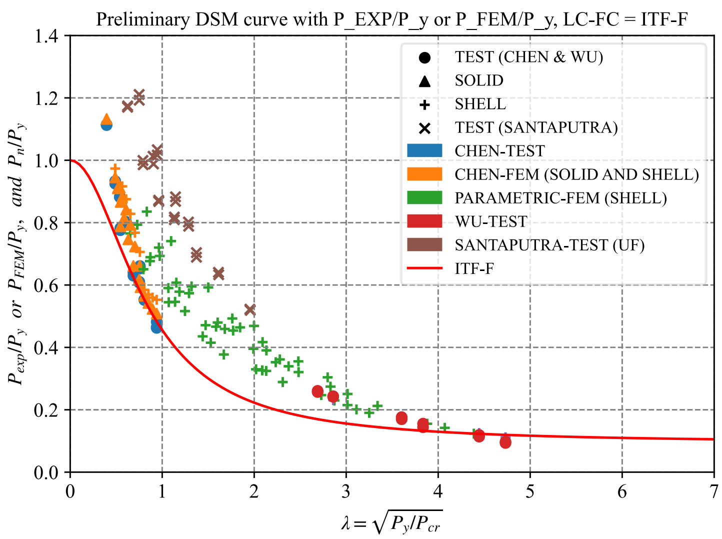

Figure 137 DSM design curve for the ITF-F loading case including ITF-UF test data

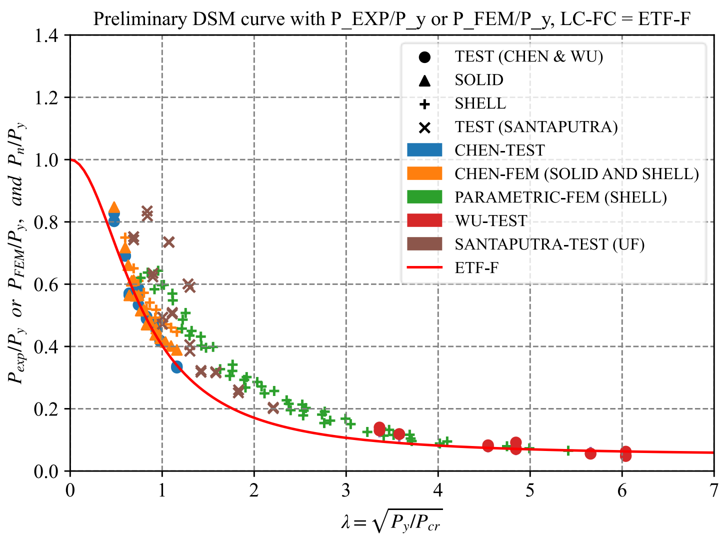

Figure 138 DSM design curve for the ETF-F loading case including ETF-UF test data

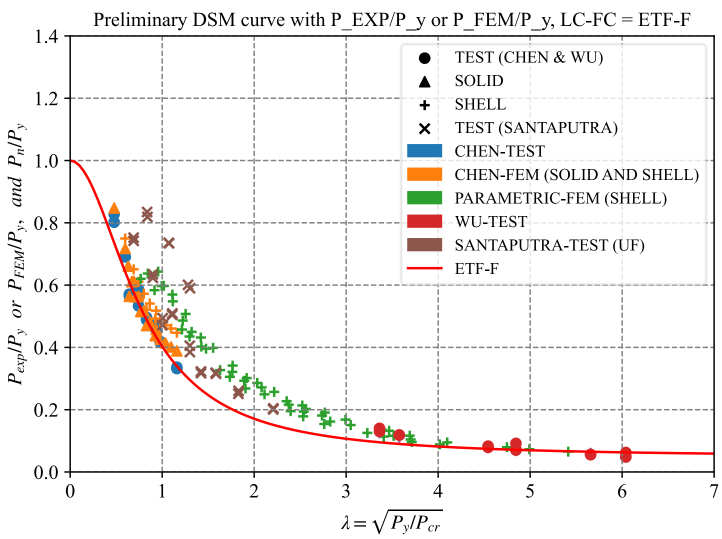

Figure 139 DSM design curve for the IOF-F loading case including IOF-UF test data

Specifically, Figure 140 is devoted exclusively to illustrating the EOF-UF loading case, displaying both shell and solid FEM simulations as well as the experimental from Chen, Wu and Santaputra's experimental studies under unfastened conditions. The DSM curve's parameters for EOF-UF case are slightly different from EOF-F case, as shown in Table 32.

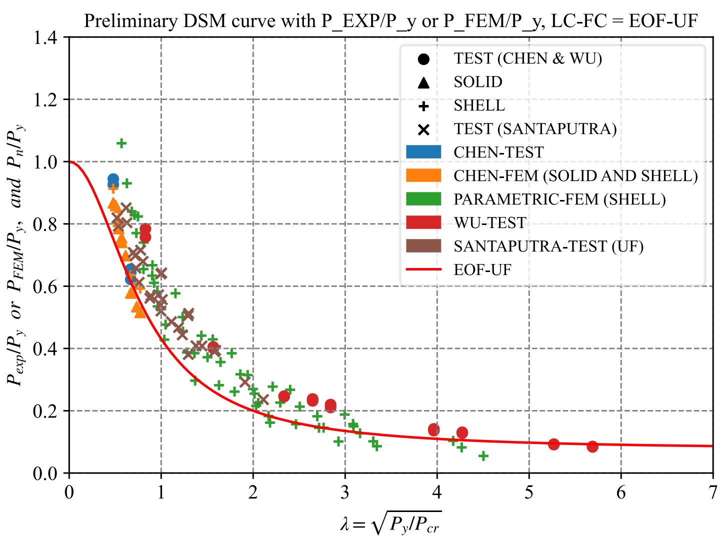

Figure 140 DSM design curve for the EOF-UF loading case including EOF-UF test data

Table 32 Comparison of the base DSM design equations coefficients between EOF-F and EOF-UF

LC	FC	a	b	c	d	k_p
EOF	F	0.12	2.28	2	2	1
EOF	UF	0.12	1.60	2	2	1

7.2.3 Discoveries from the DSM curves with datapoints

Based on the figures provided above, four major findings have been proposed regarding the application of the Direct Strength Method (DSM) in the design of hat sections under localised loading. These findings offer a valuable guidance for the Advanced DSM design equation selection specific to this chapter.

Uniformity: The DSM curves for both IOF and ITF cases with fasteners in Figures 135 and 133 demonstrate consistent behaviour. Similarly, for both EOF and ETF in Figures 136 and 134 with fasteners also consistent behaviour is also observed.

Baseline DSM curves selection consistency: The DSM curves for IOF/ITF cases are established based on the lower bound data derived from Chen's test in Chapter 4 and Wu's tests in Wu et al. [16]. And the curves show a good consistency against the data points from the other data sources. Similarly, for EOF and ETF with fasteners, this observation also applies. The baseline DSM curves have been published by Chen, Pham and Hancock in 2022 for TF cases [61] and in 2023 for OF cases [62] although minor adjustments have been made in some of the DSM parameters since those publications and summarised in Chen et al. [36].

Fastener's impact for different loading cases: In the IOF/ITF cases, the distinction between fastened (F) and unfastened (UF) conditions appears to be minimal as demonstrated in Figures 139 and 137. This is evidenced by the similar performance of Santaputra's (UF) data to Wu's (F) data.

In the ETF cases, the distinction between fastened (F) and unfastened (UF) conditions appears to be minimal as demonstrated in Figure 138. This is evidenced by the similar performance of Santaputra's (UF) data to Chen's (F) data.

The general conclusion therefore is that distinguishing between fastened (F) and unfastened (UF) conditions might not be necessary for certain loading cases and certain sections. Yet, for accurate predictions in specific cases, employing a distinct set of DSM equation coefficients could be advantageous. Specifically, the importance of fasteners cannot be overruled for hat sections with sloped webs, as the fasteners are acting efficiently in stopping the slippage and splaying effect.

Behaviour for different loading cases with varying e/t: There is a notable increase in load with increasing in e/t ratios probably due to the rolling mechanism. The necessity for a recalibration above the base curves to accommodate higher e/t

values is required. The EOF-F and ETF-F cases display a significantly narrower range or spread with increasing e/t compared to the IOF/ITF cases which have a wider range or spread, indicating a minimal involvement of the top flange rolling mechanism. This also applies to Santaputra's UF data.

7.2.4 Exploration of potential variables in DSM design equations

Acknowledging the significant role of the e/t ratio in the selection of DSM curves, further investigation is carried out to explore the possibility of incorporating e/t as a variable in the design equations. As a starting point for the investigation, a novel method is adopted to replot all the data for each loading case. In this approach, the data points are grouped and colour-coded based on their e/t values to facilitate a clear visual differentiation:

- Data points with $e/t < 1.5$ are coloured in blue.
- Data points where $1.5 \leq e/t < 3$ are coloured in orange.
- Data points where of $3 \leq e/t < 4.5$ are coloured in green.
- Data points with $e/t \geq 4.5$ are coloured in red.

In this study, the ITF, ETF, IOF and EOF loading cases, both with and without fasteners, are presented in Figures 141 to 148, respectively. To facilitate comparison, these figures have been standardized to identical X and Y axis scales.

While the shell element data yields an average P_exp/P_shell ratio of 0.908 as in Chapter 5—indicating a slight underestimation—it's crucial to point out the dearth of experimental data within the slenderness ratio range of $1 \leq \lambda \leq 3$ for most of the loading cases. This is especially true for the EOF-F loading case, where experimental data is absent at higher slenderness ratios. Consequently, Finite Element Method (FEM) simulation results using shell elements have been added to these plots to provide guidance on the trends in the graphs with increasing e/t values. This inclusion aims to enrich the understanding of behaviour within the intermediate slenderness range.

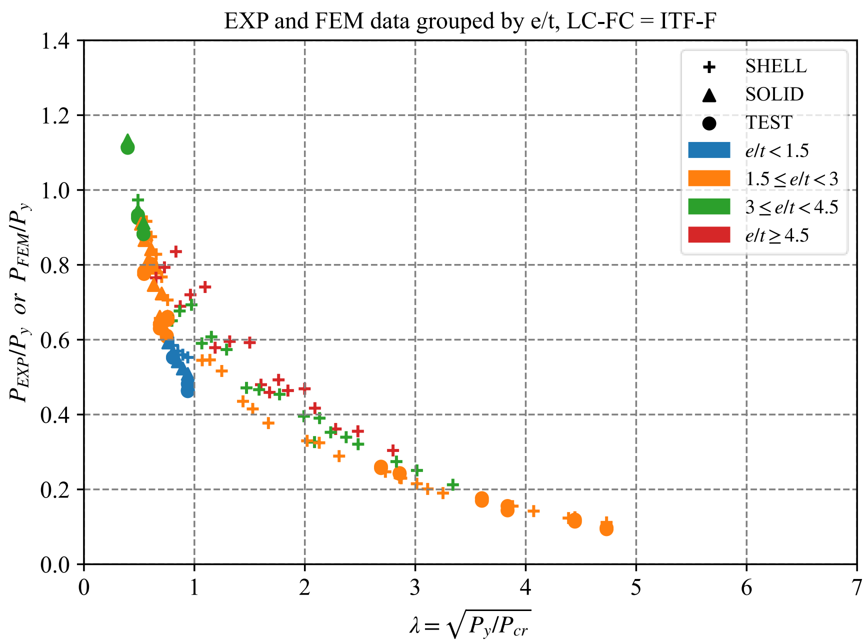

Figure 141 ITF experimental and numerical data group by e/t range

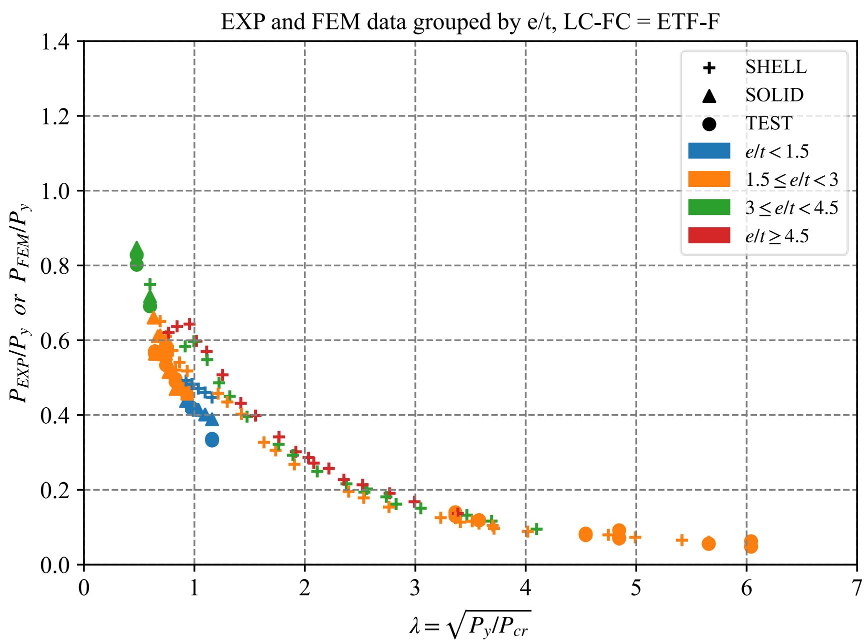

Figure 142 ETF experimental and numerical data grouped by e/t range

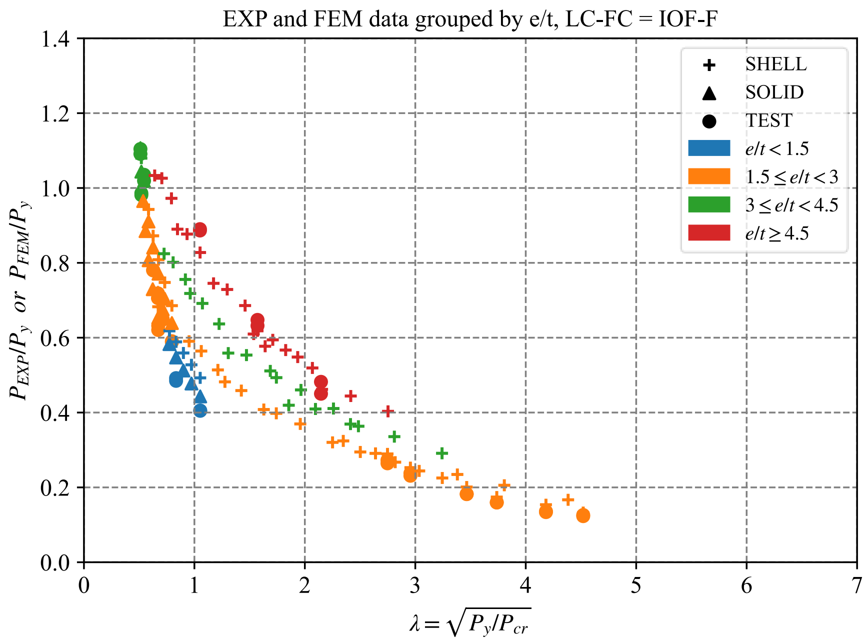

Figure 143 IOF experimental and numerical data grouped by e/t range

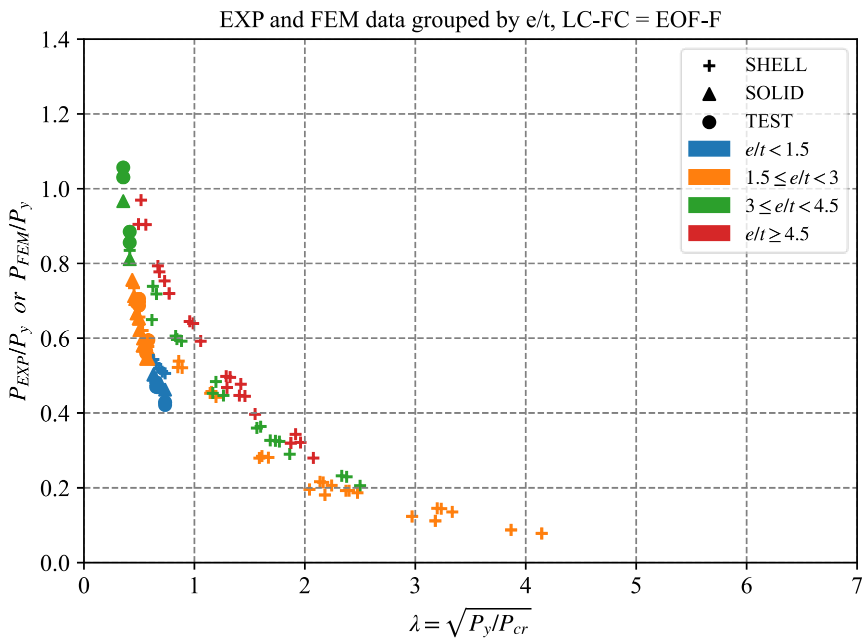

Figure 144 EOF-F experimental and numerical data grouped by e/t range

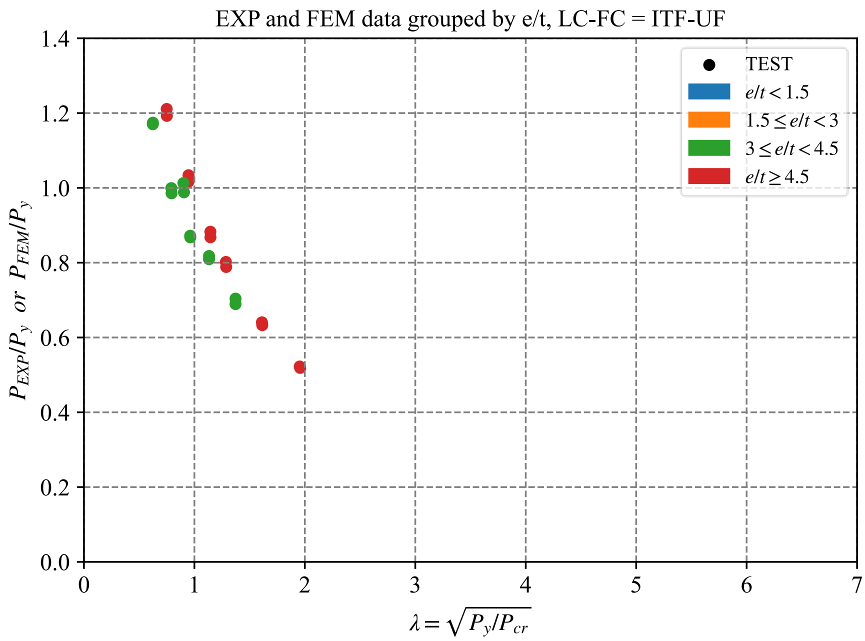

Figure 145 ITF-UF experimental and numerical data grouped by e/t range

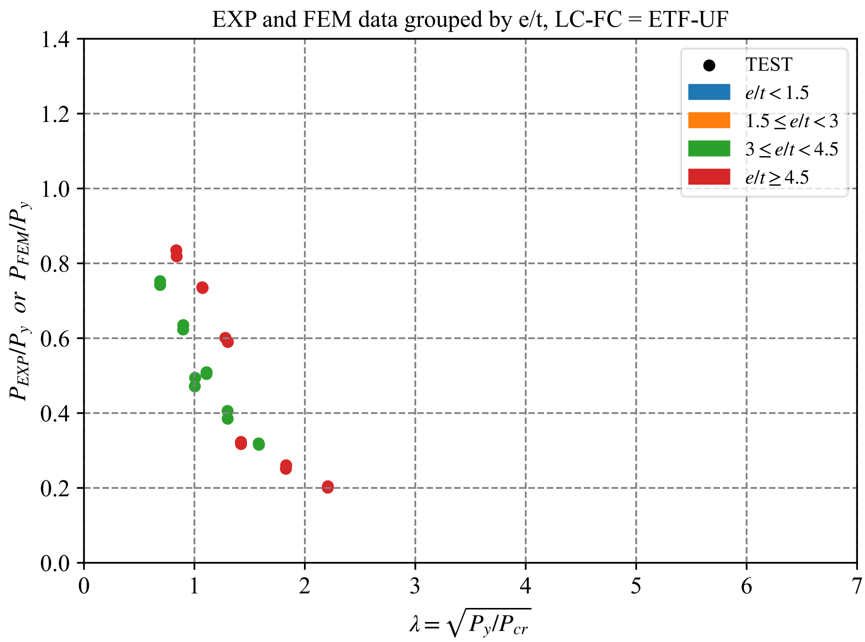

Figure 146 ETF-UF experimental and numerical data grouped by e/t range

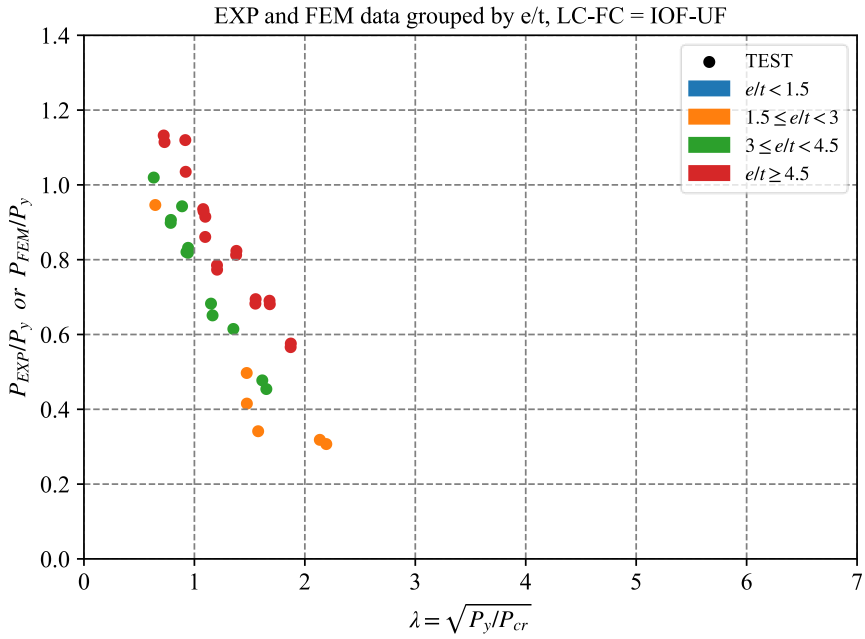

Figure 147 IOF-UF experimental and numerical data grouped by e/t range

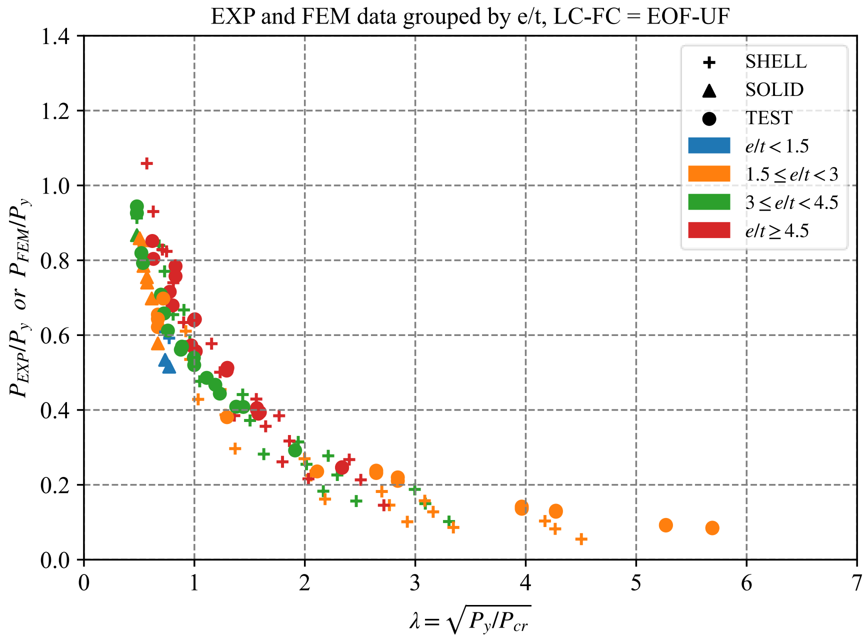

Figure 148 EOF-UF experimental and numerical data grouped by e/t range

According to Figures 141 to 148, in the instances of ITF, ETF, IOF, and EOF with Fasteners (F), data points grouped by the e/t ratio exhibit a distinct trend that forms a unique curve for each set. As the e/t ratio increases, these curves tend to shift from the bottom left towards the top right, indicating a consistent pattern across these loading cases. Data from Santaputra concerning ITF-UF, ETF-UF, and IOF-UF also exhibit similar trends, despite the smaller sample size of this data group compared to others.

For the EOF-UF loading case in Figure 148, the highly localised plastic deformation observed in the specimens results in a broader scatter in the data points, leading to less definitive evidence compared to the other loading cases. Nevertheless, a discernible trend remains apparent from the plotted data points.

While the difference between the results from solid and shell elements are minimal in the lower slenderness range, in the higher slenderness range, the shell elements simulation results generally align well with Wu's experimental dataset. Since yielding behaviour is less critical in this higher slenderness range, these figures provide strong support for the use of shell element models in simulating high slenderness sections, offering valuable insights for future research.

7.3 SELECTION OF DSM DESIGN CURVES

Based on the figures and findings presented in Sections 7.2, it is evident that using a single curve for each loading case in DSM applications can be overly conservative, particularly for sections characterised by small slenderness values and large corner radii. Moreover, a distinct trend is observed for a single e/t value, which supports the adoption of a multiple curve solution as a more accurate and reasonable approach.

The design equation can be developed in two distinct ways:

- By determining the minimum design capacity within a specific range. This method focuses on establishing the lowest acceptable capacity for safe and effective structural performance. This method is defined as Minimum Design Method (MDM) and is discussed in Section 7.3.1.
- By creating a design equation that incorporates a smooth transition within the range. This approach aims to ensure a gradual and continuous variation

in the design values. This method is defined as Smooth Transition Method (STM). The details are discussed in Section 7.3.2.

In this section, only experimental data are used for the DSM design curve calibration. FE results are used as references only and not to be used for deviation and reliability analysis.

7.3.1 Minimum Design Method (MDM)

The DSM design equation for hat sections under localised loading, when applied using the Minimum Design Method (MDM), incorporates three distinct sets of coefficients. These sets are specifically designed to accommodate common hat section profiles, each characterised by a different range of the e/t value.

The basic design equation is given as Equations (7-1) and (7-2).

The factors a, b, c, d, and k_p in the DSM design equation are specifically determined based on the e/t value, which is categorized into three distinct groups for the purpose of this design approach:

Group 1: Defined for sections where e/t is less than 3.

Group 2: Applicable to sections where e/t is in the range of 3 to less than 4.5.

Group 3: Encompasses sections with e/t values of 4.5 or higher.

With the shift in the curve fitting approach from applying a single curve to fit all data points, to instead grouping them by the e/t ratio, it is anticipated that the coefficients will differ from those listed in the previous Table 31. The coefficients for each group, categorized according to the e/t ratio and reflecting this new methodology, are now presented in the updated Table 33.

Table 33 Coefficients for each design group using MDM

GROUP	LC-FC	a	b	c	d	k_p
1	ITF-F	0.11	1.15	2	2	1
1	ETF-F	0.08	1.75	2	2	1
1	IOF-F	0.11	1.10	2	2	1
1	EOF-F	0.12	2.20	2	2	1
1	ITF-UF	0.11	1.10	2	2	1
1	ETF-UF	0.05	1.40	2	2	1
1	IOF-UF	0.11	1.10	2	2	1
1	EOF-UF	0.11	1.54	2	2	1
2	ITF-F	0.05	0.66	2	2	1.1

GROUP	LC-FC	a	b	c	d	k_p
2	ETF-F	0.04	1.25	2	2	1.1
2	IOF-F	0.05	0.65	2	2	1.1
2	EOF-F	0.07	1.45	2	2	1.1
2	ITF-UF	0.05	0.65	2	2	1.1
2	ETF-UF	0.03	1.05	2	2	1.1
2	IOF-UF	0.05	0.65	2	2	1.1
2	EOF-UF	0.07	1.26	2	2	1.1
3	ITF-F	0.03	0.46	2	2	1.2
3	ETF-F	0.02	0.95	2	2	1.2
3	IOF-F	0.03	0.45	2	2	1.2
3	EOF-F	0.05	1.05	2	2	1.2
3	ITF-UF	0.03	0.45	2	2	1.2
3	ETF-UF	0.02	0.82	2	2	1.2
3	IOF-UF	0.03	0.45	2	2	1.2
3	EOF-UF	0.05	1.05	2	2	1.2

Figures 149 to 152 demonstrate the Direct Strength Method (DSM) design curves for various loading cases with the MDM. Each figure includes **three** DSM design curves, each corresponding to distinct groups identified by their varying k_p values, as detailed in Table 33. Alongside these curves, the experimental data points, expressed as P_{exp}/P_y ratios on Y axis, are plotted to correspond with their respective DSM design curve. The colour coding of the data points is intentionally synchronized with the colours of the DSM design curves to facilitate easy reference. Importantly, the experimental data points with $e/t < 3$ (coloured in blue and orange) should use the Group 1 DSM design curve (colour in orange).

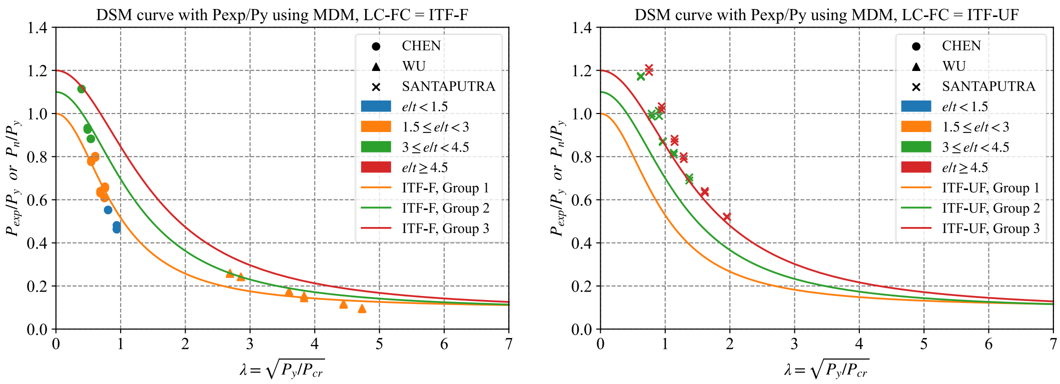

Figure 149 DSM design curves for the ITF-F/UF loading cases (MDM)

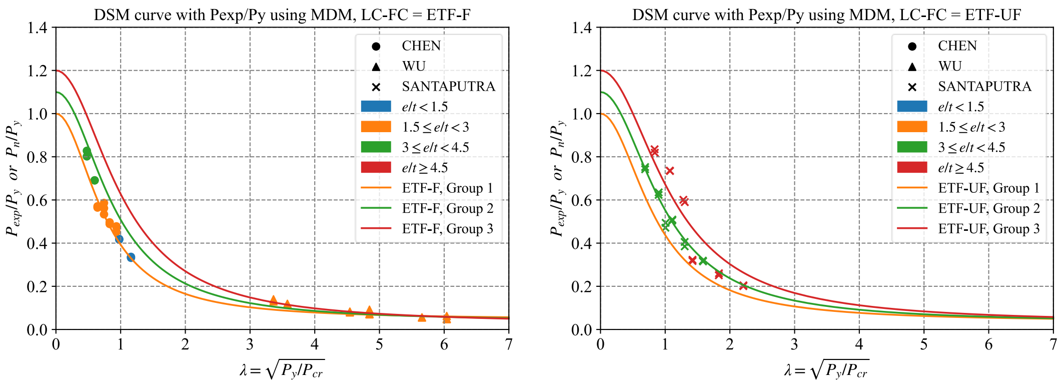

Figure 150 DSM design curves for the ETF-F/UF loading cases (MDM)

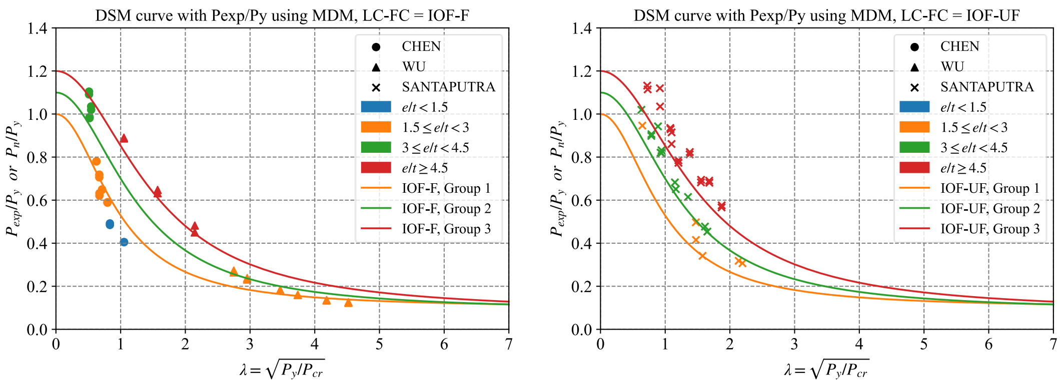

Figure 151 DSM design curves for the IOF-F/UF loading cases (MDM)

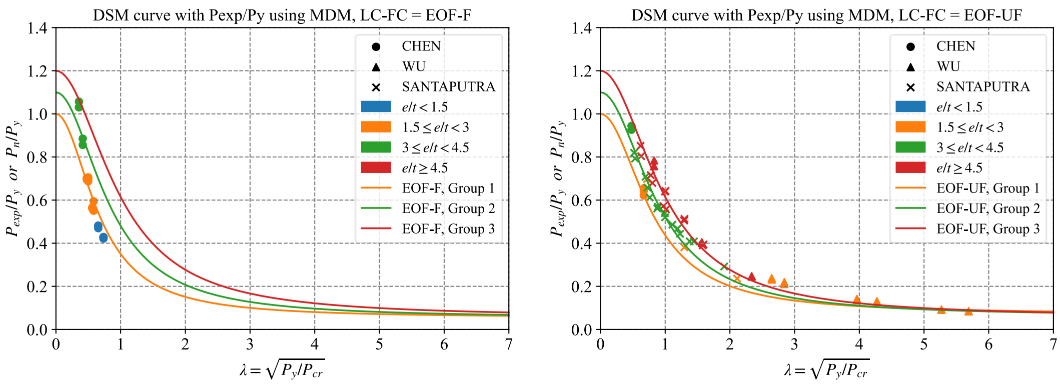

Figure 152 DSM design curves for the EOF-F/UF loading case (MDM)

For

7.3.2 Smooth Transition Method (STM)

The Smooth Transition Method (STM), developed to account for the varying e/t values, involves incorporating the e/t ratio directly into the original DSM equation. This modification aims to create a more continuous and accurate representation of the structural behaviour across different e/t values. In this method,

$\zeta = t/e$ is introduced to consider the contribution of rolling mechanism in large corner radii sections. The modified DSM design equation is given as follows:

$$\frac{P_n}{P_y} = k_p \frac{1+a\lambda^c\zeta^k}{1+b\lambda^d\zeta^k} \quad (7\text{-}3)$$

where

$\zeta = t/e$, the inverse of e/t, with a limit of $1.5 \le e/t \le 4.5$;

k is an exponent of ζ as given in Table 34.

Table 34 Coefficient for each design group using STM

LC-FC	a	b	c	d	k_p	k
ITF-F	0.12	1.92	2	2	1.1	1
ETF-F	0.06	2.20	2	2	1.1	0.5
IOF-F	0.12	1.92	2	2	1.1	1
EOF-F	0.15	3.60	2	2	1.1	1
ITF-UF	0.12	1.92	2	2	1.1	1
ETF-UF	0.10	2.70	2	2	1.1	1
IOF-UF	0.12	1.92	2	2	1.1	1
EOF-UF	0.11	2.31	2	2	1.1	0.5

Figures 153 to 156 demonstrate the Direct Strength Method (DSM) design curves for various loading cases with Smooth Transition Method. Each figure includes **two** DSM design curves. The bottom (orange) and top (red) curves are corresponding to e/t values equal to 1.5 and 4.5 respectively. A dotted green DSM curve based on the e/t values equal to 3 is also presented for reference. The smooth design method aims to provide a smooth transition curve within the specific e/t ratio range of $1.5 \le e/t \le 4.5$. This approach is intended to avoid overly conservative predictions and to keep the design equations simple, reducing the number of required coefficients.

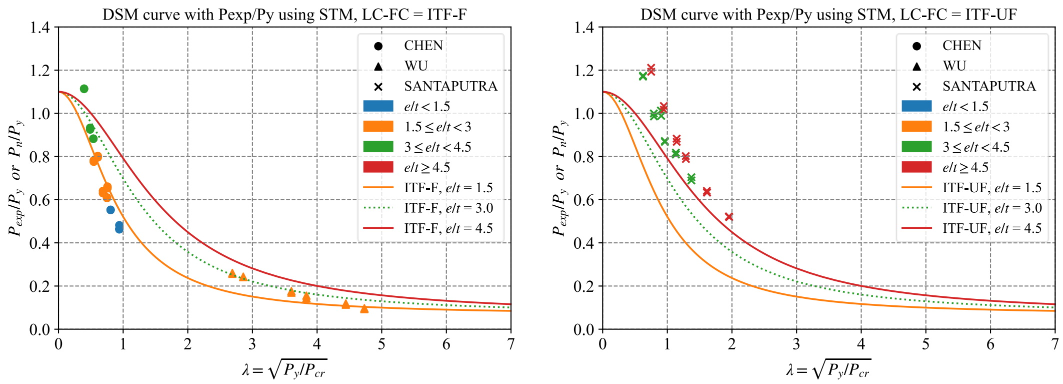

Figure 153 DSM design curves for the ITF-F/UF loading cases (STM)

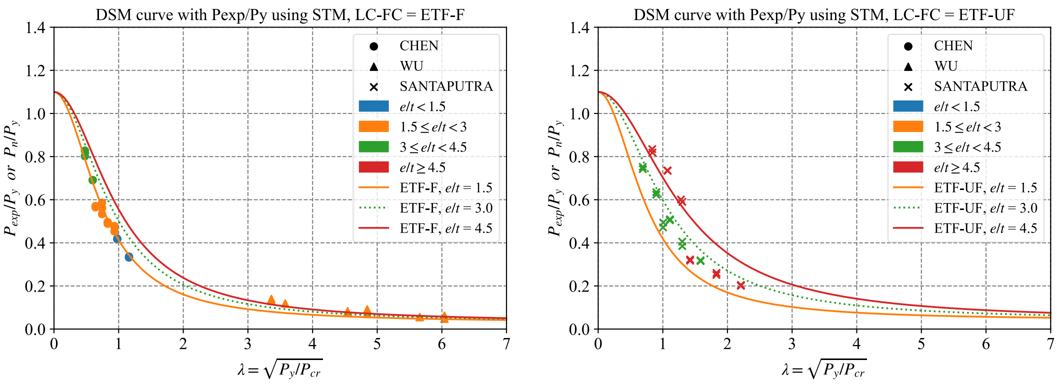

Figure 154 DSM design curves for the ETF-F/UF loading cases (STM)

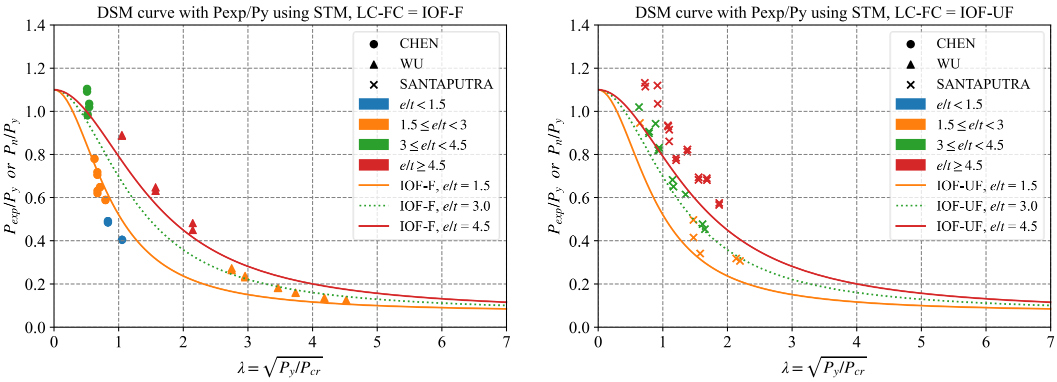

Figure 155 DSM design curves for the IOF-F/UF loading cases (STM)

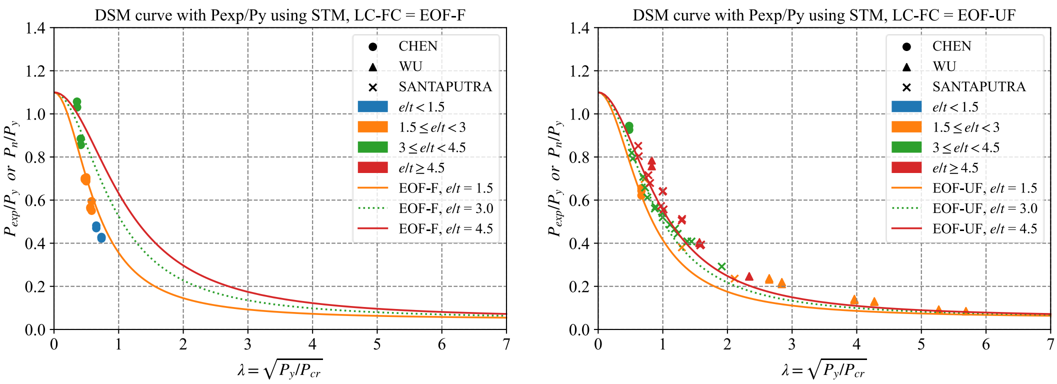

Figure 156 DSM design curves for the EOF-F/UF loading case (STM)

7.3.3 Deviation analysis

A comparison between P_{exp} and P_n has been carried out for the DSM design equations developed for the MDM and STM respectively using the experimental data. Tables 35 to 37 present the average value (AVE), standard deviation (StdDev) and coefficient of variation (COV) of P_{exp}/P_n for MDM, and Table 38 to Table 40 present the AVE, StdDev and COV of P_{exp}/P_n for STM.

For each table, P_{exp} is sourced from capacity data based on tests, categorized by material type as provided by the author. Chen's data represents mild steel with low strength (323 MPa), Wu's data pertains to mild steel with high strength (717 MPa), and Santaputra's data include a broad range of steel strengths, from 400 MPa to over 1000 MPa.

Table 35 Summary of AVE of Pexp/Pn (MDM)

AVE of Pexp/Pn	CHEN	WU	SANTAPUTRA	Grand Total
EOF-F	0.976			0.976
EOF-UF	1.050	1.199	1.032	1.091
ETF-F	1.012	1.130		1.064
ETF-UF			0.952	0.952
IOF-F	0.976	1.087		1.029
IOF-UF			1.143	1.143
ITF-F	0.974	1.073		1.008
ITF-UF			1.200	1.200
Grand Total	0.988	1.127	1.086	1.063

Table 36 Summary of StdDev of Pexp/Pn (MDM)

StdDev of Pexp/Pn	CHEN	WU	SANTAPUTRA	Grand Total
EOF-F	0.084			0.084
EOF-UF	0.033	0.219	0.091	0.163
ETF-F	0.072	0.241		0.175
ETF-UF			0.151	0.151
IOF-F	0.117	0.145		0.141
IOF-UF			0.084	0.084
ITF-F	0.078	0.234		0.154
ITF-UF			0.094	0.094
Grand Total	0.088	0.210	0.138	0.156

Table 37 Summary of COV of Pexp/Pn (MDM)

COV of Pexp/Pn	CHEN	WU	SANTAPUTRA	Grand Total
EOF-F	0.086			0.086
EOF-UF	0.032	0.183	0.088	0.150
ETF-F	0.071	0.214		0.165
ETF-UF			0.159	0.159
IOF-F	0.120	0.133		0.137
IOF-UF			0.074	0.074
ITF-F	0.080	0.218		0.153
ITF-UF			0.079	0.079
Grand Total	0.089	0.186	0.127	0.146

Table 38 Summary of AVE of Pexp/Pn (STM)

AVE of Pexp/Pn	CHEN	WU	SANTAPUTRA	Grand Total
EOF-F	0.910			0.910
EOF-UF	1.054	1.417	1.062	1.182
ETF-F	0.941	1.351		1.120
ETF-UF			0.830	0.830
IOF-F	0.943	1.240		1.084
IOF-UF			1.142	1.142
ITF-F	0.928	1.210		1.025
ITF-UF			1.195	1.195
Grand Total	0.938	1.311	1.066	1.082

Table 39 Summary of StdDev of Pexp/Pn (STM)

StdDev of Pexp/Pn	CHEN	WU	SANTAPUTRA	Grand Total
EOF-F	0.094			0.094
EOF-UF	0.037	0.254	0.081	0.232
ETF-F	0.050	0.220		0.254
ETF-UF			0.175	0.175
IOF-F	0.114	0.148		0.198
IOF-UF			0.104	0.104
ITF-F	0.065	0.213		0.189
ITF-UF			0.069	0.069
Grand Total	0.087	0.223	0.171	0.215

Table 40 Summary of COV of Pexp/Pn (STM)

COV of Pexp/Pn	CHEN	WU	SANTAPUTRA	Grand Total
EOF-F	0.103			0.103
EOF-UF	0.035	0.179	0.076	0.196
ETF-F	0.053	0.163		0.226
ETF-UF			0.210	0.210
IOF-F	0.121	0.119		0.183
IOF-UF			0.091	0.091
ITF-F	0.070	0.176		0.185
ITF-UF			0.058	0.058
Grand Total	0.093	0.170	0.161	0.199

Based on these statistics, it is evident that both DSM design equations provide accurate predictions of the web crippling capacity, with deviations falling within an acceptable range. The MDM method is more reliable with a COV of 0.146 compared with the STM method with a COV of 0.199.

7.3.4 Discussion

Section 7.3.3 has effectively shown the Direct Strength Method's (DSM) capability in accurately predicting the localised loading capacity for the majority of cases. However, there's a noted inconsistency in the Average (AVE) value for the ETF-UF loading case. Specifically, the AVE value of P_{exp}/P_n for the ETF-UF case, as listed in Table 35, is observed to be the lowest at 0.952.

The test data summarized from Santaputra's report for ETF-UF loading case was carefully reviewed. The AVE, StdDev and COV are calculated by different material (yield strength) as shown in Table 41.

Table 41 AVE, StdDev and COV of Pexp/Pn grouped by yield strength

fy (MPa)	Average of P_EXP/Pn	StdDev of P_EXP/Pn	COV of P_EXP/Pn
401.275	1.124	0.043	0.039
531.586	1.018	0.015	0.015
805.997	0.934	0.049	0.053
1138.325	0.733	0.042	0.058
Grand Total	0.952	0.151	0.159

According to Table 41, the average value of P_{exp}/P_n shows a descending trend and begins to appear unconservative as the yield strength (fy) exceeds 800 MPa. This observation suggests that the Direct Strength Method (DSM) design equation may not be suitable for materials with a yield stress over 800 MPa.

To gain a deeper insight into this discrepancy, a comprehensive investigation has been carried out. Due to the lack of additional experimental data for End Two Flange Unfastened (ETF-UF) cases, an extensive series of numerical analyses was conducted. A hat section, mirroring the dimensions and properties of those tested as height (H) = 120 mm, thickness (t) = 3 mm, yield strength (f_y) = 323 MPa, sloping angle (DEG) = 0°, and bearing length (N) = 50 mm, was chosen for Finite Element Method (FEM) analysis in ABAQUS. The study aimed to examine the impact of varying the radius of rounded corners or the e/t value, selecting Internal Radius (RIN) values of 3, 7.5, 8, 12, 13.5, 16.5, and 21 mm, thereby covering a broad e/t range from 1.5 to 7.5. Employing the Minimum Design Method (MDM), the nominal load (P_n) was calculated and subsequently compared with the FEM-predicted load (P_{FEM}) using solid elements. The findings of this analysis are documented in Table 42, which details the P_{FEM} and P_n values obtained from this investigative effort.

Table 42 FEM result vs DSM design equation prediction using Minimum Design Method

r_{in} (mm)	e/t	P_{FEM} (kN)	P_n (kN)	P_{FEM}/P_n
3	1.5	35.948	32.964	1.091
7.5	3.0	29.399	28.622	1.027
8	3.167	28.894	27.687	1.044
12	4.5	24.636	25.199	0.978
13.5	5.0	22.928	23.266	0.985
16.5	6.0	20.233	20.147	1.004
21	7.5	17.566	16.765	1.048

H = 120 mm, t = 3 mm, f_y = 323 MPa, DEG = 0° and N = 50 mm

The analysis of data from Table 42 yields an Average (AVE) of 1.025, a standard deviation (StdDev) of 0.040, and a coefficient of variation (COV) of 0.039. These statistical outcomes significantly reinforce the credibility of the Direct Strength Method (DSM) equation when applied using the MDM for the ETF-UF loading case within the low strength range. The dimension of the section is found to be not related to this discrepancy.

The underlying cause for the descending trend could be attributed to significant differences in material properties observed at f_y values above 800 MPa (116 ksi), which in turn affect the loading behaviour and capacity of the steel. Supporting evidence from the stress-strain curve provided by Santaputra as shown in Figure 157 further emphasizes the material property variations at higher yield strengths, reinforcing the need for caution in applying the DSM design equation in such cases.

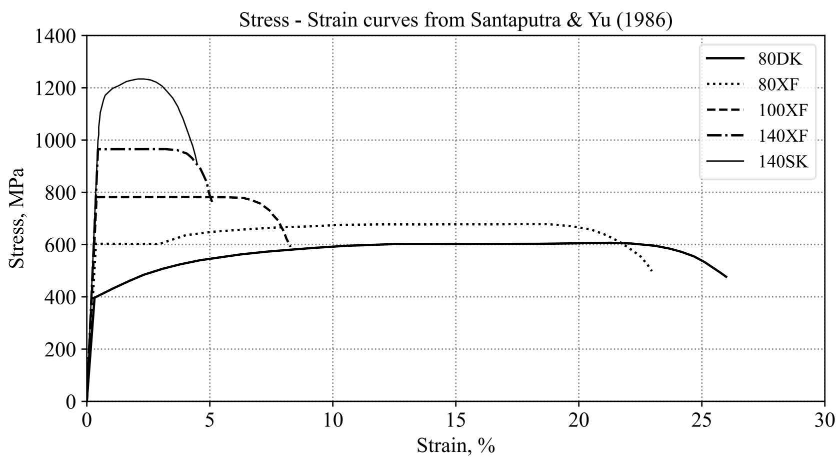

Figure 157 Typical stress-strain curves of five sheet steels in Longitudinal tension given by Santaputra

It's worth noting that the initial purpose of Santaputra's research was for the design of automotive structural components using high strength sheet steel, justifying the use of steel with a yield stress exceeding 800 MPa. However, in the context of construction, the application of cold-formed steel members typically adheres to a specified nominal yield stress limit.

For instance, the AISI S100-16 standard, within Table B4.1-1, sets forth a limit for the applicability of member design across Chapters E through H (with Web crippling discussed in Chapter G) by employing both the Effective Width Method and the Direct Strength Method. These limits are specified as less than 80 ksi (552 MPa) and less than 95 ksi (655 MPa) respectively, as illustrated in Table 43. Similarly, the AS/NZS 4600:2018 standard, in Table 1.5.2, indicates that the maximum strength of steels for construction use is classified as G550 Grade, with yield stress and tensile strength at 550 MPa. This delineation underscores the distinct considerations between automotive and construction applications in terms of the acceptable range of yield stress for steel materials.

Table 43 Limit of applicability for member design in Chapters E through H by the EWM and DSM

Criteria	**Limit Variables**	**Effective Width Method**	**Direct Strength method**
Stiffened element in compression	w/t	≤ 500	≤ 500
Edge-stiffened element in compression	b/t	$\leq 90\ for\ I_s \geq I_a$ $\leq 60\ for\ I_s < I_a$	≤ 160
Unstiffened element in compression	d/t	≤ 60	≤ 60
Stiffened element in bending (e.g. a web)	h/t	< 200 for unstiffened web ≤ 260 for bearing stiffener ≤ 300 for bearing and intermediate stiffener	≤ 300
Inside bending radius	R/t	≤ 10	≤ 20
Simple edge stiffener length/width ratio	d_o/b_o	≤ 0.7	≤ 0.7
Edge stiffener type		Sample only	Simple and complex
Maximum number of intermediate stiffeners in w	n_f	4	4
Maximum number of intermediate stiffeners in web	n_{fe}	2	2
Number of intermediate stiffeners in h	n_w	0	4
Nominal yield stress	F_y	$<$ 80 ksi (522 MPa)	$<$ 95 ksi (655 MPa)

Hence, the applicable range for steel materials is established by imposing a yield stress limit of no more than 800 MPa. This limit is set to meet the needs of construction applications while also allowing room for future advancements.

7.3.5 Review of deviation analysis

Table 44 presents a summary of the materials used in Santaputra's research. A detailed deviation analysis is performed on all available test data, with the exclusion of specimens where the yield stress (f_y) surpasses 800 MPa. Consequently, specimens labelled as 100XF-2, 140XF, and 140SK are omitted from this deviation analysis review. The detailed revision of deviation analysis includes the calculation of AVE, StdDev and COV for both design equations. Tables 45 to 47 presents the result of AVE, StdDev and COV respectively using MDM and Tables 48 to 50 presents the result using STM, respectively.

By comparing the AVE value before and after the application of the imposed limitations, it is concluded that the application of these limitations effectively brings the AVE value of the P_{exp}/P_n ratio back to the idealized value, which should be slightly above 1.0.

In conclusion, it is evident that both the Direct Strength Method (DSM) design equations provide accurate predictions of the web crippling capacity for the test cases covered in this research. However, a limitation on the application range of these design equations should be instituted for better overall performance, particularly due to the differences observed in the behaviour of high-strength steel materials compared to the more commonly used construction steels.

Table 44 Summary of material used by Santaputra

Material	**80DK**	**80XF**	**80XF-2**	**100XF**	**100XF-2**	**140XF**	**140SK**
Fy (ksi)	58.2	77.1	88.3	113.1	116.9	141.2	165.1
fy (MPa)	401.275	531.586	608.807	779.797	805.997	973.540	1138.325
EOF	6		6	6		6	6
ETF	6	6			6		6
IOF	6		6	6		12	6
ITF	6	6			6		6
Summary	24	12	12	12	12	18	24

Table 45 Summary of AVE of Pexp/Pn (MDM) with 800MPa limit

AVE of Pexp/Pn	CHEN	WU	SANTAPUTRA	Grand Total
EOF-F	0.976			0.976
EOF-UF	1.050	1.199	0.983	1.086
ETF-F	1.012	1.130		1.064
ETF-UF			1.071	1.071
IOF-F	0.976	1.087		1.029
IOF-UF			1.157	1.157
ITF-F	0.974	1.073		1.008
ITF-UF			1.212	1.212
Grand Total	0.988	1.127	1.099	1.061

Table 46 Summary of StdDev of Pexp/Pn (MDM) with 800MPa limit

StdDev of Pexp/Pn	CHEN	WU	SANTAPUTRA	Grand Total
EOF-F	0.084			0.084
EOF-UF	0.033	0.219	0.069	0.182
ETF-F	0.072	0.241		0.175
ETF-UF			0.063	0.063
IOF-F	0.117	0.145		0.141
IOF-UF			0.084	0.084
ITF-F	0.078	0.234		0.154
ITF-UF			0.063	0.063
Grand Total	0.088	0.210	0.113	0.154

Table 47 Summary of COV of Pexp/Pn (MDM) with 800MPa limit

COV of Pexp/Pn	CHEN	WU	SANTAPUTRA	Grand Total
EOF-F	0.086			0.086
EOF-UF	0.032	0.183	0.071	0.168
ETF-F	0.071	0.214		0.165
ETF-UF			0.059	0.059
IOF-F	0.120	0.133		0.137
IOF-UF			0.073	0.073
ITF-F	0.080	0.218		0.153
ITF-UF			0.052	0.052
Grand Total	0.089	0.186	0.103	0.145

Table 48 Summary of AVE of Pexp/Pn (STM) with 800MPa limit

AVE of Pexp/Pn	CHEN	WU	SANTAPUTRA	Grand Total
EOF-F	0.910			0.910
EOF-UF	1.054	1.417	1.013	1.195
ETF-F	0.941	1.351		1.120
ETF-UF			0.989	0.989
IOF-F	0.943	1.240		1.084
IOF-UF			1.145	1.145
ITF-F	0.928	1.210		1.025
ITF-UF			1.242	1.242
Grand Total	0.938	1.311	1.093	1.094

Table 49 Summary of StdDev of Pexp/Pn (STM) with 800MPa limit

StdDev of Pexp/Pn	CHEN	WU	SANTAPUTRA	Grand Total
EOF-F	0.094			0.094
EOF-UF	0.037	0.254	0.038	0.260
ETF-F	0.050	0.220		0.254
ETF-UF			0.084	0.084
IOF-F	0.114	0.148		0.198
IOF-UF			0.084	0.084
ITF-F	0.065	0.213		0.189
ITF-UF			0.060	0.060
Grand Total	0.087	0.223	0.118	0.214

Table 50 Summary of COV of Pexp/Pn (STM) with 800MPa limit

COV of Pexp/Pn	CHEN	WU	SANTAPUTRA	Grand Total
EOF-F	0.103			0.103
EOF-UF	0.035	0.179	0.038	0.218
ETF-F	0.053	0.163		0.226
ETF-UF			0.085	0.085
IOF-F	0.121	0.119		0.183
IOF-UF			0.073	0.073
ITF-F	0.070	0.176		0.185
ITF-UF			0.048	0.048
Grand Total	0.093	0.170	0.108	0.196

7.4 COMPARISON BETWEEN THE PREDICTION RESULTS AND AS4600

7.4.1 Design rules in current standards

The nominal capacity of hat sections can be calculated using either AS/NZS 4600:2018, published by Standards Australia, or its similar counterpart, AISI S100, published by the American Iron and Steel Institute. According to AS/NZS 4600:2018, Clause 3.3.6.2, the nominal capacity for concentrated load or reaction for one solid web connecting top flange and bottom flanges (Rb) shall be determined as follows:

$$R_b = C t_w^2 f_y \sin\theta \left(1 - C_r\sqrt{\frac{r_i}{t_w}}\right)\left(1 + C_l\sqrt{\frac{l_b}{t_w}}\right)\left(1 - C_w\sqrt{\frac{d_1}{t_w}}\right) \quad (7\text{-}4)$$

where

C, C_r, C_l, C_w are factors given in Tables 3.3.6.2 in the standard.

It's important to note that AS/NZS 4600:2018 provides two calculation options applicable to multi-web sections. One option is to use the hat section table labelled as Table 3.3.6.2(D) as shown in Table 51, while the other is to use the multi-web decking table, referred to as Table 3.3.6.2(E) as shown in Table 52. Despite the title of Table 3.3.6.2(D) being "SINGLE HAT SECTIONS", there is a restriction in this table limiting the θ (theta) value to 90 degrees only. Consequently, Table 3.3.6.2(D) is not suitable for hat sections with sloped webs.

Table 51 Table 3.3.6.2(D) in AS/NZS 4600:2018 (single hat sections)

Load cases	C	C_r	C_l	C_w	ϕ_w	Limits
EOF-F	4	0.25	0.68	0.04	0.75	$r_i/t_w \leq 5$
IOF-F	17	0.13	0.13	0.04	0.80	$r_i/t_w \leq 10$
ETF-F	9	0.10	0.07	0.03	0.85	$r_i/t_w \leq 10$
ITF-F	10	0.14	0.22	0.02	0.85	$r_i/t_w \leq 10$
EOF-UF	4	0.25	0.68	0.04	0.75	$r_i/t_w \leq 4$
IOF-UF	17	0.13	0.13	0.04	0.90	$r_i/t_w \leq 4$

NOTE: The coefficients in this table apply if $d_1/t_w \leq 200$, $l_b/t_w \leq 200$, $l_b/d_1 \leq 2.0$ and $\theta = 90°$

Table 52 Table 3.3.6.2(E) in AS/NZS 4600:2018 (multiple-web deck sections)

Load cases	C	C_r	C_l	C_w	ϕ_w	Limits
EOF-F	4	0.04	0.25	0.025	0.90	$r_i/t_w \leq 20$
IOF-F	8	0.10	0.17	0.004	0.85	$r_i/t_w \leq 10$
ETF-F	9	0.12	0.14	0.040	0.85	$r_i/t_w \leq 10$
ITF-F	10	0.11	0.21	0.020	0.85	$r_i/t_w \leq 10$

Load cases	C	C_r	C_l	C_w	ϕ_w	Limits
EOF-UF	3	0.04	0.29	0.028	0.60	$r_i/t_w \leq 20$
IOF-UF	8	0.10	0.17	0.004	0.85	$r_i/t_w \leq 20$
ETF-UF	6	0.16	0.15	0.050	0.90	$r_i/t_w \leq 5$
ITF-UF	17	0.10	0.10	0.046	0.90	$r_i/t_w \leq 5$

NOTE: The coefficient in this table apply if $d_1/t_w \leq 200$, $l_b/t_w \leq 210$, $l_b/d_1 \leq 3.0$ and $45° < \theta \leq 90°$

7.4.2 Comparison process

Given that Table 3.3.6.2(E) is designed for multi-web decking sections, which bear similarities to hat sections but offer a range from 45 degrees to 90 degrees, a comparison has been made between the newly developed DSM equations and the AS4600:2018 method. The nominal capacity of the hat section is calculated using two different approaches:

1) Considering the section with a vertical web only, as per Table 3.3.6.2(D), and

2) Considering the section with both vertical and sloped webs using Table 3.3.6.2(E).

In both scenarios, the data set is selected as the reduced experimental dataset described in section 7.3.3. In addition, the specimen falls outside the limits specified in Table 3.3.6.2(D) and (E) are excluded from consideration.

In order to carry out the comparison, R_b is first calculated accordingly. Because the Rb value is given as per web, the P_n value is equal to 2 times the R_b value.

Tables 53 to 55 demonstrate the AVE, StdDev and COV values of the P_{exp}/P_n ratio for the two methods outlined in AS/NZS 4600:2018, as well as for the two newly developed DSM (Direct Strength Method) design equations. P_n(D) and P_n(E) are the 2Rb value from Table 3.3.6.2(D) and Table 3.3.6.2(E). It is important to mention that the P_{exp}/P_n (E) column values are calculated under the assumption that the hat section represents a single rib deck. This approach allows for the inclusion of sloped web sections in the analysis for comparative purposes. The data presented in this column is intended for informational use only.

Data set used in previous Section 7.3.5 is selected for this analysis.

Table 53 Comparison of AVE values of different design equations

AVE	Pexp/Pn(D)	Pexp/Pn(E)	Pexp/Pn_MDM	Pexp/Pn_STM
EOF-F	0.903	1.146	0.976	0.910
EOF-UF	0.632	0.880	1.086	1.195
ETF-F	0.751	0.636	1.064	1.120
ETF-UF		0.844	1.071	0.989
IOF-F	0.630	0.834	1.029	1.084
IOF-UF	0.607	0.818	1.157	1.145
ITF-F	0.877	0.863	1.008	1.025
ITF-UF		0.769	1.212	1.242
Grand Total	0.715	0.850	1.061	1.094

Table 54 Comparison of StdDev values of different design equations

StdDev	Pexp/Pn(D)	Pexp/Pn(E)	Pexp/Pn_MDM	Pexp/Pn_STM
EOF-F	0.032	0.166	0.084	0.094
EOF-UF	0.108	0.191	0.182	0.260
ETF-F	0.093	0.122	0.175	0.254
ETF-UF		0.016	0.063	0.084
IOF-F	0.106	0.090	0.141	0.198
IOF-UF	0.053	0.053	0.084	0.084
ITF-F	0.081	0.100	0.154	0.189
ITF-UF		0.042	0.063	0.060
Grand Total	0.146	0.183	0.154	0.214

Table 55 Comparison of COV values of different design equations

COV	Pexp/Pn(D)	Pexp/Pn(E)	Pexp/Pn_MDM	Pexp/Pn_STM
EOF-F	0.035	0.145	0.086	0.103
EOF-UF	0.170	0.217	0.168	0.218
ETF-F	0.123	0.192	0.165	0.226
ETF-UF		0.019	0.059	0.085
IOF-F	0.169	0.108	0.137	0.183
IOF-UF	0.088	0.065	0.073	0.073
ITF-F	0.092	0.116	0.153	0.185
ITF-UF		0.055	0.052	0.048
Grand Total	0.204	0.215	0.145	0.196

7.4.3 Discussion

Table 53 reveals that the calculation method prescribed by the current standard for hat sections tends to yield unconservative predictions in comparison to actual test results, with an average P_{exp}/P_n ratio of 0.715. When evaluated individually, the majority of P_{exp}/P_n ratios derived using the approach detailed in Table 3.3.6.2(D) exhibit unconservative outcomes. Notably, the methodology specified in Table 3.3.6.2(D) does not only fall short in accommodating sloped web sections but also does not address Two-Flange loading cases in unfastened conditions. This omission suggests a potential gap in the current standard's ability to accurately predict the structural behaviour under certain loading cases, particularly for hat sections with varying web slopes and fastening conditions. Employing the decking table for calculating hat section, does not confer any notable benefits despite its allowance for a range of theta values.

Regarding the two DSM design equations based on different concepts, the P_{exp}/P_n values are found to be 1.061 for the MDM design and 1.094 for the STM design. The corresponding COV values are 0.145 and 0.196, respectively. These results are considered adequate, displaying slightly conservative AVE results and smaller COV values, which indicate a more consistent prediction across different scenarios. This suggests that both MDM and STM methodologies provide a dependable and cautiously conservative framework for DSM applications, with MDM exhibiting less variability compared to the STM approach.

7.5 RELIABILITY ANALYSIS

7.5.1 Reliability analysis method

The test results gathered from previous sections have been utilised to calibrate the reliability indices of the design equations, following the methodology outlined in the AISI S100-16 specification, specifically in section K2.1.1.

According to the specification, for the Load and Resistance Factor Design (LRFD), the strength of the test elements, assembles, connections or members shall satisfy the following equation:

$$\sum \gamma_i Q_i \leq \phi R_n \tag{7-5}$$

where

$\sum \gamma_i Q_i$ is the required strength [effect of factored loads] based on the most critical load combination, determined in accordance with Section B2, γ_i and Q_i and load factors and load effects, respectively.

ϕ is resistance factor (capacity factor in AS/NZS 4600).

The resistance factor is given by

$$\phi = C_\phi (M_m F_m P_m) e^{-\beta_0 \sqrt{V_M^2 + V_F^2 + C_P^2 V_P^2 + V_Q^2}} \quad (7\text{-}6)$$

where

$C_\phi = 1.52$ for LRFD, is the calibration coefficient;

M_m is mean value of material factor;

F_m is mean value of fabrication factor;

$P_m = \frac{\sum_{i=1}^{n} \frac{R_{t,i}}{R_{n,i}}}{n}$, when the available strength [factored resistance] is determined in accordance with Section K2.1.1(b) in AISI S100-16, where i is the index of tests, n is total number of tests, $R_{t,i}$ is test strengths [resistance] of test i, and $R_{n,i}$ is calculated nominal strength [resistance] of test i per rational engineering analysis model;

$e = 2.718$, is natural logarithmic base;

$\beta_0 = 2.5$, is target reliability index for structural members;

V_M is coefficient of variation of material factor;

V_F is coefficient of variation of fabrication factor;

C_P is correction factor, equals to $\frac{\left(1+\frac{1}{n}\right)m}{m-2}$ for $n \geq 4$ or 5.7 for $n = 3$, where n is number of tests and $m = n - 1$;

V_P is the coefficient of variation of test results but not less than 0.065;

V_Q is coefficient of variation of load effect, taken as 0.21 for LRFD.

In accordance with Table K2.1.1-1 in AISI S100-16, demonstrated in Table 56, the M_m, V_M, F_m and V_F values are taken as 1.10, 1.10, 1.00 and 0.05 respectively.

Table 56 Statistical data for the determination of resistance factor (Table K2.1.1-1 in AISI S100-16)

Type of Component	M_m	V_M	F_m	V_F
Members				
Tension	1.10	0.10	1.00	0.05
Compression	1.10	0.10	1.00	0.05
Flexure	1.10	0.10	1.00	0.05
Shear and *Web Crippling*	1.10	0.10	1.00	0.05
Under Combined Forces	1.05	0.10	1.00	0.05
Other Member Limit States[1]	1.00	0.10	1.00	0.05
Connections and Joints				
Weld *Connections*	1.10	0.10	1.00	0.10
Bolted *Connections*	1.10	0.08	1.00	0.05
Screw *Connections*	1.10	0.10	1.00	0.10
Power-Actuated Fasteners	1.10	0.10	1.00	0.10
Other Connectors or Fasteners[2]	1.10	0.10	1.00	0.15
Connections to Structural Concrete	1.10	0.10	0.90	0.10
Connections to Wood	1.10	0.15	1.00	0.15

Notes:
1. For member limit states captured in testing but not covered in AISI S100.
2. For steel-to-steel connectors and fasteners not already listed in the table.

7.5.2 Result of reliability analysis

Following the calculation methodology outlined in Section 7.5, a reliability analysis has been conducted on the newly developed Direct Strength Method (DSM) design equations, utilising both the Minimum Design Method (MDM) and the Smooth Transition Method (STM). This analysis includes a comparison of the resistance factors derived from these new equations with those stipulated by the current design standards as shown in Table 57 for MDM and Table 58 for STM respectively.

Table 57 Reliability Analysis for DSM design equation using MDM

LC-FC	P_m	C_P	V_P	φ_b	φ_{hat}	φ_{deck}
EOF-F	0.976	1.174	0.086	0.823	0.75	0.90
EOF-UF	1.086	1.078	0.168	0.829	0.75	0.60
ETF-F	1.064	1.102	0.165	0.814	0.85	0.85
ETF-UF	1.071	1.324	0.065	0.917		0.90
IOF-F	1.029	1.085	0.137	0.821	0.80	0.85
IOF-UF	1.157	1.196	0.073	0.986	0.90	0.90
ITF-F	1.008	1.093	0.153	0.786	0.85	0.85
ITF-UF	1.212	1.324	0.065	1.037		0.90
Summary	1.061	1.015	0.145	0.842		

Table 58 Reliability Analysis for DSM design equation using STM

LC-FC	P_m	C_P	V_P	φ_b	φ_{hat}	φ_{deck}
EOF-F	0.910	1.174	0.103	0.753	0.75	0.90
EOF-UF	1.195	1.078	0.218	0.840	0.75	0.60
ETF-F	1.120	1.102	0.226	0.771	0.85	0.85
ETF-UF	0.989	1.324	0.085	0.830		0.90
IOF-F	1.084	1.085	0.183	0.808	0.80	0.85
IOF-UF	1.145	1.196	0.073	0.976	0.90	0.90
ITF-F	1.025	1.093	0.185	0.760	0.85	0.85
ITF-UF	1.242	1.324	0.065	1.063		0.90
Summary	1.094	1.015	0.196	0.806		

The reliability analysis yields a broad conclusion that for the majority of loading cases, the resistance/capacity factors are similar or surpass those offered by the current standard AS/NZS 4600:2018 Table 3.3.6.2(D), as indicated in the φ_{hat} column as shown in Table 57 and Table 58. Although certain cases, such as the ETF-F loading cases under both MDM and STM design equations, exhibit a marginally lower resistance/capacity factor, this difference is considered insignificant.

Of note, the enhanced prediction accuracy in P_{exp}/P_n values without applying the resistance factor compensates for any minor shortfall in the safety factor's application, marking a notable advancement over the methodologies currently adopted by the standards.

7.6 CALCULATION EXAMPLE

A calculation example is provided for demonstrating the localised loading capacity prediction procedure for hat section subject to ITF-F loading case.

The cross-section drawing of the hat section is shown in Figure 158. The length of the specimen is 600 mm, and the yield stress of the steel is 323 MPa.

The buckling load calculation is performed by using the THIN-WALL-PYTHON program introduced in Chapter 3. The yield load is calculated in accordance with the yield mechanism model and P_y calculation equations presented in Chapter 6.

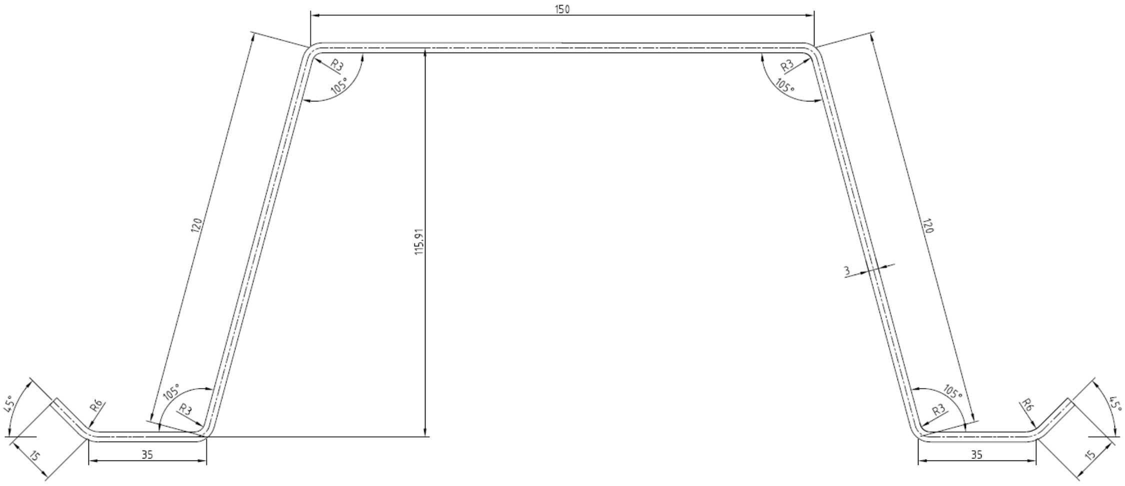

Figure 158 Hat section cross-section dimensions for calculation example (Unit: mm)

The buckling load has been calculated using THIN-WALL-PYTHON. $P_{cr} = 221.63\ kN$.

7.6.1 Calculation of Py

$$P_y = k_w F_{sw} \quad (7\text{-}7)$$

where

k_w is the number of the web. For hat sections, $k_w = 2$.

$$F_{sw} = \frac{M_p}{k_\theta r_c \tan\beta} \times \sum_{i=1}^{n} k_{\omega_i} L_i \quad (7\text{-}8)$$

M_p is the plastic moment per unit length of plate,

$$M_p = \frac{f_y t^2}{4} = \frac{323 \times 3^2}{4} = 726.75\ Nmm/mm \quad (7\text{-}9)$$

k_θ is a factor for the number of loaded flanges, for ITF-F loading case, $k_\theta = 2$;

r_c is the corner radius measured from the centreline,

$$r_c = r_{in} + 0.5t = 3 + 0.5 \times 3 = 4.5\ mm \quad (7\text{-}10)$$

$\tan\beta$ is the adjustment factor for the sloped web sections to consider the change of eccentricity applied on r_c where β is calculated in accordance with Figure 131.

$$\beta = \frac{180° - (90 + \alpha)}{2} = \frac{90° - \alpha}{2} = 37.5 \quad (7\text{-}11)$$

Thus, $\tan\beta = 0.7673$.

The eccentricity of load e is calculated as

$$e = r_c \tan\beta = 3.453\ mm \quad (7\text{-}12)$$

Thus,

$$\frac{e}{t} = \frac{3.453}{3} = 1.151 \tag{7-13}$$

7.6.1.1 Length of yield lines

In the calculation of yield line length for a typical hat section subject to ITF-F loading case, there are four yield lines identified.

The yield line on the top flange (L_{TF}) is calculated by:

$$L_{CT} = L_{TF} + 2 \times k_{dc} \times r_c \tan\beta$$

$$L_{CT} = 56 + 2 \times 2.5 \times 3.4529 = 73.265\, mm \tag{7-14}$$

$$L_{TW} = L_{CT} + 2 \times k_{dw} \times (a - r_c \tan\beta) = 179.453\, mm \tag{7-15}$$

where

$k_{dw} = 2$, given in the Table of summary of the exponents (Table 25) and factors for the P_y model;

a is the distance between the top yield line to the top flange, calculated by:

$$a = H \times k_H = 120 \times 0.25 = 30\, mm \tag{7-16}$$

The yield line on the bottom flange (L_{BF}) and the bottom of the web (L_{BW}) is identical to L_{TF} and L_{TW} respectively. Hence, all the yield line lengths are identified.

A summary of the yield line lengths from top to bottom are given as below:

$L_{TF} = L_1 = 56\, mm$;

$L_{TW} = L_2 = 179.453\ \ mm$;

$L_{BW} = L_3 = 179.453\ \ mm$;

$L_{BF} = L_4 = 56\, mm$.

7.6.1.2 Rotation factor

The rotation factors k_{ω_i} are calculated based on the yield line location as shown in Table 26. The relationship between the yield line locations and rotation angle is demonstrated in Figure 159.

For a typical hat section subject to ITF-F loading case,

$$h_a = h_c, h_b = h_d \tag{7-17}$$

In this case, $h_a = h_b = h_c = h_d = 30\, mm$.

The rotation angle for each yield line on one web from top to bottom is calculated as follows:

$$\omega_1 = \theta_1 \tag{7-18}$$

$$\omega_2 = \theta_1 + \phi \tag{7-19}$$

$$\omega_3 = \theta_2 + \phi \tag{7-20}$$

$$\omega_4 = \theta_2 \tag{7-21}$$

$$\phi = \frac{\theta_1 h_a + \theta_2 h_c}{h_b + h_d} \tag{7-22}$$

The hinge locations on the webs are symmetrical between the top and bottom which result in $\theta_1 = \theta_2 = \theta$, hence $\omega_1 = \omega_4 = \theta, \omega_2 = \omega_3 = 2\theta$.

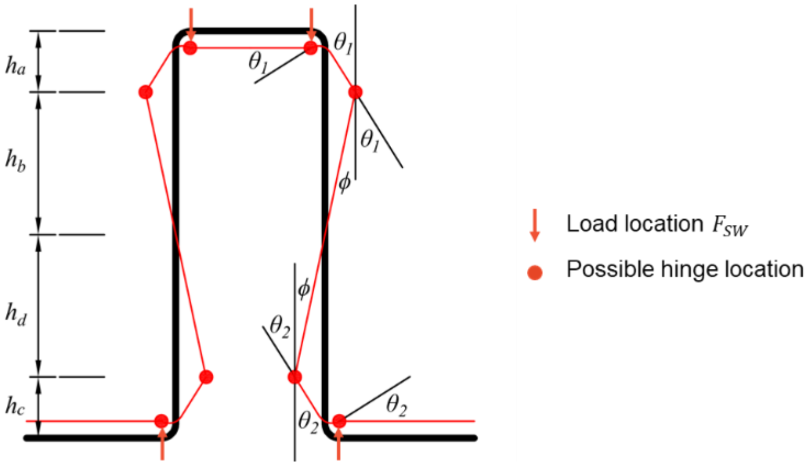

Figure 159 Plastic mechanism model for a typical hat section: ITF loading case

Thus, a summary of the k_{ω_i} is given as below:

$k_{\omega_1} = k_{\omega_4} = 1$;

$k_{\omega_2} = k_{\omega_3} = 2$.

7.6.1.3 Py calculation and plastic moment capacity reduction

A Python software has been developed for the calculation of P_y using the proposed method introduced in Section 6.2.3.2.

```
 The quadratic equation is given as Ax^2 + Bx + C = 0, where:
  A = 2.817e-08
  B = 9.503e-03
  C = -8.298e+02
 The solution is as follows: (Only the positive solution is the valid
solution.)
  Sol1 = 7.197e+04 N
  Sol2 = -4.092e+05 N
 Fsw = 71.969 kN
```

Thus, the yield load is given as

$$P_y = 71.969 \times 2 = 143.938\ kN \tag{7-23}$$

The slenderness is given as

$$\lambda = \sqrt{\frac{P_y}{P_{cr}}} = \sqrt{\frac{143.938}{221.63}} = 0.81 \tag{7-24}$$

7.6.2 Pn calculation using DSM (MDM)

The general DSM design equation using MDM is written as

$$\frac{P_n}{P_y} = k_p \frac{1+a\lambda^c}{1+b\lambda^d} \tag{7-25}$$

Where a, b, c, d and kp are DSM design equation coefficients determined from Table 33.

The e/t ratio is equal to 1.151, which falls in the Design Group 1. Thus,

$$\frac{P_n}{P_y} = 1.0 \times \frac{1+0.11\times0.81^2}{1+1.15\times0.81^2} = 0.613 \tag{7-26}$$

The nominal capacity is calculated by

$$P_n = \frac{P_n}{P_y} \times P_y = 0.613 \times 143.938 = 88.284\ kN \tag{7-27}$$

For the safety index $\beta_0 = 2.5$ scenario, the design capacity is given by

$$\phi P_n = 0.786 \times 90.294 = 70.971 kN \tag{7-28}$$

7.6.3 Pn calculation using DSM (STM)

The general design equation using STM is written as

$$\frac{P_n}{P_y} = k_p \frac{1+a\lambda^c\times\zeta^k}{1+b\lambda^d\times\zeta^k} \tag{7-29}$$

where

$\zeta = t/e$, the inverse of e/t, with a limit of $1.5 \leq e/t \leq 4.5$;

$\frac{e}{t}$ is equal to 1.151, taken as 1.5, thus $\zeta = 0.667$;

k is a coefficient of ζ. $k = 0.5$ for EOF-UF loading case; $k = 1$ for all other cases.

The DSM design equation coefficient is given in Table 34, For ITF-F loading case, $k_p = 1.1, a = 0.12, b = 1.92, c = d = 2$.

Thus,

$$\frac{P_n}{P_y} = 1.1 \times \frac{1+0.12\times 0.81^2 \times 0.667^1}{1+1.92\times 0.81^2 \times 0.667^1} = 0.632 \quad (7\text{-}30)$$

The nominal capacity is calculated by

$$\frac{P_n}{P_y} \times P_y = 0.632 \times 143.938 = 90.951\ kN \quad (7\text{-}31)$$

For the safety index $\beta_0 = 2.5$ scenario, the design capacity is given by

$$\phi P_n = 0.760 \times 90.951 = 69.123\ kN \quad (7\text{-}32)$$

7.7 COMAPRSION BETWEEN CURRENT DESIGN STANDARD AND DSM DESIGN EQUATIONS

A comparison is conducted between the prediction results from the current standard AS4600:2018 Table 3.3.6.2(D) to the newly proposed DSM design equations using MDM as an example. The test results are benchmarked against both of the prediction methods (AS4600 method and DSM method, noted as P_{AS} and P_{DSM}), without the application of safety factors. The complete data is attached in Appendix I.

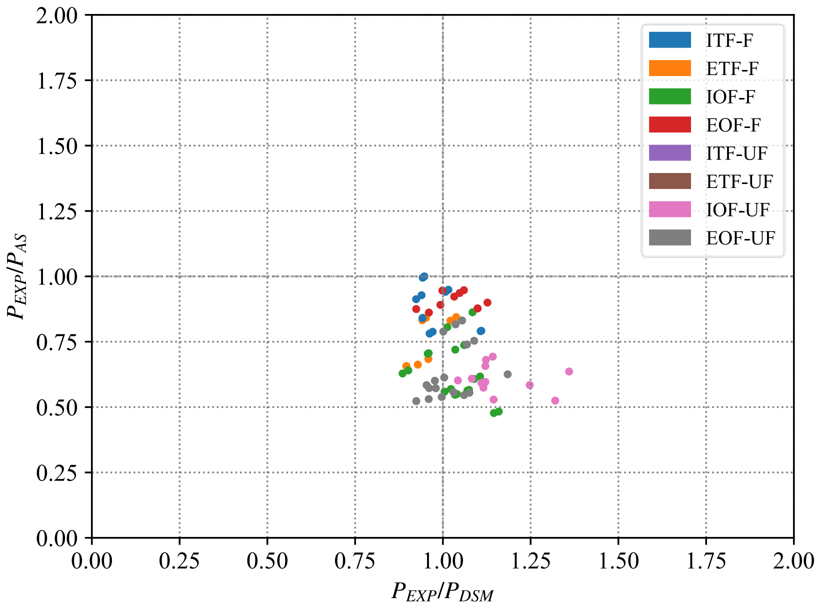

Figure 160 Comparison of the experimental results (P_{EXP}) against prediction results: AS4600 (P_{AS}) and DSM design equations (P_{DSM}), for vertical sections without safety factors

According to the Figure 160, most of the data points show the P_{EXP}/P_{AS} value lower than 1.0, indicating an unconservative prediction when using AS4600. However, for the value of P_{EXP}/P_{DSM} most of the data points scatter around 1.0, demonstrating that the advanced DSM design equation provides a more precise prediction.

A deviation analysis is also performed using the data listed in Appendix I, including both vertical and sloped web sections. Average (AVE), Standard Deviation (StdDev) and Coefficient of Variation (COV) are calculated for P_{EXP}/P_{AS} and P_{EXP}/P_{DSM} as shown in Table 59. The slight over 1.0 AVE value along with the smaller COV value confirm the improved accuracy of the advanced DSM design equations.

Table 59 Deviation analysis regarding P_{EXP}/P_{AS} and P_{EXP}/P_{DSM}

	AVE	**StdDev**	**COV**
P_{EXP}/P_{AS}	0.715	0.146	0.204
P_{EXP}/P_{DSM}	1.061	0.154	0.145

7.8 CONCLUSION

This chapter comprehensively analyses the developments and insights surrounding the Direct Strength Method (DSM) design equations, particularly focusing on the improvement of the design equations using the basic/lower bound versions proposed in conference papers in 2022 and 2023. The discussions have underscored the e/t value's important role, affirming its necessity in the DSM design equations for hat sections.

Two innovative concepts for the DSM design equation, the Minimum Design Method (MDM) and the Smooth Transition Method (STM), were introduced, each based on distinct principles for determining design curves. A critical observation made is the importance of imposing an upper yield stress limit of 800 MPa on the newly proposed DSM design equations to ensure their applicability and reliability.

A comparative evaluation of the new design equations against the current AS/NZS 4600:2018 standard revealed that the updated DSM equations offer enhanced capacity predictions. These improvements are attributed to the inclusion of sloped web sections, resulting in broader section coverage, improved average values, and comparable or better coefficients of variation (COV) across various cases.

Furthermore, a reliability analyses conducted in this chapter demonstrate that the newly developed DSM design equations exhibit similar or improved resistance/capacity factors when compared to existing benchmarks.

In conclusion, the advancements in DSM design equations discussed in this chapter signify a substantial step forward in the application of DSM for structural design, offering more accurate, reliable, and comprehensive solutions for the prediction of localised loading capacity.

Chapter 8 Conclusions and future study

8.1 INTRODUCTION

This chapter summarizes the key outcomes of this thesis based on the study utilising the Direct Strength Method (DSM) for the design of hat-shaped sections subjected to localised loading. Section 8.2 covers the main findings of this research.

The advancements made in the calculation of both the buckling load and the yield load are discussed first, followed by an introduction to the development of the DSM design equations. This development is based on the latest formulation of the DSM equation that has been recently proposed.

Finally, Section 8.3 discusses the limitations of the current research and provides recommendations for future research directions.

8.2 CONCLUSION OF THE THESIS

8.2.1 Buckling load

The buckling load serves as an important input for the application of the Direct Strength Method. In this thesis, the author has developed a new version of the THIN-WALL-PYTHON program that incorporates the improved bfinst10R.cpp module. This module applies the Semi-Analytical Finite Strip Method (SAFSM) to perform the buckling analysis of hat-shaped sections subjected to localised loading, covering all the commonly encountered loading cases.

The results obtained from this advanced Finite Strip Method (FSM) approach have been benchmarked against the results from the Finite Element Method (FEM)-based ABAQUS software. The promising agreement between the two sets of results has proven the validity of extending the SAFSM for the purpose of buckling analysis of hat-shaped sections. Consequently, the updated THIN-WALL-PYTHON program can be considered as a viable alternative for conducting the necessary buckling analyses. Relevant discussion is presented in Chapter 3.

8.2.2 Yield load

The yield load is the other important input for the application of the Direct Strength Method. In this thesis, a simplified and consistent finite element model has been developed for hat sections subjected to localised loading, covering all four loading cases. Each of the loading cases includes two fastening conditions: with and without the presence of fasteners. A comprehensive experimental program has been carried out to investigate the yielding behaviours of these hat sections. During the experimental program, both of the failure mechanisms, namely yield arc mechanism and rolling mechanism, have been observed in sections with different rounded corners. This part has been discussed in Chapter 4.

Simultaneously, two sets of numerical models have been developed using different types of finite elements, based on the data collected from the experimental study. It has been discovered that the results from the solid element models provide better predictive accuracy compared to the shell element models, particularly for the stockier sections. To further enhance the understanding of the behaviours, a thorough parametric study was also conducted to investigate the sensitivity of the loading capacity against the change in various parameters. In addition, the Minimum Clear Distance has been reviewed and it is suggested that the height of the web including the rounded corner should be used for determining the MCD, as the rounded corner should be considered as part of the web for transferring the load and introducing the eccentricity. This part has been discussed in Chapter 5.

8.2.3 Plastic mechanism models and DSM design equations

Based on the observations gathered from the experiments and the numerical modelling, plastic mechanism models have been developed to calculate the yield load for use in the DSM design equations. This generic model not only covers hat sections with both vertical webs and sloped webs, but also includes the reduction in plastic moment capacity that is subject to the presence of axial force. The eccentricity of the load, or the non-dimensioned value e/t was found to be of great importance in the determination of Load – Displacement behaviours rather than purely the rounded corner radius.

A preliminary and lower bound version of the DSM design equation has been proposed to offer insights into the DSM design curves for localised loading using the new and consistent format. The preliminary version of DSM design equation demonstrates a reasonably accurate prediction for small e/t ratio sections and conservative prediction for large e/t ratio sections. This part has been covered in Chapter 6.

In Chapter 7, using the preliminary version of the DSM design equation as a baseline, all experimental and numerical data were plotted in different ways to explore possible solutions that could facilitate the improved design of hat sections with large e/t ratios. Two distinct concepts were proposed for the design rules within the DSM design equations - the Minimum Design Method (MDM) and the Smooth Transition Method (STM).

The predicted results obtained with the updated versions of the DSM design equations, incorporating these two proposed methods, have been benchmarked against the current design standard AS/NZS4600:2018. The results from the updated DSM equations demonstrate a great enhancement in the capacity predictions. This not only expands the range of applicable sections, but also offers significantly better accuracy in predicting the localised loading capacity compared to the current standard.

8.3 LIMITATIONS AND SUGGESTIONS FOR FUTURE RESEARCH

This research provides valuable insights into the yielding behaviour of hat-shaped sections subjected to localised loading under various loading cases. However, the scope of this research has certain limitations. The following discussion is useful to identify areas for further investigations.

Throughout this research, the main purpose was to understand the yielding behaviour. As a result, the material selected for manufacturing the test specimens was HA250 steel with a thickness of 3 mm, as this material had a clear yield strength, and the sections were stocky enough to reach yielding failure before the buckling load was attained. Consequently, the experimental data points fall within the stocky section range. To fill the gap between the stocky sections and the high slenderness sections, datapoints from numerical studies using verified models were used in this study.

In terms of the section dimensions, future research is suggested to fill the gap between the 0.7366 mm thickness tested by Wu et al. and the 3 mm thickness used by the author. Additionally, the e/t ratio range of 1.5 to 6 still has a large gap that needs to be addressed. The effect of longitudinal web stiffeners on the behaviour is yet to be investigated. However, some of the commercially available hat-shaped sections come with longitudinal web stiffeners, so testing of these commercial sections with a variety of thicknesses and dimensions would be a good starting point for further experimental studies. Additional experimental validation is recommended for sections with large corner radii (Group 3). While limited numerical analyses demonstrate these sections develop capacity through rolling mechanisms and require deformations potentially exceeding serviceability limits, physical testing would strengthen the reliability of proposed design methods and enhance understanding of their structural behaviour. This additional testing was not conducted due to time constraints.

Regarding the material, while the newly proposed Direct Strength Method (DSM) design equations are deemed adequate for materials with yield strengths under 800 MPa, in the foreseeable future, people may seek the use of higher strength steels in other industries. Thus, future research is suggested to expand the material range from low-strength to high-strength steel (e.g., G450 and G550) and even super-high-strength steel up to 1000 MPa. While the behaviour of super-high-strength materials is known to differ from those typically used in the construction industry, it is necessary to carry out further experimental investigations to determine the appropriate coefficients for these higher-strength materials.

In terms of the loading cases, the scope of this study has focused on the loading cases listed in the relevant standards – the four basic loading cases, each with two fastening conditions. However, it is important to note that hat-shaped sections are singly symmetric about the Y-axis. As a result, there might be differences in the behaviour when the hat section is loaded downwards versus loaded upwards. This study has primarily investigated the loading of the hat sections in the downward direction. Therefore, future research is recommended to expand the investigation to include the loading of hat sections in the upward direction as well.

In addition to the typical loading cases listed in the standards, a previous study has demonstrated a loading case that is not currently included in the AISI S909-17 specification. This involves the specimen being placed on a flat surface and subjected to localised loading from the top, or vice versa. While not covered in the current standards, this additional loading scenario could provide valuable insights and should be considered for future research.

A significant advancement has been made in the numerical study, with the utilisation of solid elements for the analysis of thick sections. However, due to the limitations of computational resources, the use of solid elements for hat sections with a thickness less than 2 mm was found to be time-consuming. This obstacle can potentially be overcome by leveraging more powerful supercomputing resources to perform the required parametric studies. The data generated from these extensive numerical simulations can subsequently be used to feed into a machine learning program, which could help streamline the analysis for better design equations for thin-walled sections.

The experimental and numerical methodology used in this thesis was found to be reliable and efficient in investigating the strength and behaviour of hat-shaped sections subjected to localised loading. The experimental data, along with the collected data from previous research, have been included in the Appendix for the benefit of future studies.

In conclusion, this thesis has made significant progress in the study of the yielding behaviour of hat sections and the development of the Direct Strength Method for the design of hat sections under localised loading. However, there remains considerable scope to expand the range of this research topic in the future.

This page intentionally left blank.

Bibliography

[1] AISI-S100-2016, Aisi-S100-2016, (2016). https://cfsei.memberclicks.net/assets/docs/publications/aisi-standards/aisi s100-12 s100-12-c_9-21-17_s.pdf.

[2] Standards Australia, AS/NZS 4600:2018 : Cold-formed steel structures, (2018).

[3] AISI S909-(2017), Test Standard for Determining the Web Crippling Strength of Cold-Formed Steel Flexural Members, (2017) 15–25.

[4] M.C.M. Bakker, Web crippling of cold-formed steel members, Technische Universiteit Eindhoven, 1992. https://doi.org/10.6100/IR387877.

[5] T. Wierzbicki, W. Abramowicz, On the Crushing Mechanics of Thin-Walled Structures, J. Appl. Mech. 50 (1983) 727–734. https://doi.org/10.1115/1.3167137.

[6] C. Santaputra, Web crippling of high strength cold-formed steel beams, UNIVERSITY OF MISSOURI-ROLLA, 1986. https://scholarsmine.mst.edu/doctoral_dissertations/630.

[7] C. Santaputra, M.B. Parks, W.W. Yu, Web Crippling Strength of Cold-Formed Steel Beams, J. Struct. Eng. 115 (1989) 2511–2527. https://doi.org/10.1061/(ASCE)0733-9445(1989)115:10(2511).

[8] K.C. Rockey, M.A. El-Gaaly, D.K. Bagchi, Failure of Thin-Walled Members under Patch Loading, J. Struct. Div. 98 (1972) 2739–2752. https://doi.org/10.1061/JSDEAG.0003400.

[9] M.C.M. Bakker, J.W.B. Stark, Theoretical and experimental research on web crippling of cold-formed flexural steel members, Thin-Walled Struct. 18 (1994) 261–290. https://doi.org/10.1016/0263-8231(94)90006-X.

[10] H. Hofmeyer, Cross-section crushing behaviour of hat-sections (Part I: Numerical modelling), Thin-Walled Struct. 43 (2005) 1143–1154. https://doi.org/10.1016/j.tws.2005.03.009.

[11] H. Hofmeyer, Cross-section crushing behaviour of hat-sections (part II: Analytical modelling), Thin-Walled Struct. 43 (2005) 1155–1165. https://doi.org/10.1016/j.tws.2005.03.012.

[12] R. Baehre, Sheet Metal Panels for Use in Building Construction., (1975) 383–455.

[13] W. Yu, Web crippling and combined web crippling and bending of steel decks, 1981. https://scholarsmine.mst.edu/ccfss-library/187.

[14] B.A. Wing, Web crippling and the interaction of bending and web crippling of unreinforced multi-web cold-formed steel sections, University of Waterloo, 1981. https://ocul-wtl.primo.exlibrisgroup.com/permalink/01OCUL_WTL/vk29fk/alma9913774

43505162.

[15] C. Santaputra, W.W. Yu, Design of automotive structural components using high strength sheet steels: web crippling of cold-formed steel beams, 1986. https://scholarsmine.mst.edu/ccfss-library/100.

[16] S. Wu, W. Yu, R.A. Laboube, Strength of flexural members using structural grade 80 of A653 steel (web crippling tests), (1997).

[17] G.J. Hancock, Z. Chen, Y. Xie, C.H. Pham, Recent developments in the DSM localised loading design of cold-formed steel sections, Ninth Int. Conf. Thin-Walled Struct. Sydney. (2023).

[18] Y. K. Cheung, Finite Strip Method in Structural Analysis, 1st ed., Pergamon Press, 1976.

[19] N.M.F. Silva, D. Camotim, N. Silvestre, Generalized beam theory formulation able to capture load application and localized web buckling effects, 19th Int. Spec. Conf. Recent Res. Dev. Cold-Formed Steel Des. Constr. (2008) 33–59.

[20] G.J. Hancock, C.H. Pham, Buckling analysis of thin-walled sections under localised loading using the semi-analytical finite strip method, Thin-Walled Struct. 86 (2015) 35–46. https://doi.org/10.1016/j.tws.2014.09.017.

[21] V.V. Nguyen, G.J. Hancock, C.H. Pham, Analyses of thin-walled sections under localised loading for general end boundary conditions – Part 1: Pre-buckling, Thin-Walled Struct. 119 (2017) 956–972. https://doi.org/10.1016/j.tws.2017.01.010.

[22] V.V. Nguyen, G.J. Hancock, C.H. Pham, Analyses of thin-walled sections under localised loading for general end boundary conditions – Part 2: Buckling, Thin-Walled Struct. 119 (2017) 973–987. https://doi.org/10.1016/j.tws.2017.01.008.

[23] V.V. Nguyen, Direct strength method for The design of cold-formed STEEL sections under localised loading, PhD Thesis. (2017).

[24] G.J. Hancock, C.H. Pham, Finite strip methods for stability analysis of thin-walled members with applications to the Direct Strength Method of design, in: Anal. Des. Plated Struct., Elsevier, 2022: pp. 177–210. https://doi.org/10.1016/B978-0-12-823570-6.00011-2.

[25] K.S. Sivakumaran, K.M. Zielonka, Web crippling strength of thin-walled steel members with web opening, Thin-Walled Struct. 8 (1989) 295–319. https://doi.org/10.1016/0263-8231(89)90035-9.

[26] V. V Degtyarev, H. Chen, C.D. Moen, K.D. Peterman, B.W. Schafer, S. Torabian, S. Zhou, Finite element analysis of web crippling behavior of cold-formed steel members : modeling recommendations based on a review of best practices, (2023). https://cloud.aisc.org/SSRC/2023/Degtyarev_et_al_SSRC_2023.pdf.

[27] B. Young, G.J. Hancock, Design of Cold-Formed Channels Subjected to Web Crippling, J. Struct. Eng. 127 (2001) 1137–1144. https://doi.org/10.1061/(ASCE)0733-9445(2001)127:10(1137).

[28] V.V. Nguyen, G.J. Hancock, C.H. Pham, Consistent and Simplified Direct Strength Method for Design of Cold-Formed Steel Structural Members under Localized Loading, J. Struct. Eng. 146 (2020). https://doi.org/10.1061/(ASCE)ST.1943-541X.0002609.

[29] V.V. Nguyen, G.J. Hancock, C.H. Pham, Development of the Thin-Wall-2 Program for Buckling Analysis of Thin-Walled Sections, Eighth Int. Conf. Adv. STEEL Struct. (2015) 1–20.

[30] P. Natário, N. Silvestre, D. Camotim, Direct strength prediction of web crippling failure of beams under ETF loading, Thin-Walled Struct. 98 (2016) 360–374. https://doi.org/10.1016/j.tws.2015.09.012.

[31] R.S. Glauz, B.W. Schafer, Modifications to the Direct Strength Method of cold-formed steel design for members unsymmetric about the axis of bending, Thin-Walled Struct. 173 (2022) 109025. https://doi.org/10.1016/j.tws.2022.109025.

[32] R.S. Glauz, Enhancements to the Direct Strength Method of cold-formed steel member design, Thin-Walled Struct. 183 (2023) 110421. https://doi.org/10.1016/j.tws.2022.110421.

[33] B.W. Schafer, R.S. Glauz, A novel functional form for the application of the Direct Strength Method, Ninth Int. Conf. THIN-WALLED Struct. - ICTWS2023. (2023).

[34] Dassault Systèmes, Abaqus 2016 Abaqus/Cae User's Guide, (2016) 1144.

[35] C.H. Pham, G.J. Hancock, Shear buckling of thin-walled channel sections, J. Constr. Steel Res. 65 (2009) 578–585. https://doi.org/10.1016/j.jcsr.2008.05.015.

[36] Z. Chen, C.H. Pham, G.J. Hancock, Plastic mechanism models for use in DSM localised loading design of hat sections, Thin-Walled Struct. 206 (2025) 112683. https://doi.org/10.1016/j.tws.2024.112683.

[37] BlueScope Steel Limited., Hot rolled strip AS / NZS 1594 – HA250, 2002 (2019) 1–2.

[38] BlueScope Steel Limited., Lysaght Topspan Design and Installation Guide for Building Professionals, (2016). https://professionals.lysaght.com/sites/default/files/LysaghtTopspanDesignAndInstallationGuideJuly14v3.pdf.

[39] M. Bakker, T. Peköz, Comparison and evaluation of web crippling prediction formulas, Cent. Cold-Formed Steel Struct. Libr. (1985). https://scholarsmine.mst.edu/ccfss-library/152.

[40] R.B. Cruise, L. Gardner, Strength enhancements induced during cold forming of stainless steel sections, J. Constr. Steel Res. 64 (2008) 1310–1316. https://doi.org/10.1016/j.jcsr.2008.04.014.

[41] L. Sundararajah, Web Crippling Studies of Cold-formed Steel Channel Beams (Experiments, numerical analyses and design rules), (2017).

[42] L. Sundararajah, M. Mahendran, P. Keerthan, New design rules for lipped channel beams subject to web crippling under two-flange load cases, Thin-Walled Struct. 119 (2017) 421–437. https://doi.org/10.1016/j.tws.2017.06.003.

[43] P. Natário, N. Silvestre, D. Camotim, Computational modelling of flange crushing in cold-formed steel sections, Thin-Walled Struct. 84 (2014) 393–405. https://doi.org/10.1016/j.tws.2014.07.006.

[44] J. He, B. Young, Behaviour of cold-formed steel built-up I-sections with perforated web under localized forces, J. Constr. Steel Res. 190 (2022) 107129. https://doi.org/10.1016/j.jcsr.2022.107129.

[45] J. He, B. Young, Web crippling of cold-formed steel built-up box sections, Thin-Walled Struct. 171 (2022) 108789. https://doi.org/10.1016/j.tws.2021.108789.

[46] H. Hofmeyer, S.W.A. Geers, H.H. Snijder, B.W. Schafer, The Direct Strength Method for first generation trapezoidal steel sheeting under Interior One Flange and Interior Two Flange web crippling, Thin-Walled Struct. 180 (2022). https://doi.org/10.1016/j.tws.2022.109795.

[47] The Unviersity of Sydney, Artemis User Guide, (2017). https://www.sydney.edu.au/dam/intranet/documents/working/it-phones/Artemis-User-Guide-Mar2017.pdf.

[48] M.M. Pastor, M. Casafont, J. Bonada, F. Roure, Imperfection amplitudes for nonlinear analysis of open thin-walled steel cross-sections used in rack column uprights, Thin-Walled Struct. 76 (2014) 28–41. https://doi.org/10.1016/j.tws.2013.10.025.

[49] C.H. Pham, G.J. Hancock, Numerical simulation of high strength cold-formed purlins in combined bending and shear, J. Constr. Steel Res. 66 (2010) 1205–1217. https://doi.org/10.1016/j.jcsr.2010.04.014.

[50] N. Silvestre, D. Camotim, GBT-Based Analysis of The Distortional Post-Buckling Behaviour of Cold-Formed Steel Z-Section Columns and Beams, in: Thin-Walled Struct., CRC Press, 2018: pp. 243–250. https://doi.org/10.1201/9781351077309-25.

[51] B.W. Schafer, T. Peköz, Computational modeling of cold-formed steel: Characterizing geometric imperfections and residual stresses, J. Constr. Steel Res. 47 (1998) 193–210. https://doi.org/10.1016/S0143-974X(98)00007-8.

[52] E. Kanthasamy, D.L. Chandramohan, G. Shanmuganathan, K. Poologanathan, P. Gatheeshgar, M. Corradi, A. Mcintosh, Web crippling behaviour of cold-formed high-strength steel unlipped channel beams under End-One-Flange load case, Case Stud. Constr. Mater. 16 (2022) e01022. https://doi.org/10.1016/j.cscm.2022.e01022.

[53] R.A.J. Heurkens, H. Hofmeyer, M. Mahendran, H.H. Snijder, Direct strength method for web crippling—Lipped channels under EOF and IOF loading, Thin-Walled Struct. 123 (2018) 126–141. https://doi.org/10.1016/j.tws.2017.11.008.

[54] B. Young, G.J. Hancock, Cold-Formed Steel Channels Subjected to Concentrated Bearing Load, J. Struct. Eng. 129 (2003) 1003–1010. https://doi.org/10.1061/(ASCE)0733-9445(2003)129:8(1003).

[55] M. MacDonald, M.A. Heiyantuduwa Don, M. Kotełko, J. Rhodes, Web crippling behaviour of thin-walled lipped channel beams, Thin-Walled Struct. 49 (2010) 682–690. https://doi.org/10.1016/j.tws.2010.09.010.

[56] M. MacDonald, M.A. Heiyantuduwa, A design rule for web crippling of cold-formed steel lipped channel beams based on nonlinear FEA, Thin-Walled Struct. 53 (2012) 123–130. https://doi.org/10.1016/j.tws.2012.01.003.

[57] G.J. Hancock, X.L. Zhao, Research into the strength of cold-formed tubular sections, J. Constr. Steel Res. 23 (1992) 55–72. https://doi.org/10.1016/0143-974X(92)90036-E.

[58] Standards Australia, AS 4100-1998 (R2016) : Steel structures, 1998 (2016).

[59] X.L. Zhao, G.J. Hancock, Experimental verification of the theory of plastic-moment capacity of an inclined yield line under axial force, Thin-Walled Struct. 15 (1993) 209–233. https://doi.org/10.1016/0263-8231(93)90027-8.

[60] X.L. Zhao, G.J. Hancock, A theoretical analysis of the plastic-moment capacity of an inclined yield line under axial force, Thin-Walled Struct. 15 (1993) 185–207. https://doi.org/10.1016/0263-8231(93)90026-7.

[61] Z. Chen, C.H. Pham, G.J. Hancock, Yield Models for use in DSM Localised Loading Design of Hat Sections, 2022 (2022) 1–13. https://jscholarship.library.jhu.edu/handle/1774.2/40427.

[62] Z. Chen, C.H. Pham, G.J. Hancock, Plastic mechanism models for use in DSM localised loading design of hat sections under one-flange-loading, Ninth Int. Conf. Thin-Walled Struct. Sydney. (2023).

This page intentionally left blank.

Appendices

Appendix A

Coupon test data (stress – strain curve)

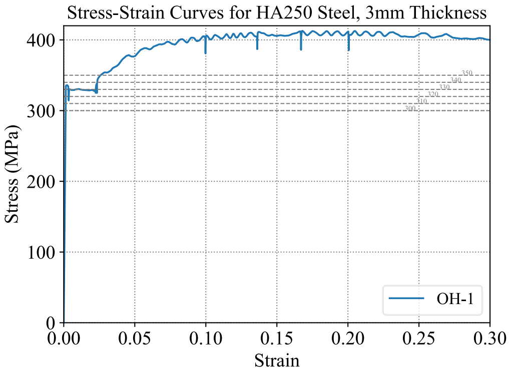

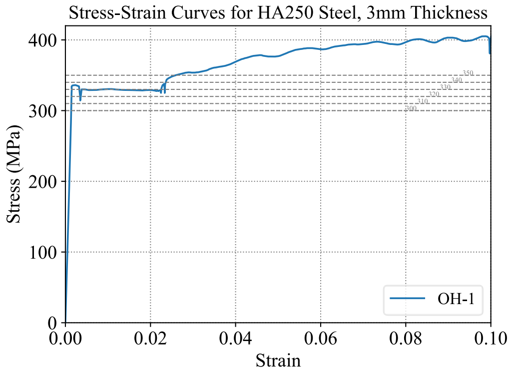

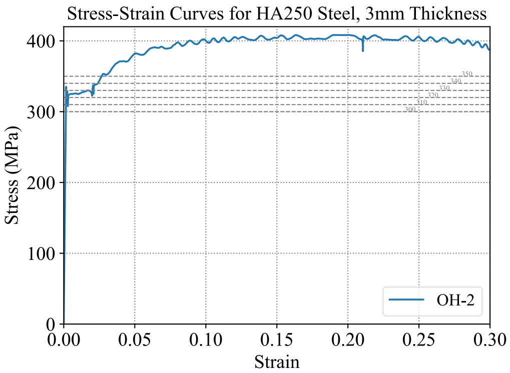

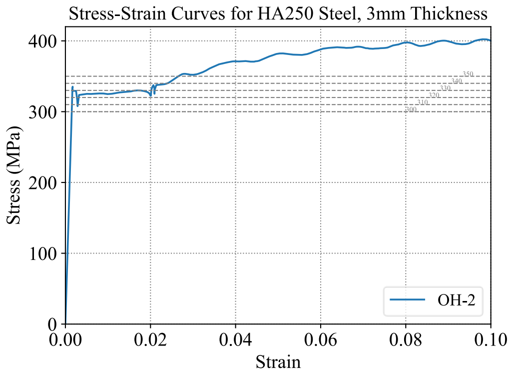

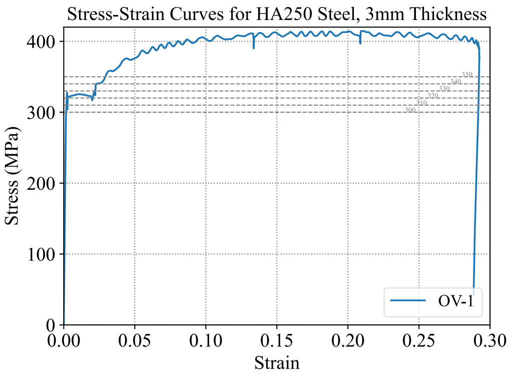

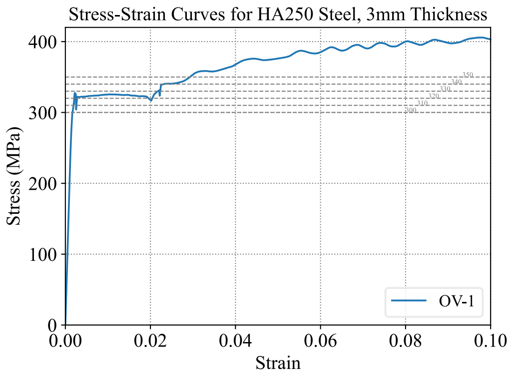

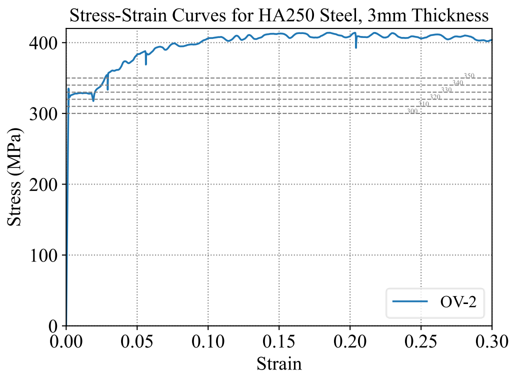
Stress-Strain Curves for HA250 Steel, 3mm Thickness
Stress (MPa)
0
100
200
300
400
0.00
0.05
0.10
0.15
0.20
0.25
0.30
Strain
OV-2

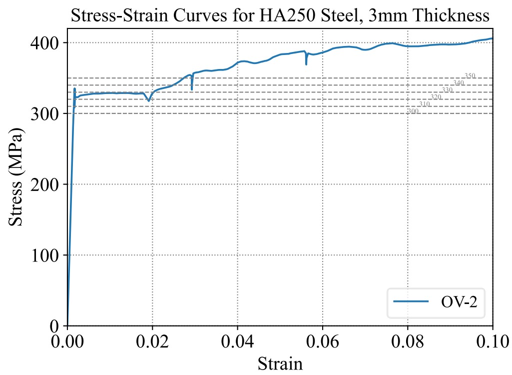
Stress-Strain Curves for HA250 Steel, 3mm Thickness
Stress (MPa)
0
100
200
300
400
0.00
0.02
0.04
0.06
0.08
0.10
Strain
OV-2

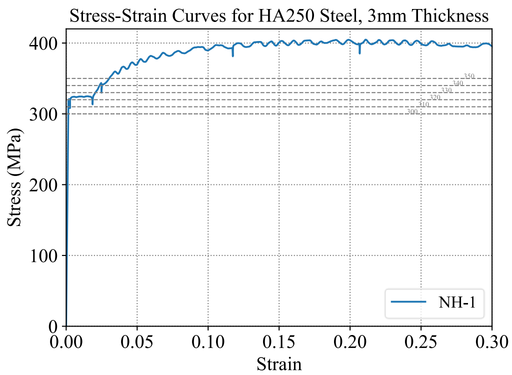
Stress-Strain Curves for HA250 Steel, 3mm Thickness
Stress (MPa)
0
100
200
300
400
0.00
0.05
0.10
0.15
0.20
0.25
0.30
Strain
NH-1

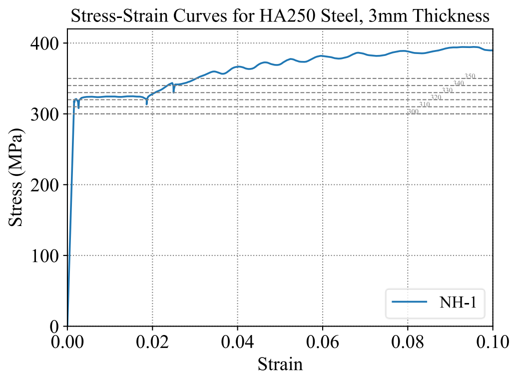
Stress-Strain Curves for HA250 Steel, 3mm Thickness
Stress (MPa)
0
100
200
300
400
0.00
0.02
0.04
0.06
0.08
0.10
Strain
NH-1

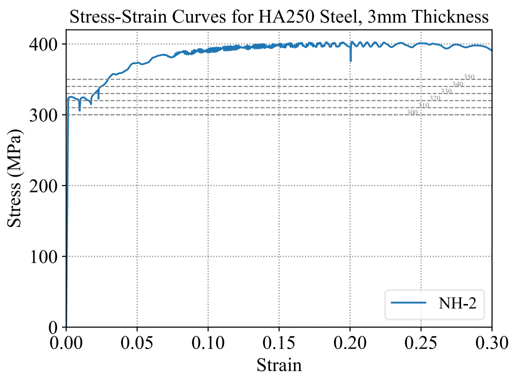
Stress-Strain Curves for HA250 Steel, 3mm Thickness
Stress (MPa)
0
100
200
300
400
0.00
0.05
0.10
0.15
0.20
0.25
0.30
Strain
NH-2

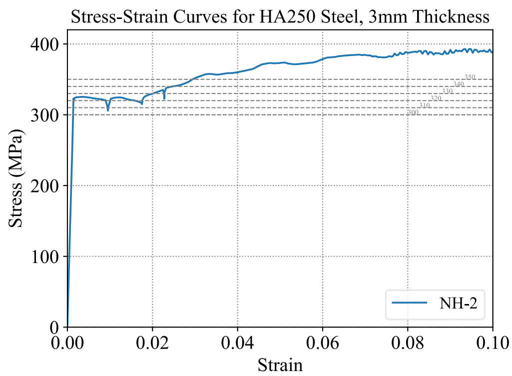
Stress-Strain Curves for HA250 Steel, 3mm Thickness
Stress (MPa)
0
100
200
300
400
0.00
0.02
0.04
0.06
0.08
0.10
Strain
NH-2

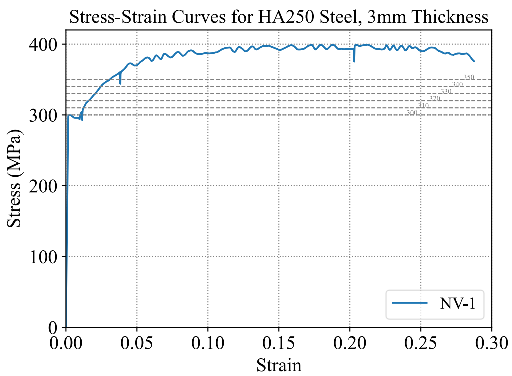
Stress-Strain Curves for HA250 Steel, 3mm Thickness
Stress (MPa)
0
100
200
300
400
0.00
0.05
0.10
0.15
0.20
0.25
0.30
Strain
NV-1

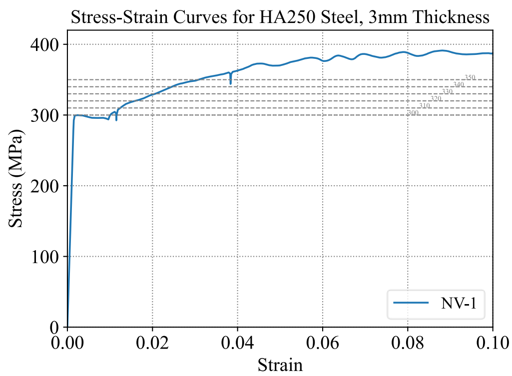
Stress-Strain Curves for HA250 Steel, 3mm Thickness
Stress (MPa)
0
100
200
300
400
0.00
0.02
0.04
0.06
0.08
0.10
Strain
NV-1

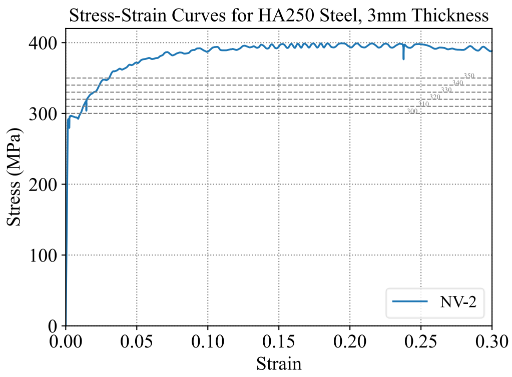

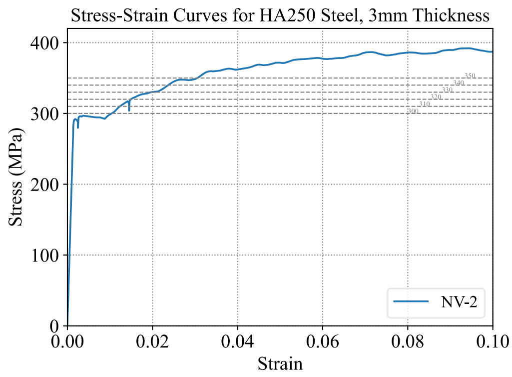

Note:
1. This appendix lists eight coupon test results from two batches of material. For each coupon test result, two figures are provided, demonstrating the strain range from 0.00 to 0.30 (left figure) and 0.00 to 0.10 (right figure), respectively.
2. The abbreviations used are as follows:
"N" and "O" represent the NEW batch and OLD batch, respectively.
"H" and "V" represent the HORIZONTAL and VERTICAL directions, respectively, where the longitudinal direction of the plate is defined as VERTICAL, and the transverse direction is defined as HORIZONTAL.

Appendix B

Measured dimensions of hat sections

Table Appendix B.1 Measured dimensions of specimens

SEQ	TS	SPECIMEN	θ_L	θ_R	D_{EL}	D_{ER}	t_{AVE}	W_{TF}	L	BFL	BFR
1	TF	H120-RIN3-DEG0-1	90.5	91.5	123.23	122.86	2.97	138.98	1200	27.94	28.26
2	TF	H120-RIN3-DEG0-2	90.5	91.5	123.03	122.99	2.98	138.35	1200	28.38	28.57
3	TF	H120-RIN3-DEG0-3	90.5	91.5	123.16	122.84	2.98	139.88	1200	28.01	27.76
4	TF	H120-RIN3-DEG15-1	105.5	106.5	119.07	117.95	2.96	141.73	1200	27.67	27.78
5	TF	H120-RIN3-DEG15-2	105	106.5	119.52	118.22	2.96	140.11	1200	27.16	27.95
6	TF	H120-RIN3-DEG15-3	105	104	119.6	119.77	2.97	139.5	1200	28.01	28.56
7	TF	H120-RIN3-DEG30-1	120	121.5	106.2	105.68	2.99	142.21	1200	26.67	25.97
8	TF	H120-RIN3-DEG30-2	119	121	107.41	106.28	2.99	142.08	1200	27.42	26.45
9	TF	H120-RIN3-DEG30-3	119.5	120.5	106.95	106.7	2.98	141.83	1200	26.53	25.60
10	TF	H120-RIN8-DEG0-1	90.5	90.5	122.19	122.8	3.02	130.62	1200	23.48	22.38
11	TF	H120-RIN8-DEG0-2	90	90.5	122.98	122.91	2.96	138.92	1200	22.78	21.58
12	TF	H120-RIN8-DEG0-3	90.5	90	122.25	123.06	2.96	130.07	1200	23.17	22.34
13	TF	H120-RIN8-DEG15-1	105	105	117.81	117.26	2.95	136.86	1200	22.80	23.00
14	TF	H120-RIN8-DEG15-2	105	104.5	117.61	117.92	2.95	136.14	1200	23.33	23.30
15	TF	H120-RIN8-DEG15-3	104	104.5	120.06	119.97	2.94	136.94	1200	22.84	23.26
16	TF	H120-RIN8-DEG30-1	120.5	120	107.64	107.81	2.95	137.34	1200	25.43	26.36
17	TF	H120-RIN8-DEG30-2	120	120	107.32	107.5	2.94	136.99	1200	25.39	26.02
18	TF	H120-RIN8-DEG30-3	120	119.5	107.58	107.86	2.95	136.75	1200	24.53	25.71
19	TF	H90-RIN3-DEG0-1	90.5	90	92.68	93.14	2.94	139.2	1200	28.16	26.65
20	TF	H90-RIN3-DEG0-2	90	90	92.66	92.29	2.94	138.91	1200	26.97	26.75
21	TF	H90-RIN3-DEG0-3	90.5	90.5	92.85	93.04	2.94	139.05	1200	27.71	26.75
22	TF	H90-RIN8-DEG0-1	91	91	93.72	93.62	2.93	126.24	1200	23.07	22.93
23	TF	H90-RIN8-DEG0-2	91.5	91.5	92.97	92.63	2.94	127.93	1200	22.54	23.17
24	TF	H90-RIN8-DEG0-3	91	91.5	93.15	92.67	2.93	126.82	1200	22.72	22.64
25	OF	H120-RIN3-DEG0-1	90	90.5	122.52	122.42	2.95	139.73	599	28.67	28.94
26	OF	H120-RIN3-DEG0-2	90.5	90.5	122.85	122.54	2.93	140.63	599.5	28.65	28.73
27	OF	H120-RIN3-DEG0-3	90	90.5	122.69	122.26	2.95	140.55	599	27.78	28.35
28	OF	H120-RIN3-DEG0-4	90.8	91	122.85	122.48	2.94	139.68	598.5	28.34	28.79
29	OF	H120-RIN3-DEG0-5	90	90	122.92	122.86	2.93	139.45	598	28.78	29.21
30	OF	H120-RIN3-DEG0-6	90.8	90	122.66	122.84	2.94	140.07	600	28.94	28.45
31	OF	H120-RIN3-DEG0-7	90	90	123.47	123.81	2.95	138.81	598.5	29.85	29.57
32	OF	H120-RIN3-DEG0-8	90.5	91	122.82	122.66	2.94	139.37	599	28.61	28.48
33	OF	H120-RIN3-DEG0-9	90.5	90.5	122.92	122.63	2.93	140.34	600	27.50	27.45
34	OF	H120-RIN3-DEG0-10	90.5	90.5	122.77	122.63	2.95	140.08	599	27.56	27.58
35	OF	H120-RIN3-DEG15-1	105.8	105	116.86	116.78	2.94	140.02	599.5	28.34	28.11
36	OF	H120-RIN3-DEG15-2	106	105	116.62	116.68	2.94	140.37	600	28.39	28.42
37	OF	H120-RIN3-DEG15-3	106	105	116.42	116.17	2.94	140.05	598.5	27.96	27.27
38	OF	H120-RIN3-DEG15-4	105.5	105	117.19	117.08	2.94	139.78	599.5	28.04	28.16
39	OF	H120-RIN3-DEG15-5	105.5	105	117.08	116.84	2.94	140.21	599.5	26.43	28.72
40	OF	H120-RIN3-DEG30-1	119.5	119.5	104.45	104.12	2.93	140.31	600	28.28	28.27
41	OF	H120-RIN3-DEG30-2	120	119	105.46	105.41	2.96	140.64	599	28.41	28.44
42	OF	H120-RIN3-DEG30-3	120	119.5	104.31	104.12	2.96	140.89	598.5	27.92	27.87
43	OF	H120-RIN3-DEG30-4	120	119.5	105.22	104.34	2.99	140.95	598	28.20	27.45
44	OF	H120-RIN3-DEG30-5	120	120	104.51	104.22	2.99	140.79	599	20.42	27.56
45	OF	H120-RIN8-DEG0-1	90.5	90.5	122.83	123.08	2.97	130.6	598	23.59	23.48
46	OF	H120-RIN8-DEG0-2	90.5	90.5	123.54	123.24	2.99	127.14	599	24.47	24.52
47	OF	H120-RIN8-DEG0-3	91	90.5	123.05	122.54	2.93	132.43	599.5	24.23	23.90
48	OF	H120-RIN8-DEG0-4	90.7	90	123.12	123.56	2.94	127.66	599.5	25.15	25.18
49	OF	H120-RIN8-DEG0-5	90.6	91	122.72	123.01	2.94	130.2	598.5	23.31	23.26
50	OF	H120-RIN8-DEG0-6	90.5	90.5	123.18	122.74	2.94	130.85	599	23.96	23.62
51	OF	H120-RIN8-DEG0-7	90.5	90.8	123.62	123.03	2.94	130.1	600	24.81	23.01
52	OF	H120-RIN8-DEG0-8	90.8	90.5	123.08	123.09	2.93	130.8	599	24.66	25.36
53	OF	H120-RIN8-DEG15-1	106	105	116.05	116.24	2.92	133.73	599.5	24.40	23.52
54	OF	H120-RIN8-DEG15-2	106	105	115.84	116.14	2.94	134.68	598	25.50	25.27
55	OF	H120-RIN8-DEG15-3	106	105	116.55	117.08	2.93	135.99	600	23.62	23.47
56	OF	H120-RIN8-DEG15-4	105.5	105	116.78	116.91	2.95	133.86	598.5	24.35	23.55
57	OF	H120-RIN8-DEG15-5	106	105	116.14	116.35	2.96	133.78	598.5	23.62	23.57
58	OF	H120-RIN8-DEG30-1	120	119.5	103.92	103.58	2.99	135.87	600	26.59	27.29
59	OF	H120-RIN8-DEG30-2	120	119	105.08	106.32	2.98	135.83	599	25.08	25.76
60	OF	H120-RIN8-DEG30-3	120	120.5	103.42	103.39	2.96	136.75	599	27.04	27.12
61	OF	H120-RIN8-DEG30-4	120	119	104.46	104.51	2.96	136.05	599	26.33	25.79
62	OF	H120-RIN8-DEG30-5	120	119.5	103.97	104.2	2.97	136.58	598	25.39	25.83
63	OF	H90-RIN3-DEG0-1	90.5	89.5	92.76	92.73	2.94	140.34	600	27.09	26.87
64	OF	H90-RIN3-DEG0-2	90	90	92.7	92.59	2.95	139.86	599.5	27.46	27.55
65	OF	H90-RIN3-DEG0-3	90	90	92.92	92.88	2.93	141.3	599.5	28.40	28.57

SEQ	TS	SPECIMEN	θ_L	θ_R	D_{EL}	D_{ER}	t_{AVE}	W_{TF}	L	BFL	BFR
66	OF	H90-RIN3-DEG0-4	91	90	92.7	92.61	2.95	140.53	599	27.52	27.08
67	OF	H90-RIN3-DEG0-5	91	90	92.78	92.73	2.95	140.28	600	26.69	26.94
68	OF	H90-RIN8-DEG0-1	90.5	90	93.23	93.08	2.93	132.67	598.5	22.92	22.73
69	OF	H90-RIN8-DEG0-2	90.5	90	93.06	93.24	2.94	132.72	599.5	23.01	22.71
70	OF	H90-RIN8-DEG0-3	90	90	94.55	95.87	2.93	134.35	600	21.88	22.28
71	OF	H90-RIN8-DEG0-4	91	91	93.13	93.18	2.94	131.59	599	23.68	23.57
72	OF	H90-RIN8-DEG0-5	91	90	93.01	92.98	2.94	131.7	598.5	23.78	23.65

Note:
1. TS = Test series, TF = two-flanges loading cases, OF = one-flange loading cases.
2. $\theta_L, \theta_R, D_{EL}, D_{ER}$ marked as shown in Figure Appendix B.1, where "E" means the dimension is measured from external, "L" and "R" stand for the web on the "left" and "right" respectively.
3. t_{AVE} = average of the thickness of material.
4. W_{TF} = Width of top flange, flat part as shown in figure.
5. L = length of the specimen. Noted that for TF series of specimens, the original manufactured length was 1200 mm. These specimens were subsequently cut in half in the laboratory to a length of 600 mm.
6. BFL and BFR are the bottom flange lengths measured by the flat part. These parameters are not significant for localised loading capacity prediction.
7. The unit of the lengths are given in mm. The unit of the angle are given in degree.

Table Appendix B.2 Deviation analysis of essential variables

H-DEG	AVE of DEG_L	AVE of DEG_R	AVE of t	AVE of D_L	AVE of D_R	Nominal D	AVE of L
H120-DEG0	0.47	0.60	2.95	119.99	119.92	120.00	599.06
H120-DEG15	15.49	15.06	2.95	114.50	114.38	115.91	599.15
H120-DEG30	29.91	29.84	2.95	102.54	102.43	103.92	598.95
H90-DEG0	0.63	0.31	2.96	90.10	90.12	90.00	599.35

Note:
1. Manufacturing tolerance: ±1.5 mm or 0.0125 rad (0.716°) equivalent for 120 mm-long cantilever plate.
2. Nominal $D = H \times \sin(DEG)$, where DEG is shown as α in degrees as shown in Figure Appendix B.2.
3. DEG_L and DEG_R are calculated by $(\theta_L - 90°)$ and $(\theta_R - 90°)$ as shown in Figure Appendix B.1, respectively.
3. D_L and D_R are calculated by $(D_{EL} - t_{AVE})$ and $(D_{ER} - t_{AVE})$, respectively.
4. AVE of L only includes OF specimens.

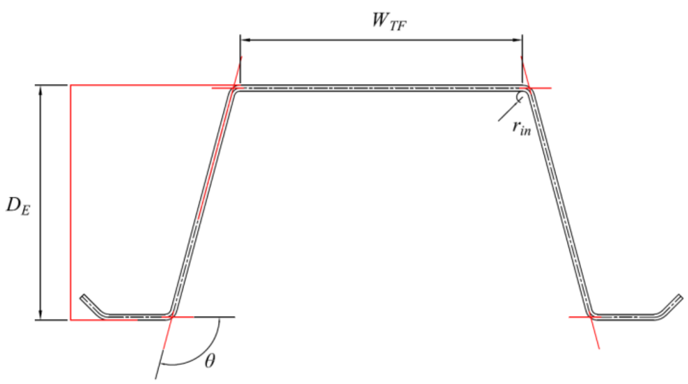

Figure Appendix B.1 Dimension definition for measurement

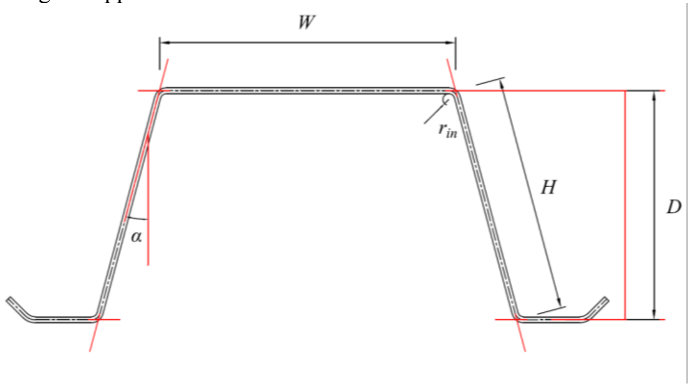

Figure Appendix B.2 Dimension definition for nomenclature

Appendix C

List of all valid experimental results by Chen (Load – Displacement curve)

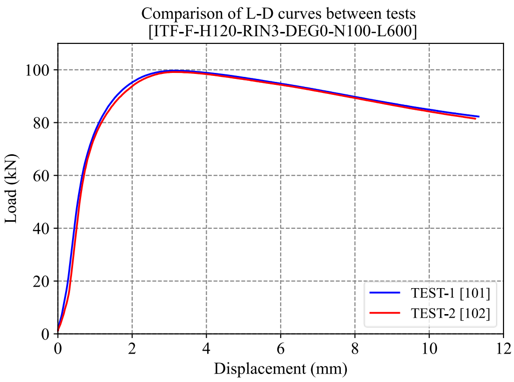

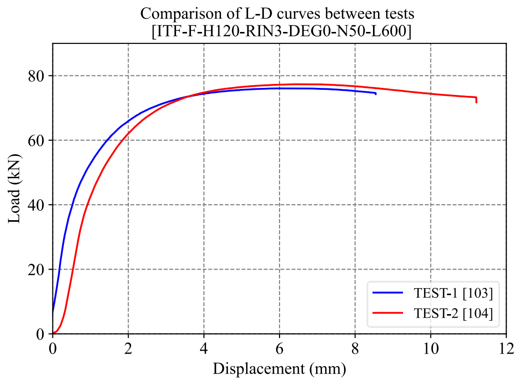

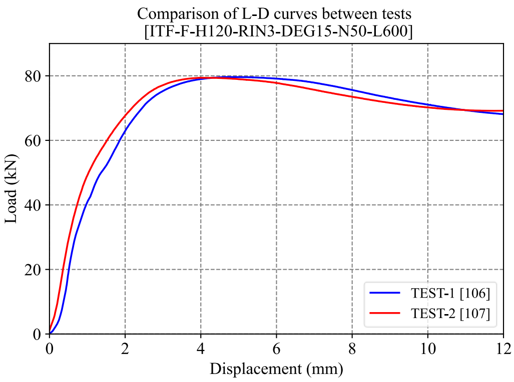

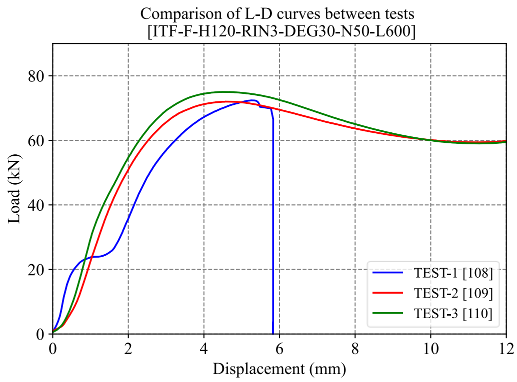

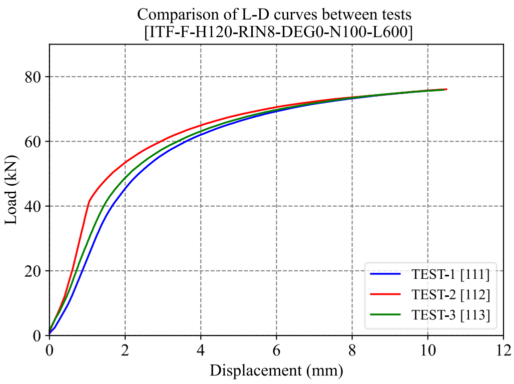

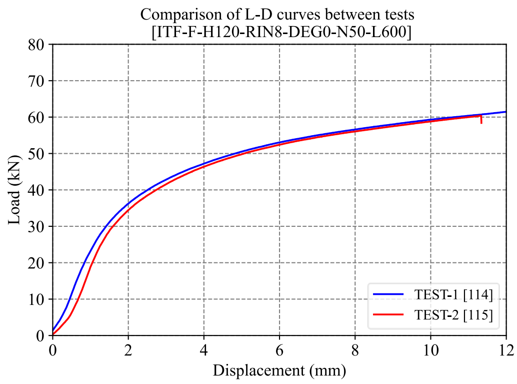

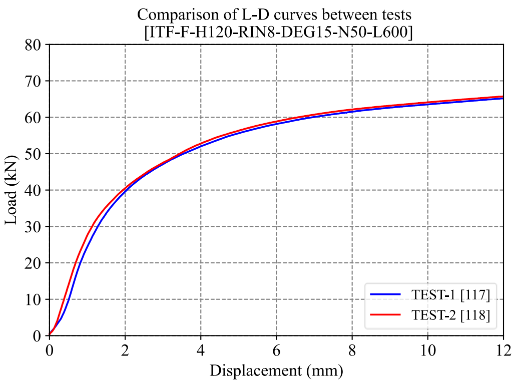

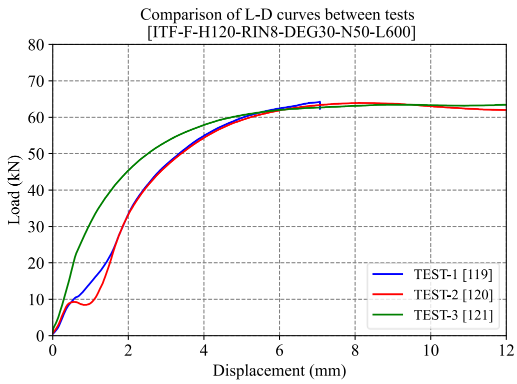

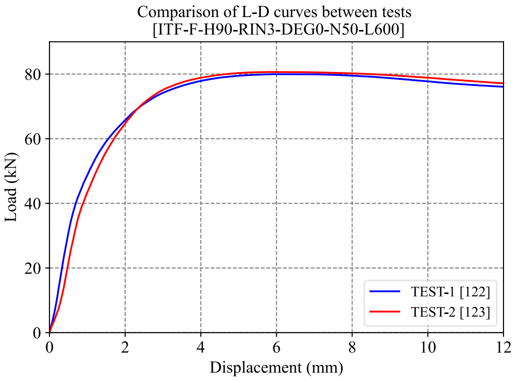
Comparison of L-D curves between tests
[ITF-F-H90-RIN3-DEG0-N50-L600]
Load (kN)
Displacement (mm)
TEST-1 [122]
TEST-2 [123]

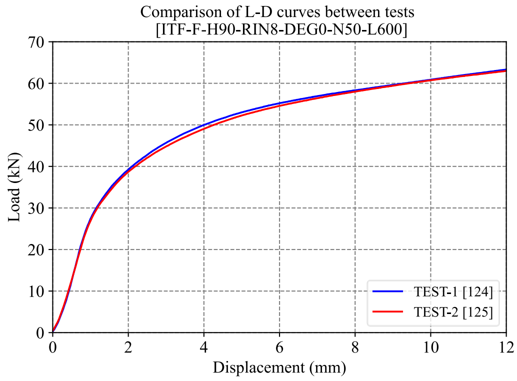
Comparison of L-D curves between tests
[ITF-F-H90-RIN8-DEG0-N50-L600]
Load (kN)
Displacement (mm)
TEST-1 [124]
TEST-2 [125]

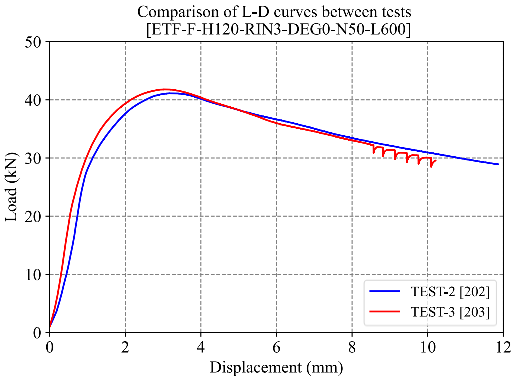
Comparison of L-D curves between tests
[ETF-F-H120-RIN3-DEG0-N50-L600]
Load (kN)
Displacement (mm)
TEST-2 [202]
TEST-3 [203]

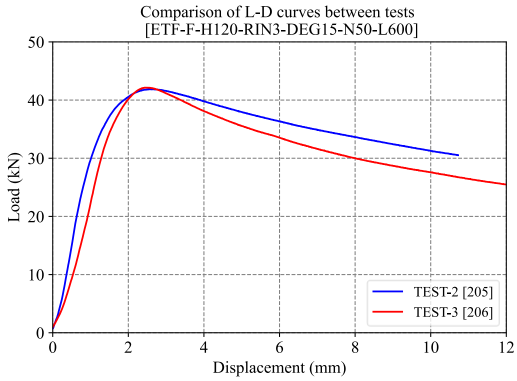
Comparison of L-D curves between tests
[ETF-F-H120-RIN3-DEG15-N50-L600]
Load (kN)
Displacement (mm)
TEST-2 [205]
TEST-3 [206]

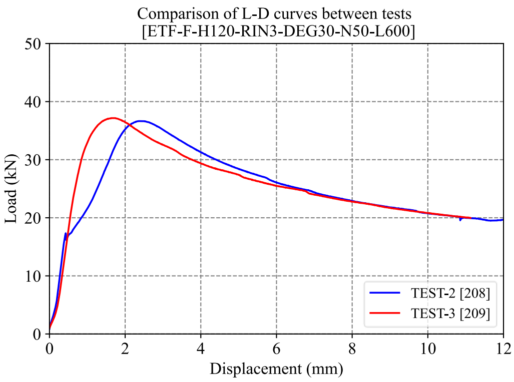
Comparison of L-D curves between tests
[ETF-F-H120-RIN3-DEG30-N50-L600]
Load (kN)
Displacement (mm)
TEST-2 [208]
TEST-3 [209]

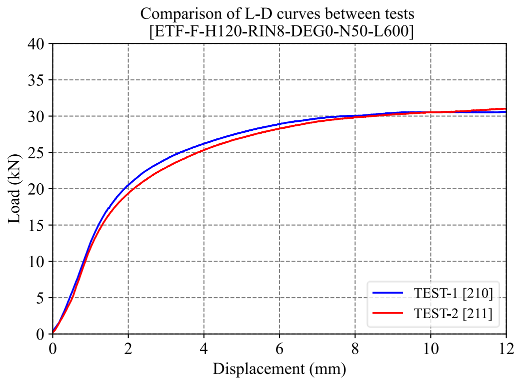
Comparison of L-D curves between tests
[ETF-F-H120-RIN8-DEG0-N50-L600]
Load (kN)
Displacement (mm)
TEST-1 [210]
TEST-2 [211]

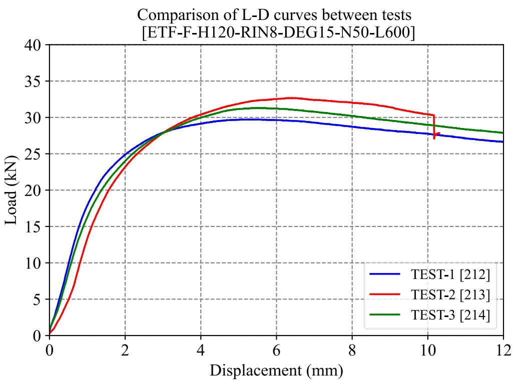
Comparison of L-D curves between tests
[ETF-F-H120-RIN8-DEG15-N50-L600]
Load (kN)
Displacement (mm)
TEST-1 [212]
TEST-2 [213]
TEST-3 [214]

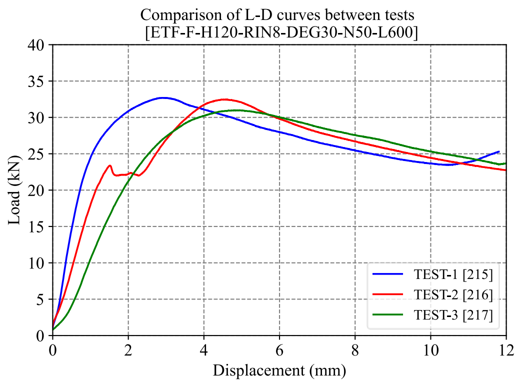
Comparison of L-D curves between tests
[ETF-F-H120-RIN8-DEG30-N50-L600]
Load (kN)
Displacement (mm)
TEST-1 [215]
TEST-2 [216]
TEST-3 [217]

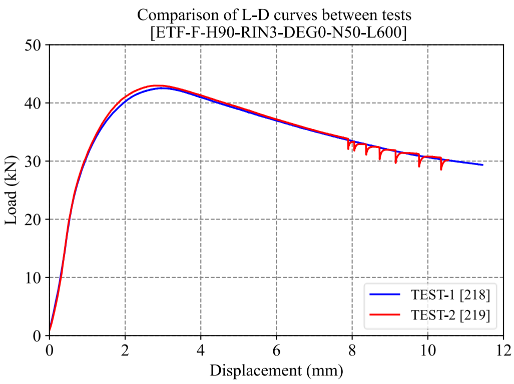
Comparison of L-D curves between tests
[ETF-F-H90-RIN3-DEG0-N50-L600]
Load (kN)
Displacement (mm)
TEST-1 [218]
TEST-2 [219]

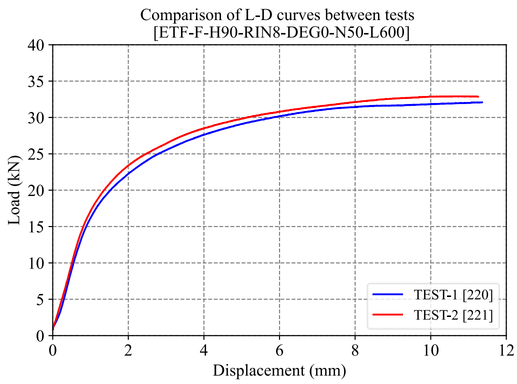
Comparison of L-D curves between tests
[ETF-F-H90-RIN8-DEG0-N50-L600]
Load (kN)
Displacement (mm)
TEST-1 [220]
TEST-2 [221]

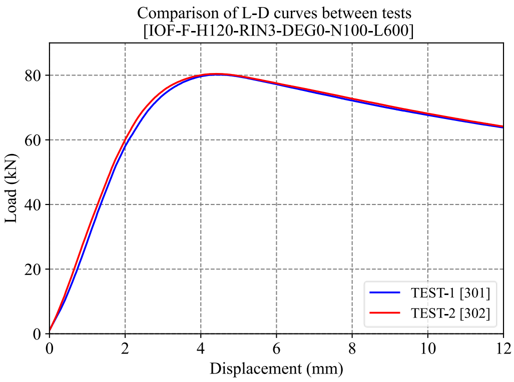
Comparison of L-D curves between tests
[IOF-F-H120-RIN3-DEG0-N100-L600]
Load (kN)
Displacement (mm)
TEST-1 [301]
TEST-2 [302]

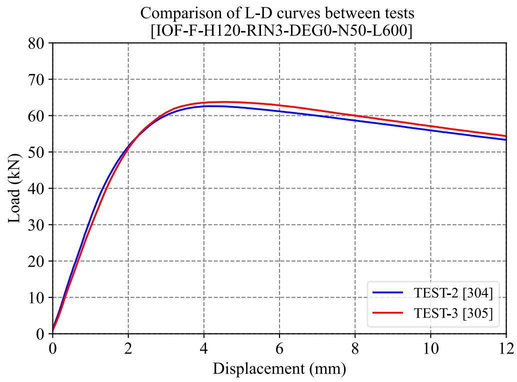
Comparison of L-D curves between tests
[IOF-F-H120-RIN3-DEG0-N50-L600]
Load (kN)
Displacement (mm)
TEST-2 [304]
TEST-3 [305]

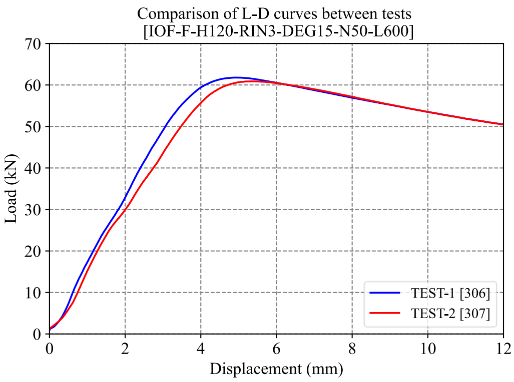
Comparison of L-D curves between tests
[IOF-F-H120-RIN3-DEG15-N50-L600]
Load (kN)
Displacement (mm)
TEST-1 [306]
TEST-2 [307]

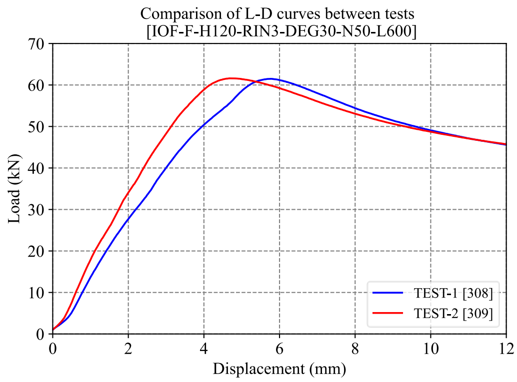
Comparison of L-D curves between tests
[IOF-F-H120-RIN3-DEG30-N50-L600]
Load (kN)
Displacement (mm)
TEST-1 [308]
TEST-2 [309]

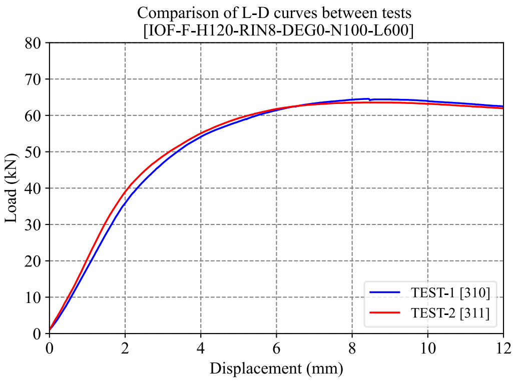
Comparison of L-D curves between tests
[IOF-F-H120-RIN8-DEG0-N100-L600]
Load (kN)
Displacement (mm)
TEST-1 [310]
TEST-2 [311]

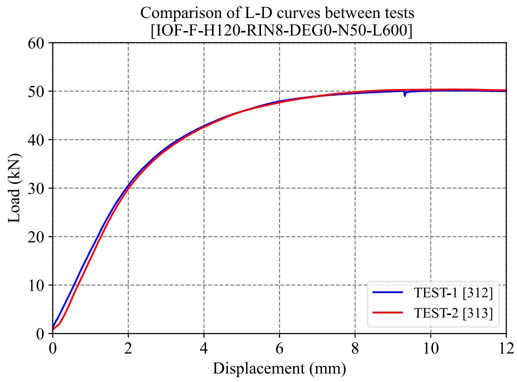
Comparison of L-D curves between tests
[IOF-F-H120-RIN8-DEG0-N50-L600]
Load (kN)
Displacement (mm)
TEST-1 [312]
TEST-2 [313]

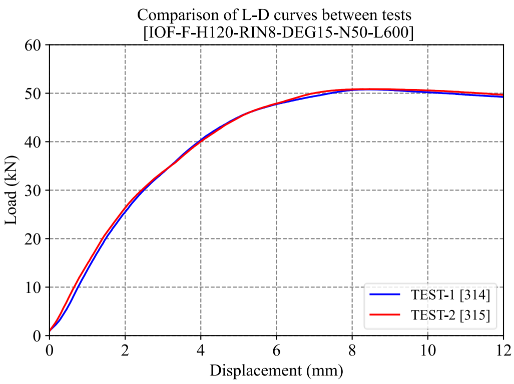
Comparison of L-D curves between tests
[IOF-F-H120-RIN8-DEG15-N50-L600]
Load (kN)
Displacement (mm)
TEST-1 [314]
TEST-2 [315]

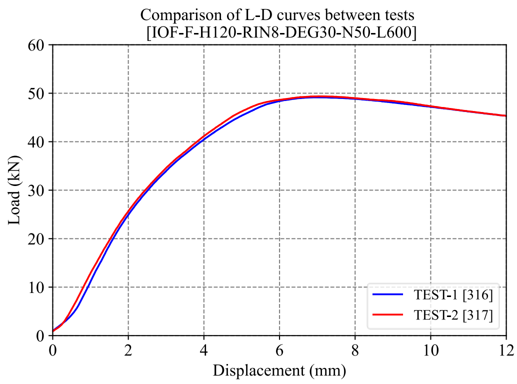
Comparison of L-D curves between tests
[IOF-F-H120-RIN8-DEG30-N50-L600]
Load (kN)
Displacement (mm)
TEST-1 [316]
TEST-2 [317]

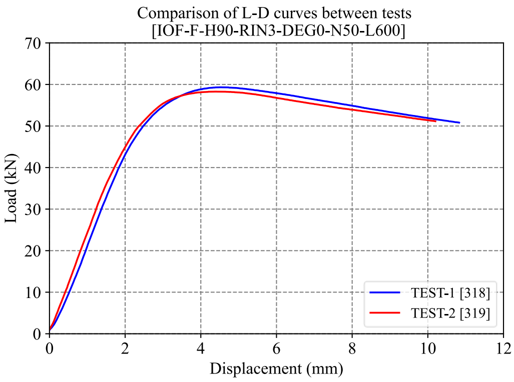
Comparison of L-D curves between tests
[IOF-F-H90-RIN3-DEG0-N50-L600]
Load (kN)
Displacement (mm)
TEST-1 [318]
TEST-2 [319]

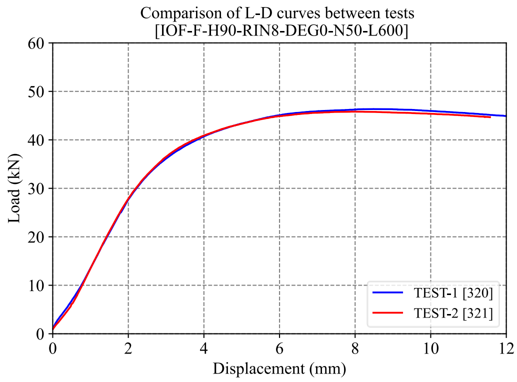
Comparison of L-D curves between tests
[IOF-F-H90-RIN8-DEG0-N50-L600]
Load (kN)
Displacement (mm)
TEST-1 [320]
TEST-2 [321]

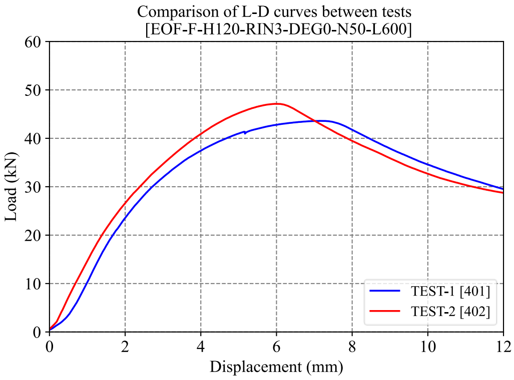
Comparison of L-D curves between tests
[EOF-F-H120-RIN3-DEG0-N50-L600]
Load (kN)
Displacement (mm)
TEST-1 [401]
TEST-2 [402]

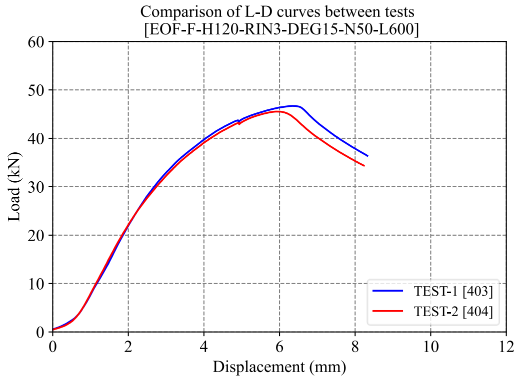
Comparison of L-D curves between tests
[EOF-F-H120-RIN3-DEG15-N50-L600]
Load (kN)
Displacement (mm)
TEST-1 [403]
TEST-2 [404]

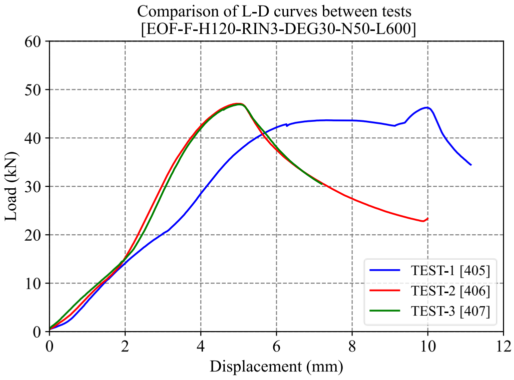
Comparison of L-D curves between tests
[EOF-F-H120-RIN3-DEG30-N50-L600]
Load (kN)
Displacement (mm)
TEST-1 [405]
TEST-2 [406]
TEST-3 [407]

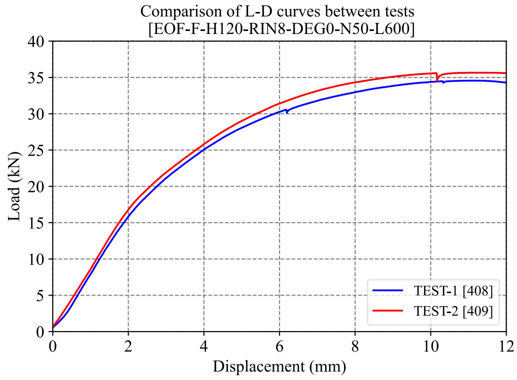
Comparison of L-D curves between tests
[EOF-F-H120-RIN8-DEG0-N50-L600]
Load (kN)
Displacement (mm)
TEST-1 [408]
TEST-2 [409]

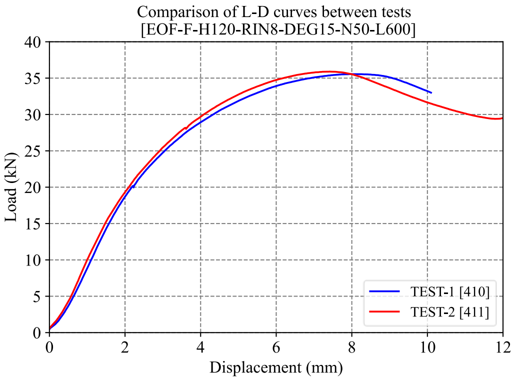
Comparison of L-D curves between tests
[EOF-F-H120-RIN8-DEG15-N50-L600]
Load (kN)
Displacement (mm)
TEST-1 [410]
TEST-2 [411]

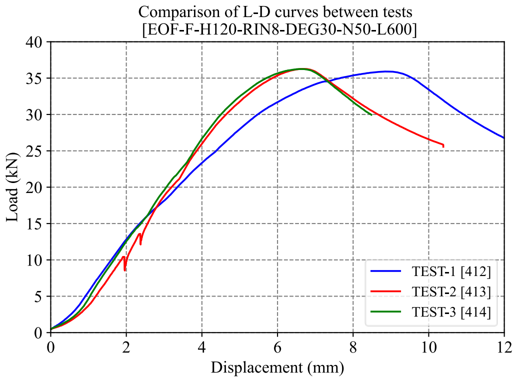
Comparison of L-D curves between tests
[EOF-F-H120-RIN8-DEG30-N50-L600]
Load (kN)
Displacement (mm)
TEST-1 [412]
TEST-2 [413]
TEST-3 [414]

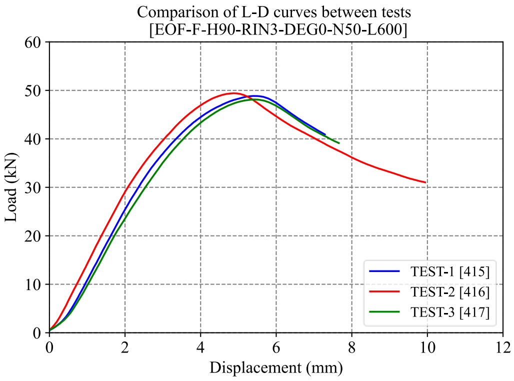
Comparison of L-D curves between tests
[EOF-F-H90-RIN3-DEG0-N50-L600]
Load (kN)
Displacement (mm)
TEST-1 [415]
TEST-2 [416]
TEST-3 [417]

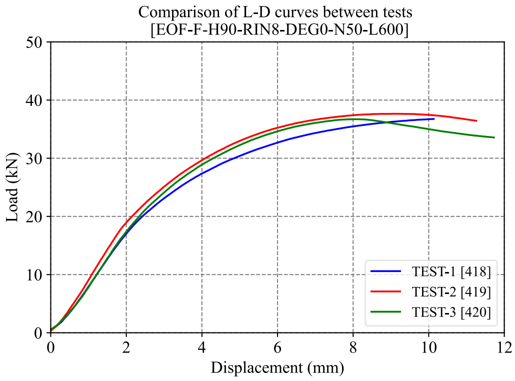
Comparison of L-D curves between tests
[EOF-F-H90-RIN8-DEG0-N50-L600]
Load (kN)
Displacement (mm)
TEST-1 [418]
TEST-2 [419]
TEST-3 [420]

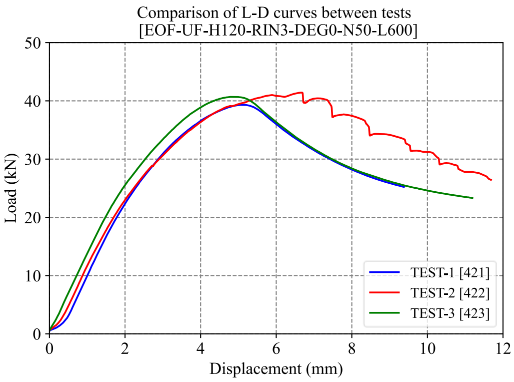
Comparison of L-D curves between tests
[EOF-UF-H120-RIN3-DEG0-N50-L600]
Load (kN)
Displacement (mm)
TEST-1 [421]
TEST-2 [422]
TEST-3 [423]

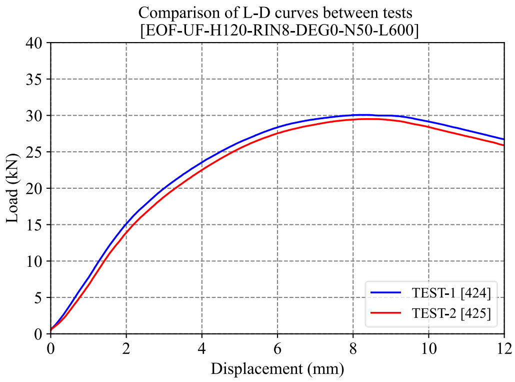
Comparison of L-D curves between tests
[EOF-UF-H120-RIN8-DEG0-N50-L600]
Load (kN)
Displacement (mm)
TEST-1 [424]
TEST-2 [425]

Table Appendix C.1 Numbering system for all tests

		N50 H120 DEG0	N50 H120 DEG15	N50 H120 DEG30	N50 H90 DEG0	N100 H120 DEG0
ITF-F	**RIN3**	103 104 105*	106 107	108 109 110	122 123	101 102
ITF-F	**RIN8**	114 115 116*	117 118	119 120 121	124 125	111 112 113
ETF-F	**RIN3**	201* 202 203	204* 205 206	207* 208 209	218 219	
ETF-F	**RIN8**	210 211	212 213 214	215 216 217	220 221	
IOF-F	**RIN3**	303* 304 305	306 307	308 309	318 319	301 302
IOF-F	**RIN8**	312 313	314 315	316 317	320 321	310 311
IOF-UF	**RIN3**		322			
IOF-UF	**RIN8**		323			
EOF-F	**RIN3**	401 402	403 404	405 406 407	415 416 417	
EOF-F	**RIN8**	408 409	410 411	412 413 414	418 419 420	
EOF-UF	**RIN3**	421 422 423				
EOF-UF	**RIN8**	424 425				

Note 1: 201, 204, 207, 303 were dummy test for specific load cases. 105 and 116 were tested with top flange fastened to the bearing plate.
Note 2: Example: For a specific section, ITF-F-H120-RIN3-DEG0-N50 has two tests: 103 and 104.

Table Appendix C.2 Full experimental result tested by the author

	P_{max_1} kN	$Disp_1$ mm	P_{max_2} kN	$Disp_2$ mm	P_{max_3} kN	$Disp_3$ mm
ITF-F-H120-RIN3-DEG0-N100	99.689	3.096	99.176	3.105		
ITF-F-H120-RIN3-DEG0-N50	76.085	6.066	77.348	6.427	79.290*	6.332*
ITF-F-H120-RIN3-DEG15-N50	79.656	4.851	79.418	4.066		
ITF-F-H120-RIN3-DEG30-N50	72.404	5.273	72.020	4.568	75.023	4.496
ITF-F-H120-RIN8-DEG0-N100	75.664	9.988	75.700	9.984	75.609	9.958
ITF-F-H120-RIN8-DEG0-N50	59.311	9.998	58.780	9.982	58.854*	9.981*
ITF-F-H120-RIN8-DEG15-N50	63.541	9.999	64.109	9.998		
ITF-F-H120-RIN8-DEG30-N50	64.274	7.068	63.908	8.001	63.468	8.906
ITF-F-H90-RIN3-DEG0-N50	80.004	6.079	80.681	6.070		
ITF-F-H90-RIN8-DEG0-N50	60.850	9.972	60.740	9.991		
ETF-F-H120-RIN3-DEG0-N50	-	-	41.128	3.161	41.787	2.999
ETF-F-H120-RIN3-DEG15-N50	-	-	41.879	2.573	42.153	2.461
ETF-F-H120-RIN3-DEG30-N50	-	-	36.660	2.384	37.154	1.631
ETF-F-H120-RIN8-DEG0-N50	30.544	9.414	30.526	9.886		
ETF-F-H120-RIN8-DEG15-N50	29.720	5.105	32.650	6.250	31.295	5.347
ETF-F-H120-RIN8-DEG30-N50	32.686	2.857	32.448	4.456	30.983	4.785
ETF-F-H90-RIN3-DEG0-N50	42.538	2.930	42.996	2.770		
ETF-F-H90-RIN8-DEG0-N50	31.844	9.983	32.869	9.950		
IOF-F-H120-RIN3-DEG0-N100	80.205	4.444	80.425	4.383		
IOF-F-H120-RIN3-DEG0-N50	-	-	62.608	4.113	63.761	4.528
IOF-F-H120-RIN3-DEG15-N50	61.802	4.900	60.886	5.318		
IOF-F-H120-RIN3-DEG30-N50	61.491	5.755	61.619	4.675		
IOF-F-H120-RIN8-DEG0-N100	64.567	8.399	63.578	8.408		
IOF-F-H120-RIN8-DEG0-N50	50.082	9.993	50.339	9.769		
IOF-F-H120-RIN8-DEG15-N50	50.815	8.455	50.870	8.453		
IOF-F-H120-RIN8-DEG30-N50	49.167	6.916	49.368	7.013		
IOF-F-H90-RIN3-DEG0-N50	59.330	4.503	58.286	4.368		
IOF-F-H90-RIN8-DEG0-N50	46.365	8.484	45.816	7.881		
IOF-UF-H120-RIN3-DEG15-N50	62.571	4.980				
IOF-UF-H120-RIN8-DEG15-N50	51.547	7.706				
EOF-F-H120-RIN3-DEG0-N50	43.609	7.130	47.125	5.951		
EOF-F-H120-RIN3-DEG15-N50	46.704	6.353	45.532	5.949		
EOF-F-H120-RIN3-DEG30-N50	46.264	9.975	47.088	4.951	46.924	5.000
EOF-F-H120-RIN8-DEG0-N50	34.380	9.973	35.552	9.989		
EOF-F-H120-RIN8-DEG15-N50	35.552	7.939	35.900	7.406		
EOF-F-H120-RIN8-DEG30-N50	35.909	8.851	36.266	6.621	36.257	6.614
EOF-F-H90-RIN3-DEG0-N50	48.846	5.384	49.414	4.859	48.132	5.402
EOF-F-H90-RIN8-DEG0-N50	36.715	9.984	37.658	9.086	36.724	8.009
EOF-UF-H120-RIN3-DEG0-N50	39.315	5.085	41.421	6.652	40.689	4.803
EOF-UF-H120-RIN8-DEG0-N50	30.077	8.264	29.509	8.367		

Note:
Ultimate web crippling capacity is collected at 10 mm displacement if maximum not reached
All EOF loading cases results are given by half of the load recorded from the load cell.
Value marked with * indicates that they are FTF case value.
- indicates that the specimen was used for dummy test.

Appendix D

e/t data in Figure 132

SEQ	RIN (mm)	DEG (deg)	t (mm)	r_c (mm)	β (deg)	$\tan\beta$	e (mm)	e/t
1	3	0	3	4.5	45	1.000	4.500	1.500
2	3	5	3	4.5	42.5	0.916	4.123	1.374
3	3	10	3	4.5	40	0.839	3.776	1.259
4	3	15	3	4.5	37.5	0.767	3.453	1.151
5	3	20	3	4.5	35	0.700	3.151	1.050
6	3	25	3	4.5	32.5	0.637	2.867	0.956
7	3	30	3	4.5	30	0.577	2.598	0.866
8	4	0	3	5.5	45	1.000	5.500	1.833
9	4	5	3	5.5	42.5	0.916	5.040	1.680
10	4	10	3	5.5	40	0.839	4.615	1.538
11	4	15	3	5.5	37.5	0.767	4.220	1.407
12	4	20	3	5.5	35	0.700	3.851	1.284
13	4	25	3	5.5	32.5	0.637	3.504	1.168
14	4	30	3	5.5	30	0.577	3.175	1.058
15	5	0	3	6.5	45	1.000	6.500	2.167
16	5	5	3	6.5	42.5	0.916	5.956	1.985
17	5	10	3	6.5	40	0.839	5.454	1.818
18	5	15	3	6.5	37.5	0.767	4.988	1.663
19	5	20	3	6.5	35	0.700	4.551	1.517
20	5	25	3	6.5	32.5	0.637	4.141	1.380
21	5	30	3	6.5	30	0.577	3.753	1.251
22	6	0	3	7.5	45	1.000	7.500	2.500
23	6	5	3	7.5	42.5	0.916	6.872	2.291
24	6	10	3	7.5	40	0.839	6.293	2.098
25	6	15	3	7.5	37.5	0.767	5.755	1.918
26	6	20	3	7.5	35	0.700	5.252	1.751
27	6	25	3	7.5	32.5	0.637	4.778	1.593
28	6	30	3	7.5	30	0.577	4.330	1.443
29	7	0	3	8.5	45	1.000	8.500	2.833
30	7	5	3	8.5	42.5	0.916	7.789	2.596
31	7	10	3	8.5	40	0.839	7.132	2.377
32	7	15	3	8.5	37.5	0.767	6.522	2.174
33	7	20	3	8.5	35	0.700	5.952	1.984
34	7	25	3	8.5	32.5	0.637	5.415	1.805
35	7	30	3	8.5	30	0.577	4.907	1.636
36	8	0	3	9.5	45	1.000	9.500	3.167
37	8	5	3	9.5	42.5	0.916	8.705	2.902
38	8	10	3	9.5	40	0.839	7.971	2.657
39	8	15	3	9.5	37.5	0.767	7.290	2.430
40	8	20	3	9.5	35	0.700	6.652	2.217
41	8	25	3	9.5	32.5	0.637	6.052	2.017
42	8	30	3	9.5	30	0.577	5.485	1.828

Appendix E

Experimental data for use in calibration of DSM design equations

Note:
(1) **UID** (Unique identifier):
UID is introduced as a unique identification number in all appendices.
(2) **MB** (Middle Bearing Length):
For ITF and ETF loading cases, MB equals N, as there is only one pair of bearing plates.
For IOF and EOF loading cases, MB is the width of the middle bearing plate.
(3) **EB** (End Bearing Length):
For ITF and ETF loading cases, EB equals zero by default.
For IOF and EOF loading cases, EB is the width of the end bearing plate.
Specifically, for EOF loading cases, EB equals N.
(4) The load and displacement measurements were recorded using calibrated data acquisition systems with high precision capabilities. The values presented in kN and mm are rounded from raw data and maintain accuracy to three decimal places.
(5) Section dimensions from the experimental work at the University of Sydney were measured and recorded to one or two decimal places.
(6) For dimensions collected from other publications, especially those given in imperial units, dimensions were converted accordingly with reasonable accuracy.

Table Appendix E.1A Dimension data for specimens from Chen, Pham and Hancock

UID	LC-FC	H (mm)	N (mm)	t (mm)	RIN (mm)	DEG (deg)	fy (MPa)	MB (mm)	EB (mm)	L (mm)
11001	ITF-F	120	100	3	3	0	323	100	0	600
11002	ITF-F	120	50	3	3	30	323	50	0	600
11003	ITF-F	120	50	3	3	15	323	50	0	600
11004	ITF-F	120	50	3	3	0	323	50	0	600
11005	ITF-F	90	50	3	3	0	323	50	0	600
11006	ITF-F	120	100	3	3	0	323	100	0	600
11007	ITF-F	120	50	3	3	30	323	50	0	600
11008	ITF-F	120	50	3	3	15	323	50	0	600
11009	ITF-F	120	50	3	3	0	323	50	0	600
11010	ITF-F	90	50	3	3	0	323	50	0	600
11011	ITF-F	120	100	3	8	0	323	100	0	600
11012	ITF-F	120	50	3	8	30	323	50	0	600
11013	ITF-F	120	50	3	8	15	323	50	0	600
11014	ITF-F	120	50	3	8	0	323	50	0	600
11015	ITF-F	90	50	3	8	0	323	50	0	600
11016	ITF-F	120	100	3	8	0	323	100	0	600
11017	ITF-F	120	50	3	8	30	323	50	0	600
11018	ITF-F	120	50	3	8	15	323	50	0	600
11019	ITF-F	120	50	3	8	0	323	50	0	600
11020	ITF-F	90	50	3	8	0	323	50	0	600
19001	ITF-F	120	50	3	3	30	323	50	0	600
19002	ITF-F	120	100	3	8	0	323	100	0	600
19003	ITF-F	120	50	3	8	30	323	50	0	600
21001	ETF-F	120	50	3	3	30	323	50	0	600
21002	ETF-F	120	50	3	3	15	323	50	0	600
21003	ETF-F	120	50	3	3	0	323	50	0	600
21004	ETF-F	90	50	3	3	0	323	50	0	600

UID	LC-FC	H (mm)	N (mm)	t (mm)	RIN (mm)	DEG (deg)	fy (MPa)	MB (mm)	EB (mm)	L (mm)
21005	ETF-F	120	50	3	3	30	323	50	0	600
21006	ETF-F	120	50	3	3	15	323	50	0	600
21007	ETF-F	120	50	3	3	0	323	50	0	600
21008	ETF-F	90	50	3	3	0	323	50	0	600
21011	ETF-F	120	50	3	8	30	323	50	0	600
21012	ETF-F	120	50	3	8	15	323	50	0	600
21013	ETF-F	120	50	3	8	0	323	50	0	600
21014	ETF-F	90	50	3	8	0	323	50	0	600
21015	ETF-F	120	50	3	8	30	323	50	0	600
21016	ETF-F	120	50	3	8	15	323	50	0	600
21017	ETF-F	120	50	3	8	0	323	50	0	600
21018	ETF-F	90	50	3	8	0	323	50	0	600
21019	ETF-F	120	50	3	8	30	323	50	0	600
21020	ETF-F	120	50	3	8	15	323	50	0	600
31001	IOF-F	120	100	3	3	0	323	100	50	600
31002	IOF-F	120	50	3	3	30	323	50	50	600
31003	IOF-F	120	50	3	3	15	323	50	50	600
31004	IOF-F	120	50	3	3	0	323	50	50	600
31005	IOF-F	90	50	3	3	0	323	50	50	600
31006	IOF-F	120	100	3	3	0	323	100	50	600
31007	IOF-F	120	50	3	3	30	323	50	50	600
31008	IOF-F	120	50	3	3	15	323	50	50	600
31009	IOF-F	120	50	3	3	0	323	50	50	600
31010	IOF-F	90	50	3	3	0	323	50	50	600
31011	IOF-F	120	100	3	8	0	323	100	50	600
31012	IOF-F	120	50	3	8	30	323	50	50	600
31013	IOF-F	120	50	3	8	15	323	50	50	600
31014	IOF-F	120	50	3	8	0	323	50	50	600
31015	IOF-F	90	50	3	8	0	323	50	50	600
31016	IOF-F	120	100	3	8	0	323	100	50	600
31017	IOF-F	120	50	3	8	30	323	50	50	600
31018	IOF-F	120	50	3	8	15	323	50	50	600
31019	IOF-F	120	50	3	8	0	323	50	50	600
31020	IOF-F	90	50	3	8	0	323	50	50	600
41001	EOF-F	120	50	3	3	30	323	100	50	600
41002	EOF-F	120	50	3	3	15	323	100	50	600
41003	EOF-F	120	50	3	3	0	323	100	50	600
41004	EOF-F	90	50	3	3	0	323	220	50	600
41005	EOF-F	120	50	3	3	30	323	100	50	600
41006	EOF-F	120	50	3	3	15	323	100	50	600
41007	EOF-F	120	50	3	3	0	323	100	50	600
41008	EOF-F	90	50	3	3	0	323	220	50	600
41009	EOF-F	120	50	3	3	30	323	100	50	600
41010	EOF-F	90	50	3	3	0	323	220	50	600
41011	EOF-F	120	50	3	8	30	323	100	50	600
41012	EOF-F	120	50	3	8	15	323	100	50	600
41013	EOF-F	120	50	3	8	0	323	100	50	600
41014	EOF-F	90	50	3	8	0	323	220	50	600
41015	EOF-F	120	50	3	8	30	323	100	50	600
41016	EOF-F	120	50	3	8	15	323	100	50	600
41017	EOF-F	120	50	3	8	0	323	100	50	600
41018	EOF-F	90	50	3	8	0	323	220	50	600
41019	EOF-F	120	50	3	8	30	323	100	50	600
41020	EOF-F	90	50	3	8	0	323	220	50	600
81001	EOF-UF	120	50	3	3	0	323	100	50	600
81002	EOF-UF	120	50	3	3	0	323	100	50	600
81003	EOF-UF	120	50	3	8	0	323	100	50	600
81004	EOF-UF	120	50	3	8	0	323	100	50	600

UID	LC-FC	H (mm)	N (mm)	t (mm)	RIN (mm)	DEG (deg)	fy (MPa)	MB (mm)	EB (mm)	L (mm)
89001	EOF-UF	120	50	3	3	0	323	100	50	600

Table Appendix E.2A Dimension data for specimens from Santaputra and Yu

UID	LC-FC	H (mm)	N (mm)	t (mm)	RIN (mm)	DEG (deg)	fy (MPa)	MB (mm)	EB (mm)	L (mm)
90001	IOF-UF	78.791	50.8	1.219	5.944	0	401.28	50.8	101.6	482.6
90002	IOF-UF	78.537	50.8	1.219	5.944	0	401.28	50.8	101.6	482.6
90003	IOF-UF	102.413	50.8	1.219	6.350	0	401.28	50.8	101.6	558.8
90004	IOF-UF	102.159	50.8	1.219	6.934	0	401.28	50.8	101.6	558.8
90005	IOF-UF	125.527	50.8	1.219	6.147	0	401.28	50.8	101.6	635
90006	IOF-UF	125.781	50.8	1.219	6.350	0	401.28	50.8	101.6	635
90007	IOF-UF	75.133	50.8	2.083	5.156	0	608.81	50.8	101.6	482.6
90008	IOF-UF	75.895	50.8	2.083	5.766	0	608.81	50.8	101.6	482.6
90009	IOF-UF	100.787	50.8	2.083	5.766	0	608.81	50.8	101.6	558.8
90010	IOF-UF	101.041	50.8	2.083	5.766	0	608.81	50.8	101.6	558.8
90011	IOF-UF	126.441	50.8	2.083	5.563	0	608.81	50.8	101.6	635
90012	IOF-UF	126.695	50.8	2.083	5.563	0	608.81	50.8	101.6	635
90013	IOF-UF	76.657	50.8	1.575	4.953	0	779.80	50.8	101.6	482.6
90014	IOF-UF	76.911	50.8	1.575	4.166	0	779.80	50.8	101.6	482.6
90015	IOF-UF	101.041	50.8	1.575	4.166	0	779.80	50.8	101.6	558.8
90016	IOF-UF	101.295	50.8	1.575	3.962	0	779.80	50.8	101.6	558.8
90017	IOF-UF	126.441	50.8	1.575	3.378	0	779.80	50.8	101.6	635
90018	IOF-UF	125.679	50.8	1.575	4.369	0	779.80	50.8	101.6	635
90037	EOF-UF	76.759	50.8	1.219	5.766	0	401.28	101.6	50.8	431.8
90038	EOF-UF	76.759	50.8	1.219	5.563	0	401.28	101.6	50.8	431.8
90039	EOF-UF	98.603	50.8	1.219	5.359	0	401.28	101.6	50.8	508
90040	EOF-UF	99.111	50.8	1.219	5.766	0	401.28	101.6	50.8	508
90041	EOF-UF	123.749	50.8	1.219	5.156	0	401.28	101.6	50.8	584.2
90042	EOF-UF	123.495	50.8	1.219	5.563	0	401.28	101.6	50.8	584.2
90043	EOF-UF	70.993	50.8	2.159	5.944	0	608.81	101.6	50.8	431.8
90044	EOF-UF	71.247	50.8	2.159	5.563	0	608.81	101.6	50.8	431.8
90045	EOF-UF	96.139	50.8	2.159	5.766	0	608.81	101.6	50.8	508
90046	EOF-UF	96.139	50.8	2.159	5.359	0	608.81	101.6	50.8	508
90047	EOF-UF	122.555	50.8	2.159	5.766	0	608.81	101.6	50.8	584.2
90048	EOF-UF	122.047	50.8	2.159	5.563	0	608.81	101.6	50.8	584.2
90049	EOF-UF	72.009	50.8	1.651	5.156	0	779.80	101.6	50.8	431.8
90050	EOF-UF	72.263	50.8	1.651	4.572	0	779.80	101.6	50.8	431.8
90051	EOF-UF	97.663	50.8	1.651	4.775	0	779.80	101.6	50.8	508
90052	EOF-UF	97.155	50.8	1.651	4.775	0	779.80	101.6	50.8	508
90053	EOF-UF	123.317	50.8	1.651	4.953	0	779.80	101.6	50.8	584.2
90054	EOF-UF	123.317	50.8	1.651	5.359	0	779.80	101.6	50.8	584.2
90067	ITF-UF	75.006	50.8	1.194	6.350	0	401.28	50.8	0	279.4
90068	ITF-UF	75.006	50.8	1.194	6.350	0	401.28	50.8	0	279.4
90069	ITF-UF	100.406	50.8	1.194	6.350	0	401.28	50.8	0	355.6
90070	ITF-UF	100.660	50.8	1.194	6.350	0	401.28	50.8	0	355.6
90071	ITF-UF	127.330	50.8	1.194	6.350	0	401.28	50.8	0	431.8
90072	ITF-UF	127.076	50.8	1.194	6.350	0	401.28	50.8	0	431.8
90073	ITF-UF	73.965	50.8	2.235	6.350	0	531.59	50.8	0	279.4
90074	ITF-UF	73.965	50.8	2.235	6.350	0	531.59	50.8	0	279.4
90075	ITF-UF	99.619	50.8	2.235	6.350	0	531.59	50.8	0	355.6
90076	ITF-UF	100.127	50.8	2.235	6.350	0	531.59	50.8	0	355.6
90077	ITF-UF	126.289	50.8	2.235	6.350	0	531.59	50.8	0	431.8
90078	ITF-UF	126.035	50.8	2.235	6.350	0	531.59	50.8	0	431.8
90091	ETF-UF	75.768	50.8	1.194	6.350	0	401.28	50.8	0	165.1
90092	ETF-UF	76.276	50.8	1.194	6.350	0	401.28	50.8	0	165.1
90093	ETF-UF	101.168	50.8	1.194	6.350	0	401.28	50.8	0	203.2
90094	ETF-UF	101.676	50.8	1.194	6.350	0	401.28	50.8	0	203.2
90095	ETF-UF	126.568	50.8	1.194	6.350	0	401.28	50.8	0	241.3
90096	ETF-UF	126.568	50.8	1.194	6.350	0	401.28	50.8	0	241.3

UID	LC-FC	H (mm)	N (mm)	t (mm)	RIN (mm)	DEG (deg)	fy (MPa)	MB (mm)	EB (mm)	L (mm)
90097	ETF-UF	73.965	50.8	2.235	6.350	0	531.59	50.8	0	165.1
90098	ETF-UF	73.965	50.8	2.235	6.350	0	531.59	50.8	0	165.1
90099	ETF-UF	99.365	50.8	2.235	6.350	0	531.59	50.8	0	203.2
90100	ETF-UF	99.365	50.8	2.235	6.350	0	531.59	50.8	0	203.2
90101	ETF-UF	125.527	50.8	2.235	6.350	0	531.59	50.8	0	241.3
90102	ETF-UF	125.273	50.8	2.235	6.350	0	531.59	50.8	0	241.3
90019	IOF-UF	77.800	50.8	1.194	2.184	0	973.54	50.8	101.6	482.6
90020	IOF-UF	78.308	50.8	1.194	1.778	0	973.54	50.8	101.6	482.6
90021	IOF-UF	104.470	50.8	1.194	3.378	0	973.54	50.8	101.6	558.8
90022	IOF-UF	105.232	50.8	1.194	3.175	0	973.54	50.8	101.6	558.8
90023	IOF-UF	129.870	50.8	1.194	2.388	0	973.54	50.8	101.6	635
90024	IOF-UF	129.870	50.8	1.194	2.591	0	973.54	50.8	101.6	635
90025	IOF-UF	73.990	50.8	1.194	6.350	0	973.54	50.8	101.6	482.6
90026	IOF-UF	73.990	50.8	1.194	6.350	0	973.54	50.8	101.6	482.6
90027	IOF-UF	99.390	50.8	1.194	6.350	0	973.54	50.8	101.6	533.4
90028	IOF-UF	99.644	50.8	1.194	6.350	0	973.54	50.8	101.6	533.4
90029	IOF-UF	124.028	50.8	1.194	6.350	0	973.54	50.8	101.6	635
90030	IOF-UF	124.028	50.8	1.194	6.350	0	973.54	50.8	101.6	635
90031	IOF-UF	75.032	50.8	1.168	6.350	0	1138.32	50.8	101.6	482.6
90032	IOF-UF	74.778	50.8	1.168	6.350	0	1138.32	50.8	101.6	482.6
90033	IOF-UF	100.940	50.8	1.168	6.350	0	1138.32	50.8	101.6	558.8
90034	IOF-UF	100.432	50.8	1.168	6.350	0	1138.32	50.8	101.6	558.8
90035	IOF-UF	125.578	50.8	1.168	6.350	0	1138.32	50.8	101.6	635
90036	IOF-UF	126.340	50.8	1.168	6.350	0	1138.32	50.8	101.6	635
90055	EOF-UF	77.800	50.8	1.194	2.972	0	973.54	101.6	50.8	431.8
90056	EOF-UF	74.752	50.8	1.194	3.962	0	973.54	101.6	50.8	431.8
90057	EOF-UF	100.660	50.8	1.194	4.166	0	973.54	101.6	50.8	508
90058	EOF-UF	100.152	50.8	1.194	4.572	0	973.54	101.6	50.8	508
90059	EOF-UF	127.330	50.8	1.194	3.759	0	973.54	101.6	50.8	584.2
90060	EOF-UF	127.076	50.8	1.194	2.972	0	973.54	101.6	50.8	584.2
90061	EOF-UF	75.794	50.8	1.168	6.350	0	1138.32	101.6	50.8	431.8
90062	EOF-UF	75.286	50.8	1.168	6.350	0	1138.32	101.6	50.8	431.8
90063	EOF-UF	101.702	50.8	1.168	6.350	0	1138.32	101.6	50.8	508
90064	EOF-UF	100.940	50.8	1.168	6.350	0	1138.32	101.6	50.8	508
90065	EOF-UF	127.610	50.8	1.168	6.350	0	1138.32	101.6	50.8	584.2
90066	EOF-UF	126.594	50.8	1.168	6.350	0	1138.32	101.6	50.8	584.2
90079	ITF-UF	75.819	50.8	1.651	6.350	0	806.00	50.8	0	279.4
90080	ITF-UF	75.057	50.8	1.651	6.350	0	806.00	50.8	0	279.4
90081	ITF-UF	99.949	50.8	1.651	6.350	0	806.00	50.8	0	355.6
90082	ITF-UF	99.949	50.8	1.651	6.350	0	806.00	50.8	0	355.6
90083	ITF-UF	126.111	50.8	1.651	6.350	0	806.00	50.8	0	431.8
90084	ITF-UF	126.111	50.8	1.651	6.350	0	806.00	50.8	0	431.8
90085	ITF-UF	76.302	50.8	1.168	6.350	0	1138.32	50.8	0	279.4
90086	ITF-UF	76.302	50.8	1.168	6.350	0	1138.32	50.8	0	279.4
90087	ITF-UF	99.924	50.8	1.168	6.350	0	1138.32	50.8	0	355.6
90088	ITF-UF	100.432	50.8	1.168	6.350	0	1138.32	50.8	0	355.6
90089	ITF-UF	127.610	50.8	1.168	6.350	0	1138.32	50.8	0	431.8
90090	ITF-UF	128.118	50.8	1.168	6.350	0	1138.32	50.8	0	431.8
90103	ETF-UF	75.057	50.8	1.651	6.350	0	806.00	50.8	0	165.1
90104	ETF-UF	75.311	50.8	1.651	6.350	0	806.00	50.8	0	165.1
90105	ETF-UF	100.711	50.8	1.651	6.350	0	806.00	50.8	0	203.2
90106	ETF-UF	100.457	50.8	1.651	6.350	0	806.00	50.8	0	203.2
90107	ETF-UF	127.381	50.8	1.651	6.350	0	806.00	50.8	0	241.3
90108	ETF-UF	126.873	50.8	1.651	6.350	0	806.00	50.8	0	241.3
90109	ETF-UF	75.794	50.8	1.168	6.350	0	1138.32	50.8	0	165.1
90110	ETF-UF	75.540	50.8	1.168	6.350	0	1138.32	50.8	0	165.1
90111	ETF-UF	101.702	50.8	1.168	6.350	0	1138.32	50.8	0	203.2
90112	ETF-UF	101.702	50.8	1.168	6.350	0	1138.32	50.8	0	203.2

UID	LC-FC	H (mm)	N (mm)	t (mm)	RIN (mm)	DEG (deg)	fy (MPa)	MB (mm)	EB (mm)	L (mm)
90113	ETF-UF	126.086	50.8	1.168	6.350	0	1138.32	50.8	0	241.3
90114	ETF-UF	125.832	50.8	1.168	6.350	0	1138.32	50.8	0	241.3

Table Appendix E.3A Dimension data for specimens from Wu, Yu and Laboube

UID	LC-FC	H (mm)	N (mm)	t (mm)	RIN (mm)	DEG (deg)	fy (MPa)	MB (mm)	EB (mm)	L (mm)
11021	ITF-F	78.916	25.4	0.7366	1.984	30	717	25.4	0	600.00
11022	ITF-F	78.458	25.4	0.7366	1.588	30	717	25.4	0	600.00
11023	ITF-F	117.016	25.4	0.7366	1.984	30	717	25.4	0	600.00
11024	ITF-F	116.558	25.4	0.7366	1.588	30	717	25.4	0	600.00
11025	ITF-F	155.116	25.4	0.7366	1.984	30	717	25.4	0	600.00
11026	ITF-F	154.658	25.4	0.7366	1.588	30	717	25.4	0	600.00
11027	ITF-F	78.916	25.4	0.7366	1.984	30	717	25.4	0	600.00
11028	ITF-F	78.458	25.4	0.7366	1.588	30	717	25.4	0	600.00
11029	ITF-F	117.016	25.4	0.7366	1.984	30	717	25.4	0	600.00
11030	ITF-F	116.558	25.4	0.7366	1.588	30	717	25.4	0	600.00
11031	ITF-F	155.116	25.4	0.7366	1.984	30	717	25.4	0	600.00
11032	ITF-F	154.658	25.4	0.7366	1.588	30	717	25.4	0	600.00
21021	ETF-F	78.916	25.4	0.7366	1.984	30	717	25.4	0	600.00
21022	ETF-F	78.458	25.4	0.7366	1.588	30	717	25.4	0	600.00
21023	ETF-F	117.016	25.4	0.7366	1.984	30	717	25.4	0	600.00
21024	ETF-F	116.558	25.4	0.7366	1.588	30	717	25.4	0	600.00
21025	ETF-F	155.116	25.4	0.7366	1.984	30	717	25.4	0	600.00
21026	ETF-F	154.658	25.4	0.7366	1.588	30	717	25.4	0	600.00
21027	ETF-F	78.916	25.4	0.7366	1.984	30	717	25.4	0	600.00
21028	ETF-F	78.458	25.4	0.7366	1.588	30	717	25.4	0	600.00
21029	ETF-F	117.016	25.4	0.7366	1.984	30	717	25.4	0	600.00
21030	ETF-F	116.558	25.4	0.7366	1.588	30	717	25.4	0	600.00
21031	ETF-F	155.116	25.4	0.7366	1.984	30	717	25.4	0	600.00
21032	ETF-F	154.658	25.4	0.7366	1.588	30	717	25.4	0	600.00
21033	ETF-F	116.558	25.4	0.7366	1.588	30	717	25.4	0	600.00
21034	ETF-F	154.658	25.4	0.7366	1.588	30	717	25.4	0	600.00
31021	IOF-F	78.916	38.1	0.7366	1.984	30	717	38.1	76.2	427.25
31022	IOF-F	78.458	38.1	0.7366	1.588	30	717	38.1	76.2	425.87
31023	IOF-F	117.016	38.1	0.7366	1.984	30	717	38.1	76.2	541.55
31024	IOF-F	116.558	38.1	0.7366	1.588	30	717	38.1	76.2	540.17
31025	IOF-F	155.116	38.1	0.7366	1.984	30	717	38.1	76.2	655.85
31026	IOF-F	154.658	38.1	0.7366	1.588	30	717	38.1	76.2	654.47
31027	IOF-F	78.916	38.1	0.7366	1.984	30	717	38.1	76.2	427.25
31028	IOF-F	78.458	38.1	0.7366	1.588	30	717	38.1	76.2	425.87
31029	IOF-F	117.016	38.1	0.7366	1.984	30	717	38.1	76.2	541.55
31030	IOF-F	116.558	38.1	0.7366	1.588	30	717	38.1	76.2	540.17
31031	IOF-F	155.116	38.1	0.7366	1.984	30	717	38.1	76.2	655.85
31032	IOF-F	154.658	38.1	0.7366	1.588	30	717	38.1	76.2	654.47
31033	IOF-F	45.187	38.1	0.7366	3.175	0	717	38.1	76.2	326.06
31034	IOF-F	83.287	38.1	0.7366	3.175	0	717	38.1	76.2	440.36
31035	IOF-F	121.387	38.1	0.7366	3.175	0	717	38.1	76.2	554.66
31036	IOF-F	45.187	38.1	0.7366	3.175	0	717	38.1	76.2	326.06
31037	IOF-F	83.287	38.1	0.7366	3.175	0	717	38.1	76.2	440.36
31038	IOF-F	121.387	38.1	0.7366	3.175	0	717	38.1	76.2	554.66
81071	EOF-UF	78.916	25.4	0.7366	1.984	30	717	101.6	25.4	389.15
81072	EOF-UF	78.458	25.4	0.7366	1.588	30	717	101.6	25.4	387.77
81073	EOF-UF	117.016	25.4	0.7366	1.984	30	717	101.6	25.4	503.45
81074	EOF-UF	116.558	25.4	0.7366	1.588	30	717	101.6	25.4	502.07
81075	EOF-UF	155.116	25.4	0.7366	1.984	30	717	101.6	25.4	617.75
81076	EOF-UF	154.658	25.4	0.7366	1.588	30	717	101.6	25.4	616.37
81077	EOF-UF	78.916	25.4	0.7366	1.984	30	717	101.6	25.4	389.15
81078	EOF-UF	78.458	25.4	0.7366	1.588	30	717	101.6	25.4	387.77
81079	EOF-UF	117.016	25.4	0.7366	1.984	30	717	101.6	25.4	503.45
81080	EOF-UF	116.558	25.4	0.7366	1.588	30	717	101.6	25.4	502.07

UID	LC-FC	H (mm)	N (mm)	t (mm)	RIN (mm)	DEG (deg)	fy (MPa)	MB (mm)	EB (mm)	L (mm)
81081	EOF-UF	155.116	25.4	0.7366	1.984	30	717	101.6	25.4	617.75
81082	EOF-UF	154.658	25.4	0.7366	1.588	30	717	101.6	25.4	616.37
81083	EOF-UF	45.187	25.4	0.7366	3.175	0	717	101.6	25.4	287.96
81084	EOF-UF	83.287	25.4	0.7366	3.175	0	717	101.6	25.4	402.26
81085	EOF-UF	121.387	25.4	0.7366	3.175	0	717	101.6	25.4	516.56
81086	EOF-UF	45.187	25.4	0.7366	3.175	0	717	101.6	25.4	287.96
81087	EOF-UF	83.287	25.4	0.7366	3.175	0	717	101.6	25.4	402.26
81088	EOF-UF	121.387	25.4	0.7366	3.175	0	717	101.6	25.4	516.56

Table Appendix E.1B Py, Pcr and Pexp for specimens tested by Chen, Pham and Hancock

UID	SPECIMEN	e/t	Py (kN)	Pcr (kN)	Pexp (kN)	AS4600 HAT (kN)
11001	ITF-F-H120-RIN3-DEG0-N100-1	1.5	163.254	290.015	99.689	99.700
11002	ITF-F-H120-RIN3-DEG30-N50-1	0.866	155.727	176.141	72.404	
11003	ITF-F-H120-RIN3-DEG15-N50-1	1.151	143.938	221.631	79.656	
11004	ITF-F-H120-RIN3-DEG0-N50-1	1.5	120.788	255.901	76.085	83.362
11005	ITF-F-H90-RIN3-DEG0-N50-1	1.5	103.151	347.760	80.004	85.045
11006	ITF-F-H120-RIN3-DEG0-N100-2	1.5	163.254	290.015	99.176	99.700
11007	ITF-F-H120-RIN3-DEG30-N50-2	0.866	155.727	176.141	72.020	
11008	ITF-F-H120-RIN3-DEG15-N50-2	1.151	143.938	221.631	79.418	
11009	ITF-F-H120-RIN3-DEG0-N50-2	1.5	120.788	255.901	77.348	83.362
11010	ITF-F-H90-RIN3-DEG0-N50-2	1.5	103.151	347.760	80.681	85.045
11011	ITF-F-H120-RIN8-DEG0-N100-1	3.167	85.738	294.505	75.664	89.998
11012	ITF-F-H120-RIN8-DEG30-N50-1	1.828	97.251	169.528	64.274	
11013	ITF-F-H120-RIN8-DEG15-N50-1	2.43	79.865	216.167	63.541	
11014	ITF-F-H120-RIN8-DEG0-N50-1	3.167	63.557	265.404	59.311	75.249
11015	ITF-F-H90-RIN8-DEG0-N50-1	3.167	54.590	348.076	60.850	76.846
11016	ITF-F-H120-RIN8-DEG0-N100-2	3.167	85.738	294.505	75.700	89.998
11017	ITF-F-H120-RIN8-DEG30-N50-2	1.828	97.251	169.528	63.908	
11018	ITF-F-H120-RIN8-DEG15-N50-2	2.43	79.865	216.167	64.109	
11019	ITF-F-H120-RIN8-DEG0-N50-2	3.167	63.557	265.404	58.780	75.249
11020	ITF-F-H90-RIN8-DEG0-N50-2	3.167	54.590	348.076	60.740	76.846
19001	ITF-F-H120-RIN3-DEG30-N50-3	0.866	155.727	176.141	75.023	
19002	ITF-F-H120-RIN8-DEG0-N100-3	3.167	85.738	294.505	75.609	89.998
19003	ITF-F-H120-RIN8-DEG30-N50-3	1.828	97.251	169.528	63.468	
21001	ETF-F-H120-RIN3-DEG30-N50-3	0.866	110.449	82.090	37.154	
21002	ETF-F-H120-RIN3-DEG15-N50-3	1.151	100.585	105.099	42.153	
21003	ETF-F-H120-RIN3-DEG0-N50-3	1.5	84.172	122.123	41.787	49.502
21004	ETF-F-H90-RIN3-DEG0-N50-1	1.5	75.334	182.510	42.538	51.112
21005	ETF-F-H120-RIN3-DEG30-N50-2	0.866	110.449	82.090	36.660	
21006	ETF-F-H120-RIN3-DEG15-N50-2	1.151	100.585	105.099	41.879	
21007	ETF-F-H120-RIN3-DEG0-N50-2	1.5	84.172	122.123	41.128	49.502
21008	ETF-F-H90-RIN3-DEG0-N50-2	1.5	75.334	182.510	42.996	51.112
21011	ETF-F-H120-RIN8-DEG30-N50-1	1.828	68.397	78.229	32.686	
21012	ETF-F-H120-RIN8-DEG15-N50-1	2.43	55.715	100.914	29.720	
21013	ETF-F-H120-RIN8-DEG0-N50-1	3.167	44.199	123.517	30.544	46.494
21014	ETF-F-H90-RIN8-DEG0-N50-1	3.167	39.712	173.788	31.844	48.077
21015	ETF-F-H120-RIN8-DEG30-N50-2	1.828	68.397	78.229	32.448	
21016	ETF-F-H120-RIN8-DEG15-N50-2	2.43	55.715	100.914	32.650	
21017	ETF-F-H120-RIN8-DEG0-N50-2	3.167	44.199	123.517	30.526	46.494
21018	ETF-F-H90-RIN8-DEG0-N50-2	3.167	39.712	173.788	32.869	48.077
21019	ETF-F-H120-RIN8-DEG30-N50-3	1.828	68.397	78.229	30.983	
21020	ETF-F-H120-RIN8-DEG15-N50-3	2.43	55.715	100.914	31.295	
31001	IOF-F-H120-RIN3-DEG0-N100-1	1.5	123.754	243.528	80.205	113.903
31002	IOF-F-H120-RIN3-DEG30-N50-1	0.866	151.969	137.185	61.491	
31003	IOF-F-H120-RIN3-DEG15-N50-1	1.151	125.611	180.556	61.802	
31004	IOF-F-H120-RIN3-DEG0-N50-1	1.5	100.879	223.190	63.761	99.600
31005	IOF-F-H90-RIN3-DEG0-N50-1	1.5	82.579	183.901	59.330	104.268
31006	IOF-F-H120-RIN3-DEG0-N100-2	1.5	123.754	243.528	80.425	113.903
31007	IOF-F-H120-RIN3-DEG30-N50-2	0.866	151.969	137.185	61.619	
31008	IOF-F-H120-RIN3-DEG15-N50-2	1.151	125.611	180.556	60.886	
31009	IOF-F-H120-RIN3-DEG0-N50-2	1.5	100.879	223.190	62.608	99.600
31010	IOF-F-H90-RIN3-DEG0-N50-2	1.5	82.579	183.901	58.286	104.268
31011	IOF-F-H120-RIN8-DEG0-N100-1	3.167	62.365	210.690	64.567	104.659
31012	IOF-F-H120-RIN8-DEG30-N50-1	1.828	83.590	131.864	49.167	

UID	SPECIMEN	e/t	Py (kN)	Pcr (kN)	Pexp (kN)	AS4600 HAT (kN)
31013	IOF-F-H120-RIN8-DEG15-N50-1	2.43	65.161	166.125	50.815	
31014	IOF-F-H120-RIN8-DEG0-N50-1	3.167	51.046	189.006	50.082	91.516
31015	IOF-F-H90-RIN8-DEG0-N50-1	3.167	41.991	160.623	46.365	95.985
31016	IOF-F-H120-RIN8-DEG0-N100-2	3.167	62.365	210.690	63.578	104.659
31017	IOF-F-H120-RIN8-DEG30-N50-2	1.828	83.590	131.864	49.368	
31018	IOF-F-H120-RIN8-DEG15-N50-2	2.43	65.161	166.125	50.870	
31019	IOF-F-H120-RIN8-DEG0-N50-2	3.167	51.046	189.006	50.339	91.516
31020	IOF-F-H90-RIN8-DEG0-N50-2	3.167	41.991	160.623	45.816	95.985
41001	EOF-F-H120-RIN3-DEG30-N50-1	0.866	109.740	203.335	46.264	
41002	EOF-F-H120-RIN3-DEG15-N50-1	1.151	96.901	226.575	46.704	
41003	EOF-F-H120-RIN3-DEG0-N50-1	1.5	79.215	233.302	43.609	49.837
41004	EOF-F-H90-RIN3-DEG0-N50-1	1.5	70.030	281.670	48.846	52.173
41005	EOF-F-H120-RIN3-DEG30-N50-2	0.866	109.740	203.335	47.088	
41006	EOF-F-H120-RIN3-DEG15-N50-2	1.151	96.901	226.575	45.532	
41007	EOF-F-H120-RIN3-DEG0-N50-2	1.5	79.215	233.302	47.125	49.837
41008	EOF-F-H90-RIN3-DEG0-N50-2	1.5	70.030	281.670	49.414	52.173
41009	EOF-F-H120-RIN3-DEG30-N50-3	0.866	109.740	203.335	46.924	
41010	EOF-F-H90-RIN3-DEG0-N50-3	1.5	70.030	281.670	48.132	52.173
41011	EOF-F-H120-RIN8-DEG30-N50-1	1.828	64.088	202.283	35.909	
41012	EOF-F-H120-RIN8-DEG15-N50-1	2.43	51.155	225.406	35.552	
41013	EOF-F-H120-RIN8-DEG0-N50-1	3.167	40.170	233.877	34.380	39.905
41014	EOF-F-H90-RIN8-DEG0-N50-1	3.167	35.637	281.419	36.715	41.853
41015	EOF-F-H120-RIN8-DEG30-N50-2	1.828	64.088	202.283	36.266	
41016	EOF-F-H120-RIN8-DEG15-N50-2	2.43	51.155	225.406	35.900	
41017	EOF-F-H120-RIN8-DEG0-N50-2	3.167	40.170	233.877	35.552	39.905
41018	EOF-F-H90-RIN8-DEG0-N50-2	3.167	35.637	281.419	37.658	41.853
41019	EOF-F-H120-RIN8-DEG30-N50-3	1.828	64.088	202.283	36.257	
41020	EOF-F-H90-RIN8-DEG0-N50-3	3.167	35.637	281.419	36.724	41.853
81001	EOF-UF-H120-RIN3-DEG0-N50-1	1.5	63.249	141.138	39.315	49.837
81002	EOF-UF-H120-RIN3-DEG0-N50-2	1.5	63.249	141.138	41.421	49.837
81003	EOF-UF-H120-RIN8-DEG0-N50-1	3.167	31.861	138.616	30.077	39.905
81004	EOF-UF-H120-RIN8-DEG0-N50-2	3.167	31.861	138.616	29.509	39.905
89001	EOF-UF-H120-RIN3-DEG0-N50-3	1.5	63.249	141.138	40.689	49.837

Table Appendix E.2B Py, Pcr and Pexp for specimens tested by Santaputra and Yu

UID	SPECIMEN	e/t	Py (kN)	Pcr (kN)	Pexp (kN)	AS4600 HAT (kN)
90001	1-HIOF-A11	5.375	11.199	21.471	12.677	
90002	1-HIOF-A12	5.375	11.176	21.007	12.455	
90003	1-HIOF-A21	5.708	12.593	14.837	13.033	
90004	1-HIOF-A22	6.187	11.639	13.820	13.033	
90005	1-HIOF-A31	5.542	14.986	12.432	12.900	
90006	1-HIOF-A32	5.708	14.587	12.083	13.345	
90007	2-HIOF-A11	2.976	50.771	121.645	48.041	91.539
90008	2-HIOF-A12	3.268	46.812	117.257	47.729	90.279
90009	2-HIOF-A21	3.268	56.346	90.912	51.065	85.651
90010	2-HIOF-A22	3.268	56.443	91.506	50.709	85.608
90011	2-HIOF-A31	3.171	68.093	76.879	55.736	81.873
90012	2-HIOF-A32	3.171	68.193	76.718	56.715	81.835
90013	3-HIOF-A11	3.645	40.483	51.304	38.166	65.317
90014	3-HIOF-A12	3.145	46.625	54.110	38.255	66.616
90015	3-HIOF-A21	3.145	55.916	42.252	38.166	62.707
90016	3-HIOF-A22	3.016	58.280	42.982	37.943	63.022
90017	3-HIOF-A31	2.645	77.410	35.644	38.477	60.482
90018	3-HIOF-A32	3.274	62.949	34.399	38.699	58.892
90037	1-HEOF-A11	5.229	7.512	19.584	24.198	
90038	1-HEOF-A12	5.062	7.749	19.628	23.131	
90039	1-HEOF-A21	4.896	9.087	14.097	24.243	
90040	1-HEOF-A22	5.229	8.552	14.176	24.376	
90041	1-HEOF-A31	4.729	10.688	10.434	24.020	
90042	1-HEOF-A32	5.062	9.995	10.587	23.398	
90043	2-HEOF-A11	3.253	31.695	117.313	22.152	45.376
90044	2-HEOF-A12	3.076	33.456	117.066	22.019	46.317
90045	2-HEOF-A21	3.171	37.611	77.398	23.353	43.451
90046	2-HEOF-A22	2.982	39.849	77.251	23.709	44.456
90047	2-HEOF-A31	3.171	43.012	55.872	22.908	41.324
90048	2-HEOF-A32	3.076	44.152	56.052	23.220	41.839
90049	3-HEOF-A11	3.623	27.716	52.648	21.040	34.368
90050	3-HEOF-A12	3.269	30.608	52.971	20.684	35.821
90051	3-HEOF-A21	3.392	34.315	34.439	22.241	33.143
90052	3-HEOF-A22	3.392	34.220	34.562	22.552	33.182
90053	3-HEOF-A31	3.5	37.972	25.093	21.930	30.867
90054	3-HEOF-A32	3.746	35.579	25.153	21.663	29.972
90067	1-HITF-A11	5.819	12.122	21.588	6.397	
90068	1-HITF-A12	5.819	12.122	21.517	6.227	
90069	1-HITF-A21	5.819	14.198	15.839	6.174	
90070	1-HITF-A22	5.819	14.219	15.864	6.121	
90071	1-HITF-A31	5.819	16.398	12.501	5.952	
90072	1-HITF-A32	5.819	16.378	12.498	5.720	
90073	2-HITF-A11	3.341	52.274	134.394	25.969	
90074	2-HITF-A12	3.341	52.274	134.160	26.520	
90075	2-HITF-A21	3.341	61.204	97.799	26.636	
90076	2-HITF-A22	3.341	61.381	97.525	27.801	
90077	2-HITF-A31	3.341	70.487	76.027	24.136	
90078	2-HITF-A32	3.341	70.398	76.085	25.132	
90091	1-HETF-A11	5.819	7.726	11.049	18.238	
90092	1-HETF-A12	5.819	7.747	10.986	18.736	
90093	1-HETF-A21	5.819	8.764	7.639	17.846	
90094	1-HETF-A22	5.819	8.785	7.608	18.460	
90095	1-HETF-A31	5.819	9.802	5.775	16.850	

UID	SPECIMEN	e/t	Py (kN)	Pcr (kN)	Pexp (kN)	AS4600 HAT (kN)
90096	1-HETF-A32	5.819	9.802	5.977	16.627	
90097	2-HETF-A11	3.341	33.406	70.246	11.681	
90098	2-HETF-A12	3.341	33.406	70.161	11.565	
90099	2-HETF-A21	3.341	37.826	46.760	10.845	
90100	2-HETF-A22	3.341	37.826	46.853	10.008	
90101	2-HETF-A31	3.341	42.378	34.371	9.679	
90102	2-HETF-A32	3.341	42.334	34.422	9.457	
90019	4-HIOF-A11	2.33	58.278	26.784	11.521	49.492
90020	4-HIOF-A12	1.989	67.766	27.238	11.432	50.317
90021	4-HIOF-A21	3.33	50.791	19.481	10.676	43.615
90022	4-HIOF-A22	3.16	53.677	19.681	10.480	43.839
90023	4-HIOF-A31	2.5	78.237	16.250	9.341	42.156
90024	4-HIOF-A32	2.67	73.507	16.116	9.208	41.807
90025	4-HIOF-A13	5.819	23.687	20.330	14.679	
90026	4-HIOF-A14	5.819	23.687	20.190	14.457	
90027	4-HIOF-A23	5.819	28.739	15.139	14.679	
90028	4-HIOF-A24	5.819	28.790	15.112	14.457	
90029	4-HIOF-A33	5.819	33.640	11.882	14.234	
90030	4-HIOF-A34	5.819	33.640	11.917	14.457	
90031	5-HIOF-A11	5.935	26.805	18.476	61.163	
90032	5-HIOF-A12	5.935	26.748	18.409	61.385	
90033	5-HIOF-A21	5.935	32.588	13.526	61.163	
90034	5-HIOF-A22	5.935	32.475	13.437	60.496	
90035	5-HIOF-A31	5.935	38.088	10.857	61.163	
90036	5-HIOF-A32	5.935	38.258	10.924	61.385	
90055	4-HEOF-A11	2.989	30.677	18.288	44.927	25.293
90056	4-HEOF-A12	3.819	23.806	19.271	45.816	23.110
90057	4-HEOF-A21	3.989	26.571	12.753	43.148	20.920
90058	4-HEOF-A22	4.33	24.487	12.885	42.703	20.125
90059	4-HEOF-A31	3.649	33.157	9.073	42.703	20.184
90060	4-HEOF-A32	2.989	40.110	8.997	41.813	21.888
90061	5-HEOF-A11	5.935	17.936	17.776	26.244	
90062	5-HEOF-A12	5.935	17.879	18.007	26.689	
90063	5-HEOF-A21	5.935	20.827	12.353	24.688	
90064	5-HEOF-A22	5.935	20.742	12.416	24.465	
90065	5-HEOF-A31	5.935	23.719	9.355	23.353	
90066	5-HEOF-A32	5.935	23.605	9.464	23.246	
90079	3-HITF-A11	4.346	45.466	55.417	6.450	
90080	3-HITF-A12	4.346	45.235	55.782	6.343	
90081	3-HITF-A21	4.346	52.759	41.133	6.450	
90082	3-HITF-A22	4.346	52.759	41.129	6.450	
90083	3-HITF-A31	4.346	60.667	32.209	5.783	
90084	3-HITF-A32	4.346	60.667	32.216	5.889	
90085	5-HITF-A11	5.935	33.282	20.068	25.132	
90086	5-HITF-A12	5.935	33.282	20.143	24.794	
90087	5-HITF-A21	5.935	38.539	14.838	24.020	
90088	5-HITF-A22	5.935	38.652	14.830	23.575	
90089	5-HITF-A31	5.935	44.700	11.709	21.574	
90090	5-HITF-A32	5.935	44.813	11.694	21.351	
90103	3-HETF-A11	4.346	28.778	28.572	13.567	
90104	3-HETF-A12	4.346	28.816	28.440	14.234	
90105	3-HETF-A21	4.346	32.655	19.277	12.571	
90106	3-HETF-A22	4.346	32.616	19.288	13.229	
90107	3-HETF-A31	4.346	36.685	14.609	11.565	
90108	3-HETF-A32	4.346	36.608	14.627	11.672	
90109	5-HETF-A11	5.935	21.030	10.394	6.672	
90110	5-HETF-A12	5.935	21.002	10.390	6.779	

UID	SPECIMEN	e/t	Py (kN)	Pcr (kN)	Pexp (kN)	AS4600 HAT (kN)
90111	5-HETF-A21	5.935	23.913	7.151	6.005	
90112	5-HETF-A22	5.935	23.913	7.134	6.227	
90113	5-HETF-A31	5.935	26.626	5.458	5.445	
90114	5-HETF-A32	5.935	26.598	5.459	5.338	

Table Appendix E.3B Py, Pcr and Pexp for specimens tested by Wu, Yu and Laboube

UID	SPECIMEN	e/t	Py (kN)	Pcr (kN)	Pexp (kN)	AS4600 HAT (kN)
11021	ITF-F-H78.916-RIN1.984-DEG30-N25.4-1	1.844	30.181	4.172	7.869	
11022	ITF-F-H78.458-RIN1.5875-DEG30-N25.4-1	1.533	34.446	4.216	8.323	
11023	ITF-F-H117.016-RIN1.984-DEG30-N25.4-1	1.844	39.343	3.031	6.672	
11024	ITF-F-H116.558-RIN1.5875-DEG30-N25.4-1	1.533	44.852	3.049	6.979	
11025	ITF-F-H155.116-RIN1.984-DEG30-N25.4-1	1.844	48.299	2.444	5.760	
11026	ITF-F-H154.658-RIN1.5875-DEG30-N25.4-1	1.533	54.965	2.455	5.356	
11027	ITF-F-H78.916-RIN1.984-DEG30-N25.4-2	1.844	30.181	4.172	7.753	
11028	ITF-F-H78.458-RIN1.5875-DEG30-N25.4-2	1.533	34.446	4.216	8.389	
11029	ITF-F-H117.016-RIN1.984-DEG30-N25.4-2	1.844	39.343	3.031	6.944	
11030	ITF-F-H116.558-RIN1.5875-DEG30-N25.4-2	1.533	44.852	3.049	6.454	
11031	ITF-F-H155.116-RIN1.984-DEG30-N25.4-2	1.844	48.299	2.444	5.498	
11032	ITF-F-H154.658-RIN1.5875-DEG30-N25.4-2	1.533	54.965	2.455	5.142	
21021	ETF-F-H78.916-RIN1.984-DEG30-N25.4-1	1.844	20.286	1.794	2.638	
21022	ETF-F-H78.458-RIN1.5875-DEG30-N25.4-1	1.533	23.231	1.815	2.749	
21023	ETF-F-H117.016-RIN1.984-DEG30-N25.4-1	1.844	25.015	1.212	1.975	
21024	ETF-F-H116.558-RIN1.5875-DEG30-N25.4-1	1.533	28.647	1.220	2.633	
21025	ETF-F-H155.116-RIN1.984-DEG30-N25.4-1	1.844	29.685	0.928	1.673	
21026	ETF-F-H154.658-RIN1.5875-DEG30-N25.4-1	1.533	33.976	0.931	2.126	
21027	ETF-F-H78.916-RIN1.984-DEG30-N25.4-2	1.844	20.286	1.794	2.842	
21028	ETF-F-H78.458-RIN1.5875-DEG30-N25.4-2	1.533	23.231	1.815	2.767	
21029	ETF-F-H117.016-RIN1.984-DEG30-N25.4-2	1.844	25.015	1.212	2.077	
21030	ETF-F-H116.558-RIN1.5875-DEG30-N25.4-2	1.533	28.647	1.220	2.073	
21031	ETF-F-H155.116-RIN1.984-DEG30-N25.4-2	1.844	29.685	0.928	1.641	
21032	ETF-F-H154.658-RIN1.5875-DEG30-N25.4-2	1.533	33.976	0.931	1.673	
21033	ETF-F-H116.558-RIN1.5875-DEG30-N25.4-3	1.533	28.647	1.220	2.011	
21034	ETF-F-H154.658-RIN1.5875-DEG30-N25.4-3	1.533	33.976	0.931	1.628	
31021	IOF-F-H78.916-RIN1.984-DEG30-N38.1-1	1.844	29.836	3.950	8.145	
31022	IOF-F-H78.458-RIN1.5875-DEG30-N38.1-1	1.533	34.952	4.000	8.078	
31023	IOF-F-H117.016-RIN1.984-DEG30-N38.1-1	1.844	40.206	3.348	7.331	
31024	IOF-F-H116.558-RIN1.5875-DEG30-N38.1-1	1.533	47.171	3.376	7.531	
31025	IOF-F-H155.116-RIN1.984-DEG30-N38.1-1	1.844	50.576	2.890	6.775	
31026	IOF-F-H154.658-RIN1.5875-DEG30-N38.1-1	1.533	59.390	2.907	7.317	
31027	IOF-F-H78.916-RIN1.984-DEG30-N38.1-2	1.844	29.836	3.950	7.887	
31028	IOF-F-H78.458-RIN1.5875-DEG30-N38.1-2	1.533	34.952	4.000	8.314	
31029	IOF-F-H117.016-RIN1.984-DEG30-N38.1-2	1.844	40.206	3.348	7.317	
31030	IOF-F-H116.558-RIN1.5875-DEG30-N38.1-2	1.533	47.171	3.376	7.535	
31031	IOF-F-H155.116-RIN1.984-DEG30-N38.1-2	1.844	50.576	2.890	6.873	
31032	IOF-F-H154.658-RIN1.5875-DEG30-N38.1-2	1.533	59.390	2.907	7.495	
31033	IOF-F-H45.1866-RIN3.175-DEG0-N38.1-1	4.81	8.460	7.671	7.500	13.310
31034	IOF-F-H83.2866-RIN3.175-DEG0-N38.1-1	4.81	12.618	5.110	7.976	11.084
31035	IOF-F-H121.3866-RIN3.175-DEG0-N38.1-1	4.81	16.776	3.643	8.087	9.375
31036	IOF-F-H45.1866-RIN3.175-DEG0-N38.1-2	4.81	8.460	7.671	7.531	13.310
31037	IOF-F-H83.2866-RIN3.175-DEG0-N38.1-2	4.81	12.618	5.110	8.171	11.084
31038	IOF-F-H121.3866-RIN3.175-DEG0-N38.1-2	4.81	16.776	3.643	7.553	9.375
81071	EOF-UF-H78.916-RIN1.984-DEG30-N25.4-1	1.844	16.364	2.337	3.892	
81072	EOF-UF-H78.458-RIN1.5875-DEG30-N25.4-1	1.533	19.180	2.375	4.217	
81073	EOF-UF-H117.016-RIN1.984-DEG30-N25.4-1	1.844	21.550	1.371	2.931	
81074	EOF-UF-H116.558-RIN1.5875-DEG30-N25.4-1	1.533	25.290	1.385	3.238	
81075	EOF-UF-H155.116-RIN1.984-DEG30-N25.4-1	1.844	26.735	0.963	2.442	
81076	EOF-UF-H154.658-RIN1.5875-DEG30-N25.4-1	1.533	31.399	0.970	2.682	
81077	EOF-UF-H78.916-RIN1.984-DEG30-N25.4-2	1.844	16.364	2.337	3.790	
81078	EOF-UF-H78.458-RIN1.5875-DEG30-N25.4-2	1.533	19.180	2.375	4.039	
81079	EOF-UF-H117.016-RIN1.984-DEG30-N25.4-2	1.844	21.550	1.371	3.056	
81080	EOF-UF-H116.558-RIN1.5875-DEG30-N25.4-2	1.533	25.290	1.385	3.309	
81081	EOF-UF-H155.116-RIN1.984-DEG30-N25.4-2	1.844	26.735	0.963	2.482	
81082	EOF-UF-H154.658-RIN1.5875-DEG30-N25.4-2	1.533	31.399	0.970	2.633	
81083	EOF-UF-H45.1866-RIN3.175-DEG0-N25.4-1	4.81	4.810	6.998	3.643	
81084	EOF-UF-H83.2866-RIN3.175-DEG0-N25.4-1	4.81	6.889	2.807	2.789	
81085	EOF-UF-H121.3866-RIN3.175-DEG0-N25.4-1	4.81	8.968	1.642	2.215	
81086	EOF-UF-H45.1866-RIN3.175-DEG0-N25.4-2	4.81	4.810	6.998	3.772	

UID	SPECIMEN	e/t	Py (kN)	Pcr (kN)	Pexp (kN)	AS4600 HAT (kN)
81087	EOF-UF-H83.2866-RIN3.175-DEG0-N25.4-2	4.81	6.889	2.807	2.762	
81088	EOF-UF-H121.3866-RIN3.175-DEG0-N25.4-2	4.81	8.968	1.642	2.202	

Appendix F

DSM design equations calculation data

Table Appendix F.1 DSM data for specimens tested by Chen, Pham and Hancock

UID	LC-FC	λ ($\sqrt{P_y/P_{cr}}$)	P_n/P_y (MDM)	P_{exp}/P_n (MDM)	P_n/P_y (STM)	P_{exp}/P_n (STM)
11001	ITF-F	0.769	0.635	0.917	0.656	0.887
11002	ITF-F	0.934	0.546	0.863	0.556	0.848
11003	ITF-F	0.820	0.606	0.882	0.623	0.858
11004	ITF-F	0.703	0.673	0.893	0.700	0.859
11005	ITF-F	0.558	0.764	0.969	0.806	0.918
11006	ITF-F	0.769	0.635	0.912	0.656	0.883
11007	ITF-F	0.934	0.546	0.859	0.556	0.843
11008	ITF-F	0.820	0.606	0.880	0.623	0.855
11009	ITF-F	0.703	0.673	0.908	0.700	0.873
11010	ITF-F	0.558	0.764	0.977	0.806	0.925
11011	ITF-F	0.543	0.934	0.932	0.943	0.922
11012	ITF-F	0.757	0.642	1.031	0.713	0.929
11013	ITF-F	0.613	0.729	1.074	0.864	0.906
11014	ITF-F	0.493	0.959	0.960	0.968	0.952
11015	ITF-F	0.399	1.003	1.096	1.009	1.089
11016	ITF-F	0.543	0.934	0.932	0.943	0.923
11017	ITF-F	0.757	0.642	1.026	0.713	0.923
11018	ITF-F	0.613	0.729	1.083	0.864	0.914
11019	ITF-F	0.493	0.959	0.951	0.968	0.943
11020	ITF-F	0.399	1.003	1.094	1.009	1.088
19001	ITF-F	0.934	0.546	0.894	0.556	0.878
19002	ITF-F	0.543	0.934	0.931	0.943	0.922
19003	ITF-F	0.757	0.642	1.019	0.713	0.917
21001	ETF-F	1.139	0.378	0.923	0.359	0.974
21002	ETF-F	0.924	0.475	0.989	0.458	1.025
21003	ETF-F	0.770	0.563	1.026	0.553	1.044
21004	ETF-F	0.588	0.685	0.983	0.693	0.971
21005	ETF-F	1.139	0.378	0.911	0.359	0.961
21006	ETF-F	0.924	0.475	0.982	0.458	1.018
21007	ETF-F	0.770	0.563	1.010	0.553	1.028
21008	ETF-F	0.588	0.685	0.994	0.693	0.982
21011	ETF-F	0.875	0.501	1.089	0.538	1.014
21012	ETF-F	0.680	0.621	1.026	0.741	0.860
21013	ETF-F	0.544	0.847	0.988	0.887	0.944
21014	ETF-F	0.429	0.927	1.075	0.956	1.042
21015	ETF-F	0.875	0.501	1.081	0.538	1.007
21016	ETF-F	0.680	0.621	1.127	0.741	0.945
21017	ETF-F	0.544	0.847	0.988	0.887	0.943
21018	ETF-F	0.429	0.927	1.109	0.956	1.075
21019	ETF-F	0.875	0.501	1.032	0.538	0.962
21020	ETF-F	0.680	0.621	1.080	0.741	0.906
31001	IOF-F	0.714	0.677	0.955	0.693	0.933
31002	IOF-F	1.041	0.510	0.810	0.501	0.826
31003	IOF-F	0.834	0.610	0.807	0.614	0.801
31004	IOF-F	0.673	0.701	0.900	0.721	0.874
31005	IOF-F	0.671	0.702	1.021	0.723	0.991
31006	IOF-F	0.714	0.677	0.958	0.693	0.935
31007	IOF-F	1.041	0.510	0.812	0.501	0.827
31008	IOF-F	0.834	0.610	0.795	0.614	0.789
31009	IOF-F	0.673	0.701	0.884	0.721	0.858

UID	LC-FC	λ ($\sqrt{P_y/P_{cr}}$)	P_n/P_y (MDM)	P_{exp}/P_n (MDM)	P_n/P_y (STM)	P_{exp}/P_n (STM)
31010	IOF-F	0.671	0.702	1.003	0.723	0.974
31011	IOF-F	0.544	0.936	1.105	0.943	1.097
31012	IOF-F	0.797	0.630	0.932	0.687	0.854
31013	IOF-F	0.627	0.728	1.069	0.856	0.910
31014	IOF-F	0.520	0.948	1.033	0.955	1.026
31015	IOF-F	0.512	0.952	1.158	0.959	1.150
31016	IOF-F	0.544	0.936	1.088	0.943	1.080
31017	IOF-F	0.797	0.630	0.935	0.687	0.857
31018	IOF-F	0.627	0.728	1.070	0.856	0.911
31019	IOF-F	0.520	0.948	1.039	0.955	1.032
31020	IOF-F	0.512	0.952	1.144	0.959	1.137
41001	EOF-F	0.603	0.648	0.965	0.634	0.985
41002	EOF-F	0.575	0.669	0.934	0.660	0.947
41003	EOF-F	0.520	0.710	0.974	0.710	0.974
41004	EOF-F	0.455	0.760	1.100	0.773	1.081
41005	EOF-F	0.603	0.648	0.982	0.634	1.003
41006	EOF-F	0.575	0.669	0.910	0.660	0.923
41007	EOF-F	0.520	0.710	1.053	0.710	1.052
41008	EOF-F	0.455	0.760	1.113	0.773	1.094
41009	EOF-F	0.603	0.648	0.979	0.634	1.000
41010	EOF-F	0.455	0.760	1.084	0.773	1.066
41011	EOF-F	0.499	0.726	0.982	0.777	0.918
41012	EOF-F	0.430	0.780	1.095	0.892	0.958
41013	EOF-F	0.377	0.942	1.096	0.966	1.068
41014	EOF-F	0.332	0.973	1.215	0.993	1.191
41015	EOF-F	0.499	0.726	0.992	0.777	0.928
41016	EOF-F	0.430	0.780	1.106	0.892	0.968
41017	EOF-F	0.377	0.942	1.133	0.966	1.105
41018	EOF-F	0.332	0.973	1.246	0.993	1.221
41019	EOF-F	0.499	0.726	0.992	0.777	0.927
41020	EOF-F	0.332	0.973	1.216	0.993	1.191
81001	EOF-UF	0.670	0.620	1.000	0.619	1.001
81002	EOF-UF	0.670	0.620	1.053	0.619	1.054
81003	EOF-UF	0.480	0.866	1.088	0.859	1.097
81004	EOF-UF	0.480	0.866	1.068	0.859	1.077
89001	EOF-UF	0.670	0.620	1.034	0.619	1.036

Table Appendix F.2 DSM data for specimens tested by Santaputra and Yu

UID	LC-FC	λ ($\sqrt{P_y/P_{cr}}$)	P_n/P_y (MDM)	P_{exp}/P_n (MDM)	P_n/P_y (STM)	P_{exp}/P_n (STM)
90001	IOF-UF	0.722	0.987	1.146	0.912	1.240
90002	IOF-UF	0.730	0.984	1.132	0.909	1.225
90003	IOF-UF	0.921	0.890	1.162	0.826	1.253
90004	IOF-UF	0.918	0.892	1.255	0.827	1.353
90005	IOF-UF	1.098	0.806	1.067	0.750	1.148
90006	IOF-UF	1.099	0.806	1.135	0.749	1.220
90007	IOF-UF	0.647	0.717	1.319	0.881	1.073
90008	IOF-UF	0.632	0.891	1.143	0.904	1.127
90009	IOF-UF	0.788	0.808	1.120	0.824	1.098
90010	IOF-UF	0.786	0.809	1.109	0.825	1.087
90011	IOF-UF	0.942	0.729	1.122	0.740	1.105
90012	IOF-UF	0.943	0.728	1.141	0.739	1.124
90013	IOF-UF	0.889	0.756	1.247	0.797	1.182
90014	IOF-UF	0.929	0.735	1.115	0.744	1.101
90015	IOF-UF	1.151	0.630	1.082	0.639	1.067
90016	IOF-UF	1.165	0.624	1.042	0.622	1.045
90017	IOF-UF	1.475	0.365	1.359	0.469	1.059
90018	IOF-UF	1.354	0.548	1.120	0.566	1.085
90037	IOF-UF	1.477	0.365	1.136	0.437	0.947
90038	IOF-UF	1.579	0.340	1.000	0.371	0.917
90039	IOF-UF	1.616	0.461	1.034	0.480	0.992
90040	IOF-UF	1.653	0.451	1.007	0.457	0.993
90041	IOF-UF	2.196	0.243	1.263	0.288	1.064
90042	IOF-UF	2.137	0.249	1.274	0.309	1.027
90043	IOF-UF	1.080	0.815	1.147	0.757	1.234
90044	IOF-UF	1.083	0.813	1.143	0.756	1.229
90045	IOF-UF	1.378	0.684	1.188	0.638	1.272
90046	IOF-UF	1.381	0.683	1.205	0.637	1.291
90047	IOF-UF	1.683	0.572	1.189	0.536	1.271
90048	IOF-UF	1.680	0.573	1.204	0.536	1.286
90049	IOF-UF	1.205	0.757	1.036	0.706	1.112
90050	IOF-UF	1.206	0.757	1.021	0.705	1.096
90051	IOF-UF	1.553	0.617	1.105	0.577	1.182
90052	IOF-UF	1.555	0.616	1.126	0.576	1.204
90053	IOF-UF	1.873	0.514	1.119	0.482	1.195
90054	IOF-UF	1.872	0.515	1.100	0.482	1.174
90067	EOF-UF	0.619	0.872	0.976	0.791	1.076
90068	EOF-UF	0.629	0.865	0.929	0.785	1.023
90069	EOF-UF	0.803	0.739	0.919	0.668	1.017
90070	EOF-UF	0.777	0.757	0.945	0.685	1.045
90071	EOF-UF	1.012	0.608	0.916	0.547	1.017
90072	EOF-UF	0.972	0.631	0.907	0.569	1.006
90073	EOF-UF	0.520	0.836	0.979	0.830	0.985
90074	EOF-UF	0.535	0.825	0.960	0.813	0.973
90075	EOF-UF	0.698	0.705	1.003	0.695	1.018
90076	EOF-UF	0.719	0.589	1.184	0.672	1.037
90077	EOF-UF	0.878	0.588	0.953	0.576	0.973
90078	EOF-UF	0.888	0.582	0.976	0.566	1.004
90091	EOF-UF	0.726	0.685	0.959	0.691	0.951
90092	EOF-UF	0.761	0.662	0.924	0.655	0.934
90093	EOF-UF	0.999	0.521	0.996	0.518	1.003
90094	EOF-UF	0.996	0.523	1.030	0.519	1.037
90095	EOF-UF	1.231	0.418	1.060	0.417	1.062

UID	LC-FC	λ ($\sqrt{P_y/P_{cr}}$)	P_n/P_y (MDM)	P_{exp}/P_n (MDM)	P_n/P_y (STM)	P_{exp}/P_n (STM)
90096	EOF-UF	1.190	0.434	1.075	0.442	1.057
90097	EOF-UF	1.296	0.330	1.151	0.375	1.013
90098	EOF-UF	1.112	0.467	1.039	0.478	1.015
90099	EOF-UF	1.444	0.347	1.173	0.359	1.134
90100	EOF-UF	1.379	0.367	1.113	0.389	1.050
90101	EOF-UF	1.913	0.246	1.184	0.246	1.188
90102	EOF-UF	2.113	0.189	1.243	0.203	1.161
90019	EOF-UF	1.005	0.612	1.049	0.551	1.164
90020	EOF-UF	0.997	0.617	1.037	0.556	1.150
90021	EOF-UF	1.299	0.470	1.091	0.422	1.215
90022	EOF-UF	1.293	0.472	1.070	0.424	1.191
90023	EOF-UF	1.593	0.369	1.067	0.331	1.190
90024	EOF-UF	1.580	0.373	1.046	0.334	1.167
90025	ITF-UF	0.751	0.973	1.239	0.900	1.340
90026	ITF-UF	0.752	0.973	1.221	0.900	1.321
90027	ITF-UF	0.949	0.877	1.174	0.814	1.265
90028	ITF-UF	0.949	0.877	1.155	0.814	1.244
90029	ITF-UF	1.148	0.783	1.104	0.729	1.186
90030	ITF-UF	1.147	0.784	1.122	0.729	1.206
90031	ITF-UF	0.627	0.893	1.295	0.910	1.271
90032	ITF-UF	0.628	0.893	1.300	0.910	1.276
90033	ITF-UF	0.796	0.804	1.229	0.825	1.198
90034	ITF-UF	0.798	0.803	1.214	0.824	1.183
90035	ITF-UF	0.968	0.716	1.199	0.739	1.161
90036	ITF-UF	0.967	0.716	1.204	0.739	1.166
90055	ITF-UF	0.909	0.745	1.317	0.824	1.191
90056	ITF-UF	0.904	0.748	1.345	0.827	1.217
90057	ITF-UF	1.136	0.637	1.276	0.725	1.120
90058	ITF-UF	1.136	0.637	1.263	0.725	1.108
90059	ITF-UF	1.377	0.539	1.296	0.630	1.110
90060	ITF-UF	1.377	0.539	1.269	0.630	1.087
90061	ITF-UF	1.290	0.720	1.091	0.672	1.169
90062	ITF-UF	1.288	0.721	1.107	0.673	1.188
90063	ITF-UF	1.615	0.595	1.072	0.557	1.146
90064	ITF-UF	1.617	0.594	1.061	0.556	1.134
90065	ITF-UF	1.958	0.491	1.060	0.460	1.131
90066	ITF-UF	1.961	0.490	1.054	0.459	1.125
90079	ETF-UF	0.838	0.772	1.077	0.745	1.116
90080	ETF-UF	0.841	0.770	1.059	0.743	1.098
90081	ETF-UF	1.073	0.631	1.161	0.620	1.182
90082	ETF-UF	1.077	0.630	1.162	0.619	1.183
90083	ETF-UF	1.305	0.518	1.135	0.516	1.139
90084	ETF-UF	1.283	0.528	1.135	0.525	1.140
90085	ETF-UF	0.693	0.742	1.004	0.764	0.974
90086	ETF-UF	0.694	0.741	0.991	0.764	0.962
90087	ETF-UF	0.904	0.606	1.036	0.632	0.994
90088	ETF-UF	0.903	0.607	1.016	0.633	0.975
90089	ETF-UF	1.116	0.494	1.019	0.520	0.968
90090	ETF-UF	1.115	0.495	1.008	0.521	0.958
90103	ETF-UF	1.007	0.549	0.853	0.645	0.727
90104	ETF-UF	1.010	0.547	0.897	0.643	0.763
90105	ETF-UF	1.306	0.414	0.923	0.507	0.755
90106	ETF-UF	1.305	0.415	0.971	0.507	0.794
90107	ETF-UF	1.590	0.324	0.967	0.407	0.770
90108	ETF-UF	1.587	0.325	0.976	0.408	0.777
90109	ETF-UF	1.425	0.469	0.675	0.470	0.672
90110	ETF-UF	1.424	0.469	0.686	0.471	0.683
90111	ETF-UF	1.832	0.341	0.733	0.349	0.717

UID	LC-FC	λ ($\sqrt{P_y/P_{cr}}$)	P_n/P_y (MDM)	P_{exp}/P_n (MDM)	P_n/P_y (STM)	P_{exp}/P_n (STM)
90112	ETF-UF	1.834	0.341	0.762	0.349	0.745
90113	ETF-UF	2.213	0.263	0.776	0.272	0.749
90114	ETF-UF	2.211	0.263	0.760	0.272	0.734

Table Appendix F.3 DSM data for specimens tested by Wu, Yu and Laboube

UID	LC-FC	λ ($\sqrt{P_y/P_{cr}}$)	P_n/P_y (MDM)	P_{exp}/P_n (MDM)	P_n/P_y (STM)	P_{exp}/P_n (STM)
11021	ITF-F	2.690	0.193	1.353	0.190	1.375
11022	ITF-F	2.858	0.183	1.323	0.161	1.505
11023	ITF-F	3.603	0.152	1.113	0.140	1.213
11024	ITF-F	3.835	0.146	1.065	0.122	1.277
11025	ITF-F	4.445	0.134	0.892	0.117	1.023
11026	ITF-F	4.732	0.129	0.753	0.104	0.935
11027	ITF-F	2.690	0.193	1.333	0.190	1.355
11028	ITF-F	2.858	0.183	1.333	0.161	1.517
11029	ITF-F	3.603	0.152	1.158	0.140	1.263
11030	ITF-F	3.835	0.146	0.985	0.122	1.181
11031	ITF-F	4.445	0.134	0.851	0.117	0.977
11032	ITF-F	4.732	0.129	0.723	0.104	0.897
21021	ETF-F	3.363	0.092	1.419	0.085	1.523
21022	ETF-F	3.577	0.087	1.368	0.075	1.576
21023	ETF-F	4.543	0.071	1.105	0.061	1.293
21024	ETF-F	4.846	0.068	1.344	0.055	1.670
21025	ETF-F	5.657	0.062	0.902	0.050	1.121
21026	ETF-F	6.040	0.060	1.036	0.046	1.353
21027	ETF-F	3.363	0.092	1.529	0.085	1.641
21028	ETF-F	3.577	0.087	1.377	0.075	1.586
21029	ETF-F	4.543	0.071	1.163	0.061	1.360
21030	ETF-F	4.846	0.068	1.058	0.055	1.315
21031	ETF-F	5.657	0.062	0.885	0.050	1.100
21032	ETF-F	6.040	0.060	0.815	0.046	1.064
21033	ETF-F	4.846	0.068	1.026	0.055	1.275
21034	ETF-F	6.040	0.060	0.793	0.046	1.036
31021	IOF-F	2.748	0.197	1.388	0.185	1.475
31022	IOF-F	2.956	0.185	1.251	0.155	1.490
31023	IOF-F	3.465	0.163	1.116	0.145	1.257
31024	IOF-F	3.738	0.155	1.030	0.125	1.282
31025	IOF-F	4.183	0.144	0.927	0.122	1.094
31026	IOF-F	4.520	0.138	0.891	0.108	1.146
31027	IOF-F	2.748	0.197	1.344	0.185	1.428
31028	IOF-F	2.956	0.185	1.287	0.155	1.534
31029	IOF-F	3.465	0.163	1.114	0.145	1.254
31030	IOF-F	3.738	0.155	1.031	0.125	1.283
31031	IOF-F	4.183	0.144	0.941	0.122	1.110
31032	IOF-F	4.520	0.138	0.912	0.108	1.174
31033	IOF-F	1.050	0.828	1.070	0.770	1.151
31034	IOF-F	1.571	0.611	1.035	0.571	1.107
31035	IOF-F	2.146	0.445	1.084	0.417	1.157
31036	IOF-F	1.050	0.828	1.074	0.770	1.156
31037	IOF-F	1.571	0.611	1.061	0.571	1.134
31038	IOF-F	2.146	0.445	1.013	0.417	1.081
81071	EOF-UF	2.646	0.150	1.583	0.134	1.782
81072	EOF-UF	2.842	0.141	1.564	0.118	1.870
81073	EOF-UF	3.964	0.108	1.256	0.090	1.509
81074	EOF-UF	4.273	0.103	1.239	0.082	1.557
81075	EOF-UF	5.269	0.093	0.986	0.074	1.233
81076	EOF-UF	5.690	0.090	0.952	0.069	1.230
81077	EOF-UF	2.646	0.150	1.542	0.134	1.735
81078	EOF-UF	2.842	0.141	1.498	0.118	1.791
81079	EOF-UF	3.964	0.108	1.310	0.090	1.573

UID	LC-FC	λ $(\sqrt{P_y/P_{cr}})$	P_n/P_y (MDM)	P_{exp}/P_n (MDM)	P_n/P_y (STM)	P_{exp}/P_n (STM)
81080	EOF-UF	4.273	0.103	1.267	0.082	1.591
81081	EOF-UF	5.269	0.093	1.002	0.074	1.253
81082	EOF-UF	5.690	0.090	0.935	0.069	1.208
81083	EOF-UF	0.829	0.721	1.051	0.652	1.162
81084	EOF-UF	1.567	0.377	1.075	0.338	1.199
81085	EOF-UF	2.337	0.227	1.089	0.203	1.216
81086	EOF-UF	0.829	0.721	1.088	0.652	1.204
81087	EOF-UF	1.567	0.377	1.065	0.338	1.188
81088	EOF-UF	2.337	0.227	1.082	0.203	1.208

Appendix G

Numerical study data set used in Chapter 7

Table Appendix G.1 Dimension data for specimens from numerical analysis

UID	LC-FC	H (mm)	N (mm)	t (mm)	RIN (mm)	DEG (deg)	fy (MPa)	MB (mm)	EB (mm)	L (mm)
11033	ITF-F	120	50	3	3	0	323	50	0	600.00
11034	ITF-F	120	50	3	3	10	323	50	0	600.00
11035	ITF-F	120	50	3	3	15	323	50	0	600.00
11036	ITF-F	120	50	3	3	20	323	50	0	600.00
11037	ITF-F	120	50	3	3	25	323	50	0	600.00
11038	ITF-F	120	50	3	3	30	323	50	0	600.00
11039	ITF-F	120	50	3	3	0	323	50	0	600.00
11040	ITF-F	120	50	3	3	10	323	50	0	600.00
11041	ITF-F	120	50	3	3	15	323	50	0	600.00
11042	ITF-F	120	50	3	3	20	323	50	0	600.00
11043	ITF-F	120	50	3	3	25	323	50	0	600.00
11044	ITF-F	120	50	3	3	30	323	50	0	600.00
11045	ITF-F	120	50	3	8	0	323	50	0	600.00
11046	ITF-F	120	50	3	8	10	323	50	0	600.00
11047	ITF-F	120	50	3	8	15	323	50	0	600.00
11048	ITF-F	120	50	3	8	20	323	50	0	600.00
11049	ITF-F	120	50	3	8	25	323	50	0	600.00
11050	ITF-F	120	50	3	8	30	323	50	0	600.00
11051	ITF-F	120	50	3	8	0	323	50	0	600.00
11052	ITF-F	120	50	3	8	10	323	50	0	600.00
11053	ITF-F	120	50	3	8	15	323	50	0	600.00
11054	ITF-F	120	50	3	8	20	323	50	0	600.00
11055	ITF-F	120	50	3	8	25	323	50	0	600.00
11056	ITF-F	120	50	3	8	30	323	50	0	600.00
11057	ITF-F	120	38.1	0.7366	0.7366	0	717	38.1	0	600.00
11058	ITF-F	120	38.1	0.7366	1.8415	0	717	38.1	0	600.00
11059	ITF-F	120	38.1	0.7366	2.9464	0	717	38.1	0	600.00
11060	ITF-F	40	38.1	0.7366	0.7366	0	717	38.1	0	600.00
11061	ITF-F	40	38.1	0.7366	1.8415	0	717	38.1	0	600.00
11062	ITF-F	40	38.1	0.7366	2.9464	0	717	38.1	0	600.00
11063	ITF-F	80	38.1	0.7366	0.7366	0	717	38.1	0	600.00
11064	ITF-F	80	38.1	0.7366	1.8415	0	717	38.1	0	600.00
11065	ITF-F	80	38.1	0.7366	2.9464	0	717	38.1	0	600.00
11066	ITF-F	120	38.1	0.7366	1.0716	15	717	38.1	0	600.00
11067	ITF-F	120	38.1	0.7366	2.5116	15	717	38.1	0	600.00
11068	ITF-F	120	38.1	0.7366	3.9515	15	717	38.1	0	600.00
11069	ITF-F	40	38.1	0.7366	1.0716	15	717	38.1	0	600.00
11070	ITF-F	40	38.1	0.7366	2.5116	15	717	38.1	0	600.00
11071	ITF-F	40	38.1	0.7366	3.9515	15	717	38.1	0	600.00
11072	ITF-F	80	38.1	0.7366	1.0716	15	717	38.1	0	600.00
11073	ITF-F	80	38.1	0.7366	2.5116	15	717	38.1	0	600.00
11074	ITF-F	80	38.1	0.7366	3.9515	15	717	38.1	0	600.00
11075	ITF-F	120	38.1	0.7366	1.5454	30	717	38.1	0	600.00
11076	ITF-F	120	38.1	0.7366	3.4592	30	717	38.1	0	600.00
11077	ITF-F	120	38.1	0.7366	5.3729	30	717	38.1	0	600.00
11078	ITF-F	40	38.1	0.7366	1.5454	30	717	38.1	0	600.00
11079	ITF-F	40	38.1	0.7366	3.4592	30	717	38.1	0	600.00
11080	ITF-F	40	38.1	0.7366	5.3729	30	717	38.1	0	600.00
11081	ITF-F	80	38.1	0.7366	1.5454	30	717	38.1	0	600.00
11082	ITF-F	80	38.1	0.7366	3.4592	30	717	38.1	0	600.00
11083	ITF-F	80	38.1	0.7366	5.3729	30	717	38.1	0	600.00
11084	ITF-F	120	38.1	1	1.0000	0	717	38.1	0	600.00
11085	ITF-F	120	38.1	1	2.5000	0	717	38.1	0	600.00
11086	ITF-F	120	38.1	1	4.0000	0	717	38.1	0	600.00
11087	ITF-F	40	38.1	1	1.0000	0	717	38.1	0	600.00
11088	ITF-F	40	38.1	1	2.5000	0	717	38.1	0	600.00

UID	LC-FC	H (mm)	N (mm)	t (mm)	RIN (mm)	DEG (deg)	fy (MPa)	MB (mm)	EB (mm)	L (mm)
11089	ITF-F	40	38.1	1	4.0000	0	717	38.1	0	600.00
11090	ITF-F	80	38.1	1	1.0000	0	717	38.1	0	600.00
11091	ITF-F	80	38.1	1	2.5000	0	717	38.1	0	600.00
11092	ITF-F	80	38.1	1	4.0000	0	717	38.1	0	600.00
11093	ITF-F	120	38.1	1	1.4548	15	717	38.1	0	600.00
11094	ITF-F	120	38.1	1	3.4097	15	717	38.1	0	600.00
11095	ITF-F	120	38.1	1	5.3645	15	717	38.1	0	600.00
11096	ITF-F	40	38.1	1	1.4548	15	717	38.1	0	600.00
11097	ITF-F	40	38.1	1	3.4097	15	717	38.1	0	600.00
11098	ITF-F	40	38.1	1	5.3645	15	717	38.1	0	600.00
11099	ITF-F	80	38.1	1	1.4548	15	717	38.1	0	600.00
11100	ITF-F	80	38.1	1	3.4097	15	717	38.1	0	600.00
11101	ITF-F	80	38.1	1	5.3645	15	717	38.1	0	600.00
11102	ITF-F	120	38.1	1	2.0981	30	717	38.1	0	600.00
11103	ITF-F	120	38.1	1	4.6962	30	717	38.1	0	600.00
11104	ITF-F	120	38.1	1	7.2942	30	717	38.1	0	600.00
11105	ITF-F	40	38.1	1	2.0981	30	717	38.1	0	600.00
11106	ITF-F	40	38.1	1	4.6962	30	717	38.1	0	600.00
11107	ITF-F	40	38.1	1	7.2942	30	717	38.1	0	600.00
11108	ITF-F	80	38.1	1	2.0981	30	717	38.1	0	600.00
11109	ITF-F	80	38.1	1	4.6962	30	717	38.1	0	600.00
11110	ITF-F	80	38.1	1	7.2942	30	717	38.1	0	600.00
11111	ITF-F	120	50	3	4	0	323	50	0	600.00
11112	ITF-F	120	50	3	5	0	323	50	0	600.00
11113	ITF-F	120	50	3	6	0	323	50	0	600.00
11114	ITF-F	120	50	3	7	0	323	50	0	600.00
21035	ETF-F	120	50	3	3	0	323	50	0	600.00
21036	ETF-F	120	50	3	3	10	323	50	0	600.00
21037	ETF-F	120	50	3	3	15	323	50	0	600.00
21038	ETF-F	120	50	3	3	20	323	50	0	600.00
21039	ETF-F	120	50	3	3	25	323	50	0	600.00
21040	ETF-F	120	50	3	3	30	323	50	0	600.00
21041	ETF-F	120	50	3	3	0	323	50	0	600.00
21042	ETF-F	120	50	3	3	10	323	50	0	600.00
21043	ETF-F	120	50	3	3	15	323	50	0	600.00
21044	ETF-F	120	50	3	3	20	323	50	0	600.00
21045	ETF-F	120	50	3	3	25	323	50	0	600.00
21046	ETF-F	120	50	3	3	30	323	50	0	600.00
21047	ETF-F	120	50	3	8	0	323	50	0	600.00
21048	ETF-F	120	50	3	8	10	323	50	0	600.00
21049	ETF-F	120	50	3	8	15	323	50	0	600.00
21050	ETF-F	120	50	3	8	20	323	50	0	600.00
21051	ETF-F	120	50	3	8	25	323	50	0	600.00
21052	ETF-F	120	50	3	8	30	323	50	0	600.00
21053	ETF-F	120	50	3	8	0	323	50	0	600.00
21054	ETF-F	120	50	3	8	10	323	50	0	600.00
21055	ETF-F	120	50	3	8	15	323	50	0	600.00
21056	ETF-F	120	50	3	8	20	323	50	0	600.00
21057	ETF-F	120	50	3	8	25	323	50	0	600.00
21058	ETF-F	120	50	3	8	30	323	50	0	600.00
21059	ETF-F	120	38.1	0.7366	0.7366	0	717	38.1	0	600.00
21060	ETF-F	120	38.1	0.7366	1.8415	0	717	38.1	0	600.00
21061	ETF-F	120	38.1	0.7366	2.9464	0	717	38.1	0	600.00
21062	ETF-F	40	38.1	0.7366	0.7366	0	717	38.1	0	600.00
21063	ETF-F	40	38.1	0.7366	1.8415	0	717	38.1	0	600.00
21064	ETF-F	40	38.1	0.7366	2.9464	0	717	38.1	0	600.00
21065	ETF-F	80	38.1	0.7366	0.7366	0	717	38.1	0	600.00
21066	ETF-F	80	38.1	0.7366	1.8415	0	717	38.1	0	600.00
21067	ETF-F	80	38.1	0.7366	2.9464	0	717	38.1	0	600.00
21068	ETF-F	120	38.1	0.7366	1.0716	15	717	38.1	0	600.00
21069	ETF-F	120	38.1	0.7366	2.5116	15	717	38.1	0	600.00
21070	ETF-F	120	38.1	0.7366	3.9515	15	717	38.1	0	600.00
21071	ETF-F	40	38.1	0.7366	1.0716	15	717	38.1	0	600.00
21072	ETF-F	40	38.1	0.7366	2.5116	15	717	38.1	0	600.00
21073	ETF-F	40	38.1	0.7366	3.9515	15	717	38.1	0	600.00

UID	LC-FC	H (mm)	N (mm)	t (mm)	RIN (mm)	DEG (deg)	fy (MPa)	MB (mm)	EB (mm)	L (mm)
21074	ETF-F	80	38.1	0.7366	1.0716	15	717	38.1	0	600.00
21075	ETF-F	80	38.1	0.7366	2.5116	15	717	38.1	0	600.00
21076	ETF-F	80	38.1	0.7366	3.9515	15	717	38.1	0	600.00
21077	ETF-F	120	38.1	0.7366	1.5454	30	717	38.1	0	600.00
21078	ETF-F	120	38.1	0.7366	3.4592	30	717	38.1	0	600.00
21079	ETF-F	120	38.1	0.7366	5.3729	30	717	38.1	0	600.00
21080	ETF-F	40	38.1	0.7366	1.5454	30	717	38.1	0	600.00
21081	ETF-F	40	38.1	0.7366	3.4592	30	717	38.1	0	600.00
21082	ETF-F	40	38.1	0.7366	5.3729	30	717	38.1	0	600.00
21083	ETF-F	80	38.1	0.7366	1.5454	30	717	38.1	0	600.00
21084	ETF-F	80	38.1	0.7366	3.4592	30	717	38.1	0	600.00
21085	ETF-F	80	38.1	0.7366	5.3729	30	717	38.1	0	600.00
21086	ETF-F	120	38.1	1	1.0000	0	717	38.1	0	600.00
21087	ETF-F	120	38.1	1	2.5000	0	717	38.1	0	600.00
21088	ETF-F	120	38.1	1	4.0000	0	717	38.1	0	600.00
21089	ETF-F	40	38.1	1	1.0000	0	717	38.1	0	600.00
21090	ETF-F	40	38.1	1	2.5000	0	717	38.1	0	600.00
21091	ETF-F	40	38.1	1	4.0000	0	717	38.1	0	600.00
21092	ETF-F	80	38.1	1	1.0000	0	717	38.1	0	600.00
21093	ETF-F	80	38.1	1	2.5000	0	717	38.1	0	600.00
21094	ETF-F	80	38.1	1	4.0000	0	717	38.1	0	600.00
21095	ETF-F	120	38.1	1	1.4548	15	717	38.1	0	600.00
21096	ETF-F	120	38.1	1	3.4097	15	717	38.1	0	600.00
21097	ETF-F	120	38.1	1	5.3645	15	717	38.1	0	600.00
21098	ETF-F	40	38.1	1	1.4548	15	717	38.1	0	600.00
21099	ETF-F	40	38.1	1	3.4097	15	717	38.1	0	600.00
21100	ETF-F	40	38.1	1	5.3645	15	717	38.1	0	600.00
21101	ETF-F	80	38.1	1	1.4548	15	717	38.1	0	600.00
21102	ETF-F	80	38.1	1	3.4097	15	717	38.1	0	600.00
21103	ETF-F	80	38.1	1	5.3645	15	717	38.1	0	600.00
21104	ETF-F	120	38.1	1	2.0981	30	717	38.1	0	600.00
21105	ETF-F	120	38.1	1	4.6962	30	717	38.1	0	600.00
21106	ETF-F	120	38.1	1	7.2942	30	717	38.1	0	600.00
21107	ETF-F	40	38.1	1	2.0981	30	717	38.1	0	600.00
21108	ETF-F	40	38.1	1	4.6962	30	717	38.1	0	600.00
21109	ETF-F	40	38.1	1	7.2942	30	717	38.1	0	600.00
21110	ETF-F	80	38.1	1	2.0981	30	717	38.1	0	600.00
21111	ETF-F	80	38.1	1	4.6962	30	717	38.1	0	600.00
21112	ETF-F	80	38.1	1	7.2942	30	717	38.1	0	600.00
21113	ETF-F	120	50	3	4	0	323	50	0	600.00
21114	ETF-F	120	50	3	5	0	323	50	0	600.00
21115	ETF-F	120	50	3	6	0	323	50	0	600.00
21116	ETF-F	120	50	3	7	0	323	50	0	600.00
31039	IOF-F	120	50	3	3	0	323	50	50	600.00
31040	IOF-F	120	50	3	3	10	323	50	50	600.00
31041	IOF-F	120	50	3	3	15	323	50	50	600.00
31042	IOF-F	120	50	3	3	20	323	50	50	600.00
31043	IOF-F	120	50	3	3	25	323	50	50	600.00
31044	IOF-F	120	50	3	3	30	323	50	50	600.00
31045	IOF-F	120	50	3	3	0	323	50	50	600.00
31046	IOF-F	120	50	3	3	10	323	50	50	600.00
31047	IOF-F	120	50	3	3	15	323	50	50	600.00
31048	IOF-F	120	50	3	3	20	323	50	50	600.00
31049	IOF-F	120	50	3	3	25	323	50	50	600.00
31050	IOF-F	120	50	3	3	30	323	50	50	600.00
31051	IOF-F	120	50	3	8	0	323	50	50	600.00
31052	IOF-F	120	50	3	8	10	323	50	50	600.00
31053	IOF-F	120	50	3	8	15	323	50	50	600.00
31054	IOF-F	120	50	3	8	20	323	50	50	600.00
31055	IOF-F	120	50	3	8	25	323	50	50	600.00
31056	IOF-F	120	50	3	8	30	323	50	50	600.00
31057	IOF-F	120	50	3	8	0	323	50	50	600.00
31058	IOF-F	120	50	3	8	10	323	50	50	600.00
31059	IOF-F	120	50	3	8	15	323	50	50	600.00
31060	IOF-F	120	50	3	8	20	323	50	50	600.00

UID	LC-FC	H (mm)	N (mm)	t (mm)	RIN (mm)	DEG (deg)	fy (MPa)	MB (mm)	EB (mm)	L (mm)
31061	IOF-F	120	50	3	8	25	323	50	50	600.00
31062	IOF-F	120	50	3	8	30	323	50	50	600.00
31063	IOF-F	120	38.1	0.7366	0.7366	0	717	38.1	76.2	550.50
31064	IOF-F	120	38.1	0.7366	1.8415	0	717	38.1	76.2	550.50
31065	IOF-F	120	38.1	0.7366	2.9464	0	717	38.1	76.2	550.50
31066	IOF-F	40	38.1	0.7366	0.7366	0	717	38.1	76.2	310.50
31067	IOF-F	40	38.1	0.7366	1.8415	0	717	38.1	76.2	310.50
31068	IOF-F	40	38.1	0.7366	2.9464	0	717	38.1	76.2	310.50
31069	IOF-F	80	38.1	0.7366	0.7366	0	717	38.1	76.2	430.50
31070	IOF-F	80	38.1	0.7366	1.8415	0	717	38.1	76.2	430.50
31071	IOF-F	80	38.1	0.7366	2.9464	0	717	38.1	76.2	430.50
31072	IOF-F	120	38.1	0.7366	1.0716	15	717	38.1	76.2	550.50
31073	IOF-F	120	38.1	0.7366	2.5116	15	717	38.1	76.2	550.50
31074	IOF-F	120	38.1	0.7366	3.9515	15	717	38.1	76.2	550.50
31075	IOF-F	40	38.1	0.7366	1.0716	15	717	38.1	76.2	310.50
31076	IOF-F	40	38.1	0.7366	2.5116	15	717	38.1	76.2	310.50
31077	IOF-F	40	38.1	0.7366	3.9515	15	717	38.1	76.2	310.50
31078	IOF-F	80	38.1	0.7366	1.0716	15	717	38.1	76.2	430.50
31079	IOF-F	80	38.1	0.7366	2.5116	15	717	38.1	76.2	430.50
31080	IOF-F	80	38.1	0.7366	3.9515	15	717	38.1	76.2	430.50
31081	IOF-F	120	38.1	0.7366	1.5454	30	717	38.1	76.2	550.50
31082	IOF-F	120	38.1	0.7366	3.4592	30	717	38.1	76.2	550.50
31083	IOF-F	120	38.1	0.7366	5.3729	30	717	38.1	76.2	550.50
31084	IOF-F	40	38.1	0.7366	1.5454	30	717	38.1	76.2	310.50
31085	IOF-F	40	38.1	0.7366	3.4592	30	717	38.1	76.2	310.50
31086	IOF-F	40	38.1	0.7366	5.3729	30	717	38.1	76.2	310.50
31087	IOF-F	80	38.1	0.7366	1.5454	30	717	38.1	76.2	430.50
31088	IOF-F	80	38.1	0.7366	3.4592	30	717	38.1	76.2	430.50
31089	IOF-F	80	38.1	0.7366	5.3729	30	717	38.1	76.2	430.50
31090	IOF-F	120	38.1	1	1.0000	0	717	38.1	76.2	550.50
31091	IOF-F	120	38.1	1	2.5000	0	717	38.1	76.2	550.50
31092	IOF-F	120	38.1	1	4.0000	0	717	38.1	76.2	550.50
31093	IOF-F	40	38.1	1	1.0000	0	717	38.1	76.2	310.50
31094	IOF-F	40	38.1	1	2.5000	0	717	38.1	76.2	310.50
31095	IOF-F	40	38.1	1	4.0000	0	717	38.1	76.2	310.50
31096	IOF-F	80	38.1	1	1.0000	0	717	38.1	76.2	430.50
31097	IOF-F	80	38.1	1	2.5000	0	717	38.1	76.2	430.50
31098	IOF-F	80	38.1	1	4.0000	0	717	38.1	76.2	430.50
31099	IOF-F	120	38.1	1	1.4548	15	717	38.1	76.2	550.50
31100	IOF-F	120	38.1	1	3.4097	15	717	38.1	76.2	550.50
31101	IOF-F	120	38.1	1	5.3645	15	717	38.1	76.2	550.50
31102	IOF-F	40	38.1	1	1.4548	15	717	38.1	76.2	310.50
31103	IOF-F	40	38.1	1	3.4097	15	717	38.1	76.2	310.50
31104	IOF-F	40	38.1	1	5.3645	15	717	38.1	76.2	310.50
31105	IOF-F	80	38.1	1	1.4548	15	717	38.1	76.2	430.50
31106	IOF-F	80	38.1	1	3.4097	15	717	38.1	76.2	430.50
31107	IOF-F	80	38.1	1	5.3645	15	717	38.1	76.2	430.50
31108	IOF-F	120	38.1	1	2.0981	30	717	38.1	76.2	550.50
31109	IOF-F	120	38.1	1	4.6962	30	717	38.1	76.2	550.50
31110	IOF-F	120	38.1	1	7.2942	30	717	38.1	76.2	550.50
31111	IOF-F	40	38.1	1	2.0981	30	717	38.1	76.2	310.50
31112	IOF-F	40	38.1	1	4.6962	30	717	38.1	76.2	310.50
31113	IOF-F	40	38.1	1	7.2942	30	717	38.1	76.2	310.50
31114	IOF-F	80	38.1	1	2.0981	30	717	38.1	76.2	430.50
31115	IOF-F	80	38.1	1	4.6962	30	717	38.1	76.2	430.50
31116	IOF-F	80	38.1	1	7.2942	30	717	38.1	76.2	430.50
31117	IOF-F	120	50	3	4	0	323	50	50	600.00
31118	IOF-F	120	50	3	5	0	323	50	50	600.00
31119	IOF-F	120	50	3	6	0	323	50	50	600.00
31120	IOF-F	120	50	3	7	0	323	50	50	600.00
41027	EOF-F	120	25.4	0.7366	0.7366	0	717	101.6	25.4	512.40
41028	EOF-F	120	25.4	0.7366	1.8415	0	717	101.6	25.4	512.40
41029	EOF-F	120	25.4	0.7366	2.9464	0	717	101.6	25.4	512.40
41030	EOF-F	40	25.4	0.7366	0.7366	0	717	101.6	25.4	272.40
41031	EOF-F	40	25.4	0.7366	1.8415	0	717	101.6	25.4	272.40

UID	LC-FC	H (mm)	N (mm)	t (mm)	RIN (mm)	DEG (deg)	fy (MPa)	MB (mm)	EB (mm)	L (mm)
41032	EOF-F	40	25.4	0.7366	2.9464	0	717	101.6	25.4	272.40
41033	EOF-F	80	25.4	0.7366	0.7366	0	717	101.6	25.4	392.40
41034	EOF-F	80	25.4	0.7366	1.8415	0	717	101.6	25.4	392.40
41035	EOF-F	80	25.4	0.7366	2.9464	0	717	101.6	25.4	392.40
41036	EOF-F	120	25.4	0.7366	1.0716	15	717	101.6	25.4	512.40
41037	EOF-F	120	25.4	0.7366	2.5116	15	717	101.6	25.4	512.40
41038	EOF-F	120	25.4	0.7366	3.9515	15	717	101.6	25.4	512.40
41039	EOF-F	40	25.4	0.7366	1.0716	15	717	101.6	25.4	272.40
41040	EOF-F	40	25.4	0.7366	2.5116	15	717	101.6	25.4	272.40
41041	EOF-F	40	25.4	0.7366	3.9515	15	717	101.6	25.4	272.40
41042	EOF-F	80	25.4	0.7366	1.0716	15	717	101.6	25.4	392.40
41043	EOF-F	80	25.4	0.7366	2.5116	15	717	101.6	25.4	392.40
41044	EOF-F	80	25.4	0.7366	3.9515	15	717	101.6	25.4	392.40
41045	EOF-F	120	25.4	0.7366	1.5454	30	717	101.6	25.4	512.40
41046	EOF-F	120	25.4	0.7366	3.4592	30	717	101.6	25.4	512.40
41047	EOF-F	120	25.4	0.7366	5.3729	30	717	101.6	25.4	512.40
41048	EOF-F	40	25.4	0.7366	1.5454	30	717	101.6	25.4	272.40
41049	EOF-F	40	25.4	0.7366	3.4592	30	717	101.6	25.4	272.40
41050	EOF-F	40	25.4	0.7366	5.3729	30	717	101.6	25.4	272.40
41051	EOF-F	80	25.4	0.7366	1.5454	30	717	101.6	25.4	392.40
41052	EOF-F	80	25.4	0.7366	3.4592	30	717	101.6	25.4	392.40
41053	EOF-F	80	25.4	0.7366	5.3729	30	717	101.6	25.4	392.40
41054	EOF-F	120	25.4	1	1.0000	0	717	101.6	25.4	512.40
41055	EOF-F	120	25.4	1	2.5000	0	717	101.6	25.4	512.40
41056	EOF-F	120	25.4	1	4.0000	0	717	101.6	25.4	512.40
41057	EOF-F	40	25.4	1	1.0000	0	717	101.6	25.4	272.40
41058	EOF-F	40	25.4	1	2.5000	0	717	101.6	25.4	272.40
41059	EOF-F	40	25.4	1	4.0000	0	717	101.6	25.4	272.40
41060	EOF-F	80	25.4	1	1.0000	0	717	101.6	25.4	392.40
41061	EOF-F	80	25.4	1	2.5000	0	717	101.6	25.4	392.40
41062	EOF-F	80	25.4	1	4.0000	0	717	101.6	25.4	392.40
41063	EOF-F	120	25.4	1	1.4548	15	717	101.6	25.4	512.40
41064	EOF-F	120	25.4	1	3.4097	15	717	101.6	25.4	512.40
41065	EOF-F	120	25.4	1	5.3645	15	717	101.6	25.4	512.40
41066	EOF-F	40	25.4	1	1.4548	15	717	101.6	25.4	272.40
41067	EOF-F	40	25.4	1	3.4097	15	717	101.6	25.4	272.40
41068	EOF-F	40	25.4	1	5.3645	15	717	101.6	25.4	272.40
41069	EOF-F	80	25.4	1	1.4548	15	717	101.6	25.4	392.40
41070	EOF-F	80	25.4	1	3.4097	15	717	101.6	25.4	392.40
41071	EOF-F	80	25.4	1	5.3645	15	717	101.6	25.4	392.40
41072	EOF-F	120	25.4	1	2.0981	30	717	101.6	25.4	512.40
41073	EOF-F	120	25.4	1	4.6962	30	717	101.6	25.4	512.40
41074	EOF-F	120	25.4	1	7.2942	30	717	101.6	25.4	512.40
41075	EOF-F	40	25.4	1	2.0981	30	717	101.6	25.4	272.40
41076	EOF-F	40	25.4	1	4.6962	30	717	101.6	25.4	272.40
41077	EOF-F	40	25.4	1	7.2942	30	717	101.6	25.4	272.40
41078	EOF-F	80	25.4	1	2.0981	30	717	101.6	25.4	392.40
41079	EOF-F	80	25.4	1	4.6962	30	717	101.6	25.4	392.40
41080	EOF-F	80	25.4	1	7.2942	30	717	101.6	25.4	392.40
41081	EOF-F	120	50	3	3	0	323	100	50	600.00
41082	EOF-F	120	50	3	3	10	323	100	50	600.00
41083	EOF-F	120	50	3	3	15	323	100	50	600.00
41084	EOF-F	120	50	3	3	20	323	100	50	600.00
41085	EOF-F	120	50	3	3	25	323	100	50	600.00
41086	EOF-F	120	50	3	3	30	323	100	50	600.00
41087	EOF-F	120	50	3	3	0	323	100	50	600.00
41088	EOF-F	120	50	3	3	10	323	100	50	600.00
41089	EOF-F	120	50	3	3	15	323	100	50	600.00
41090	EOF-F	120	50	3	3	20	323	100	50	600.00
41091	EOF-F	120	50	3	3	25	323	100	50	600.00
41092	EOF-F	120	50	3	3	30	323	100	50	600.00
41093	EOF-F	120	50	3	8	0	323	100	50	600.00
41094	EOF-F	120	50	3	8	10	323	100	50	600.00
41095	EOF-F	120	50	3	8	15	323	100	50	600.00
41096	EOF-F	120	50	3	8	20	323	100	50	600.00

UID	LC-FC	H (mm)	N (mm)	t (mm)	RIN (mm)	DEG (deg)	fy (MPa)	MB (mm)	EB (mm)	L (mm)
41097	EOF-F	120	50	3	8	25	323	100	50	600.00
41098	EOF-F	120	50	3	8	30	323	100	50	600.00
41099	EOF-F	120	50	3	8	0	323	100	50	600.00
41100	EOF-F	120	50	3	8	10	323	100	50	600.00
41101	EOF-F	120	50	3	8	15	323	100	50	600.00
41102	EOF-F	120	50	3	8	20	323	100	50	600.00
41103	EOF-F	120	50	3	8	25	323	100	50	600.00
41104	EOF-F	120	50	3	8	30	323	100	50	600.00
81005	EOF-UF	120	50	3	3	0	323	100	50	600.00
81006	EOF-UF	120	50	3	3	10	323	100	50	600.00
81007	EOF-UF	120	50	3	3	15	323	100	50	600.00
81008	EOF-UF	120	50	3	8	0	323	100	50	600.00
81009	EOF-UF	120	50	3	8	10	323	100	50	600.00
81010	EOF-UF	120	50	3	8	15	323	100	50	600.00
81011	EOF-UF	120	50	3	3	0	323	100	50	600.00
81012	EOF-UF	120	50	3	3	10	323	100	50	600.00
81013	EOF-UF	120	50	3	3	15	323	100	50	600.00
81014	EOF-UF	120	50	3	8	0	323	100	50	600.00
81015	EOF-UF	120	50	3	8	10	323	100	50	600.00
81016	EOF-UF	120	50	3	8	15	323	100	50	600.00
81017	EOF-UF	120	25.4	0.7366	0.7366	0	717	101.6	25.4	512.40
81018	EOF-UF	120	25.4	0.7366	1.8415	0	717	101.6	25.4	512.40
81019	EOF-UF	120	25.4	0.7366	2.9464	0	717	101.6	25.4	512.40
81020	EOF-UF	40	25.4	0.7366	0.7366	0	717	101.6	25.4	272.40
81021	EOF-UF	40	25.4	0.7366	1.8415	0	717	101.6	25.4	272.40
81022	EOF-UF	40	25.4	0.7366	2.9464	0	717	101.6	25.4	272.40
81023	EOF-UF	80	25.4	0.7366	0.7366	0	717	101.6	25.4	392.40
81024	EOF-UF	80	25.4	0.7366	1.8415	0	717	101.6	25.4	392.40
81025	EOF-UF	80	25.4	0.7366	2.9464	0	717	101.6	25.4	392.40
81026	EOF-UF	120	25.4	0.7366	1.0716	15	717	101.6	25.4	512.40
81027	EOF-UF	120	25.4	0.7366	2.5116	15	717	101.6	25.4	512.40
81028	EOF-UF	120	25.4	0.7366	3.9515	15	717	101.6	25.4	512.40
81029	EOF-UF	40	25.4	0.7366	1.0716	15	717	101.6	25.4	272.40
81030	EOF-UF	40	25.4	0.7366	2.5116	15	717	101.6	25.4	272.40
81031	EOF-UF	40	25.4	0.7366	3.9515	15	717	101.6	25.4	272.40
81032	EOF-UF	80	25.4	0.7366	1.0716	15	717	101.6	25.4	392.40
81033	EOF-UF	80	25.4	0.7366	2.5116	15	717	101.6	25.4	392.40
81034	EOF-UF	80	25.4	0.7366	3.9515	15	717	101.6	25.4	392.40
81035	EOF-UF	120	25.4	0.7366	1.5454	30	717	101.6	25.4	512.40
81036	EOF-UF	120	25.4	0.7366	3.4592	30	717	101.6	25.4	512.40
81037	EOF-UF	120	25.4	0.7366	5.3729	30	717	101.6	25.4	512.40
81038	EOF-UF	40	25.4	0.7366	1.5454	30	717	101.6	25.4	272.40
81039	EOF-UF	40	25.4	0.7366	3.4592	30	717	101.6	25.4	272.40
81040	EOF-UF	40	25.4	0.7366	5.3729	30	717	101.6	25.4	272.40
81041	EOF-UF	80	25.4	0.7366	1.5454	30	717	101.6	25.4	392.40
81042	EOF-UF	80	25.4	0.7366	3.4592	30	717	101.6	25.4	392.40
81043	EOF-UF	80	25.4	0.7366	5.3729	30	717	101.6	25.4	392.40
81044	EOF-UF	120	25.4	1	1.0000	0	717	101.6	25.4	512.40
81045	EOF-UF	120	25.4	1	2.5000	0	717	101.6	25.4	512.40
81046	EOF-UF	120	25.4	1	4.0000	0	717	101.6	25.4	512.40
81047	EOF-UF	40	25.4	1	1.0000	0	717	101.6	25.4	272.40
81048	EOF-UF	40	25.4	1	2.5000	0	717	101.6	25.4	272.40
81049	EOF-UF	40	25.4	1	4.0000	0	717	101.6	25.4	272.40
81050	EOF-UF	80	25.4	1	1.0000	0	717	101.6	25.4	392.40
81051	EOF-UF	80	25.4	1	2.5000	0	717	101.6	25.4	392.40
81052	EOF-UF	80	25.4	1	4.0000	0	717	101.6	25.4	392.40
81053	EOF-UF	120	25.4	1	1.4548	15	717	101.6	25.4	512.40
81054	EOF-UF	120	25.4	1	3.4097	15	717	101.6	25.4	512.40
81055	EOF-UF	120	25.4	1	5.3645	15	717	101.6	25.4	512.40
81056	EOF-UF	40	25.4	1	1.4548	15	717	101.6	25.4	272.40
81057	EOF-UF	40	25.4	1	3.4097	15	717	101.6	25.4	272.40
81058	EOF-UF	40	25.4	1	5.3645	15	717	101.6	25.4	272.40
81059	EOF-UF	80	25.4	1	1.4548	15	717	101.6	25.4	392.40
81060	EOF-UF	80	25.4	1	3.4097	15	717	101.6	25.4	392.40
81061	EOF-UF	80	25.4	1	5.3645	15	717	101.6	25.4	392.40

UID	LC-FC	H (mm)	N (mm)	t (mm)	RIN (mm)	DEG (deg)	fy (MPa)	MB (mm)	EB (mm)	L (mm)
81062	EOF-UF	120	25.4	1	2.0981	30	717	101.6	25.4	512.40
81063	EOF-UF	120	25.4	1	4.6962	30	717	101.6	25.4	512.40
81064	EOF-UF	120	25.4	1	7.2942	30	717	101.6	25.4	512.40
81065	EOF-UF	40	25.4	1	2.0981	30	717	101.6	25.4	272.40
81066	EOF-UF	40	25.4	1	4.6962	30	717	101.6	25.4	272.40
81067	EOF-UF	40	25.4	1	7.2942	30	717	101.6	25.4	272.40
81068	EOF-UF	80	25.4	1	2.0981	30	717	101.6	25.4	392.40
81069	EOF-UF	80	25.4	1	4.6962	30	717	101.6	25.4	392.40
81070	EOF-UF	80	25.4	1	7.2942	30	717	101.6	25.4	392.40
81089	EOF-F	120	50	3	4	0	323	100	50	600.00
81090	EOF-F	120	50	3	5	0	323	100	50	600.00
81091	EOF-F	120	50	3	6	0	323	100	50	600.00
81092	EOF-F	120	50	3	7	0	323	100	50	600.00
81093	EOF-UF	120	50	3	4	0	323	100	50	600.00
81094	EOF-UF	120	50	3	5	0	323	100	50	600.00
81095	EOF-UF	120	50	3	6	0	323	100	50	600.00
81096	EOF-UF	120	50	3	7	0	323	100	50	600.00
91001	ITF-F	78.916	25.4	0.7366	1.984	30	717	25.4	0	600.00
91002	ITF-F	78.458	25.4	0.7366	1.5875	30	717	25.4	0	600.00
91003	ITF-F	117.016	25.4	0.7366	1.984	30	717	25.4	0	600.00
91004	ITF-F	116.558	25.4	0.7366	1.5875	30	717	25.4	0	600.00
91005	ITF-F	155.116	25.4	0.7366	1.984	30	717	25.4	0	600.00
91006	ITF-F	154.658	25.4	0.7366	1.5875	30	717	25.4	0	600.00
91007	ETF-F	78.916	25.4	0.7366	1.984	30	717	25.4	0	600.00
91008	ETF-F	78.458	25.4	0.7366	1.5875	30	717	25.4	0	600.00
91009	ETF-F	117.016	25.4	0.7366	1.984	30	717	25.4	0	600.00
91010	ETF-F	116.558	25.4	0.7366	1.5875	30	717	25.4	0	600.00
91011	ETF-F	155.116	25.4	0.7366	1.984	30	717	25.4	0	600.00
91012	ETF-F	154.658	25.4	0.7366	1.5875	30	717	25.4	0	600.00
91013	IOF-F	78.916	38.1	0.7366	1.984	30	717	38.1	76.2	427.25
91014	IOF-F	78.458	38.1	0.7366	1.5875	30	717	38.1	76.2	425.87
91015	IOF-F	117.016	38.1	0.7366	1.984	30	717	38.1	76.2	541.55
91016	IOF-F	116.558	38.1	0.7366	1.5875	30	717	38.1	76.2	540.17
91017	IOF-F	155.116	38.1	0.7366	1.984	30	717	38.1	76.2	655.85
91018	IOF-F	154.658	38.1	0.7366	1.5875	30	717	38.1	76.2	654.47
91019	IOF-F	45.1866	38.1	0.7366	3.175	0	717	38.1	76.2	326.06
91020	IOF-F	83.2866	38.1	0.7366	3.175	0	717	38.1	76.2	440.36
91021	IOF-F	121.3866	38.1	0.7366	3.175	0	717	38.1	76.2	554.66
91022	EOF-F	78.916	25.4	0.7366	1.984	30	717	101.6	25.4	389.15
91023	EOF-F	78.458	25.4	0.7366	1.5875	30	717	101.6	25.4	387.77
91024	EOF-F	117.016	25.4	0.7366	1.984	30	717	101.6	25.4	503.45
91025	EOF-F	116.558	25.4	0.7366	1.5875	30	717	101.6	25.4	502.07
91026	EOF-F	155.116	25.4	0.7366	1.984	30	717	101.6	25.4	617.75
91027	EOF-F	154.658	25.4	0.7366	1.5875	30	717	101.6	25.4	616.37
91028	EOF-F	45.1866	25.4	0.7366	3.175	0	717	101.6	25.4	287.96
91029	EOF-F	83.2866	25.4	0.7366	3.175	0	717	101.6	25.4	402.26
91030	EOF-F	121.3866	25.4	0.7366	3.175	0	717	101.6	25.4	516.56
91031	EOF-F	78.916	25.4	0.7366	1.984	30	717	101.6	25.4	389.15
91032	EOF-F	78.458	25.4	0.7366	1.5875	30	717	101.6	25.4	387.77
91033	EOF-F	117.016	25.4	0.7366	1.984	30	717	101.6	25.4	503.45
91034	EOF-F	116.558	25.4	0.7366	1.5875	30	717	101.6	25.4	502.07
91035	EOF-F	155.116	25.4	0.7366	1.984	30	717	101.6	25.4	617.75
91036	EOF-F	154.658	25.4	0.7366	1.5875	30	717	101.6	25.4	616.37
91037	EOF-F	45.1866	25.4	0.7366	3.175	0	717	101.6	25.4	287.96
91038	EOF-F	83.2866	25.4	0.7366	3.175	0	717	101.6	25.4	402.26
91039	EOF-F	121.3866	25.4	0.7366	3.175	0	717	101.6	25.4	516.56
92001	ITF-F	120	100	3	3	0	323	100	0	600.00
92002	ITF-F	120	100	3	8	0	323	100	0	600.00
92003	ITF-F	90	50	3	3	0	323	50	0	600.00
92004	ITF-F	90	50	3	8	0	323	50	0	600.00
92005	IOF-F	120	100	3	3	0	323	100	50	600.00
92006	IOF-F	120	100	3	8	0	323	100	50	600.00
92007	IOF-F	90	50	3	3	0	323	50	50	600.00
92008	IOF-F	90	50	3	8	0	323	50	50	600.00
92009	ETF-F	90	50	3	3	0	323	50	0	600.00

UID	LC-FC	H (mm)	N (mm)	t (mm)	RIN (mm)	DEG (deg)	fy (MPa)	MB (mm)	EB (mm)	L (mm)
92010	ETF-F	90	50	3	8	0	323	50	0	600.00
92011	EOF-F	90	50	3	3	0	323	220	50	600.00
92012	EOF-F	90	50	3	8	0	323	220	50	600.00

Table Appendix G.2 Group, Py, Pcr and Pexp for specimens from numerical analysis

UID	Group	P_y (kN)	P_{cr} (kN)	P_{FEM} (kN)	λ	P_{FEM}/P_y
11033	2	120.788	255.901	79.330	0.687	0.657
11034	6	136.871	234.584	82.684	0.764	0.604
11035	2	143.938	221.631	84.157	0.806	0.585
11036	6	149.768	207.375	85.275	0.850	0.569
11037	6	153.858	192.095	86.132	0.895	0.560
11038	2	155.727	176.141	86.067	0.940	0.553
11039	3	120.788	255.901	79.893	0.687	0.661
11040	7	136.871	234.584	81.116	0.764	0.593
11041	3	143.938	221.631	81.425	0.806	0.566
11042	7	149.768	207.375	81.210	0.850	0.542
11043	7	153.858	192.095	80.473	0.895	0.523
11044	3	155.727	176.141	79.181	0.940	0.508
11045	2	63.557	265.404	61.869	0.489	0.973
11046	6	74.160	232.069	67.950	0.565	0.916
11047	2	79.865	216.167	69.900	0.608	0.875
11048	6	85.742	200.516	71.017	0.654	0.828
11049	6	91.628	184.988	70.336	0.704	0.768
11050	2	97.251	169.528	68.662	0.757	0.706
11051	3	63.557	265.404	60.043	0.489	0.945
11052	7	74.160	232.069	65.385	0.565	0.882
11053	3	79.865	216.167	67.224	0.608	0.842
11054	7	85.742	200.516	67.939	0.654	0.792
11055	7	91.628	184.988	66.287	0.704	0.723
11056	3	97.251	169.528	64.354	0.757	0.662
11057	4	57.130	3.793	8.869	3.881	0.155
11058	4	31.026	3.876	8.510	2.829	0.274
11059	4	21.151	4.073	7.645	2.279	0.361
11060	4	31.494	15.185	13.710	1.440	0.435
11061	4	17.303	15.191	10.213	1.067	0.590
11062	4	11.872	15.616	8.184	0.872	0.689
11063	4	44.320	5.949	10.948	2.729	0.247
11064	4	24.166	6.093	9.558	1.992	0.395
11065	4	16.512	6.426	7.922	1.603	0.480
11066	4	56.033	3.379	7.956	4.072	0.142
11067	4	30.835	3.392	7.729	3.015	0.251
11068	4	21.089	3.428	7.493	2.480	0.355
11069	4	31.054	13.296	12.888	1.528	0.415
11070	4	17.225	12.937	10.467	1.154	0.608
11071	4	11.846	12.741	8.530	0.964	0.720
11072	4	43.588	5.282	10.025	2.873	0.230
11073	4	24.038	5.282	9.384	2.133	0.390
11074	4	16.470	5.304	8.115	1.762	0.493
11075	4	52.613	2.733	6.490	4.388	0.123
11076	4	30.176	2.704	6.409	3.341	0.212
11077	4	20.872	2.665	6.346	2.798	0.304
11078	4	29.628	10.622	11.176	1.670	0.377
11079	4	16.951	10.161	9.724	1.292	0.574
11080	4	11.755	9.767	8.709	1.097	0.741
11081	4	41.259	4.261	8.301	3.112	0.201
11082	4	23.592	4.185	8.009	2.374	0.339
11083	4	16.323	4.088	7.653	1.998	0.469
11084	4	78.063	9.486	17.959	2.869	0.230
11085	4	42.487	9.749	13.868	2.088	0.326
11086	4	29.024	10.276	13.327	1.681	0.459
11087	4	43.258	37.711	23.574	1.071	0.545
11088	4	23.857	37.661	15.521	0.796	0.651

UID	Group	P_y (kN)	P_{cr} (kN)	P_{FEM} (kN)	λ	P_{FEM}/P_y
11089	4	16.427	38.601	12.573	0.652	0.765
11090	4	60.672	14.863	20.008	2.020	0.330
11091	4	33.174	15.312	15.633	1.472	0.471
11092	4	22.726	16.110	13.151	1.188	0.579
11093	4	76.570	8.429	16.468	3.014	0.215
11094	4	42.226	8.459	14.885	2.234	0.353
11095	4	28.940	8.485	13.431	1.847	0.464
11096	4	42.655	32.817	23.292	1.140	0.546
11097	4	23.749	31.613	16.070	0.867	0.677
11098	4	16.392	30.857	13.004	0.729	0.793
11099	4	59.672	13.148	19.367	2.130	0.325
11100	4	32.998	13.123	15.394	1.586	0.467
11101	4	22.669	13.018	13.499	1.320	0.595
11102	4	71.914	6.805	13.668	3.251	0.190
11103	4	41.325	6.705	13.255	2.483	0.321
11104	4	28.642	6.549	11.944	2.091	0.417
11105	4	40.698	26.138	21.016	1.248	0.516
11106	4	23.370	24.651	16.201	0.974	0.693
11107	4	16.266	23.452	13.588	0.833	0.835
11108	4	56.492	10.583	16.320	2.310	0.289
11109	4	32.386	10.326	14.703	1.771	0.454
11110	4	22.467	9.970	13.306	1.501	0.592
11111	9	102.573	257.008	76.539	0.632	0.746
11112	9	88.977	258.835	72.378	0.586	0.813
11113	9	78.511	261.176	68.006	0.548	0.866
11114	9	70.240	263.605	63.902	0.516	0.910
21035	2	84.172	122.123	43.804	0.830	0.520
21036	6	95.459	111.648	46.998	0.925	0.492
21037	2	100.585	105.099	48.549	0.978	0.483
21038	6	105.011	97.846	49.450	1.036	0.471
21039	6	108.414	90.098	49.922	1.097	0.460
21040	2	110.449	82.090	49.364	1.160	0.447
21041	3	84.172	122.123	39.558	0.830	0.470
21042	7	95.459	111.648	41.750	0.925	0.437
21043	3	100.585	105.099	42.855	0.978	0.426
21044	7	105.011	97.846	43.494	1.036	0.414
21045	7	108.414	90.098	43.532	1.097	0.402
21046	3	110.449	82.090	42.942	1.160	0.389
21047	2	44.199	123.517	33.136	0.598	0.750
21048	6	51.668	108.426	33.621	0.690	0.651
21049	2	55.715	100.914	34.031	0.743	0.611
21050	6	59.924	93.362	34.296	0.801	0.572
21051	6	64.204	85.784	34.730	0.865	0.541
21052	2	68.397	78.229	35.431	0.935	0.518
21053	3	44.199	123.517	31.717	0.598	0.718
21054	7	51.668	108.426	31.676	0.690	0.613
21055	3	55.715	100.914	31.418	0.743	0.564
21056	7	59.924	93.362	31.038	0.801	0.518
21057	7	64.204	85.784	30.943	0.865	0.482
21058	3	68.397	78.229	31.286	0.935	0.457
21059	4	37.733	1.674	3.006	4.748	0.080
21060	4	20.546	1.709	2.718	3.467	0.132
21061	4	14.000	1.828	2.671	2.768	0.191
21062	4	24.886	9.366	8.140	1.630	0.327
21063	4	13.679	9.140	6.650	1.223	0.486
21064	4	9.358	9.027	5.594	1.018	0.598
21065	4	31.316	3.001	3.929	3.230	0.125
21066	4	17.114	3.031	3.698	2.376	0.216
21067	4	11.679	3.174	3.524	1.918	0.302
21068	4	37.160	1.491	2.710	4.992	0.073
21069	4	20.445	1.501	2.385	3.691	0.117
21070	4	13.967	1.559	2.348	2.993	0.168
21071	4	24.568	8.153	7.505	1.736	0.305
21072	4	13.622	7.816	6.129	1.320	0.450
21073	4	9.340	7.564	5.322	1.111	0.570
21074	4	30.880	2.658	3.511	3.408	0.114

UID	Group	P_y (kN)	P_{cr} (kN)	P_{FEM} (kN)	λ	P_{FEM}/P_y
21075	4	17.037	2.642	3.306	2.539	0.194
21076	4	11.654	2.692	3.165	2.081	0.272
21077	4	35.320	1.205	2.309	5.414	0.065
21078	4	20.095	1.196	1.908	4.098	0.095
21079	4	13.852	1.209	1.890	3.385	0.136
21080	4	23.527	6.479	6.307	1.906	0.268
21081	4	13.421	6.154	5.313	1.477	0.396
21082	4	9.273	5.888	4.707	1.255	0.508
21083	4	29.465	2.138	2.837	3.713	0.096
21084	4	16.767	2.099	2.715	2.827	0.162
21085	4	11.566	2.088	2.628	2.353	0.227
21086	4	51.643	4.178	5.988	3.516	0.116
21087	4	28.167	4.292	5.701	2.562	0.202
21088	4	19.223	4.648	5.498	2.034	0.286
21089	4	34.202	23.174	15.644	1.215	0.457
21090	4	18.844	22.427	10.998	0.917	0.584
21091	4	12.922	22.003	8.015	0.766	0.620
21092	4	42.931	7.475	8.387	2.397	0.195
21093	4	23.507	7.563	7.559	1.763	0.322
21094	4	16.073	7.967	6.939	1.420	0.432
21095	4	50.861	3.713	5.309	3.701	0.104
21096	4	28.029	3.739	5.082	2.738	0.181
21097	4	19.178	3.899	4.931	2.218	0.257
21098	4	33.765	20.057	14.688	1.297	0.435
21099	4	18.766	18.957	11.205	0.995	0.597
21100	4	12.896	18.127	8.218	0.843	0.637
21101	4	42.335	6.599	7.560	2.533	0.179
21102	4	23.401	6.536	6.850	1.892	0.293
21103	4	16.038	6.645	6.394	1.554	0.399
21104	4	48.348	2.994	4.279	4.018	0.088
21105	4	27.550	2.963	4.151	3.049	0.151
21106	4	19.021	2.988	4.061	2.523	0.214
21107	4	32.335	15.898	13.018	1.426	0.403
21108	4	18.489	14.849	10.130	1.116	0.548
21109	4	12.805	14.003	8.237	0.956	0.643
21110	4	40.398	5.296	6.223	2.762	0.154
21111	4	23.031	5.161	5.743	2.112	0.249
21112	4	15.916	5.104	5.437	1.766	0.342
21113	9	71.505	121.832	36.821	0.766	0.515
21114	9	62.015	121.862	34.881	0.713	0.562
21115	9	54.690	122.195	33.404	0.669	0.611
21116	9	48.891	122.775	32.302	0.631	0.661
31039	2	100.879	223.190	68.870	0.672	0.683
31040	6	117.023	195.341	72.352	0.774	0.618
31041	2	125.611	180.556	73.968	0.834	0.589
31042	6	134.434	165.775	75.167	0.901	0.559
31043	6	143.316	151.265	75.613	0.973	0.528
31044	2	151.969	137.185	74.867	1.053	0.493
31045	3	100.879	223.190	65.944	0.672	0.654
31046	7	117.023	195.341	68.216	0.774	0.583
31047	3	125.611	180.556	68.731	0.834	0.547
31048	7	134.434	165.775	68.878	0.901	0.512
31049	7	143.316	151.265	68.447	0.973	0.478
31050	3	151.969	137.185	67.350	1.053	0.443
31051	2	51.046	189.006	55.115	0.520	1.080
31052	6	60.049	175.696	56.610	0.585	0.943
31053	2	65.161	166.125	56.838	0.626	0.872
31054	6	70.754	155.329	57.197	0.675	0.808
31055	6	76.884	143.784	57.480	0.731	0.748
31056	2	83.590	131.864	57.309	0.796	0.686
31057	3	51.046	189.006	53.277	0.520	1.044
31058	7	60.049	175.696	54.672	0.585	0.910
31059	3	65.161	166.125	54.793	0.626	0.841
31060	7	70.754	155.329	54.553	0.675	0.771
31061	7	76.884	143.784	54.138	0.731	0.704
31062	3	83.590	131.864	53.430	0.796	0.639

UID	Group	P_y (kN)	P_{cr} (kN)	P_{FEM} (kN)	λ	P_{FEM}/P_y
31063	4	50.040	4.378	11.736	3.381	0.235
31064	4	26.239	4.248	9.535	2.485	0.363
31065	4	17.737	3.816	8.193	2.156	0.462
31066	4	23.442	14.388	11.300	1.276	0.482
31067	4	12.368	13.365	8.883	0.962	0.718
31068	4	8.412	11.730	7.486	0.847	0.890
31069	4	36.741	6.664	11.911	2.348	0.324
31070	4	19.304	6.359	9.522	1.742	0.493
31071	4	13.074	5.534	7.972	1.537	0.610
31072	4	49.852	3.441	10.251	3.806	0.206
31073	4	26.211	3.318	8.796	2.810	0.336
31074	4	17.728	3.038	7.874	2.416	0.444
31075	4	23.354	11.501	10.713	1.425	0.459
31076	4	12.355	10.738	8.545	1.073	0.692
31077	4	8.408	9.648	7.372	0.934	0.877
31078	4	36.603	5.253	10.647	2.640	0.291
31079	4	19.283	4.994	8.879	1.965	0.460
31080	4	13.068	4.471	7.766	1.710	0.594
31081	4	49.189	2.560	8.206	4.384	0.167
31082	4	26.109	2.484	7.600	3.242	0.291
31083	4	17.697	2.335	7.135	2.753	0.403
31084	4	23.043	8.689	9.404	1.628	0.408
31085	4	12.307	8.221	7.838	1.224	0.637
31086	4	8.393	7.595	6.946	1.051	0.828
31087	4	36.116	3.920	8.813	3.035	0.244
31088	4	19.208	3.764	7.890	2.259	0.411
31089	4	13.045	3.483	7.152	1.935	0.548
31090	4	68.246	10.901	20.107	2.502	0.295
31091	4	35.854	10.425	15.040	1.855	0.419
31092	4	24.282	9.022	14.014	1.641	0.577
31093	4	32.137	35.453	18.976	0.952	0.590
31094	4	17.024	32.348	14.035	0.725	0.824
31095	4	11.623	28.330	12.011	0.641	1.033
31096	4	50.191	16.549	19.971	1.742	0.398
31097	4	26.439	15.483	14.776	1.307	0.559
31098	4	17.953	13.040	13.379	1.173	0.745
31099	4	67.989	8.561	18.178	2.818	0.267
31100	4	35.816	8.151	14.668	2.096	0.410
31101	4	24.270	7.276	13.760	1.826	0.567
31102	4	32.016	28.366	18.067	1.062	0.564
31103	4	17.006	26.094	13.628	0.807	0.801
31104	4	11.617	23.373	11.921	0.705	1.026
31105	4	50.003	13.034	18.480	1.959	0.370
31106	4	26.411	12.198	14.619	1.471	0.554
31107	4	17.944	10.669	13.078	1.297	0.729
31108	4	67.085	6.373	15.102	3.244	0.225
31109	4	35.677	6.126	13.170	2.413	0.369
31110	4	24.227	5.663	12.578	2.068	0.519
31111	4	31.590	21.478	16.234	1.213	0.514
31112	4	16.940	20.081	12.801	0.918	0.756
31113	4	11.597	18.474	11.277	0.792	0.972
31114	4	49.337	9.739	15.803	2.251	0.320
31115	4	26.309	9.241	13.450	1.687	0.511
31116	4	17.912	8.414	12.285	1.459	0.686
31117	9	84.410	217.756	61.582	0.623	0.730
31118	9	72.521	211.532	58.518	0.586	0.807
31119	9	63.572	204.566	56.252	0.557	0.885
31120	9	56.609	196.987	54.638	0.536	0.965
41027	4	30.984	3.028	4.500	3.199	0.145
41028	4	16.330	2.998	3.790	2.334	0.232
41029	4	11.042	3.007	3.790	1.916	0.343
41030	4	17.652	13.517	8.000	1.143	0.453
41031	4	9.390	13.620	5.690	0.830	0.606
41032	4	6.378	14.229	5.060	0.669	0.793
41033	4	24.323	5.326	5.260	2.137	0.216
41034	4	12.861	5.246	4.630	1.566	0.360

UID	Group	P_y (kN)	P_{cr} (kN)	P_{FEM} (kN)	λ	P_{FEM}/P_y
41035	4	8.710	5.250	4.340	1.288	0.498
41036	4	30.509	2.915	4.400	3.235	0.144
41037	4	16.256	2.874	3.730	2.378	0.229
41038	4	11.019	2.866	3.540	1.961	0.321
41039	4	17.457	13.099	7.980	1.154	0.457
41040	4	9.359	13.210	5.590	0.842	0.597
41041	4	6.368	13.644	4.950	0.683	0.777
41042	4	24.004	5.116	5.150	2.166	0.215
41043	4	12.811	5.006	4.660	1.600	0.364
41044	4	8.694	4.966	4.310	1.323	0.496
41045	4	28.986	2.606	3.930	3.335	0.136
41046	4	15.998	2.559	3.290	2.500	0.206
41047	4	10.936	2.535	3.060	2.077	0.280
41048	4	16.813	11.762	7.440	1.196	0.443
41049	4	9.250	11.854	5.480	0.883	0.592
41050	4	6.333	11.877	4.770	0.730	0.753
41051	4	22.964	4.566	4.740	2.243	0.206
41052	4	12.635	4.441	4.130	1.687	0.327
41053	4	8.638	4.362	3.860	1.407	0.447
41054	4	42.420	7.540	8.163	2.372	0.192
41055	4	22.393	7.450	7.300	1.734	0.326
41056	4	15.164	7.519	7.239	1.420	0.477
41057	4	24.319	33.678	12.700	0.850	0.522
41058	4	12.971	34.235	8.423	0.616	0.649
41059	4	8.832	36.198	7.992	0.494	0.905
41060	4	33.377	13.230	9.334	1.588	0.280
41061	4	17.683	12.993	8.013	1.167	0.453
41062	4	11.999	13.087	7.741	0.958	0.645
41063	4	41.774	7.248	8.044	2.401	0.193
41064	4	22.293	7.119	7.220	1.770	0.324
41065	4	15.133	7.122	6.737	1.458	0.445
41066	4	24.052	32.657	12.965	0.858	0.539
41067	4	12.928	33.183	9.557	0.624	0.739
41068	4	8.819	33.012	8.549	0.517	0.969
41069	4	32.941	12.683	9.377	1.612	0.285
41070	4	17.615	12.336	8.521	1.195	0.484
41071	4	11.977	12.255	7.661	0.989	0.640
41072	4	39.703	6.473	7.412	2.477	0.187
41073	4	21.941	6.320	6.367	1.863	0.290
41074	4	15.020	6.256	5.963	1.550	0.397
41075	4	23.166	29.306	12.067	0.889	0.521
41076	4	12.778	29.630	9.179	0.657	0.718
41077	4	8.771	27.955	7.927	0.560	0.904
41078	4	31.521	11.298	8.853	1.670	0.281
41079	4	17.375	10.889	7.766	1.263	0.447
41080	4	11.900	10.654	7.049	1.057	0.592
41081	2	79.215	233.302	45.741	0.583	0.577
41082	6	91.150	230.701	49.467	0.629	0.543
41083	2	96.901	226.575	51.346	0.654	0.530
41084	6	102.165	220.607	53.126	0.681	0.520
41085	6	106.582	212.839	54.451	0.708	0.511
41086	2	109.740	203.335	55.532	0.735	0.506
41087	3	79.215	233.302	43.199	0.583	0.545
41088	7	91.150	230.701	45.820	0.629	0.503
41089	3	96.901	226.575	47.479	0.654	0.490
41090	7	102.165	220.607	48.912	0.681	0.479
41091	7	106.582	212.839	49.982	0.708	0.469
41092	3	109.740	203.335	50.783	0.735	0.463
41093	2	40.170	233.877	33.557	0.414	0.835
41094	6	47.241	229.823	34.712	0.453	0.735
41095	2	51.155	225.406	35.478	0.476	0.694
41096	6	55.311	219.352	36.326	0.502	0.657
41097	6	59.659	211.641	37.018	0.531	0.620
41098	2	64.088	202.283	37.982	0.563	0.593
41099	3	40.170	233.877	32.582	0.414	0.811
41100	7	47.241	229.823	33.666	0.453	0.713

UID	Group	P_y (kN)	P_{cr} (kN)	P_{FEM} (kN)	λ	P_{FEM}/P_y
41101	3	51.155	225.406	34.080	0.476	0.666
41102	7	55.311	219.352	34.370	0.502	0.621
41103	7	59.659	211.641	34.611	0.531	0.580
41104	3	64.088	202.283	34.936	0.563	0.545
81005	3	63.249	141.138	36.556	0.669	0.578
81006	7	73.420	135.938	39.200	0.735	0.534
81007	3	78.832	132.348	40.650	0.772	0.516
81008	3	31.861	138.616	27.630	0.479	0.867
81009	7	37.532	129.246	29.461	0.539	0.785
81010	3	40.751	124.494	30.175	0.572	0.740
81011	2	63.249	141.138	40.211	0.669	0.636
81012	6	73.420	135.938	44.676	0.735	0.608
81013	2	78.832	132.348	46.663	0.772	0.592
81014	2	31.861	138.616	29.091	0.479	0.913
81015	6	37.532	129.246	31.479	0.539	0.839
81016	2	40.751	124.494	32.660	0.572	0.801
81017	4	26.787	1.537	2.766	4.174	0.103
81018	4	14.041	1.565	2.637	2.996	0.188
81019	4	9.488	1.644	2.537	2.402	0.267
81020	4	13.488	8.814	6.130	1.237	0.454
81021	4	7.106	8.668	4.741	0.905	0.667
81022	4	4.825	8.624	3.975	0.748	0.824
81023	4	20.138	2.769	3.669	2.697	0.182
81024	4	10.573	2.809	3.326	1.940	0.315
81025	4	7.157	2.938	3.071	1.561	0.429
81026	4	26.686	1.466	2.196	4.267	0.082
81027	4	14.026	1.468	2.100	3.091	0.150
81028	4	9.483	1.509	2.022	2.507	0.213
81029	4	13.437	8.184	5.202	1.281	0.387
81030	4	7.098	7.729	4.136	0.958	0.583
81031	4	4.823	7.364	3.569	0.809	0.740
81032	4	20.062	2.623	2.923	2.765	0.146
81033	4	10.562	2.601	2.692	2.015	0.255
81034	4	7.153	2.643	2.549	1.645	0.356
81035	4	26.331	1.298	1.445	4.504	0.055
81036	4	13.972	1.279	1.423	3.305	0.102
81037	4	9.466	1.284	1.376	2.716	0.145
81038	4	13.259	7.075	3.934	1.369	0.297
81039	4	7.071	6.439	3.370	1.048	0.477
81040	4	4.814	5.906	3.051	0.903	0.634
81041	4	19.795	2.309	2.005	2.928	0.101
81042	4	10.521	2.240	1.925	2.167	0.183
81043	4	7.140	2.209	1.867	1.798	0.261
81044	4	36.611	3.844	5.765	3.086	0.157
81045	4	19.224	3.929	5.335	2.212	0.277
81046	4	13.013	4.167	5.005	1.767	0.385
81047	4	18.557	21.818	11.330	0.922	0.611
81048	4	9.809	21.169	8.236	0.681	0.840
81049	4	6.684	20.615	7.076	0.569	1.059
81050	4	27.584	6.913	7.441	1.998	0.270
81051	4	14.517	7.026	6.405	1.437	0.441
81052	4	9.849	7.375	5.684	1.156	0.577
81053	4	36.473	3.649	4.661	3.162	0.128
81054	4	19.204	3.649	4.345	2.294	0.226
81055	4	13.007	3.757	4.124	1.861	0.317
81056	4	18.487	19.981	9.892	0.962	0.535
81057	4	9.799	18.376	7.550	0.730	0.770
81058	4	6.680	16.959	6.214	0.628	0.930
81059	4	27.480	6.505	6.184	2.055	0.225
81060	4	14.501	6.412	5.393	1.504	0.372
81061	4	9.844	6.475	4.930	1.233	0.501
81062	4	35.988	3.217	3.098	3.345	0.086
81063	4	19.130	3.147	2.997	2.466	0.157
81064	4	12.984	3.143	2.803	2.033	0.216
81065	4	18.241	17.056	7.814	1.034	0.428
81066	4	9.761	14.964	6.391	0.808	0.655

UID	Group	P_y (kN)	P_{cr} (kN)	P_{FEM} (kN)	λ	P_{FEM}/P_y
81067	4	6.669	13.214	5.525	0.710	0.829
81068	4	27.114	5.691	4.387	2.183	0.162
81069	4	14.445	5.447	4.074	1.629	0.282
81070	4	9.826	5.301	3.782	1.361	0.385
81089	9	66.443	232.819	39.822	0.534	0.599
81090	9	57.136	232.590	37.275	0.496	0.652
81091	9	50.089	232.664	35.293	0.464	0.705
81092	9	44.582	233.084	33.719	0.437	0.756
81093	9	52.875	140.316	36.906	0.614	0.698
81094	9	45.387	139.662	34.253	0.570	0.755
81095	9	39.750	139.173	32.107	0.534	0.808
81096	9	35.365	138.832	30.374	0.505	0.859
91001	8	30.181	4.172	7.855	2.690	0.260
91002	8	34.446	4.216	7.968	2.858	0.231
91003	8	39.343	3.031	6.627	3.603	0.168
91004	8	44.852	3.049	6.674	3.835	0.149
91005	8	48.299	2.444	6.062	4.445	0.126
91006	8	54.965	2.455	6.145	4.732	0.112
91007	8	20.286	1.794	2.520	3.363	0.124
91008	8	23.231	1.815	2.555	3.577	0.110
91009	8	25.015	1.212	1.904	4.543	0.076
91010	8	28.647	1.220	1.919	4.846	0.067
91011	8	29.685	0.928	1.825	5.657	0.061
91012	8	33.976	0.931	1.903	6.040	0.056
91013	8	29.836	3.950	8.636	2.748	0.289
91014	8	34.952	4.000	8.835	2.956	0.253
91015	8	40.206	3.348	8.081	3.465	0.201
91016	8	47.171	3.376	8.217	3.738	0.174
91017	8	50.576	2.890	7.775	4.183	0.154
91018	8	59.390	2.907	7.879	4.520	0.133
91019	8	8.460	7.671	7.501	1.050	0.887
91020	8	12.618	5.110	7.803	1.571	0.618
91021	8	16.776	3.643	8.000	2.146	0.477
91022	8	19.287	4.625	3.774	2.042	0.196
91023	8	22.345	4.694	4.044	2.182	0.181
91024	8	24.176	2.739	2.986	2.971	0.123
91025	8	27.995	2.765	3.127	3.182	0.112
91026	8	28.998	1.939	2.537	3.867	0.087
91027	8	33.544	1.953	2.618	4.145	0.078
91028	8	6.265	10.519	4.509	0.772	0.720
91029	8	8.345	4.975	3.905	1.295	0.468
91030	8	10.424	2.971	3.333	1.873	0.320
91031	11	19.287	4.625	3.774	2.042	0.196
91032	11	22.345	4.694	4.044	2.182	0.181
91033	11	24.176	2.739	2.986	2.971	0.123
91034	11	27.995	2.765	3.127	3.182	0.112
91035	11	28.998	1.939	2.537	3.867	0.087
91036	11	33.544	1.953	2.618	4.145	0.078
91037	11	6.265	10.519	4.509	0.772	0.720
91038	11	8.345	4.975	3.905	1.295	0.468
91039	11	10.424	2.971	3.333	1.873	0.320
92001	13	163.254	290.015	100.788	0.750	0.617
92002	13	85.738	294.505	78.200	0.540	0.912
92003	13	103.151	347.760	81.291	0.545	0.788
92004	13	54.590	348.076	61.828	0.396	1.133
92005	13	123.754	243.528	83.650	0.713	0.676
92006	13	62.365	210.690	63.512	0.544	1.018
92007	13	82.579	183.901	59.483	0.670	0.720
92008	13	41.991	160.623	46.466	0.511	1.107
92009	13	75.334	182.510	42.483	0.642	0.564
92010	13	39.712	173.788	33.659	0.478	0.848
92011	13	70.030	281.670	45.728	0.499	0.653
92012	13	35.637	281.419	34.446	0.356	0.967

Note: Group number is corresponding to Table 29.

Appendix H

Alternative method for the calculation of reduced plastic moment capacity

As discussed in previous Chapter 6.2.3.2, a reduced plastic moment capacity is required for the calculation of P_y. The M_p' is given as

$$M_p' = \frac{f_y t^2}{4}\left[1 - \left(\frac{P}{f_y b t}\right)^2\right] \quad \text{(AH-1)}$$

where

b is the length corresponding to the relevant yield line;

f_y is the yield stress of the material.

In previous discussion, a complex quadratic equation is developed for solving the F_{SW}. An iteration method for calculating the P_y is also developed as an alternative for the case when the application of solving quadratic equation is limited.

In terms of the calculation of M_p', it's easy to find that the M_p' cannot be directly calculated easily from the external load P especially for sloped web sections. According to Figure 122, the action from the external load P does not directly acting as the axial force to the web but can be considered as a combination of two actions: one is the axial force along the web and the other is axial along the flange. Thus, calculating the M_p' for each of the load separately is considered as a feasible alternative. For each of the calculation iteration, the separated calculation of M_p' and F_{SW} includes the following steps:

Step 1: Decompose the plastic mechanism force for a single web (F_{SW}) into two components: P_F, which is the force acting along the flange, and P_W, the force acting along the web.

Step 2: For each decomposed force, apply the reduced plastic moment capacity equation to calculate the modified plastic moment capacity per unit length (M_p') using the M_p' equation, recording the results as $M_{p,f}'$ for the flange and $M_{p,w}'$ for the web.

Step 3: Recalculate the plastic mechanism force (F_{SW}') using the following equation, where M_{p_i}' represents the specific reduced plastic moment capacity corresponding to each yield line.

$$F'_{SW} = \sum_{i=1}^{n} \frac{M'_{p_i}}{k_\theta r_c \tan\beta} k_{\omega_i} L_i \quad (1\text{-}1)$$

Step 4: Using the F'_{SW} calculated in Step 3 as an input for Step 1, repeat Step 1 to Step 3 until desired accuracy is achieved.

A comparison is carried out between the yield load (P_y) values calculated using the iterative method (I-method) and the quadratic method (Q-method). A total of 711 specimen configurations were calculated, spanning all four loading cases and the two fastening conditions – with and without fasteners. For each specimen, two P_y values were calculated using the I-method: Py_I_10 (10 iterations) and Py_I_100 (100 iterations). The P_y values from the I-method were plotted on the y-axis, while the Py values from the Q-method were plotted on the x-axis for comparison. Figure 161 shows the comparison between Py_I_10 and Py_Q, while Figure 162 illustrates the comparison between Py_I_100 and Py_Q .

According to the static analysis performed on the 711 specimen configurations, the following statistical measures were obtained for the ratio of yield loads calculated by the iterative (Py_I) and quadratic (Py_Q) methods.

For P_y with 10 iterations:

- Average of [Py_I/Py_Q]: 1.00302
- Coefficient of Variation (COV) of [Py_I/Py_Q]: 0.0256

For Py with 100 iterations:

- Average of [Py_I/Py_Q]: 1.00009
- Coefficient of Variation (COV) of [Py_I/Py_Q]: 0.00102

The statistical results indicate a good agreement between the iterative and quadratic methods for calculating the yield load across the comprehensive set of 711 specimen configurations, provided that a sufficient number of iterations is performed in the I-method. Although using the Q-method for calculating the yield load is considered relatively more complex when assembling the quadratic equation, the I-method seemed to require a large number of iteration calculations to achieve the desired accuracy level. Therefore, both calculation approaches demonstrate viability, with the choice between them depending on the user's consideration.

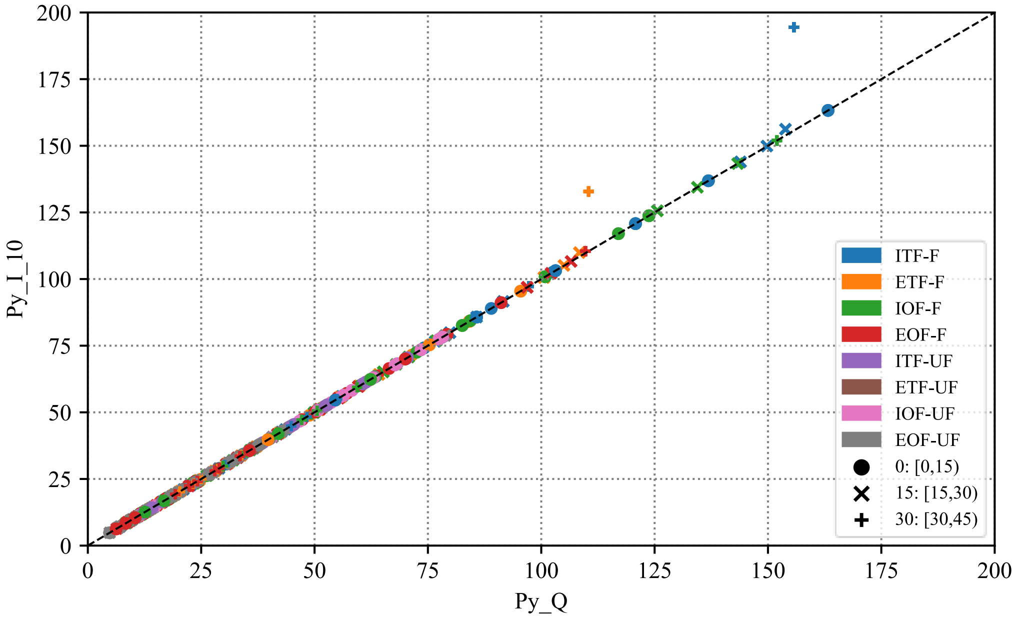

Figure 161 Comparison of Py using I-method (10 iterations) and Q-method

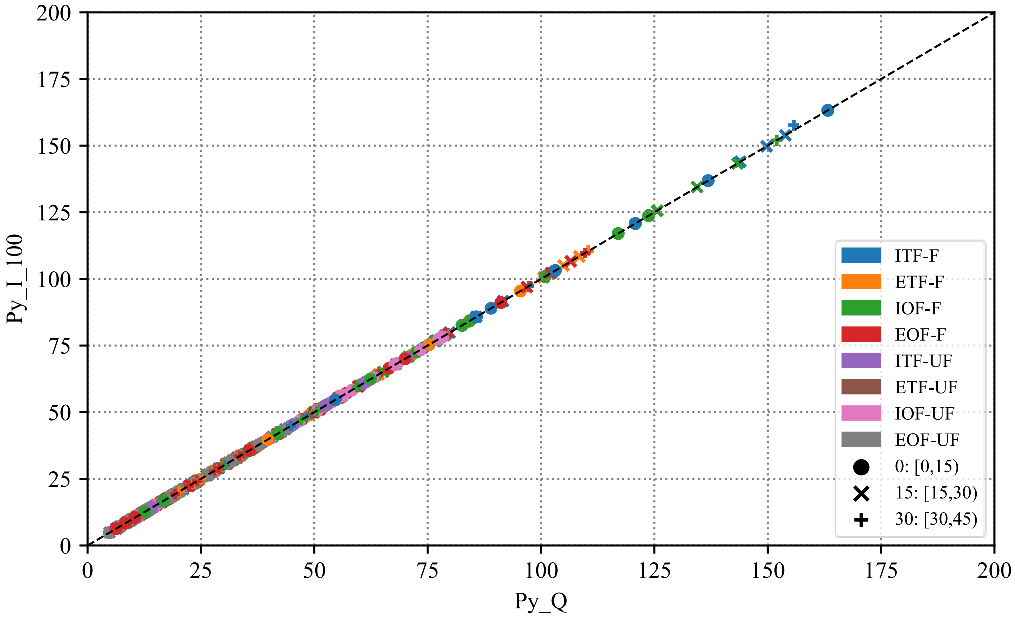

Figure 162 Comparison of Py using I-method (100 iterations) and Q-method

Table Appendix H.1 List of data used in Appendix H

UID	Py_Q (kN)	Py_I_10 (kN)	Py_I_100 (kN)	UID	Py_Q (kN)	Py_I_10 (kN)	Py_I_100 (kN)
11001	163.254	163.254	163.254	41027	30.984	30.984	30.984
11002	155.727	194.465	157.624	41028	16.330	16.330	16.330
11003	143.938	143.944	143.938	41029	11.042	11.042	11.042
11004	120.788	120.788	120.788	41030	17.652	17.652	17.652
11005	103.151	103.151	103.151	41031	9.390	9.390	9.390
11006	163.254	163.254	163.254	41032	6.378	6.378	6.378
11007	155.727	194.465	157.624	41033	24.323	24.323	24.323
11008	143.938	143.944	143.938	41034	12.861	12.861	12.861
11009	120.788	120.788	120.788	41035	8.710	8.710	8.710
11010	103.151	103.151	103.151	41036	30.509	30.509	30.509
11011	85.738	85.738	85.738	41037	16.256	16.256	16.256
11012	97.251	97.251	97.251	41038	11.019	11.019	11.019
11013	79.865	79.865	79.865	41039	17.457	17.457	17.457
11014	63.557	63.557	63.557	41040	9.359	9.359	9.359
11015	54.590	54.590	54.590	41041	6.368	6.368	6.368
11016	85.738	85.738	85.738	41042	24.004	24.004	24.004
11017	97.251	97.251	97.251	41043	12.811	12.811	12.811
11018	79.865	79.865	79.865	41044	8.694	8.694	8.694
11019	63.557	63.557	63.557	41045	28.986	28.986	28.986
11020	54.590	54.590	54.590	41046	15.998	15.998	15.998
11021	30.181	30.181	30.181	41047	10.936	10.936	10.936
11022	34.446	34.447	34.446	41048	16.813	16.813	16.813
11023	39.343	39.343	39.343	41049	9.250	9.250	9.250
11024	44.852	44.854	44.852	41050	6.333	6.333	6.333
11025	48.299	48.299	48.299	41051	22.964	22.964	22.964
11026	54.965	54.970	54.965	41052	12.635	12.635	12.635
11027	30.181	30.181	30.181	41053	8.638	8.638	8.638
11028	34.446	34.447	34.446	41054	42.420	42.420	42.420
11029	39.343	39.343	39.343	41055	22.393	22.393	22.393
11030	44.852	44.854	44.852	41056	15.164	15.164	15.164
11031	48.299	48.299	48.299	41057	24.319	24.319	24.319
11032	54.965	54.970	54.965	41058	12.971	12.971	12.971
11033	120.788	120.788	120.788	41059	8.832	8.832	8.832
11034	136.871	136.871	136.871	41060	33.377	33.377	33.377
11035	143.938	143.944	143.938	41061	17.683	17.683	17.683
11036	149.768	149.884	149.768	41062	11.999	11.999	11.999
11037	153.858	156.225	153.858	41063	41.774	41.774	41.774
11038	155.727	194.465	157.624	41064	22.293	22.293	22.293
11039	120.788	120.788	120.788	41065	15.133	15.133	15.133
11040	136.871	136.871	136.871	41066	24.052	24.052	24.052
11041	143.938	143.944	143.938	41067	12.928	12.928	12.928
11042	149.768	149.884	149.768	41068	8.819	8.819	8.819
11043	153.858	156.225	153.858	41069	32.941	32.941	32.941
11044	155.727	194.465	157.624	41070	17.615	17.615	17.615
11045	63.557	63.557	63.557	41071	11.977	11.977	11.977
11046	74.160	74.160	74.160	41072	39.703	39.703	39.703
11047	79.865	79.865	79.865	41073	21.941	21.941	21.941
11048	85.742	85.742	85.742	41074	15.020	15.020	15.020
11049	91.628	91.628	91.628	41075	23.166	23.166	23.166
11050	97.251	97.251	97.251	41076	12.778	12.778	12.778
11051	63.557	63.557	63.557	41077	8.771	8.771	8.771
11052	74.160	74.160	74.160	41078	31.521	31.521	31.521
11053	79.865	79.865	79.865	41079	17.375	17.375	17.375
11054	85.742	85.742	85.742	41080	11.900	11.900	11.900

UID	Py_Q (kN)	Py_I_10 (kN)	Py_I_100 (kN)	UID	Py_Q (kN)	Py_I_10 (kN)	Py_I_100 (kN)
11055	91.628	91.628	91.628	41081	79.215	79.215	79.215
11056	97.251	97.251	97.251	41082	91.150	91.150	91.150
11057	57.130	57.130	57.130	41083	96.901	96.901	96.901
11058	31.026	31.026	31.026	41084	102.165	102.165	102.164
11059	21.151	21.151	21.151	41085	106.582	106.606	106.582
11060	31.494	31.494	31.494	41086	109.740	110.452	109.740
11061	17.303	17.303	17.303	41087	79.215	79.215	79.215
11062	11.872	11.872	11.872	41088	91.150	91.150	91.150
11063	44.320	44.320	44.320	41089	96.901	96.901	96.901
11064	24.166	24.166	24.166	41090	102.165	102.165	102.164
11065	16.512	16.512	16.512	41091	106.582	106.606	106.582
11066	56.033	56.033	56.033	41092	109.740	110.452	109.740
11067	30.835	30.835	30.835	41093	40.170	40.170	40.170
11068	21.089	21.089	21.089	41094	47.241	47.241	47.241
11069	31.054	31.054	31.054	41095	51.155	51.155	51.155
11070	17.225	17.225	17.225	41096	55.311	55.311	55.311
11071	11.846	11.846	11.846	41097	59.659	59.659	59.659
11072	43.588	43.588	43.588	41098	64.088	64.088	64.088
11073	24.038	24.038	24.038	41099	40.170	40.170	40.170
11074	16.470	16.470	16.470	41100	47.241	47.241	47.241
11075	52.613	52.615	52.613	41101	51.155	51.155	51.155
11076	30.176	30.176	30.176	41102	55.311	55.311	55.311
11077	20.872	20.872	20.872	41103	59.659	59.659	59.659
11078	29.628	29.629	29.628	41104	64.088	64.088	64.088
11079	16.951	16.951	16.951	81001	63.249	63.249	63.249
11080	11.755	11.755	11.755	81002	63.249	63.249	63.249
11081	41.259	41.260	41.259	81003	31.861	31.861	31.861
11082	23.592	23.592	23.592	81004	31.861	31.861	31.861
11083	16.323	16.323	16.323	81005	63.249	63.249	63.249
11084	78.063	78.063	78.063	81006	73.420	73.420	73.420
11085	42.487	42.487	42.487	81007	78.832	78.832	78.832
11086	29.024	29.024	29.024	81008	31.861	31.861	31.861
11087	43.258	43.258	43.258	81009	37.532	37.532	37.532
11088	23.857	23.857	23.857	81010	40.751	40.751	40.751
11089	16.427	16.427	16.427	81011	63.249	63.249	63.249
11090	60.672	60.672	60.672	81012	73.420	73.420	73.420
11091	33.174	33.174	33.174	81013	78.832	78.832	78.832
11092	22.726	22.726	22.726	81014	31.861	31.861	31.861
11093	76.570	76.570	76.570	81015	37.532	37.532	37.532
11094	42.226	42.226	42.226	81016	40.751	40.751	40.751
11095	28.940	28.940	28.940	81017	26.787	26.787	26.787
11096	42.655	42.655	42.655	81018	14.041	14.041	14.041
11097	23.749	23.749	23.749	81019	9.488	9.488	9.488
11098	16.392	16.392	16.392	81020	13.488	13.488	13.488
11099	59.672	59.672	59.672	81021	7.106	7.106	7.106
11100	32.998	32.998	32.998	81022	4.825	4.825	4.825
11101	22.669	22.669	22.669	81023	20.138	20.138	20.138
11102	71.914	71.916	71.914	81024	10.573	10.573	10.573
11103	41.325	41.325	41.325	81025	7.157	7.157	7.157
11104	28.642	28.642	28.642	81026	26.686	26.686	26.686
11105	40.698	40.698	40.698	81027	14.026	14.026	14.026
11106	23.370	23.370	23.370	81028	9.483	9.483	9.483
11107	16.266	16.266	16.266	81029	13.437	13.437	13.437
11108	56.492	56.493	56.492	81030	7.098	7.098	7.098
11109	32.386	32.386	32.386	81031	4.823	4.823	4.823
11110	22.467	22.467	22.467	81032	20.062	20.062	20.062
21001	110.449	132.849	110.568	81033	10.562	10.562	10.562
21002	100.585	100.591	100.585	81034	7.153	7.153	7.153

UID	Py_Q (kN)	Py_I_10 (kN)	Py_I_100 (kN)	UID	Py_Q (kN)	Py_I_10 (kN)	Py_I_100 (kN)
21003	84.172	84.172	84.172	81035	26.331	26.331	26.331
21004	75.334	75.334	75.334	81036	13.972	13.972	13.972
21005	110.449	132.849	110.568	81037	9.466	9.466	9.466
21006	100.585	100.591	100.585	81038	13.259	13.259	13.259
21007	84.172	84.172	84.172	81039	7.071	7.071	7.071
21008	75.334	75.334	75.334	81040	4.814	4.814	4.814
21011	68.397	68.397	68.397	81041	19.795	19.795	19.795
21012	55.715	55.715	55.715	81042	10.521	10.521	10.521
21013	44.199	44.199	44.199	81043	7.140	7.140	7.140
21014	39.712	39.712	39.712	81044	36.611	36.611	36.611
21015	68.397	68.397	68.397	81045	19.224	19.224	19.224
21016	55.715	55.715	55.715	81046	13.013	13.013	13.013
21017	44.199	44.199	44.199	81047	18.557	18.557	18.557
21018	39.712	39.712	39.712	81048	9.809	9.809	9.809
21019	68.397	68.397	68.397	81049	6.684	6.684	6.684
21020	55.715	55.715	55.715	81050	27.584	27.584	27.584
21021	20.286	20.287	20.286	81051	14.517	14.517	14.517
21022	23.231	23.231	23.231	81052	9.849	9.849	9.849
21023	25.015	25.016	25.015	81053	36.473	36.473	36.473
21024	28.647	28.648	28.647	81054	19.204	19.204	19.204
21025	29.685	29.685	29.685	81055	13.007	13.007	13.007
21026	33.976	33.977	33.977	81056	18.487	18.487	18.487
21027	20.286	20.287	20.286	81057	9.799	9.799	9.799
21028	23.231	23.231	23.231	81058	6.680	6.680	6.680
21029	25.015	25.016	25.015	81059	27.480	27.480	27.480
21030	28.647	28.648	28.647	81060	14.501	14.501	14.501
21031	29.685	29.685	29.685	81061	9.844	9.844	9.844
21032	33.976	33.977	33.977	81062	35.988	35.988	35.988
21033	28.647	28.648	28.647	81063	19.130	19.130	19.130
21034	33.976	33.977	33.977	81064	12.984	12.984	12.984
21035	84.172	84.172	84.172	81065	18.241	18.241	18.241
21036	95.459	95.460	95.460	81066	9.761	9.761	9.761
21037	100.585	100.591	100.585	81067	6.669	6.669	6.669
21038	105.011	105.102	105.011	81068	27.114	27.114	27.114
21039	108.414	109.935	108.414	81069	14.445	14.445	14.445
21040	110.449	132.849	110.568	81070	9.826	9.826	9.826
21041	84.172	84.172	84.172	81071	16.364	16.364	16.364
21042	95.459	95.460	95.460	81072	19.180	19.180	19.180
21043	100.585	100.591	100.585	81073	21.550	21.550	21.550
21044	105.011	105.102	105.011	81074	25.290	25.290	25.290
21045	108.414	109.935	108.414	81075	26.735	26.735	26.735
21046	110.449	132.849	110.568	81076	31.399	31.399	31.399
21047	44.199	44.199	44.199	81077	16.364	16.364	16.364
21048	51.668	51.668	51.668	81078	19.180	19.180	19.180
21049	55.715	55.715	55.715	81079	21.550	21.550	21.550
21050	59.924	59.924	59.924	81080	25.290	25.290	25.290
21051	64.204	64.204	64.204	81081	26.735	26.735	26.735
21052	68.397	68.397	68.397	81082	31.399	31.399	31.399
21053	44.199	44.199	44.199	81083	4.810	4.810	4.810
21054	51.668	51.668	51.668	81084	6.889	6.889	6.889
21055	55.715	55.715	55.715	81085	8.968	8.968	8.968
21056	59.924	59.924	59.924	81086	4.810	4.810	4.810
21057	64.204	64.204	64.204	81087	6.889	6.889	6.889
21058	68.397	68.397	68.397	81088	8.968	8.968	8.968
21059	37.733	37.733	37.733	11111	102.573	102.573	102.573
21060	20.546	20.546	20.546	11112	88.977	88.977	88.977
21061	14.000	14.000	14.000	11113	78.511	78.511	78.511
21062	24.886	24.886	24.886	11114	70.240	70.240	70.240

UID	Py_Q (kN)	Py_I_10 (kN)	Py_I_100 (kN)	UID	Py_Q (kN)	Py_I_10 (kN)	Py_I_100 (kN)
21063	13.679	13.679	13.679	21113	71.505	71.505	71.505
21064	9.358	9.358	9.358	21114	62.015	62.015	62.015
21065	31.316	31.316	31.316	21115	54.690	54.690	54.690
21066	17.114	17.114	17.114	21116	48.891	48.891	48.891
21067	11.679	11.679	11.679	31117	84.410	84.409	84.409
21068	37.160	37.160	37.160	31118	72.521	72.521	72.521
21069	20.445	20.446	20.446	31119	63.572	63.572	63.572
21070	13.967	13.967	13.967	31120	56.609	56.609	56.609
21071	24.568	24.568	24.568	81089	66.443	66.443	66.443
21072	13.622	13.622	13.622	81090	57.136	57.136	57.136
21073	9.340	9.340	9.340	81091	50.089	50.089	50.089
21074	30.880	30.880	30.880	81092	44.582	44.582	44.582
21075	17.037	17.037	17.037	81093	52.875	52.875	52.875
21076	11.654	11.654	11.654	81094	45.387	45.386	45.386
21077	35.320	35.321	35.320	81095	39.750	39.750	39.750
21078	20.095	20.095	20.095	81096	35.365	35.365	35.365
21079	13.852	13.852	13.852	90001	11.199	11.199	11.199
21080	23.527	23.528	23.527	90002	11.176	11.176	11.176
21081	13.421	13.421	13.421	90003	12.593	12.593	12.593
21082	9.273	9.273	9.273	90004	11.639	11.639	11.639
21083	29.465	29.466	29.465	90005	14.986	14.986	14.986
21084	16.767	16.767	16.767	90006	14.587	14.587	14.587
21085	11.566	11.566	11.566	90007	50.771	50.771	50.771
21086	51.643	51.643	51.643	90008	46.812	46.812	46.812
21087	28.167	28.167	28.167	90009	56.346	56.346	56.346
21088	19.223	19.223	19.223	90010	56.443	56.443	56.443
21089	34.202	34.202	34.202	90011	68.093	68.093	68.093
21090	18.844	18.844	18.844	90012	68.193	68.193	68.193
21091	12.922	12.922	12.922	90013	40.483	40.483	40.483
21092	42.931	42.931	42.931	90014	46.625	46.625	46.625
21093	23.507	23.507	23.507	90015	55.916	55.916	55.916
21094	16.073	16.073	16.073	90016	58.280	58.280	58.280
21095	50.861	50.861	50.861	90017	77.410	77.410	77.410
21096	28.029	28.029	28.029	90018	62.949	62.948	62.948
21097	19.178	19.178	19.178	90019	58.278	58.278	58.278
21098	33.765	33.765	33.765	90020	67.766	67.766	67.766
21099	18.766	18.766	18.766	90021	50.791	50.791	50.791
21100	12.896	12.896	12.896	90022	53.677	53.677	53.677
21101	42.335	42.335	42.335	90023	78.237	78.237	78.237
21102	23.401	23.401	23.401	90024	73.507	73.507	73.507
21103	16.038	16.038	16.038	90025	23.687	23.687	23.687
21104	48.348	48.349	48.348	90026	23.687	23.687	23.687
21105	27.550	27.550	27.550	90027	28.739	28.739	28.739
21106	19.021	19.021	19.021	90028	28.790	28.790	28.790
21107	32.335	32.335	32.335	90029	33.640	33.640	33.640
21108	18.489	18.489	18.489	90030	33.640	33.640	33.640
21109	12.805	12.805	12.805	90031	26.805	26.805	26.805
21110	40.398	40.398	40.398	90032	26.748	26.748	26.748
21111	23.031	23.031	23.031	90033	32.588	32.588	32.588
21112	15.916	15.916	15.916	90034	32.475	32.475	32.475
31001	123.754	123.754	123.754	90035	38.088	38.088	38.088
31002	151.969	151.974	151.969	90036	38.258	38.258	38.258
31003	125.611	125.611	125.611	90037	7.512	7.512	7.512
31004	100.879	100.879	100.879	90038	7.749	7.749	7.749
31005	82.579	82.579	82.579	90039	9.087	9.087	9.087
31006	123.754	123.754	123.754	90040	8.552	8.552	8.552
31007	151.969	151.974	151.969	90041	10.688	10.688	10.688
31008	125.611	125.611	125.611	90042	9.995	9.995	9.995

UID	Py_Q (kN)	Py_I_10 (kN)	Py_I_100 (kN)	UID	Py_Q (kN)	Py_I_10 (kN)	Py_I_100 (kN)
31009	100.879	100.879	100.879	90043	31.695	31.695	31.695
31010	82.579	82.579	82.579	90044	33.456	33.456	33.456
31011	62.365	62.365	62.365	90045	37.611	37.611	37.611
31012	83.590	83.590	83.590	90046	39.849	39.849	39.849
31013	65.161	65.161	65.161	90047	43.012	43.012	43.012
31014	51.046	51.046	51.046	90048	44.152	44.152	44.152
31015	41.991	41.991	41.991	90049	27.716	27.716	27.716
31016	62.365	62.365	62.365	90050	30.608	30.608	30.608
31017	83.590	83.590	83.590	90051	34.315	34.315	34.315
31018	65.161	65.161	65.161	90052	34.220	34.220	34.220
31019	51.046	51.046	51.046	90053	37.972	37.972	37.972
31020	41.991	41.991	41.991	90054	35.579	35.579	35.579
31021	29.836	29.835	29.835	90055	30.677	30.677	30.677
31022	34.952	34.952	34.952	90056	23.806	23.806	23.806
31023	40.206	40.206	40.206	90057	26.571	26.571	26.571
31024	47.171	47.171	47.171	90058	24.487	24.487	24.487
31025	50.576	50.576	50.576	90059	33.157	33.157	33.157
31026	59.390	59.390	59.390	90060	40.110	40.110	40.110
31027	29.836	29.835	29.835	90061	17.936	17.935	17.935
31028	34.952	34.952	34.952	90062	17.879	17.879	17.879
31029	40.206	40.206	40.206	90063	20.827	20.827	20.827
31030	47.171	47.171	47.171	90064	20.742	20.742	20.742
31031	50.576	50.576	50.576	90065	23.719	23.719	23.719
31032	59.390	59.390	59.390	90066	23.605	23.605	23.605
31033	8.460	8.460	8.460	90067	12.122	12.122	12.122
31034	12.618	12.618	12.618	90068	12.122	12.122	12.122
31035	16.776	16.776	16.776	90069	14.198	14.198	14.198
31036	8.460	8.460	8.460	90070	14.219	14.219	14.219
31037	12.618	12.618	12.618	90071	16.398	16.398	16.398
31038	16.776	16.776	16.776	90072	16.378	16.378	16.378
31039	100.879	100.879	100.879	90073	52.274	52.274	52.274
31040	117.023	117.022	117.022	90074	52.274	52.274	52.274
31041	125.611	125.611	125.611	90075	61.204	61.204	61.204
31042	134.434	134.433	134.433	90076	61.381	61.381	61.381
31043	143.316	143.317	143.316	90077	70.487	70.487	70.487
31044	151.969	151.974	151.969	90078	70.398	70.398	70.398
31045	100.879	100.879	100.879	90079	45.466	45.466	45.466
31046	117.023	117.022	117.022	90080	45.235	45.235	45.235
31047	125.611	125.611	125.611	90081	52.759	52.759	52.759
31048	134.434	134.433	134.433	90082	52.759	52.759	52.759
31049	143.316	143.317	143.316	90083	60.667	60.667	60.667
31050	151.969	151.974	151.969	90084	60.667	60.667	60.667
31051	51.046	51.046	51.046	90085	33.282	33.282	33.282
31052	60.049	60.049	60.049	90086	33.282	33.282	33.282
31053	65.161	65.161	65.161	90087	38.539	38.539	38.539
31054	70.754	70.754	70.754	90088	38.652	38.652	38.652
31055	76.884	76.884	76.884	90089	44.700	44.700	44.700
31056	83.590	83.590	83.590	90090	44.813	44.813	44.813
31057	51.046	51.046	51.046	90091	7.726	7.726	7.726
31058	60.049	60.049	60.049	90092	7.747	7.747	7.747
31059	65.161	65.161	65.161	90093	8.764	8.764	8.764
31060	70.754	70.754	70.754	90094	8.785	8.785	8.785
31061	76.884	76.884	76.884	90095	9.802	9.802	9.802
31062	83.590	83.590	83.590	90096	9.802	9.802	9.802
31063	50.040	50.040	50.040	90097	33.406	33.406	33.406
31064	26.239	26.239	26.239	90098	33.406	33.406	33.406
31065	17.737	17.737	17.737	90099	37.826	37.826	37.826
31066	23.442	23.442	23.442	90100	37.826	37.826	37.826

UID	Py_Q (kN)	Py_I_10 (kN)	Py_I_100 (kN)	UID	Py_Q (kN)	Py_I_10 (kN)	Py_I_100 (kN)
31067	12.368	12.368	12.368	90101	42.378	42.378	42.378
31068	8.412	8.412	8.412	90102	42.334	42.334	42.334
31069	36.741	36.741	36.741	90103	28.778	28.778	28.778
31070	19.304	19.304	19.304	90104	28.816	28.816	28.816
31071	13.074	13.074	13.074	90105	32.655	32.655	32.655
31072	49.852	49.852	49.852	90106	32.616	32.616	32.616
31073	26.211	26.211	26.211	90107	36.685	36.685	36.685
31074	17.728	17.728	17.728	90108	36.608	36.608	36.608
31075	23.354	23.354	23.354	90109	21.030	21.030	21.030
31076	12.355	12.355	12.355	90110	21.002	21.002	21.002
31077	8.408	8.408	8.408	90111	23.913	23.913	23.913
31078	36.603	36.603	36.603	90112	23.913	23.913	23.913
31079	19.283	19.283	19.283	90113	26.626	26.626	26.626
31080	13.068	13.068	13.068	90114	26.598	26.598	26.598
31081	49.189	49.189	49.189	91001	30.181	30.181	30.181
31082	26.109	26.109	26.109	91002	34.446	34.447	34.446
31083	17.697	17.697	17.697	91003	39.343	39.343	39.343
31084	23.043	23.043	23.043	91004	44.852	44.854	44.852
31085	12.307	12.307	12.307	91005	48.299	48.299	48.299
31086	8.393	8.393	8.393	91006	54.965	54.970	54.965
31087	36.116	36.116	36.116	91007	20.286	20.287	20.286
31088	19.208	19.208	19.208	91008	23.231	23.231	23.231
31089	13.045	13.045	13.045	91009	25.015	25.016	25.015
31090	68.246	68.246	68.246	91010	28.647	28.648	28.647
31091	35.854	35.854	35.854	91011	29.685	29.685	29.685
31092	24.282	24.282	24.282	91012	33.976	33.977	33.977
31093	32.137	32.137	32.137	91013	29.836	29.835	29.835
31094	17.024	17.024	17.024	91014	34.952	34.952	34.952
31095	11.623	11.623	11.623	91015	40.206	40.206	40.206
31096	50.191	50.191	50.191	91016	47.171	47.171	47.171
31097	26.439	26.439	26.439	91017	50.576	50.576	50.576
31098	17.953	17.953	17.953	91018	59.390	59.390	59.390
31099	67.989	67.989	67.989	91019	8.460	8.460	8.460
31100	35.816	35.816	35.816	91020	12.618	12.618	12.618
31101	24.270	24.270	24.270	91021	16.776	16.776	16.776
31102	32.016	32.016	32.016	91022	19.287	19.287	19.287
31103	17.006	17.005	17.005	91023	22.345	22.345	22.345
31104	11.617	11.617	11.617	91024	24.176	24.176	24.176
31105	50.003	50.003	50.003	91025	27.995	27.995	27.995
31106	26.411	26.411	26.411	91026	28.998	28.997	28.997
31107	17.944	17.944	17.944	91027	33.544	33.544	33.544
31108	67.085	67.085	67.085	91028	6.265	6.265	6.265
31109	35.677	35.677	35.677	91029	8.345	8.345	8.345
31110	24.227	24.227	24.227	91030	10.424	10.424	10.424
31111	31.590	31.590	31.590	91031	19.287	19.287	19.287
31112	16.940	16.940	16.940	91032	22.345	22.345	22.345
31113	11.597	11.597	11.597	91033	24.176	24.176	24.176
31114	49.337	49.337	49.337	91034	27.995	27.995	27.995
31115	26.309	26.309	26.309	91035	28.998	28.997	28.997
31116	17.912	17.912	17.912	91036	33.544	33.544	33.544
41001	109.740	110.452	109.740	91037	6.265	6.265	6.265
41002	96.901	96.901	96.901	91038	8.345	8.345	8.345
41003	79.215	79.215	79.215	91039	10.424	10.424	10.424
41004	70.030	70.030	70.030	92001	163.254	163.254	163.254
41005	109.740	110.452	109.740	92002	85.738	85.738	85.738
41006	96.901	96.901	96.901	92003	103.151	103.151	103.151
41007	79.215	79.215	79.215	92004	54.590	54.590	54.590
41008	70.030	70.030	70.030	92005	123.754	123.754	123.754

UID	Py_Q (kN)	Py_I_10 (kN)	Py_I_100 (kN)	UID	Py_Q (kN)	Py_I_10 (kN)	Py_I_100 (kN)
41009	109.740	110.452	109.740	92006	62.365	62.365	62.365
41010	70.030	70.030	70.030	92007	82.579	82.579	82.579
41011	64.088	64.088	64.088	92008	41.991	41.991	41.991
41012	51.155	51.155	51.155	92009	75.334	75.334	75.334
41013	40.170	40.170	40.170	92010	39.712	39.712	39.712
41014	35.637	35.637	35.637	92011	70.030	70.030	70.030
41015	64.088	64.088	64.088	92012	35.637	35.637	35.637
41016	51.155	51.155	51.155	19001	155.727	194.465	157.624
41017	40.170	40.170	40.170	19002	85.738	85.738	85.738
41018	35.637	35.637	35.637	19003	97.251	97.251	97.251
41019	64.088	64.088	64.088	89001	63.249	63.249	63.249
41020	35.637	35.637	35.637				

Appendix I

Comparison between AS4600 and DSM design equations (MDM)

Table Appendix I.1 Data for comparison between AS4600 and DSM design equations (MDM)

SEQ	LC-FC	P_{EXP} (kN)	P_{AS} (kN)	P_{DSM} (kN)	P_{EXP}/P_{AS}	P_{EXP}/P_{DSM}
11001	ITF-F	99.689	99.700	105.237	1.000	0.947
11002	ITF-F	72.404	N/A	84.727		0.855
11003	ITF-F	79.656	N/A	88.284		0.902
11004	ITF-F	76.085	83.362	82.356	0.913	0.924
11005	ITF-F	80.004	85.045	79.424	0.941	1.007
11006	ITF-F	99.176	99.700	105.237	0.995	0.942
11007	ITF-F	72.020	N/A	84.727		0.850
11008	ITF-F	79.418	N/A	88.284		0.900
11009	ITF-F	77.348	83.362	82.356	0.928	0.939
11010	ITF-F	80.681	85.045	79.424	0.949	1.016
11011	ITF-F	75.664	89.998	80.263	0.841	0.943
11012	ITF-F	64.274	N/A	62.293		1.032
11013	ITF-F	63.541	N/A	58.328		1.089
11014	ITF-F	59.311	75.249	61.094	0.788	0.971
11015	ITF-F	60.850	76.846	54.843	0.792	1.110
11016	ITF-F	75.700	89.998	80.263	0.841	0.943
11017	ITF-F	63.908	N/A	62.293		1.026
11018	ITF-F	64.109	N/A	58.328		1.099
11019	ITF-F	58.780	75.249	61.094	0.781	0.962
11020	ITF-F	60.740	76.846	54.843	0.790	1.108
11021	ITF-F	7.869	N/A	5.816		1.353
11022	ITF-F	8.323	N/A	6.291		1.323
11023	ITF-F	6.672	N/A	5.997		1.113
11024	ITF-F	6.979	N/A	6.554		1.065
11025	ITF-F	5.760	N/A	6.461		0.892
11026	ITF-F	5.356	N/A	7.116		0.753
11027	ITF-F	7.753	N/A	5.816		1.333
11028	ITF-F	8.389	N/A	6.291		1.333
11029	ITF-F	6.944	N/A	5.997		1.158
11030	ITF-F	6.454	N/A	6.554		0.985
11031	ITF-F	5.498	N/A	6.461		0.851
11032	ITF-F	5.142	N/A	7.116		0.723
21001	ETF-F	37.154	N/A	36.469		1.019
21002	ETF-F	42.153	N/A	40.483		1.041
21003	ETF-F	41.787	49.502	40.257	0.844	1.038
21004	ETF-F	42.538	51.112	45.183	0.832	0.941
21005	ETF-F	36.660	N/A	36.469		1.005
21006	ETF-F	41.879	N/A	40.483		1.034
21007	ETF-F	41.128	49.502	40.257	0.831	1.022
21008	ETF-F	42.996	51.112	45.183	0.841	0.952
21011	ETF-F	32.686	N/A	28.925		1.130
21012	ETF-F	29.720	N/A	29.588		1.004
21013	ETF-F	30.544	46.494	34.074	0.657	0.896
21014	ETF-F	31.844	48.077	34.289	0.662	0.929
21015	ETF-F	32.448	N/A	28.925		1.122
21016	ETF-F	32.650	N/A	29.588		1.103
21017	ETF-F	30.526	46.494	34.074	0.657	0.896
21018	ETF-F	32.869	48.077	34.289	0.684	0.959
21019	ETF-F	30.983	N/A	28.925		1.071
21020	ETF-F	31.295	N/A	29.588		1.058

SEQ	LC-FC	P_{EXP} (kN)	P_{AS} (kN)	P_{DSM} (kN)	P_{EXP}/P_{AS}	P_{EXP}/P_{DSM}
21021	ETF-F	2.638	N/A	1.859		1.419
21022	ETF-F	2.749	N/A	2.010		1.368
21023	ETF-F	1.975	N/A	1.787		1.105
21024	ETF-F	2.633	N/A	1.959		1.344
21025	ETF-F	1.673	N/A	1.854		0.902
21026	ETF-F	2.126	N/A	2.053		1.036
21027	ETF-F	2.842	N/A	1.859		1.529
21028	ETF-F	2.767	N/A	2.010		1.377
21029	ETF-F	2.077	N/A	1.787		1.163
21030	ETF-F	2.073	N/A	1.959		1.058
21031	ETF-F	1.641	N/A	1.854		0.885
21032	ETF-F	1.673	N/A	2.053		0.815
21033	ETF-F	2.011	N/A	1.959		1.026
21034	ETF-F	1.628	N/A	2.053		0.793
31001	IOF-F	80.205	113.903	83.818	0.704	0.957
31002	IOF-F	61.491	N/A	76.846		0.800
31003	IOF-F	61.802	N/A	76.602		0.807
31004	IOF-F	63.761	99.600	70.729	0.640	0.901
31005	IOF-F	59.330	104.268	58.006	0.569	1.023
31006	IOF-F	80.425	113.903	83.818	0.706	0.960
31007	IOF-F	61.619	N/A	76.846		0.802
31008	IOF-F	60.886	N/A	76.602		0.795
31009	IOF-F	62.608	99.600	70.729	0.629	0.885
31010	IOF-F	58.286	104.268	58.006	0.559	1.005
31011	IOF-F	64.567	104.659	58.383	0.617	1.106
31012	IOF-F	49.167	N/A	52.683		0.933
31013	IOF-F	50.815	N/A	47.484		1.070
31014	IOF-F	50.082	91.516	48.411	0.547	1.035
31015	IOF-F	46.365	95.985	39.998	0.483	1.159
31016	IOF-F	63.578	104.659	58.383	0.607	1.089
31017	IOF-F	49.368	N/A	52.683		0.937
31018	IOF-F	50.870	N/A	47.484		1.071
31019	IOF-F	50.339	91.516	48.411	0.550	1.040
31020	IOF-F	45.816	95.985	39.998	0.477	1.145
31021	IOF-F	8.145	N/A	5.868		1.388
31022	IOF-F	8.078	N/A	6.460		1.251
31023	IOF-F	7.331	N/A	6.567		1.116
31024	IOF-F	7.531	N/A	7.311		1.030
31025	IOF-F	6.775	N/A	7.306		0.927
31026	IOF-F	7.317	N/A	8.216		0.891
31027	IOF-F	7.887	N/A	5.868		1.344
31028	IOF-F	8.314	N/A	6.460		1.287
31029	IOF-F	7.317	N/A	6.567		1.114
31030	IOF-F	7.535	N/A	7.311		1.031
31031	IOF-F	6.873	N/A	7.306		0.941
31032	IOF-F	7.495	N/A	8.216		0.912
31033	IOF-F	7.500	13.310	7.009	0.563	1.070
31034	IOF-F	7.976	11.084	7.704	0.720	1.035
31035	IOF-F	8.087	9.375	7.457	0.863	1.084
31036	IOF-F	7.531	13.310	7.009	0.566	1.074
31037	IOF-F	8.171	11.084	7.704	0.737	1.061
31038	IOF-F	7.553	9.375	7.457	0.806	1.013
41001	EOF-F	46.264	N/A	53.420		0.866
41002	EOF-F	46.704	N/A	52.488		0.890
41003	EOF-F	43.609	49.837	47.191	0.875	0.924
41004	EOF-F	48.846	52.173	46.620	0.936	1.048
41005	EOF-F	47.088	N/A	53.420		0.881
41006	EOF-F	45.532	N/A	52.488		0.867

SEQ	LC-FC	P_{EXP} (kN)	P_{AS} (kN)	P_{DSM} (kN)	P_{EXP}/P_{AS}	P_{EXP}/P_{DSM}
41007	EOF-F	47.125	49.837	47.191	0.946	0.999
41008	EOF-F	49.414	52.173	46.620	0.947	1.060
41009	EOF-F	46.924	N/A	53.420		0.878
41010	EOF-F	48.132	52.173	46.620	0.923	1.032
41011	EOF-F	35.909	N/A	39.201		0.916
41012	EOF-F	35.552	N/A	35.049		1.014
41013	EOF-F	34.380	39.905	35.802	0.862	0.960
41014	EOF-F	36.715	41.853	33.413	0.877	1.099
41015	EOF-F	36.266	N/A	39.201		0.925
41016	EOF-F	35.900	N/A	35.049		1.024
41017	EOF-F	35.552	39.905	35.802	0.891	0.993
41018	EOF-F	37.658	41.853	33.413	0.900	1.127
41019	EOF-F	36.257	N/A	39.201		0.925
41020	EOF-F	36.724	41.853	33.413	0.877	1.099
81001	EOF-UF	39.315	49.837	39.267	0.789	1.001
81002	EOF-UF	41.421	49.837	39.267	0.831	1.055
81003	EOF-UF	30.077	39.905	27.614	0.754	1.089
81004	EOF-UF	29.509	39.905	27.614	0.739	1.069
81071	EOF-UF	3.892	N/A	2.458		1.583
81072	EOF-UF	4.217	N/A	2.696		1.564
81073	EOF-UF	2.931	N/A	2.333		1.256
81074	EOF-UF	3.238	N/A	2.613		1.239
81075	EOF-UF	2.442	N/A	2.477		0.986
81076	EOF-UF	2.682	N/A	2.816		0.952
81077	EOF-UF	3.790	N/A	2.458		1.542
81078	EOF-UF	4.039	N/A	2.696		1.498
81079	EOF-UF	3.056	N/A	2.333		1.310
81080	EOF-UF	3.309	N/A	2.613		1.267
81081	EOF-UF	2.482	N/A	2.477		1.002
81082	EOF-UF	2.633	N/A	2.816		0.935
81083	EOF-UF	3.643	N/A	3.468		1.051
81084	EOF-UF	2.789	N/A	2.595		1.075
81085	EOF-UF	2.215	N/A	2.034		1.089
81086	EOF-UF	3.772	N/A	3.468		1.088
81087	EOF-UF	2.762	N/A	2.595		1.065
81088	EOF-UF	2.202	N/A	2.034		1.082
90001	IOF-UF	12.677	N/A	11.054		1.147
90002	IOF-UF	12.455	N/A	10.993		1.133
90003	IOF-UF	13.033	N/A	11.213		1.162
90004	IOF-UF	13.033	N/A	10.384		1.255
90005	IOF-UF	12.900	N/A	12.080		1.068
90006	IOF-UF	13.345	N/A	11.753		1.135
90007	IOF-UF	48.041	91.539	36.394	0.525	1.320
90008	IOF-UF	47.729	90.279	41.700	0.529	1.145
90009	IOF-UF	51.065	85.651	45.551	0.596	1.121
90010	IOF-UF	50.709	85.608	45.685	0.592	1.110
90011	IOF-UF	55.736	81.873	49.641	0.681	1.123
90012	IOF-UF	56.715	81.835	49.656	0.693	1.142
90013	IOF-UF	38.166	65.317	30.596	0.584	1.247
90014	IOF-UF	38.255	66.616	34.291	0.574	1.116
90015	IOF-UF	38.166	62.707	35.253	0.609	1.083
90016	IOF-UF	37.943	63.022	36.386	0.602	1.043
90017	IOF-UF	38.477	60.482	28.299	0.636	1.360
90018	IOF-UF	38.699	58.892	34.519	0.657	1.121
90037	EOF-UF	6.397	N/A	6.549		0.977
90038	EOF-UF	6.227	N/A	6.704		0.929
90039	EOF-UF	6.174	N/A	6.713		0.920
90040	EOF-UF	6.121	N/A	6.472		0.946

SEQ	LC-FC	P_{EXP} (kN)	P_{AS} (kN)	P_{DSM} (kN)	P_{EXP}/P_{AS}	P_{EXP}/P_{DSM}
90041	EOF-UF	5.952	N/A	6.496		0.916
90042	EOF-UF	5.720	N/A	6.308		0.907
90043	EOF-UF	25.969	45.376	26.502	0.572	0.980
90044	EOF-UF	26.520	46.317	27.600	0.573	0.961
90045	EOF-UF	26.636	43.451	26.533	0.613	1.004
90046	EOF-UF	27.801	44.456	23.468	0.625	1.185
90047	EOF-UF	24.136	41.324	25.311	0.584	0.954
90048	EOF-UF	25.132	41.839	25.719	0.601	0.977
90049	EOF-UF	18.238	34.368	19.005	0.531	0.960
90050	EOF-UF	18.736	35.821	20.271	0.523	0.924
90051	EOF-UF	17.846	33.143	17.903	0.538	0.997
90052	EOF-UF	18.460	33.182	17.909	0.556	1.031
90053	EOF-UF	16.850	30.867	15.892	0.546	1.060
90054	EOF-UF	16.627	29.972	15.459	0.555	1.076
90067	ITF-UF	14.679	N/A	11.808		1.243
90068	ITF-UF	14.457	N/A	11.801		1.225
90069	ITF-UF	14.679	N/A	12.467		1.177
90070	ITF-UF	14.457	N/A	12.486		1.158
90071	ITF-UF	14.234	N/A	12.861		1.107
90072	ITF-UF	14.457	N/A	12.849		1.125
90073	ITF-UF	61.163	N/A	46.790		1.307
90074	ITF-UF	61.385	N/A	46.775		1.312
90075	ITF-UF	61.163	N/A	49.355		1.239
90076	ITF-UF	60.496	N/A	49.424		1.224
90077	ITF-UF	61.163	N/A	50.623		1.208
90078	ITF-UF	61.385	N/A	50.593		1.213
90091	ETF-UF	6.450	N/A	5.975		1.079
90092	ETF-UF	6.343	N/A	5.974		1.062
90093	ETF-UF	6.450	N/A	5.543		1.164
90094	ETF-UF	6.450	N/A	5.540		1.164
90095	ETF-UF	5.783	N/A	5.085		1.137
90096	ETF-UF	5.889	N/A	5.181		1.137
90097	ETF-UF	25.132	N/A	24.858		1.011
90098	ETF-UF	24.794	N/A	24.849		0.998
90099	ETF-UF	24.020	N/A	23.044		1.042
90100	ETF-UF	23.575	N/A	23.064		1.022
90101	ETF-UF	21.574	N/A	21.067		1.024
90102	ETF-UF	21.351	N/A	21.073		1.013
19001	ITF-F	75.023	N/A	84.727		0.885
19002	ITF-F	75.609	89.998	80.263	0.840	0.942
19003	ITF-F	63.468	N/A	62.293		1.019
89001	EOF-UF	40.689	49.837	39.267	0.816	1.036

Appendix J

Miscellaneous

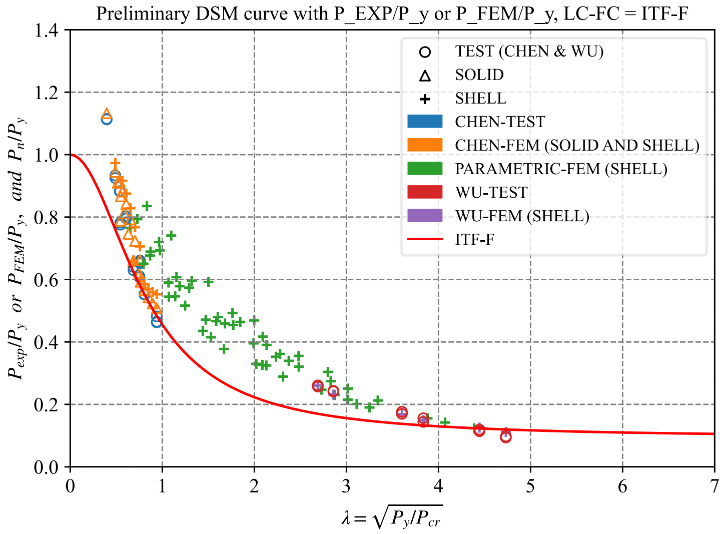

Figure Appendix J.1 DSM design curve for the ITF-F loading case

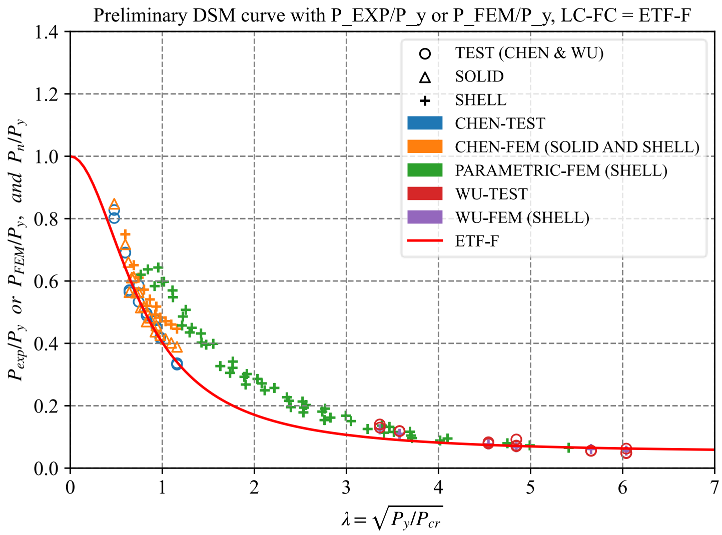

Figure Appendix J.2 DSM design curve for the ETF-F loading case